

DISS. ETH NO. 28037

***Hydrogen Bonding Structure Of Water At Interfaces Relevant For  
Ice Nucleation***

A thesis submitted to attain the degree of  
DOCTOR OF SCIENCES of ETH ZURICH

(Dr. sc. ETH Zurich)

presented by

*HUANYU YANG*

*MSc., Physics, Università degli Studi di Roma "La Sapienza"*

born on 11.09.1990

citizen of People's Republic of China

accepted on the recommendation of

*Prof. Markus Ammann*

*Prof. Thomas Peter*

*Dr. Hendrik Bluhm*

2021

---

# TABLE OF CONTENTS

---

Abstract.....	4
Abstract (ITA).....	5
1 Introduction.....	6
1.1 Ice nucleation.....	6
1.2 Questions towards better understanding the surface science of ice nucleation and thesis goal 10	
1.3 Overview of interface techniques to probe water structure.....	11
1.4 Overview of XPS and NEXAFS at the Swiss Light Source .....	14
1.5 Outline of the thesis .....	17
2 Water adsorption on TiO <sub>2</sub> Nanoparticle surface .....	22
2.1 Disordered Adsorbed Water Layers on TiO <sub>2</sub> Nanoparticles under Subsaturated Humidity Conditions at 235 K .....	22
2.2 Supporting information.....	32
2.2.1 Experimental Methods and Data Analysis.....	32
2.2.2 Electron yield NEXAFS spectra and analysis.....	35
3 Water adsorption on Silver Iodide surface.....	38
3.1 Ordered Hydrogen Bonding Structure of Water Molecules Adsorbed on Silver Iodide Particles under Subsaturated Conditions.....	38
3.1.1 Introduction.....	38
3.1.2 Materials and experimental methods .....	41
3.1.3 Results and discussion .....	42
3.1.4 Conclusion .....	50
3.2 Supporting Information.....	55
3.2.1 Experimental setup.....	55
3.2.2 XPS normalization and Gaussian deconvolution parameters .....	56
3.2.3 Attenuation model and fitting of the O1s <sub>ads</sub> /I3d ratio.....	62
3.2.4 Fitting results .....	66
3.2.5 O K edge NEXAFS of liquid water and ice.....	67
3.2.6 Gaussian peak deconvolution of O K edge NEXAFS .....	67
4 Water adsorption on K-feldspar particle surface .....	72
4.1 Surface potassium ion exchange controls the coordination of water molecules on the surface of feldspar .....	72
4.1.1 Introduction.....	72
4.1.2 Materials and Methods.....	74

---

4.1.3	Results and discussion .....	75
4.1.4	Conclusion .....	82
4.2	Supporting information .....	86
4.2.1	C1s spectra and elements depth profile of single crystal sample .....	86
4.2.2	Attenuation model for adsorption thickness determination .....	89
4.2.3	O K NEXAFS of K-feldspars at dry and humid condition .....	91
4.2.4	Experiments on the K-feldspar powder sample .....	93
5	Water molecules ordering at the liquid-vapor interface.....	97
5.1	Resorcinol and Orcinol Lead to Local Ordering of Water Molecules near the Liquid-Vapor Interface .....	97
5.1.1	Introduction.....	97
5.1.2	Sample and experimental methods .....	99
5.1.3	Results and discussion .....	103
5.1.4	Conclusions.....	113
5.2	Supporting information.....	118
5.2.1	Molecular dynamics and Density of States Computational Details .....	118
5.2.2	XPS of O1s for RES and ORC at 155eV Kinetic Energy .....	127
5.2.3	Raw valence level spectra with gas phase water molecules contribution .....	128
5.2.4	Attenuation model for XPS.....	129
6	Conclusion and Outlook.....	134
6.1	Conclusion .....	134
6.2	Outlook .....	138

---

## ABSTRACT

---

Solid-vapor and liquid vapor interfaces have a strong influence on heterogeneous ice nucleation and cloud droplet activation; they are providing a large space for chemical and physical phenomena. The interaction between a substrate and water molecules at these interfaces plays a role in the coordination of water molecules among themselves, which is represented by the hydrogen bonding (HB) structure of water molecules. However, the knowledge gap in understanding the interfacial water structure at a molecular level and the implications for ice nucleation is still very big. Especially, our knowledge for the key properties controlling the water structure at different interfaces is far from complete. The aim of this thesis is to understand how different surfaces or organic molecules can orchestrate a structural change for interfacial water. This is achieved by probing the surface composition of humid solid surfaces (at subsaturated condition with respect to ice) or the liquid-vapor interface of aqueous organic solutions.

To evaluate the HB network of interfacial water molecules, we need depth resolved and structure specific information from the surface down to the nm range. For this purpose, X-ray photoelectron spectroscopy (XPS) was used to probe the chemical composition at the sample surface. Conventional XPS experiments have been limited to ultrahigh vacuum conditions because of the inelastic scattering of electrons in the gas phase. Our recent advances in instrumentation coupled with a third generation synchrotron radiation source enabled *in-situ* XPS measurements at several mbar pressure. This makes our experiment on solid materials under humid conditions possible. Meanwhile, Auger electron yield near-edge X-ray absorption fine structure (NEXAFS) spectroscopy was used to locally assess the HB structure of adsorbed water molecules. The NEXAFS spectroscopy is based on the excitation of core electrons into the lowest unoccupied molecular orbitals (LUMO). NEXAFS probes the local LUMO structure of water molecules, and exhibits major differences between liquid water and ice. By detecting NEXAFS via the yield of Auger electrons from the relaxation of the core-hole state, the method becomes surface sensitive. It is an ideal tool to study the HB structure of interfacial water molecules.

Liquid water and ice are considered as reference for two extremely different configurations of the HB network. When comparing to the structure of liquid water or ice, our results confirm that on different solid/liquid surfaces, water molecules are showing different coordination structure. TiO<sub>2</sub> and AgI induced disordered and ordered HB structure of water molecules, respectively, which parallels with their established efficiency to nucleate ice. On a K-feldspar mineral surface, water structure appeared controlled by framework K<sup>+</sup> cations segregating into the adsorbed water layer. In turn, after depletion of K<sup>+</sup>, the surface promoted tetrahedral coordination. On the liquid-vapor interface, water molecules are influenced by the presence of organic molecules. Resorcinol and orcinol molecules were taken as simple proxies for a range of phenolic compounds in the atmosphere. Due to the preferential hydration of their OH groups and the tendency for aggregation via stacking, these molecules exhibit significant propensity and molecular orientation at the liquid-vapor interface, which was confirmed by our XPS data. Considering also molecular dynamics simulations, our results suggest that the presence of these molecules induce a local more tetrahedral coordination among interfacial water molecules.

Overall, this work reveals the water HB structure at different interfaces is the result of a complex interplay of interactions of water molecules among each other and with the solid substrates or organic molecules on a molecular level. These findings have significant atmospheric relevance, as the studied solid materials and organic molecules are considered important ice nucleating materials originating from both anthropogenic and biogenic nature, and their changing abundance and composition is implicated in climate change. This work will spur future investigations towards interfacial water molecules on other materials or aqueous solutions in an atmospheric but also other scientific contexts.

---

## ABSTRACT (ITA)

---

Le caratteristiche chimico-fisiche delle interfacce solido-vapore e liquido-vapore possono influenzare notevolmente la nucleazione eterogenea del ghiaccio e l'attivazione delle goccioline di acqua nelle nubi. L'interazione tra un substrato solido e le molecole d'acqua svolge un ruolo nella coordinazione tra queste ultime, arrivando a modificare la struttura del legame a idrogeno. Tuttavia, il grado di conoscenza e comprensione della struttura molecolare dell'acqua all'interfaccia, e di quali siano le proprietà chiave a controllarla, è ancora molto limitato. Lo scopo di questa tesi è capire come diverse superfici solide o molecole organiche possano influenzare la struttura locale dell'acqua a livello interfacciale. Ciò si ottiene analizzando la composizione superficiale di superfici umide (in condizioni subsature rispetto al ghiaccio) o l'interfaccia liquido-vapore di soluzioni acquose contenenti soluti organici.

Per valutare la rete del legame a idrogeno di molecole d'acqua all'interfaccia, è necessario ottenere informazioni specifiche risolte in profondità e relative alla struttura locale delle molecole nel range del nanometro. A tale scopo, è stata utilizzata la spettroscopia fotoelettronica a raggi X (XPS). Gli esperimenti XPS convenzionali sono limitati a condizioni di ultra alto vuoto a causa dello scattering anelastico dei fotoelettroni in fase gas. Recenti sviluppi tecnologici nella strumentazione, abbinati all'utilizzo di sorgenti di radiazione di sincrotrone di terza generazione, hanno consentito misurazioni XPS in situ a diversi mbar di pressione. Questo rende possibili esperimenti su materiali solidi a diversi gradi di umidità relativa. In parallelo agli studi XPS, l'analisi di spettri di assorbimento di raggi X near edge (NEXAFS) della soglia K dell'ossigeno, ha consentito la valutazione della struttura locale di molecole d'acqua adsorbite. La spettroscopia NEXAFS, basata sull'eccitazione di elettroni da livelli di core a orbitali molecolari liberi a bassa energia, mostra grandi differenze tra acqua liquida e ghiaccio, associabili alla struttura degli orbitali molecolari vuoti. In questo lavoro, gli spettri NEXAFS della soglia K dell'ossigeno sono stati acquisiti valutando la resa di elettroni Auger derivanti dal rilassamento dello stato di core-hole, consentendo quindi di preservare sensibilità alla superficie. Tale spettroscopia rappresenta uno strumento ideale per studiare la struttura dei legami a idrogeno tra le molecole d'acqua all'interfaccia. A questo scopo, acqua liquida e ghiaccio sono stati presi come riferimenti per due configurazioni diverse della rete dei legami a idrogeno. I risultati ottenuti confermano che le molecole d'acqua mostrano una struttura di coordinazione diversa se adsorbite su diverse superfici solide. Ossido di titanio e ioduro d'argento inducono rispettivamente una organizzazione disordinata e ordinata dei legami a idrogeno. Su di una superficie minerale di feldspato di potassio, la struttura dell'acqua viene controllata dai cationi  $K^+$  che segregano verso le molecole d'acqua adsorbite. Se gli ioni  $K^+$  vengono rimossi, viene favorita una coordinazione tetraedrica tra le molecole di acqua. All'interfaccia liquido-vapore, le molecole d'acqua sono influenzate dalla presenza di molecole organiche. Le molecole di resorcinolo e orcinolo sono state prese come semplici proxy per una serie di composti fenolici presenti in atmosfera. A causa dell'idratazione preferenziale dei loro gruppi ossidrilici e della tendenza all'aggregazione tramite impilamento, queste molecole mostrano una significativa propensione e un orientamento molecolare preferenziale all'interfaccia, confermati dai dati XPS. Dati sperimentali, supportati da simulazioni di dinamica molecolare, suggeriscono infine che la presenza di tali composti organici induca una coordinazione locale più tetraedrica tra le molecole d'acqua all'interfaccia.

Ricapitolando, questo lavoro rivela che la struttura dei legami a idrogeno dell'acqua, analizzata in corrispondenza di diverse interfacce, è il risultato di complesse interazioni tra le molecole d'acqua stesse e con substrati solidi o molecole organiche in soluzioni acquose. Questi risultati hanno una implicazione significativa per lo studio di fenomeni atmosferici, perché dimostrano che materiali di natura antropogenica e biogenica, la cui abbondanza e composizione sono condizionate dal cambiamento climatico, influenzano la nucleazione del ghiaccio. Questo lavoro stimolerà ulteriori indagini volte alla caratterizzazione della struttura locale dell'acqua su altri solidi e/o soluzioni acquose.

# 1 INTRODUCTION

---

## 1.1 ICE NUCLEATION

More than 70 percent of our Earth surface is covered by water, it is one of the most common substances in our daily life. There are roughly more than 1,300,000,000 cubic kilometers of water in our Earth. Sea water consists of 97 percent of Earth's water amount, and only three percent is freshwater. Water plays an important role in a wide range of scientific disciplines, including physics, chemistry, medicine, biology, geography, atmospheric science and astronomy.

Water states are generally described by the water phase diagram, that predicts the thermodynamically distinct phases at a given pressure and temperature. Depending on the thermodynamic condition, water can occur in three states on our Earth: solid (ice, covers 10 percent of Earth's surface), liquid (covers 71 percent of Earth's surface) or gas phase (vapor, 2 percent of the atmosphere by composition). When looking at the ice side, it can assume 19 known solid crystalline phases, among which  $I_h$  and  $I_c$  are most atmospherically relevant. Ice nucleation (IN) is one of the most common and important physical processes associated with water. In the atmosphere, the formation of ice is controlled by IN, which can influence the cloud microphysics, precipitation (Cantrell and Heymsfield 2005) and Earth's radiation budget (Borduas and Donahue 2018). In nature, IN can occur in two different modes: homogeneously and heterogeneously.

### Homogeneous ice nucleation

Homogeneous IN of water molecules is not influenced by any foreign material. In the gas phase or in pure liquid water homogenous IN requires overcoming a free energy barrier at a supersaturation ratio much greater than 1.0 (Wang 2013).

Homogeneous IN is typically described by classical nucleation theory (Pruppacher and Klett 1997), in which the nucleation rate  $J$  is proportional to a Boltzmann distribution factor:

$$J \propto \exp\left(-\frac{\Delta G}{kT}\right)$$

where  $\Delta G$  is the activation energy barrier.  $\Delta G$  depends on the size of a water molecule, the interfacial surface tension, temperature and saturation ratio (Zobrist, Koop et al. 2007). Prior to homogeneous IN, water molecules cluster forming what is known as either a liquid or ice germ. When the cluster grows and reaches a critical size with an energy corresponding to  $\Delta G$ , then nucleation occurs followed by a bulk phase change and a decrease in energy due to latent heat release. The maximum of  $\Delta G$  is thus the energy barrier that water molecular clusters need to overcome in order to activate the IN process, this can be more easily triggered at low temperature due to the fact that  $\Delta G$  and the critical cluster size requirement both decrease with temperature. Water molecules rapidly form and evaporate clusters, however, it is not at all likely that clusters grow large enough to overcome the energy barrier close to saturation. From a probabilistic point of view, low temperature facilitates super saturation ratios much higher than 1.0 for constant water partial pressure, and increases the probability that a water molecular

cluster will grow larger than that of the critical size and spontaneously nucleate. For pure water, IN requires a low temperature at  $-38\text{ }^{\circ}\text{C}$ . At these conditions, homogeneous IN is most likely involved in the formation of high cirrus clouds or in convective storms (Wang 2013). However, for middle and low clouds, most ice particles are formed at much warmer temperature, via heterogeneous ice nucleation.

### Heterogeneous ice nucleation

The heterogeneous IN is the dominant mechanism by which ice forms in a mixed-phase cloud, it refers to the formation of ice with a condensed material involved, such as solid aerosol particles. By providing energetically favorable conditions for the activation process, those solid particles that facilitate the ice nucleation are called ice nucleating particles (INP). This way, heterogeneous IN plays an important role for ice formation in the atmosphere at temperatures higher than  $-38\text{ }^{\circ}\text{C}$ . The interface between an ice nucleating material and the surrounding liquid or gas phase water is the key region of interest that provides the relevant environment for an ice nucleus to grow to sufficient size to allow formation of ice. Heterogeneous IN can occur at solid-liquid or at solid-gas interfaces, or at the interface between biogenic organic macromolecules and water molecules (Pummer, Budke et al. 2015, Pandey, Usui et al. 2016). Heterogeneous IN can take place via different pathways, among which the typical examples are: 1) Deposition ice nucleation: This refers to the formation of ice on the surface of INPs exposed to gas phase water vapor, without liquid phase water involved. Ice nucleation is potentially occurring after the formation of a stabilized structure, such as a water molecules cluster or monolayers of adsorbed water on the solid surface. The solid-gas interface plays an important role in this process, as the chemical and physical properties of the solid material impacts the coordination of water molecules near the surface. 2) Immersion nucleation: The main difference between immersion and deposition nucleation is the pre-existing phase before the formation of ice. Immersion nucleation occurs when the IN particle is immersed in a pre-existing liquid droplet, thus the solid-liquid interface is crucial for this process. 3) Contact freezing: The IN causes a liquid to freeze upon contact. Initially, the INP is supposed to be outside of the liquid. When this INP gets into contact with the surface of a super-cooled droplet, it may trigger the ice nucleation. The surface property of INP influence the nucleation efficiency, but the microscopic requirements are probably similar to the case of immersion freezing. 4) Condensation freezing, the droplet is initially formed by a cloud droplet condensation nucleus and then freezes after the condensation. As a special case, pore condensation and freezing (PCF) is an IN process that happens at low ice supersaturation. PCF is a process in which liquid water condenses in pores of solid materials (e.g. aerosol particles) below the water saturation ratio, under conditions where liquid water would not exist on a flat surface (David, Marcolli et al. 2019). PCF may be an alternative explanation for some cases previously attributed to deposition freezing.

### Interface science of ice nucleation: some important examples

IN particles for heterogeneous IN can be found among a wide range of biogenic, and anthropogenic species, comprising from biological aerosols to secondary organic aerosol components; they include proteins, mineral dusts, soot, primary and secondary organic aerosol compounds, lipids and saccharides (Pummer, Budke et al. 2015, Pandey, Usui et al. 2016), and their changing abundance and composition is implicated in climate change. The above mentioned materials in nature provide solid-gas, solid-liquid or liquid-gas interfaces for

important physical and chemical processes. In the context of INPs, these interfaces have an extremely important role in heterogeneous IN. Interface investigations in the context of IN certainly open up an important research field, which has attracted some attention recently.

The solid-gas interface is where deposition IN takes place. Solid substrates may favor ice nucleation by structuring water molecules on its surface. A high surface lattice match with the ice basal face has been considered as a favorable condition for the activation of ice nucleation (Fitzner, Sosso et al. 2015, Bi, Cabriolu et al. 2016, Qiu, Odendahl et al. 2017). Studying the local ordering of the water molecules near the surface (but not necessarily among the water molecules in direct contact with the substrate) is also an important approach to explain the IN ability (Fitzner, Pedevilla et al. 2020). In the context of IN, investigations related to the role of these interfaces with both computer simulation and lab experiment approach have become increasingly important.

As an example of an IN material that involves the interaction of a solid surface with the gas phase, we focus on feldspar. Feldspars are a group of tectosilicate minerals that make up 41% of the Earth's continental crust (Anderson and Anderson 2010). They are considered the most efficient INPs of the minerals commonly present in atmospheric mineral dust (Harrison, Whale et al. 2016). K-feldspar ( $\text{KAlSi}_3\text{O}_8$ ) is a potassium-rich alkali feldspar, namely called microcline. Other typical feldspars are albite ( $\text{NaAlSi}_3\text{O}_8$ , sodium rich), and anorthite ( $\text{CaAl}_2\text{Si}_2\text{O}_8$ , calcium rich). K-feldspar is a very important dust mineral INP type showing pronounced IN ability (Harrison, Whale et al. 2016), which attracted notable research attention. Kiselev et al. experimentally identified the IN active sites on the surface of K-feldspar, as surface patches associated with the (100) crystal face. Those patches consist of surface features like steps, cracks and cavities, which arise during the fracturing process. The presence of those patches is dominating the IN on defects (Kiselev, Bachmann et al. 2017). Through ab initio DFT calculation, Pedevilla et al. found single water molecules are able to bind strongly to the surface of the 001 face of K-feldspar (Pedevilla, Cox et al. 2016), as water molecules accumulate, the adsorption energy per water molecule will decrease until coverage reach 1.0 ML. The contact layers with a coverage of 1.0 and 1.5 ML were found to be ideal candidates to stabilize ice-like structures, possibly being the reason for K-feldspar particles being good INPs. This work reveal that a substrate like K-feldspar without an apparent match of its crystal structure to that of hexagonal ice can still behave as a prominent IN particle. This makes the hypothesis of the potential link of lattice match (between the substrate and basal face of ice) and IN ability becoming questionable, or the lattice match alone is not a sufficient descriptor for the IN ability of a given material. The exchange of charge balancing cations may also play a role for the IN ability of K-feldspar, and extensive investigations on this perspective were conducted (Busenberg and Clemency 1976, Fenter, Teng et al. 2000, Fenter, Cheng et al. 2003, Chardon, Livens et al. 2006). Kumar et al. suggest that the presence of additional  $\text{K}^+$  in the aqueous phase of a microcline suspension rather had a negative effect on its IN ability (Kumar, Marcolli et al. 2018). Therefore, under the context of deposition IN, we believe there are chances to contribute new insight to understand the K-feldspar's IN ability. If we can directly probe the hydrogen bonding (HB) network of water molecules on the surface of K-feldspar, we may obtain an understanding of the feedbacks between the HB network and the interaction with the solid substrate and compare it to the theoretical predictions mentioned above.

Another efficient IN material is silver iodide (AgI), which is commonly used for cloud seeding and as antiseptics. AgI features prominent ice nucleation ability in simulation and lab

experiments (Vonnegut 1947, Marcolli, Nagare et al. 2016). Many studies attributed its high ice nucleation activity (ability) to its lattice structure similarity with ice, which could be expected to promote the formation of ice crystals both in super cooled water, and in water vapor super saturated with respect to ice. Back in 1947, Vonnegut already started the investigation on AgI's IN ability, attributing the high IN ability to its lattice match with Ih ice (Vonnegut 1947). Nowadays there are various studies showing the IN efficiency of AgI. Lab observation by Zielke et al. confirmed that a structured contact water layer was imposed by the surface of AgI, and ice was suggested to nucleate on this layer and further grow successive layers (Zielke, Bertram et al. 2015). In contrast to K-feldspar, this study also points out that defects are not necessarily responsible for the effective IN ability of AgI. While the structure of AgI and K-feldspar are considerably different, it is intriguing why they both show prominent IN ability. Investigations into the structure of water in contact with AgI surfaces would certainly provide new insight into this question.

Apart from the typical heterogeneous IN process with a solid material involved, dissolved macromolecules in water can efficiently induce ice nucleation as well (Pummer, Budke et al. 2015). Additionally, lipids or surfactants may lead to structuring of water molecules near the aqueous solution- gas interface, which is another way of initiating heterogeneous ice nucleation (Knopf and Forrester 2011).

*Pseudomonas Syringae* (*P. Syringae*) bacteria are very good IN agents. The macromolecules, in fact proteins, associated with these bacteria induce ice formation at temperatures just slightly below the ice melting point. Due to this, it is widely used in artificial snow production. To obtain the structural information on water molecules in contact with *P. Syringae* bacteria (as protein extract in heave water), sum frequency generation (SFG) spectroscopy investigations on *P. Syringae* bacteria and other control substances (DPPG lipid, lysozyme, fragment and extract) were conducted by Pandey et al. (Pandey, Usui et al. 2016). Upon decreasing the temperature from 22 °C to 5 °C, water in contact with protein exhibited a strong enhancement of tetrahedral coordination of water molecules. In turn, SFG spectra of parallel experiments on water in contact with control substances showed no such variation. This is a clear evidence of the alignment of water molecules into an ordered structure by the bacteria. Based on the SFG spectra and MD simulations, the IN active sites within *P. Syringae* display a unique hydrophilic-hydrophobic pattern, which is believed to be responsible for the effective IN ability of *P. Syringae* (Pandey, Usui et al. 2016). Molecular simulation had emerged in the past years as a powerful tool to study the ice nucleation mechanism (Lupi and Molinero 2014, Sosso, Tribello et al. 2016, Lupi, Hudait et al. 2017, Metya and Molinero 2021). In another example of an IN active organic material, ice nucleation on the surface of solid Phloroglucinol Dihydrate (1,3,5 trihydroxybenzene), probably one of the most IN active materials overall (Fukuta 1966), was assessed by Metya et al. through molecular simulations. These suggest that the (010) face shows the best ice nucleation ability, attributed to the specific molecular orientation, as in this configuration the OH groups have the highest density in a plane perpendicular to the aromatic rings and exhibit a pattern roughly commensurable with the basal face of ice (Metya and Molinero 2021).

Organic molecules are widely present in the atmosphere, and they are potentially a significant player in atmospheric ice nucleation (Knopf, Alpert et al. 2018). They are present as organic aerosol or coated on other particles, sometimes in the form of surfactant monolayers. Consequently, the freezing of water with organic monolayers on liquid droplet surface had

attracted some attention. The mobility of the long-chain alcohol molecules on the water surface may facilitate a structural rearrangement into an ordered 2D lattice, leading to OH group patterns commensurate with the ice lattice and eventually raise the freezing temperature (Gavish, Popovitz-Biro et al. 1990, Popovitz-Biro, Wang et al. 1994, Zobrist, Koop et al. 2007). Knopf et al. reported that when NaCl droplets are coated by organic monolayers, such as by 1-nonadecanol and 1-nonadecanoic acid monolayers, the freezing temperature becomes relatively higher than that of uncoated droplets (Knopf and Forrester 2011). Molecular simulations of ice nucleation by an OH terminated alkane monolayer by Qiu et al. showed that the ordering and fluctuation of hydroxyl groups in organic molecules impacts the freezing temperature (Qiu, Odendahl et al. 2017). Another class of organic molecules with OH groups in the atmosphere are phenolic compounds, which originate from oxidation of aromatic compounds, as mentioned above. The preferential hydration of the OH groups in water is driving the surface propensity of these molecules. The hydrophobicity of the aromatic moieties in between leads to proper periodic modulation of HB that then facilitates pre-ordering of water, similar to the crystal faces of phloroglucinol mentioned above. We suspect that the self-aggregation of phenolic compounds on the surface of an aqueous solution can influence heterogeneous IN.

These are all evidences supporting the idea that the structure of water near a solid substrate or near organic molecules is playing a role in heterogeneous ice nucleation. That depends strongly on the surface properties, which is the consequence of the physical environment at an interface that controls the local HB structure of interfacial water. This aspect is the basis for the research direction of this thesis work.

## **1.2 QUESTIONS TOWARDS BETTER UNDERSTANDING THE SURFACE SCIENCE OF ICE NUCLEATION AND THESIS GOAL**

As introduced, heterogeneous ice nucleation had been discussed and studied since long, but the understanding of it at a molecular level is still far from complete (Hoose and Möhler 2012, Pummer, Budke et al. 2015). Extensive literature attest the importance of the interaction between surface and water molecules at the solid-vapor interface, yet the knowledge about the structure of the water-solid, or water-organic molecule interface is still limited. In view of the importance of solid/liquid-gas interface for the understanding of ice nucleation at a molecular level, we hypothesize that these interfaces are crucial for understanding the IN ability of different materials, irrespective of whether this is a solid material interacting with gas phase or liquid water or whether liquid water interacts with a surfactant on the surface of water, or with a protein within aqueous solution. The ability of a substrate or molecule to initiate nucleation of ice may be related to the ability to affect the HB structure of water in its vicinity by promoting the formation of tetrahedrally coordinated water molecules over spatial scales compatible with the critical size of an ice nucleus. We intend to probe the structure of interfacial water molecules either on a solid substrate surface or on a solution surface. These are the goals of this thesis work.

The arrangement of water molecules in any form of condensed phase water, be it ice or liquid water or also adsorbed water on a surface is best represented by its HB network. Probing the HB structure of water requires accessing the electronic structure of water and of dissolved or

substrate species at the same time. Within this frame, we develop our interface science by looking at: solid-gas interface and liquid-gas interface, split into four chapters.

To reach our goal, our main method is to investigate the HB structure of water molecules physisorbed at solid surfaces and of water near the surface of aqueous solutions containing dissolved, surface active organic ice nucleating agents and to link this information with the surface chemical composition.

In the following I present my objectives in detail:

**Project 1. Hydrogen bonding structure of water molecules adsorbed on solid substrates under sub-saturated conditions**

Interface interactions between water and solid oxide materials are important drivers of heterogeneous IN, among which K-rich feldspars and silver iodide are particularly IN active. As first objective, we attempt at understanding the interaction of water vapor with these solid materials in detail and at comparing with theoretical predictions. Our spectroscopic results show that upon adsorption of water molecules on the surface of known IN active solid materials, the HB network between water molecules shows different structural trends on different samples: more ice-like structure on silver iodide and the K-depleted surface of an originally K-rich feldspar, and a more liquid water-like structure on TiO<sub>2</sub> surface, when referencing the degree of ordering to the cases of liquid water and crystalline ice.

In this thesis, these studies are reported in three chapters. Chapter 2 for TiO<sub>2</sub>, Chapter 3 for silver iodide and Chapter 4 for K-rich feldspars. Those findings will open new lines of inquiry for water structure investigations in the context of ice nucleation.

**Project 2. In situ characterization of the liquid vapor interface of phenolic compound aqueous solutions.**

The second objective is to study the impact of the surface active resorcinol and orcinol molecules on the HB structure of water at the interface. Resorcinol and orcinol are simple proxies for a range of phenolic compounds found in the atmosphere resulting from oxidation of aromatic compounds or from pyrolysis of lignin in biomass. We provide an insight into how the IN process may be leveraged by the presence of these phenolic compounds and link this to enhanced ordering of water molecules due to the hydration of the OH groups. This has strong implication for ice nucleation under atmospheric conditions. Results of this part are reported in Chapter 5.

In the following sections, a general overview of interface techniques to investigate the HB structure of water will be presented.

### **1.3 OVERVIEW OF INTERFACE TECHNIQUES TO PROBE WATER STRUCTURE**

There are numerous experimental techniques capable to investigate the water structure. Among these, we list some notable examples: Raman Spectroscopy, Infrared Spectroscopy (IR), Sum Frequency Generation (SFG), Second-Harmonic Generation (SHG), Scattering, Nuclear Magnetic Resonance (NMR) Spectroscopy, X-ray Photoemission Spectroscopy (XPS), and Near Edge X Ray Absorption Fine Structure Spectroscopy (NEXAFS).

### IR and Raman Spectroscopy:

IR spectroscopy measures the interaction of infrared radiation (IR) with a sample via the absorption of IR by excitation of vibrational motions within molecules; it can identify chemical species or functional groups in solid, liquid or gas. Raman spectroscopy relies on inelastic scattering of photons, known as Raman scattering. Monochromatic light sources (e.g., a laser in the near infrared or near ultraviolet range) are usually used for Raman spectroscopy. The laser light interacts with vibrating molecules, resulting in the energy shift of the laser photons. The vibrational modes of the system are identified by this energy shift. Raman spectroscopy is commonly used in chemistry to provide structural information by which molecules are identified. As Raman and IR spectroscopy are sensitive to the OH stretch vibration, these are used jointly to understand the structure and dynamics of liquid water (Auer and Skinner 2008).

By combining Raman and IR spectroscopy, dynamical properties of water and inorganic aqueous solutions using Raman and IR spectroscopy was investigated by Rull (Rull 2002). Schmidt et al. interpreted the IR vibrational mode of pure water, based on the “bond ordering” of HB that can be expressed as an order parameter, to characterize the water structure (Schmidt and Miki 2007). Raman and IR were used to probe the water in polymer systems (Maeda and Kitano 1995), in nanopores (Ratajska-Gadomska and Gadomski 2004), for alkaline halide aqueous solutions (Terpstra, Combes et al. 1990) and water-ethanol mixtures (Burikov, Dolenko et al. 2010).

### SHG and SFG:

SHG is a non linear optical process in which two photons with the same frequency  $\nu$  interact with a nonlinear material, and generate a third photon with twice the frequency ( $2\nu$ ) of the initial photons. SHG provide molecular property information at an interface between two isotropic media. Its response is related to the overall arrangement of molecules at the interface (Goh, Hicks et al. 1988, Fordyce, Bullock et al. 2001). Since it is exclusively selective for molecules in a non-isotropic environment, SHG is the most surface or interface sensitive method discussed here. However, the probe depth is not entirely well defined as the depth to which the molecules feel the asymmetry, has to be discussed case by case.

As an extension of SHG, SFG is a second order nonlinear optical process in which two photons with different frequency  $\nu_1$  and  $\nu_2$  mix at an interface and generate one photon with a sum frequency at  $\nu_3 = \nu_1 + \nu_2$ .

Back to 1993, Shen and coworkers were the first to employ an SFG experiment to study the structure of water at the air-water interface (Du, Superfine et al. 1993, Du, Freysz et al. 1994). The stretching vibration mode of HB and dangling OH groups of water molecules at the air-water interface was identified in-situ. SFG was also used to probe the water structure at the interface between air and different classes of aqueous acid and salt solutions (Simonelli, Baldelli et al. 1998, Schnitzer, Baldelli et al. 2000). Gragson et al. examined the water structure at the air/water and water/ $\text{CCl}_4$  interfaces in detail showing that the interfacial water molecules were highly ordered when charged surfactants were included in the solution (Gragson, McCarty et al. 1996, Gragson and Richmond 1997, Gragson and Richmond 1998). Another example is related to understanding the effect of surface charges on the heterogeneous IN ability of an  $\alpha$ -alumina surface. A vibrational SFG experiment was used to probe the interfacial water

structure, revealing that the charged surface is suppressing IN on the  $\alpha$ -alumina surface, regardless of the sign of the surface charge (Abdelmonem, Backus et al. 2017). As mentioned earlier, the interface between biological macromolecules and water interface was also attracting SFG community's attention. Pandey investigated the order and dynamics of interfacial water near ice-nucleating bacteria, *P.Syringae*, revealing how the bacteria control the interfacial water structure (Pandey, Usui et al. 2016).

#### X-ray and Neutron Scattering techniques:

X-ray and neutron scattering experiments provide information about the structural properties of the water coordination through the structure factor and its related radial distribution function, providing indirect information about the three-dimensional tetrahedral nature of the HB network (Head-Gordon and Hura 2002). Scattering experiments with X-rays or neutrons have been widely used to probe the water structure (Bellissent-Funel, Bradley et al. 1993, Bellissent - Funel, Sridi - Dorbez et al. 1996, Bellissent-Funel 1998, Dore, Sufi et al. 2000, Head-Gordon and Hura 2002, Hura, Russo et al. 2003), showing that scattering techniques may be effective methods to investigate the dynamics and structural properties of water.(Dorémieux-Morin, Heeribout et al. 1996, El Seoud 1997, Bellissent-Funel 1998, Dore, Sufi et al. 2000, Head-Gordon and Hura 2002, Hura, Russo et al. 2003)

#### NMR:

NMR probes the local magnetic field around an atomic nucleus. By applying a magnetic field, sample nuclei (usually  $^1\text{H}$  or  $^{13}\text{C}$ ) will be excited by absorbing electromagnetic radiation into nuclear magnetic resonance at a specific frequency. The resonance frequency depends on the intramolecular magnetic fields around an atom, the value of each frequency gives information about the surroundings of the atom in question (e.g., its neighboring atoms and their relative positions). NMR can access the electronic structure of molecules and functional groups, making it as a useful tool to probe the surface structure of water on solid interface. NMR spectroscopy was employed to probe the structure of water-surfactant interface(Cabane 1981) water on silica surface (Dorémieux-Morin, Heeribout et al. 1996, Totland, Steinkopf et al. 2011), on other oxide surfaces (Gun'ko and Turov 1999) and in a classes of organized assemblies (El Seoud 1997).

#### XPS and NEXAFS:

Probing the HB network of water molecules and chemical composition of solid substrate or solutions in the context of IN requires accessing the electronic structure of the water molecules. The surface-sensitive technique X-ray Photoemission Spectroscopy (XPS) and Auger electron yield near-edge X-ray Absorption Fine Structure (NEXAFS) spectroscopy at the oxygen K-edge are powerful tools to probe the electronic structure and local coordination of water molecules and the chemical composition in one and the same experiment (Cavalleri, Ogasawara et al. 2002, Wilson, Cavalleri et al. 2002, Winter and Faubel 2006, Nilsson, Nordlund et al. 2010, Schiros, Andersson et al. 2010, Fransson, Harada et al. 2016).

XPS has been extensively used to study the surface of aqueous solutions (Winter and Faubel 2006, Brown, Redondo et al. 2013, Lee, Brown et al. 2015, Lee, Orlando et al. 2016, Lee, Orlando et al. 2019, Artiglia, Edebeli et al. 2017, Bruce, Zhang et al. 2021), ice (Bluhm et al., 2002; Křepelová, Newberg et al.; Kong, Waldner et al. 2017, Waldner, Artiglia et al. 2018), as well as adsorbed water on solid substrates (Verdaguer, Weis et al. 2007, Bluhm 2010,

Newberg, Starr et al. 2011, Kendelewicz, Kaya et al. 2013, Orlando, Artiglia et al. 2019, Yang, Boucly et al. 2021). This technique provides important information through its high surface sensitivity in the nm range, which arises from the short inelastic mean free path of photoelectrons in condensed matter, solid or liquid (Seah and Dench 1979, Ottosson, Faubel et al. 2010, Shinotsuka, Da et al. 2017). Liquid Jet XPS has recently become possible with differentially pumped lens systems, which enables to host samples for in situ XPS analysis in the mbar range, which is especially relevant for samples relevant for the atmosphere, as they can be equilibrated with water vapor (Bluhm, Hävecker et al. 2011).

The advantage of the NEXAFS-based method is the combination with XPS to have parallel chemical information. This is the reason XPS and NEXAFS were chosen for this thesis work. In the next session we will give a broad overview of XPS and NEXAFS technique coupled with our experimental chambers at the Swiss Light Source.

## 1.4 OVERVIEW OF XPS AND NEXAFS AT THE SWISS LIGHT SOURCE

### Experiment technique: XPS

One of our most extensively used experimental technique is X-ray Photoelectron Spectroscopy. XPS is a surface sensitive technique based on the photoelectric effect, able to provide surface elemental information, the electronic state of a specific element, or the thickness of an adsorbate layer within a depth down to several *nm*; thus it covers the adsorbate layer, the substrate surface and the near surface bulk underneath, and thus provides quite an ideal probe depth range. The spectra of XPS are obtained by irradiating the sample with an X-ray beam at a given photon energy and measuring the kinetic energy distribution of the electrons leaving the sample. The binding energy of the electron level, from which an electron was excited, can be determined by an energy conservation equation between the kinetic energy of the emitted electron and the binding energy:

$$E_{binding} = h\nu - (E_{kinetic} + \psi)$$

Where  $\psi$  is the work function for the sample surface, corresponding to the energy barrier for the electron to leave the sample surface. Other factors, such as the energy calibration of the analyzer or surface charging are separated out by calibration. The precise value of the binding energy of the emitted electron is then used to identify the element and its chemical state.

The probing depth of XPS is strongly depending on the inelastic mean free path (noted as  $\lambda$ ) of the excited out-going photoelectrons, which increases with its kinetic energy. The relationship between the probing depth and  $\lambda$  is connected by a factor of  $\cos(\theta)$ : Probing depth =  $\lambda \cdot \cos(\theta)$ , where  $\theta$  is the angle between the electron detection direction with respect to the sample surface normal (in our case  $\theta = 30^\circ$ ). This way, as the binding energies of core levels are fixed, by choosing the appropriate excitation photon energy, we can selectively probe the elemental composition across the surface down to an expected depth, because  $\lambda$  increases with kinetic energy and thus with increasing photon energy.

The photoemission intensity (*I*) in XPS experiment is expressed as:

$$I \propto \lambda \cdot n \cdot \phi \cdot \sigma \cdot \gamma \cdot y \cdot A \cdot T$$

Where  $n$  is the number of atoms per  $\text{cm}^3$  of the sample,  $\phi$  is the X-ray photon flux (photons/ $\text{cm}^2$ ),  $\sigma$  is the total photo-electron ionization cross section,  $\gamma$  is the angular efficiency factor of the instrument and  $\eta$  the efficiency of the photoelectric process,  $A$  is the area of the analyzed sample and  $T$  is the detection frequency.

#### Experiment technique: NEXAFS

While in XPS, non-resonant excitation of core or valence electrons is used, NEXAFS is based on the resonant absorption of electro-magnetic radiation by excitation of core electrons into unoccupied molecular orbitals. This excitation is followed by the hole being filled by an electron, resulting in either radiative emission of a fluorescent photon, or in emission of an Auger electron as non-radiative process. Due to the involvement of the lowermost unoccupied, thus outermost, molecular orbitals, NEXAFS is sensitive to the local HB network among water molecules, as well as their molecular arrangement in a tetrahedral coordination (e.g., ice) or in a more disordered configuration (e.g., liquid water) (Cavalleri, Ogasawara et al. 2002, Myneni, Luo et al. 2002, Wilson, Cavalleri et al. 2002, Smith, Cappa et al. 2004). The NEXAFS spectrum of gas phase water shows sharp features related to the excitation into  $4a_1$ ,  $2b_2$  and Rydberg orbitals as HB is absent in the gas phase. Upon condensation, HB form, which are similar in strength as the O-H bond strength in free water molecules. The sharp features associated with the free molecules disappear and are replaced by new features related to quite a variety of different HB configurations. They can be grossly distinguished by weak asymmetric HB more prevalent in liquid water and stronger symmetric ones in ice. The relative population of these configurations vary with temperature and depends on the presence of solutes or ions in electrolyte solutions. In the vicinity of a substrate or dissolved molecule in the bulk or at the aqueous solution – air interface, the changing HB structure of water molecules is the result of the interaction between water molecules and solid substrates or organic molecules at the surface or in the bulk aqueous phase. With this technique, we are able to probe the HB structure of the adsorbed water on solid substrates, or the water molecules in the vicinity of organic molecules at the surface of an aqueous solution.

In this thesis work, we made use of two experimental chambers to perform XPS and NEXAFS experiments: the so-called solid-gas interface (SGI) XPS chamber and the liquid-jet XPS chamber, connected at the *in situ* spectroscopy (ISS) beamline and at the *surface-interface* spectroscopy (SIM) beamline, respectively, at the Swiss Light Source.

#### Experiment chamber: SGI at ISS

Conventional XPS experiments are typically limited to ultrahigh vacuum (UHV) conditions due to the short mean free path of electrons in the gas phase. Our SGI chamber can host XPS and NEXAFS experiments at near-ambient pressure, thus at environmentally relevant conditions (Orlando, Waldner et al. 2016) with respect to water vapor. Synchrotron radiation is tunable over a wide range of photon energies at the ISS beamline, and can be made polarized in different ways, this allows users to select an optimum configuration (photoionization cross-section, and  $\lambda$ ) for probing a particular core level. The SGI chamber is used for *in-situ* investigations of equilibrated samples, for example, ice (Kong, Waldner et al. 2017, Waldner, Artiglia et al. 2018) or adsorbed water on AgI and feldspar samples as presented here. This experiment chamber allows water vapor pressures of up to several mbar during XPS analysis, and the surface of the sample can be cooled down by liquid nitrogen. This setup is feasible for multiphase investigations, it allows users to dose water vapor into the experimental chamber

by a capillary or leak-valve from a reservoir, so that water molecules are reversibly adsorbed or irreversibly taken up on a solid substrate. Depending on the physical conditions, ice or liquid water droplets can be formed and equilibrated on the sample holder.

#### Experimental chamber: Liquid-Jet at SIM

The experiments of project 2 are performed with the endstation configured with the liquid-jet chamber at the SIM beamline (Brown, Redondo et al. 2013). Inside this experimental chamber we deliver our sample solutions with a quartz nozzle, it forms a liquid microjet with a diameter corresponding to the aperture of the nozzle, typically ranging from 20-25  $\mu\text{m}$ . The liquid temperature can be controlled by a cooling jacket. The position of the liquid microjet is controlled by a piezoelectric stage with a spatial resolution of 1  $\mu\text{m}$ . During the experiment, the downward travelling liquid sample experiences the photoemission process by the irradiation by the X-ray beam of ca. 50  $\mu\text{m}$  spot size, 1 mm below the exit of the nozzle. The speed of the liquid microjet formed by the nozzle is in the range of 10-20 m/s. This way, the beam damage to the sample can be ignored as the liquid jet continuously delivers fresh sample solution.

Considering the interfacial equilibration, the HB exchange dynamics of water molecules is much faster than desorption, and the time for solute diffusion to build up a ML on the surface is on the order of  $\mu\text{s}$  for the lowest concentration used in this work. For liquid water, the bulk diffusion constant  $D = 0.6 \times 10^{-5} \text{cm}^2 \text{s}^{-1}$  at  $T = 298 \text{ }^\circ\text{C}$ , this makes the typical diffusion time to build a ML in the range of nanoseconds (Winter and Faubel 2006). This means that before the X-ray beam hits the liquid, the residence time of the solution in the chamber (around 0.1 ms) is long enough to allow the stabilization of surface excess of the solute by diffusion from the bulk. Evaporative cooling also plays a role in the sample temperature, before being captured by X-ray, an average decrease of ca. 2K in sample temperature was estimated (Faubel, Schlemmer et al. 1988). This experiment has been well established in previous studies to prove consistency between XPS results and surface tension data (Lee, Orlando et al. 2016), or for the interplay between surface active organics and halide ions (Chen, Artiglia et al. 2019; Lee, Orlando et al. 2019)

Below the measurement spot on the liquid jet, the sample solution was collected by a cryospheric catcher.

As each chapter of the thesis refers to an individual experiment, we report the detailed experimental setup of each specific experiment in every chapter.

#### A commissioning work: Probing the water structure on $\text{TiO}_2$ surface

We have conducted a commissioning experiment to investigate the interaction of water with  $\text{TiO}_2$ , this work demonstrated the feasibility of our experiment setup. The NEXAFS results indicate that the HB structure in adsorbed water at high RHs and at 235 K resembles that of a liquid-like water film. This work had shown the capability of our experimental setup and our ability to tackle challenging issues related to the analysis of the NEXAFS spectra. It revealed the structure of adsorbed water at a saturation ratio where homogeneous or heterogeneous freezing of bulk water is expected to occur at just a little higher water vapor pressure.

## **1.5 OUTLINE OF THE THESIS**

### Chapter 1: introduction

In the first chapter we introduce the basic research background, an overview of experimental techniques and my objectives.

### Chapter 2: Disordered Adsorbed Water Layers on TiO<sub>2</sub> Nanoparticles under Subsaturated Humidity Conditions at 235 K

This chapter belongs to project 1. In this commissioning work, we see the potential of our experiment setup (SGI chamber in ISS) to perform X-ray photoelectron spectroscopy and electron yield near-edge X-ray absorption fine structure (NEXAFS) spectroscopy at the oxygen K-edge to investigate the HB structure of adsorbed water on solid substrates. This chapter is adopted from the publication, DOI: 10.1021/acs.jpcclett.9b02779

### Chapter 3: Ordered hydrogen bonding structure of water molecules adsorbed on silver iodide particles under subsaturated conditions.

This chapter belongs to project 1. In this chapter we determined the chemical properties of the surface water layers, the thickness of adsorbed water, and the amount of contaminating carbon species on AgI particle surfaces. The approach used here opens up important perspectives for characterizing adsorbed water molecules on a wide variety of solids, which provides an important basis for understanding ice nucleation and other interfacial processes at the molecular level. This chapter is adopted from the publication, DOI <https://doi.org/10.1021/acs.jpcc.1c01767>

### Chapter 4: Surface potassium ion exchange controls the coordination of water molecules on the surface of feldspar

This chapter belongs to project 1. We expand our work on investigating the HB network of interfacial water to the feldspar surface. The segregation of potassium cations was directly probed, and we discuss the potential link between the IN ability of feldspar and this cation exchange with adsorbed water. This chapter is adopted from a manuscript in preparation for publication.

### Chapter 5: Resorcinol and Orcinol lead to local ordering of water molecules near the gas liquid interface

This chapter belongs to project 2. Based on core level and valence level XPS, the surface composition of resorcinol and orcinol aqueous solution is experimentally measured. NEXAFS spectroscopic data show that the presence of these phenolic compounds influence the HB network of water molecules in their vicinity. This chapter is adopted from a manuscript in preparation for publication.

### Chapter 6: Conclusion and outlook

## References

- Abdelmonem, A., E. H. G. Backus, N. Hoffmann, M. A. Sánchez, J. D. Cyran, A. Kiselev and M. Bonn (2017). "Surface-charge-induced orientation of interfacial water suppresses heterogeneous ice nucleation on  $\alpha$ -alumina (0001)." *Atmos. Chem. Phys.* **17**(12): 7827-7837.
- Anderson, R. S. and S. P. Anderson (2010). *Geomorphology: the mechanics and chemistry of landscapes*. Cambridge University Press.
- Artiglia, L., J. Edebeli, F. Orlando, S. Chen, M.-T. Lee, P. Corral Arroyo, A. Gilgen, T. Bartels-Rausch, A. Kleibert, M. Vazdar, M. Andres Carignano, J. S. Francisco, P. B. Shepson, I. Gladich and M. Ammann (2017). "A surface-stabilized ozonide triggers bromide oxidation at the aqueous solution-vapour interface." *Nature Communications* **8**(1): 700.
- Auer, B. M. and J. L. Skinner (2008). "IR and Raman spectra of liquid water: Theory and interpretation." *The Journal of Chemical Physics* **128**(22): 224511.
- Bellissent-Funel, M. (1998). "Evidence of a possible liquid-liquid phase transition in supercooled water by neutron diffraction." *Nuovo Cimento-D* **20**(12): 2107-2122.
- Bellissent-Funel, M. C., K. F. Bradley, S. H. Chen, J. Lal and J. Teixeira (1993). "Slow dynamics of water molecules in confined space." *Physica A: Statistical Mechanics and its Applications* **201**(1): 277-285.
- Bellissent-Funel, M. C., R. Sridi-Dorbez and L. Bosio (1996). "X-ray and neutron scattering studies of the structure of water at a hydrophobic surface." *The Journal of Chemical Physics* **104**(24): 10023-10029.
- Bi, Y., R. Cabriolu and T. Li (2016). "Heterogeneous Ice Nucleation Controlled by the Coupling of Surface Crystallinity and Surface Hydrophilicity." *The Journal of Physical Chemistry C* **120**(3): 1507-1514.
- Bluhm, H., M. Hävecker, A. Knop-Gericke, M. Kiskinova, R. Schlögl and M. Salmeron (2011). "In Situ X-Ray Photoelectron Spectroscopy Studies of Gas-Solid Interfaces at Near-Ambient Conditions." *MRS Bulletin* **32**(12): 1022-1030.
- Bluhm, H. (2010). "Photoelectron spectroscopy of surfaces under humid conditions." *Journal of Electron Spectroscopy and Related Phenomena* **177**(2): 71-84.
- Borduas, N. and N. M. Donahue (2018). Chapter 3.1 - The Natural Atmosphere. *Green Chemistry*. B. Török and T. Dransfield, Elsevier: 131-150.
- Brown, M. A., A. B. Redondo, I. Jordan, N. Duyckaerts, M.-T. Lee, M. Ammann, F. Nolting, A. Kleibert, T. Huthwelker, J.-P. Mächler, M. Birrer, J. Honegger, R. Wetter, H. J. Wörner and J. A. v.
- Bokhoven (2013). "A new endstation at the Swiss Light Source for ultraviolet photoelectron spectroscopy, X-ray photoelectron spectroscopy, and X-ray absorption spectroscopy measurements of liquid solutions." *Review of Scientific Instruments* **84**(7): 073904.
- Bruce, J. P., K. Zhang, S. G. Balasubramani, A. R. Haines, R. P. Galhenage, V. K. Voora, F. Furche and J. C. Hemminger (2021). "Exploring the Solvation of Acetic Acid in Water Using Liquid Jet X-ray Photoelectron Spectroscopy and Core Level Electron Binding Energy Calculations." *The Journal of Physical Chemistry B* **125**(31): 8862-8868.
- Burikov, S., T. Dolenko, S. Patsaeva, Y. Starokurov and V. Yuzhakov (2010). "Raman and IR spectroscopy research on hydrogen bonding in water-ethanol systems." *Molecular Physics* **108**(18): 2427-2436.
- Busenberg, E. and C. V. Clemency (1976). "The dissolution kinetics of feldspars at 25°C and 1 atm CO<sub>2</sub> partial pressure." *Geochimica et Cosmochimica Acta* **40**(1): 41-49.
- Cabane, B. (1981). "Structure of the water/surfactant interface in micelles : an NMR study of SDS micelles labelled with paramagnetic ions." *J. Phys. France* **42**(6): 847-859.
- Cantrell, W. and A. Heymsfield (2005). "Production of Ice in Tropospheric Clouds: A Review." *Bulletin of the American Meteorological Society* **86**(6): 795-808.
- Cavalleri, M., H. Ogasawara, L. G. M. Pettersson and A. Nilsson (2002). "The interpretation of X-ray absorption spectra of water and ice." *Chemical Physics Letters* **364**(3): 363-370.
- Chardon, E. S., F. R. Livens and D. J. Vaughan (2006). "Reactions of feldspar surfaces with aqueous solutions." *Earth-Science Reviews* **78**(1): 1-26.
- Chen, S., L. Artiglia, J. Edebeli, X. Kong, H. Yang, P. Corral-Arroyo and M. Ammann (2019). *Impact of tetrabutylammonium on the oxidation of bromide by ozone*. Geophysical Research Abstracts.
- David, R. O., C. Marcolli, J. Fahrni, Y. Qiu, Y. A. Perez Sirkin, V. Molinero, F. Mahrt, D. Brühwiler, U. Lohmann and Z. A. Kanji (2019). "Pore condensation and freezing is responsible for ice formation below water saturation for porous particles." *Proceedings of the National Academy of Sciences* **116**(17): 8184-8189.
- Dore, J. C., M. A. M. Sufi and M. C. Bellissent-Funel (2000). "Structural change in D<sub>2</sub>O water as a function of temperature: the isochoric temperature derivative function for neutron diffraction." *Physical Chemistry Chemical Physics* **2**(8): 1599-1602.
- Dorémieux-Morin, C., L. Heeribout, C. Dumousseaux, J. Fraissard, H. Hommel and A. P. Legrand (1996). "Study of the Constitutive Superficial Water of Precipitated Amorphous Silicas using 1H NMR: Broad-Line at 4 K and HR MAS at 300 K." *Journal of the American Chemical Society* **118**(51): 13040-13045.

- Du, Q., R. Superfine, E. Freysz and Y. R. Shen (1993). "Vibrational spectroscopy of water at the vapor/water interface." *Physical Review Letters* **70**(15): 2313-2316.
- Du, Q., E. Freysz and Y. R. Shen (1994). "Vibrational spectra of water molecules at quartz/water interfaces." *Physical Review Letters* **72**(2): 238-241.
- El Seoud, O. A. (1997). "Use of NMR to probe the structure of water at interfaces of organized assemblies." *Journal of Molecular Liquids* **72**(1): 85-103.
- Faubel, M., S. Schlemmer and J. P. Toennies (1988). "A molecular beam study of the evaporation of water from a liquid jet." *Zeitschrift für Physik D Atoms, Molecules and Clusters* **10**(2): 269-277.
- Fenter, P., L. Cheng, C. Park, Z. Zhang and N. C. Sturchio (2003). "Structure of the orthoclase (001)- and (010)-water interfaces by high-resolution X-ray reflectivity." *Geochimica et Cosmochimica Acta* **67**(22): 4267-4275.
- Fenter, P., H. Teng, P. Geissbühler, J. M. Hanchar, K. L. Nagy and N. C. Sturchio (2000). "Atomic-scale structure of the orthoclase (001)-water interface measured with high-resolution X-ray reflectivity" The submitted manuscript has been created by the University of Chicago as operator of Argonne National Laboratory under Contract No. W-31-109-ENG-38 with the U.S. Department of Energy. The U.S. government retains for itself, and others acting on its behalf, a paid-up, nonexclusive, irrevocable worldwide license in said article to reproduce, prepare derivative works, distribute copies to the public, and perform publicly and display publicly, by or on behalf of the government." *Geochimica et Cosmochimica Acta* **64**(21): 3663-3673.
- Fitzner, M., P. Pedevilla and A. Michaelides (2020). "Predicting heterogeneous ice nucleation with a data-driven approach." *Nature Communications* **11**(1): 4777.
- Fitzner, M., G. C. Sosso, S. J. Cox and A. Michaelides (2015). "The Many Faces of Heterogeneous Ice Nucleation: Interplay Between Surface Morphology and Hydrophobicity." *Journal of the American Chemical Society* **137**(42): 13658-13669.
- Fordyce, A. J., W. J. Bullock, A. J. Timson, S. Haslam, R. D. Spencer-Smith, A. Alexander and J. G. Frey (2001). "The temperature dependence of surface second-harmonic generation from the air-water interface." *Molecular Physics* **99**(8): 677-687.
- Fransson, T., Y. Harada, N. Kosugi, N. A. Besley, B. Winter, J. J. Rehr, L. G. M. Pettersson and A. Nilsson (2016). "X-ray and Electron Spectroscopy of Water." *Chemical Reviews* **116**(13): 7551-7569.
- Fukuta, N. (1966). "Experimental Studies of Organic Ice Nuclei." *Journal of the Atmospheric Sciences* **23**(2): 191-196.
- Gavish, M., R. Popovitz-Biro, M. Lahav and L. Leiserowitz (1990). "Ice nucleation by alcohols arranged in monolayers at the surface of water drops." *Science* **250**(4983): 973-975.
- Goh, M. C., J. M. Hicks, K. Kemnitz, G. R. Pinto, T. F. Heinz, K. B. Eisenthal and K. Bhattacharyya (1988). "Absolute orientation of water molecules at the neat water surface." *The Journal of Physical Chemistry* **92**(18): 5074-5075.
- Gragson, D. E., B. M. McCarty and G. L. Richmond (1996). "Surfactant/Water Interactions at the Air/Water Interface Probed by Vibrational Sum Frequency Generation." *The Journal of Physical Chemistry* **100**(34): 14272-14275.
- Gragson, D. E. and G. L. Richmond (1997). "Comparisons of the Structure of Water at Neat Oil/Water and Air/Water Interfaces As Determined by Vibrational Sum Frequency Generation." *Langmuir* **13**(18): 4804-4806.
- Gragson, D. E. and G. L. Richmond (1998). "Investigations of the Structure and Hydrogen Bonding of Water Molecules at Liquid Surfaces by Vibrational Sum Frequency Spectroscopy." *The Journal of Physical Chemistry B* **102**(20): 3847-3861.
- Gun'ko, V. M. and V. V. Turov (1999). "Structure of Hydrogen Bonds and <sup>1</sup>H NMR Spectra of Water at the Interface of Oxides." *Langmuir* **15**(19): 6405-6415.
- Harrison, A. D., T. F. Whale, M. A. Carpenter, M. A. Holden, L. Neve, D. O'Sullivan, J. Vergara Temprado and B. J. Murray (2016). "Not all feldspars are equal: a survey of ice nucleating properties across the feldspar group of minerals." *Atmos. Chem. Phys.* **16**(17): 10927-10940.
- Head-Gordon, T. and G. Hura (2002). "Water Structure from Scattering Experiments and Simulation." *Chemical Reviews* **102**(8): 2651-2670.
- Hoose, C. and O. Möhler (2012). "Heterogeneous ice nucleation on atmospheric aerosols: a review of results from laboratory experiments." *Atmos. Chem. Phys.* **12**(20): 9817-9854.
- Hura, G., D. Russo, R. M. Glaeser, T. Head-Gordon, M. Krack and M. Parrinello (2003). "Water structure as a function of temperature from X-ray scattering experiments and ab initio molecular dynamics." *Physical Chemistry Chemical Physics* **5**(10): 1981-1991.
- Kendelewicz, T., S. Kaya, J. T. Newberg, H. Bluhm, N. Mulakaluri, W. Moritz, M. Scheffler, A. Nilsson, R. Pentcheva and G. E. Brown (2013). "X-ray Photoemission and Density Functional Theory Study of the Interaction of Water Vapor with the Fe<sub>3</sub>O<sub>4</sub>(001) Surface at Near-Ambient Conditions." *The Journal of Physical Chemistry C* **117**(6): 2719-2733.

- Kiselev, A., F. Bachmann, P. Pedevilla, S. J. Cox, A. Michaelides, D. Gerthsen and T. Leisner (2017). "Active sites in heterogeneous ice nucleation—the example of K-rich feldspars." *Science* **355**(6323): 367-371.
- Knopf, D. A., P. A. Alpert and B. Wang (2018). "The Role of Organic Aerosol in Atmospheric Ice Nucleation: A Review." *ACS Earth and Space Chemistry* **2**(3): 168-202.
- Knopf, D. A. and S. M. Forrester (2011). "Freezing of Water and Aqueous NaCl Droplets Coated by Organic Monolayers as a Function of Surfactant Properties and Water Activity." *The Journal of Physical Chemistry A* **115**(22): 5579-5591.
- Kong, X., A. Waldner, F. Orlando, L. Artiglia, T. Huthwelker, M. Ammann and T. Bartels-Rausch (2017). "Coexistence of Physisorbed and Solvated HCl at Warm Ice Surfaces." *The Journal of Physical Chemistry Letters* **8**(19): 4757-4762.
- Křepelová, A., J. Newberg, T. Huthwelker, H. Bluhm and M. Ammann (2010). "The nature of nitrate at the ice surface studied by XPS and NEXAFS." *Physical Chemistry Chemical Physics* **12**(31): 8870-8880
- Kumar, A., C. Marcolli, B. Luo and T. Peter (2018). "Ice nucleation activity of silicates and aluminosilicates in pure water and aqueous solutions – Part 1: The K-feldspar microcline." *Atmos. Chem. Phys.* **18**(10): 7057-7079.
- Lee, M.-T., M. A. Brown, S. Kato, A. Kleibert, A. Türler and M. Ammann (2015). "Competition between Organics and Bromide at the Aqueous Solution–Air Interface as Seen from Ozone Uptake Kinetics and X-ray Photoelectron Spectroscopy." *The Journal of Physical Chemistry A* **119**(19): 4600-4608.
- Lee, M.-T., F. Orlando, L. Artiglia, S. Chen and M. Ammann (2016). "Chemical Composition and Properties of the Liquid–Vapor Interface of Aqueous C1 to C4 Monofunctional Acid and Alcohol Solutions." *The Journal of Physical Chemistry A* **120**(49): 9749-9758.
- Lee, M.-T., F. Orlando, M. Khabiri, M. Roeselová, M. A. Brown and M. Ammann (2019). "The opposing effect of butanol and butyric acid on the abundance of bromide and iodide at the aqueous solution–air interface." *Physical Chemistry Chemical Physics* **21**(16): 8418-8427.
- Lupi, L., A. Hudait, B. Peters, M. Grünwald, R. Gotchy Mullen, A. H. Nguyen and V. Molinero (2017). "Role of stacking disorder in ice nucleation." *Nature* **551**: 218.
- Lupi, L. and V. Molinero (2014). "Does Hydrophilicity of Carbon Particles Improve Their Ice Nucleation Ability?" *The Journal of Physical Chemistry A* **118**(35): 7330-7337.
- Maeda, Y. and H. Kitano (1995). "The structure of water in polymer systems as revealed by Raman spectroscopy." *Spectrochimica Acta Part A: Molecular and Biomolecular Spectroscopy* **51**(14): 2433-2446.
- Marcolli, C., B. Nagare, A. Welti and U. Lohmann (2016). "Ice nucleation efficiency of AgI: review and new insights." *Atmos. Chem. Phys.* **16**(14): 8915-8937.
- Metya, A. K. and V. Molinero (2021). "Is Ice Nucleation by Organic Crystals Nonclassical? An Assessment of the Monolayer Hypothesis of Ice Nucleation." *Journal of the American Chemical Society* **143**(12): 4607-4624.
- Myneni, S., Y. Luo, L. Å. Näslund, M. Cavalleri, L. Ojamäe, H. Ogasawara, A. Pelmenschikov, W. Ph, P. Väterlein, C. Heske, Z. Hussain, L. G. M. Pettersson and A. Nilsson (2002). "Spectroscopic probing of local hydrogen-bonding structures in liquid water." *Journal of Physics: Condensed Matter* **14**(8): L213.
- Newberg, J. T., D. E. Starr, S. Yamamoto, S. Kaya, T. Kendelewicz, E. R. Mysak, S. Porsgaard, M. B. Salmeron, G. E. Brown, A. Nilsson and H. Bluhm (2011). "Formation of hydroxyl and water layers on MgO films studied with ambient pressure XPS." *Surface Science* **605**(1): 89-94.
- Nilsson, A., D. Nordlund, I. Waluyo, N. Huang, H. Ogasawara, S. Kaya, U. Bergmann, L. Å. Näslund, H. Öström, P. Wernet, K. J. Andersson, T. Schiros and L. G. M. Pettersson (2010). "X-ray absorption spectroscopy and X-ray Raman scattering of water and ice; an experimental view." *Journal of Electron Spectroscopy and Related Phenomena* **177**(2): 99-129.
- Orlando, F., L. Artiglia, H. Yang, X. Kong, K. Roy, A. Waldner, S. Chen, T. Bartels-Rausch and M. Ammann (2019). "Disordered Adsorbed Water Layers on TiO<sub>2</sub> Nanoparticles under Subsaturated Humidity Conditions at 235 K." *The Journal of Physical Chemistry Letters* **10**(23): 7433-7438.
- Orlando, F., A. Waldner, T. Bartels-Rausch, M. Birrer, S. Kato, M.-T. Lee, C. Proff, T. Huthwelker, A. Kleibert, J. van Bokhoven and M. Ammann (2016). "The Environmental Photochemistry of Oxide Surfaces and the Nature of Frozen Salt Solutions: A New in Situ XPS Approach." *Topics in Catalysis* **59**(5): 591-604.
- Ottosson, N., M. Faubel, S. E. Bradforth, P. Jungwirth and B. Winter (2010). "Photoelectron spectroscopy of liquid water and aqueous solution: Electron effective attenuation lengths and emission-angle anisotropy." *Journal of Electron Spectroscopy and Related Phenomena* **177**(2): 60-70.
- Pandey, R., K. Usui, R. A. Livingstone, S. A. Fischer, J. Pfaendtner, E. H. G. Backus, Y. Nagata, J. Fröhlich-Nowoisky, L. Schmöser, S. Mauri, J. F. Scheel, D. A. Knopf, U. Pöschl, M. Bonn and T. Weidner (2016). "Ice-nucleating bacteria control the order and dynamics of interfacial water." *Science Advances* **2**(4).
- Pedevilla, P., S. J. Cox, B. Slater and A. Michaelides (2016). "Can Ice-Like Structures Form on Non-Ice-Like Substrates? The Example of the K-feldspar Microcline." *The Journal of Physical Chemistry C* **120**(12): 6704-6713.

- Popovitz-Biro, R., J. Wang, J. Majewski, E. Shavit, L. Leiserowitz and M. Lahav (1994). "Induced freezing of supercooled water into ice by self-assembled crystalline monolayers of amphiphilic alcohols at the air-water interface." *Journal of the American Chemical Society* **116**(4): 1179-1191.
- Pruppacher, H. R. and J. D. Klett (1997). *Microphysics of Clouds and Precipitation*.
- Pummer, B. G., C. Budke, S. Augustin-Bauditz, D. Niedermeier, L. Felgitsch, C. J. Kampf, R. G. Huber, K. R. Liedl, T. Loerting, T. Moschen, M. Schauerperl, M. Tollinger, C. E. Morris, H. Wex, H. Grothe, U. Pöschl, T. Koop and J. Fröhlich-Nowoisky (2015). "Ice nucleation by water-soluble macromolecules." *Atmos. Chem. Phys.* **15**(8): 4077-4091.
- Qiu, Y., N. Odendahl, A. Hudait, R. Mason, A. K. Bertram, F. Paesani, P. J. DeMott and V. Molinero (2017). "Ice Nucleation Efficiency of Hydroxylated Organic Surfaces Is Controlled by Their Structural Fluctuations and Mismatch to Ice." *Journal of the American Chemical Society* **139**(8): 3052-3064.
- Ratajska-Gadomska, B. and W. Gadomski (2004). "Water structure in nanopores of agarose gel by Raman spectroscopy." *The Journal of Chemical Physics* **121**(24): 12583-12588.
- Rull, F. (2002). "Structural investigation of water and aqueous solutions by Raman spectroscopy." *Pure and Applied Chemistry* **74**(10): 1859-1870.
- Schiros, T., K. J. Andersson, L. G. M. Pettersson, A. Nilsson and H. Ogasawara (2010). "Chemical bonding of water to metal surfaces studied with core-level spectroscopies." *Journal of Electron Spectroscopy and Related Phenomena* **177**(2): 85-98.
- Schmidt, D. A. and K. Miki (2007). "Structural Correlations in Liquid Water: A New Interpretation of IR Spectroscopy." *The Journal of Physical Chemistry A* **111**(40): 10119-10122.
- Schnitzer, C., S. Baldelli and M. J. Shultz (2000). "Sum Frequency Generation of Water on NaCl, NaNO<sub>3</sub>, KHSO<sub>4</sub>, HCl, HNO<sub>3</sub>, and H<sub>2</sub>SO<sub>4</sub> Aqueous Solutions." *The Journal of Physical Chemistry B* **104**(3): 585-590.
- Seah, M. P. and W. A. Dench (1979). "Quantitative electron spectroscopy of surfaces: A standard data base for electron inelastic mean free paths in solids." *Surface and Interface Analysis* **1**(1): 2-11.
- Shinotsuka, H., B. Da, S. Tanuma, H. Yoshikawa, C. J. Powell and D. R. Penn (2017). "Calculations of electron inelastic mean free paths. XI. Data for liquid water for energies from 50 eV to 30 keV." *Surface and Interface Analysis* **49**(4): 238-252.
- Simonelli, D., S. Baldelli and M. J. Shultz (1998). "Ammonia-water complexes on the surface of aqueous solutions observed with sum frequency generation." *Chemical Physics Letters* **298**(4): 400-404.
- Smith, J. D., C. D. Cappa, K. R. Wilson, B. M. Messer, R. C. Cohen and R. J. Saykally (2004). "Energetics of Hydrogen Bond Network Rearrangements in Liquid Water." *Science* **306**(5697): 851-853.
- Sosso, G. C., G. A. Tribello, A. Zen, P. Pedevilla and A. Michaelides (2016). "Ice formation on kaolinite: Insights from molecular dynamics simulations." *The Journal of Chemical Physics* **145**(21): 211927.
- Terpstra, P., D. Combes and A. Zwick (1990). "Effect of salts on dynamics of water: A Raman spectroscopy study." *The Journal of Chemical Physics* **92**(1): 65-70.
- Totland, C., S. Steinkopf, A. M. Blokhuis and W. Nerdal (2011). "Water Structure and Dynamics at a Silica Surface: Pake Doublets in 1H NMR Spectra." *Langmuir* **27**(8): 4690-4699.
- Verdager, A., C. Weis, G. Oncins, G. Ketteler, H. Bluhm and M. Salmeron (2007). "Growth and Structure of Water on SiO<sub>2</sub> Films on Si Investigated by Kelvin Probe Microscopy and in Situ X-ray Spectroscopies." *Langmuir* **23**(19): 9699-9703.
- Vonnegut, B. (1947). "The Nucleation of Ice Formation by Silver Iodide." *Journal of Applied Physics* **18**(7): 593-595.
- Waldner, A., L. Artiglia, X. Kong, F. Orlando, T. Huthwelker, M. Ammann and T. Bartels-Rausch (2018). "Pre-melting and the adsorption of formic acid at the air-ice interface at 253 K as seen by NEXAFS and XPS." *Physical Chemistry Chemical Physics* **20**(37): 24408-24417.
- Wang, P. K. (2013). *Physics and Dynamics of Clouds and Precipitation*. Cambridge, Cambridge University Press.
- Wilson, K. R., M. Cavalleri, B. S. Rude, R. D. Schaller, A. Nilsson, L. Pettersson, N. Goldman, T. Catalano, J. Bozek and R. Saykally (2002). "Characterization of hydrogen bond acceptor molecules at the water surface using near-edge x-ray absorption fine-structure spectroscopy and density functional theory." *Journal of Physics: Condensed Matter* **14**(8): L221.
- Winter, B. and M. Faubel (2006). "Photoemission from Liquid Aqueous Solutions." *Chemical Reviews* **106**(4): 1176-1211.
- Yang, H., A. Boucly, J. P. Gabathuler, T. Bartels-Rausch, L. Artiglia and M. Ammann (2021). "Ordered Hydrogen Bonding Structure of Water Molecules Adsorbed on Silver Iodide Particles under Subsaturated Conditions." *The Journal of Physical Chemistry C*.
- Zielke, S. A., A. K. Bertram and G. N. Patey (2015). "A Molecular Mechanism of Ice Nucleation on Model AgI Surfaces." *The Journal of Physical Chemistry B* **119**(29): 9049-9055.

Zobrist, B., T. Koop, B. P. Luo, C. Marcolli and T. Peter (2007). "Heterogeneous Ice Nucleation Rate Coefficient of Water Droplets Coated by a Nonadecanol Monolayer." The Journal of Physical Chemistry C **111**(5): 2149-2155.

## **2 WATER ADSORPTION ON TiO<sub>2</sub> NANOPARTICLE SURFACE**

---

**This Chapter is adopted from the publication: Fabrizio Orlando, Luca Artiglia, Huanyu Yang, Xiangrui Kong, Kanak Roy, Astrid Waldner, Shuzhen Chen, Thorsten Bartels-Rausch, and Markus Ammann (2019). "Disordered Adsorbed Water Layers on TiO<sub>2</sub> Nanoparticles under Subsaturated Humidity Conditions at 235 K" J. Phys. Chem. Lett. 2019, 10, 23, 7433–7438**

**My contribution to this publication was to obtain and analyze the spectra of adsorbed water and subtract the adventitious carbon contribution.**

### **2.1 DISORDERED ADSORBED WATER LAYERS ON TiO<sub>2</sub> NANOPARTICLES UNDER SUBSATURATED HUMIDITY CONDITIONS AT 235 K**

ABSTRACT. The interaction of water with TiO<sub>2</sub> is of substantial scientific and technological interest as it determines the activity of TiO<sub>2</sub> in photocatalytic and environmental applications in nanoparticle suspensions in water, in complex appliances or in pure form interacting with water vapor. The influence of TiO<sub>2</sub> nanoparticles on the hydrogen bonding structure of water molecules is an important factor that controls hydration of other species, reactions, or nucleation processes. We use a combination of ambient pressure X-ray photoelectron spectroscopy (APXPS) and electron yield near-edge X-ray absorption fine structure (NEXAFS) spectroscopy at the oxygen K-edge to investigate the hydrogen bonding structure of adsorbed water on titania nanoparticles in equilibrium with nearly saturated water vapor at 235 K. The results clearly show that the net NEXAFS spectrum of adsorbed water resembles that of liquid, disordered water at 235 K, a temperature at which both homogeneous and heterogeneous freezing of bulk water is anticipated.

The interaction of water with TiO<sub>2</sub> has wide importance. TiO<sub>2</sub> is used as a photocatalyst for waste removal in water (Hoffmann, Martin et al. 1995) and for air pollution remediation appliances as coatings (George, Beeldens et al. 2016, Binas, Venieri et al. 2017). TiO<sub>2</sub> has been considered as light scattering aerosol for solar radiation management purposes (Pope, Braesicke et al. 2012). TiO<sub>2</sub> is also a common occurrence in mineral dust particles in the atmosphere, which act as substrates for chemical reactions and nucleation of liquid water to cloud droplets or nucleation of ice (Chen, Nanayakkara et al. 2012). In these widely different contexts, water at the interface between TiO<sub>2</sub> and the gaseous or aqueous environment is at the origin of either chemical effects via the primary radical source (e.g., superoxide and hydroxyl radicals from the interaction with photoinduced electrons and holes), via representing a HB medium to accommodate chemical reactions, or via providing critical nuclei or sites in nucleation processes (Hosseinpour, Tang et al. 2017). The interaction of water with TiO<sub>2</sub> has also spurred a long-lasting debate about the degree of hydrophilicity of TiO<sub>2</sub> related materials, which was suggested to change under irradiation (Takeuchi, Sakamoto et al. 2005, Drelich and Chibowski 2010, Schneider, Matsuoka et al. 2014). One aspect therein is the adsorption of contaminating or ambient aliphatic carboxylic acids, which leads to a hydrophobic surface, because the hydrophilic carboxyl groups are bound to the TiO<sub>2</sub> surface. These organic species are oxidized and thus removed under irradiation by the oxidizing radicals generated by electron-hole pairs in TiO<sub>2</sub> (Hosseinpour, Tang et al. 2017, Balajka, Hines et al. 2018).

In this study we find that water adsorbed to TiO<sub>2</sub> nanoparticles exhibits a HB structure similar to that in liquid water at a temperature as low as -35°C even though homogeneous and heterogeneous freezing would be expected for just a little larger partial pressures of water at this temperature (Hoose and Möhler 2012). The HB structure is characterized by in situ electron yield near-edge X-ray absorption fine structure (NEXAFS) spectroscopy at the oxygen K-edge, which is sensitive to the local order around the individual water molecules (Myneni, Luo et al.). This technique provides complementary information to that from non-linear optical spectroscopy (Hosseinpour, Tang et al. 2017). NEXAFS spectra of liquid water and ice are differentiated by distinct main and postedge absorption features, corresponding to the abundance of strong HB in tetrahedrally coordinated water molecules in ice in comparison to liquid water (Niskanen, Fondell et al. 2019). The present experiments were performed under ambient pressure conditions with respect to water vapor, i.e., at subsaturated conditions with respect to the saturation vapor pressure of ice. To obtain surface sensitive data secondary electrons of kinetic energy (KE) between 460 and 520 eV were collected from Auger decay of the core excited state of the O 1s level which corresponds to an inelastic mean free path of around 2 nm. The NEXAFS measurements were accompanied by X-ray photoelectron spectroscopy (XPS) measurements to control surface composition with respect to the adsorbed water, contaminating carbon species and the bulk TiO<sub>2</sub>. A few reports demonstrated feasibility of this approach to obtain NEXAFS spectra from water on SiO<sub>2</sub> (Verdaguer, Weis et al.). This is the first study of this kind on a powder material. While less well defined in terms of structure than single crystals of well-defined orientation, it offers more relevance for practical environments of technical appliances or in the atmospheric environment.

Figure 2-1 shows a representative photoemission (PE) spectrum of the dry O 1s core level acquired at room temperature and at 0.05 mbar O<sub>2</sub> pressure. The main peak at 530.5 eV is associated to lattice oxygen atoms. The other features are related to the adsorption of water molecules and to the intrinsic presence of oxygen-containing adventitious carbon species

(532.2 eV). The sample was prepared from air-exposed powder and a small trace of organic contaminants were inherently present on the sample even at high vacuum conditions (Balajka, Hines et al.). In this and all other O 1s spectra shown further below, these species are represented by a single broad peak. While adding separate components for individual species might somewhat remove the slight mismatch with the measured spectrum, there are not enough constraints to justify this fit. The Ti 2p and C 1s spectra measured along with the O 1s series shown in Figure 2-1 are provided in the Supporting Information. In total, about 50 % of the total C 1s intensity is attributed to oxygenated species. Taking into account differences in probe depth and cross section, the observed C 1s intensity translates into about 1-2 % contribution to the O 1s intensity, reasonably consistent with the fitted component (see SI for calculation). The water-related components of the O 1s spectrum are assigned to OH groups at bridging O sites (O<sub>br</sub>-H, 531.6 eV) or at Ti sites (Ti-OH, 533.0 eV), and to molecularly adsorbed water (533.9 eV). The measured binding energy shifts for O<sub>br</sub>-H and Ti-OH components from the lattice O (1.1 and 2.5 eV, respectively) are consistent with TiO<sub>2</sub> nanopowder (1.2 and 2.2 eV (Krishnan, Liu et al.)) and rutile single crystal (1.3-1.6 and 2.5-2.6 eV (Sham and Lazarus, Bullock, Patthey et al., Perron, Vandenborre et al.)) surfaces. Partial hydroxylation of the sample prior to introducing water vapor arises from ambient moisture during preparation. Also, O<sub>2</sub> can displace water molecules from the chamber walls, which then might adsorb and/or dissociate on the sample surface. Surface hydroxylation takes place already at very low RH (Ketteler, Yamamoto et al.), thus in line with our observations, which also agree with those reported in Ref (Krishnan, Liu et al.) for a powder sample measured in vacuum conditions, as judged from the O 1s core level spectrum reported therein. The adsorption of molecular water causes a new spectral feature at about 3.3-3.6 eV for nanopowders (Benkoula, Sublemontier et al., Krishnan, Liu et al.) and 2.4-3.5 eV for rutile single crystals (Ketteler, Yamamoto et al., Perron, Vandenborre et al.) higher than bulk O, thus in line with our findings. It is important to note that peak deconvolution is affected by the intrinsically large FWHM of the individual components, ranging from 1.0 to 1.2 eV. These relatively large peak widths likely result from a broad distribution of different surface sites and the high defect density in the TiO<sub>2</sub> nanopowder. Nevertheless, as we shall see below, the peak identification is supported by the fact that the molecular water component grows at increasing RH while the hydroxyl components mostly retain their intensity. This behavior is in line with the generally accepted picture of dissociative adsorption of water on both pristine and defective TiO<sub>2</sub> surfaces followed by molecular adsorption at higher coverage (Walle, Ragazzon et al., Jackman, Thomas et al.).

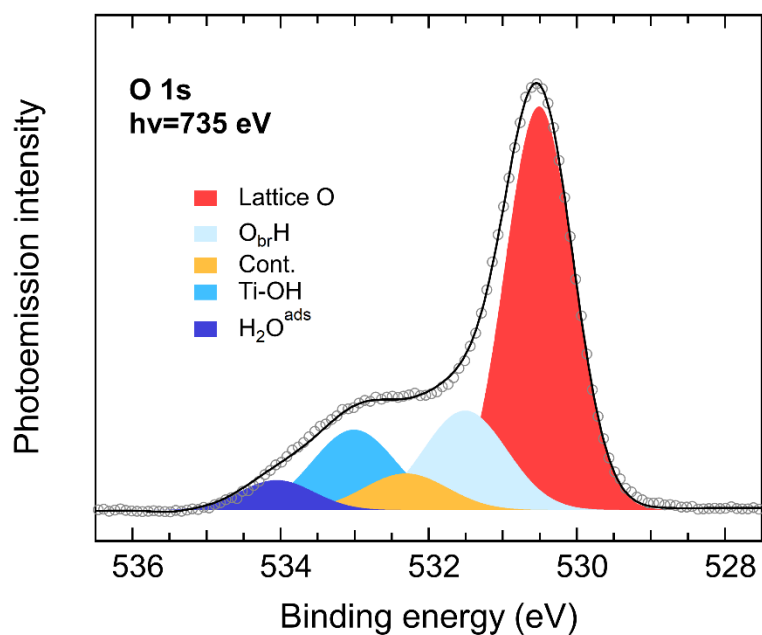


**Figure 2-1:** O 1s photoemission spectrum of the TiO<sub>2</sub> nanopowder measured under dry conditions. The fitted curve is represented by a thick black line, while the individual components are reported with different color shadings.

Figure 2-2a shows the evolution of the O 1s core level at increasing RH values. This is obtained by decreasing the sample temperature at constant water vapor pressure. A new spectral feature in the O 1s core level appears at 4.5-5.1 eV higher binding energy and is attributed to gas phase water. The component assigned to molecular water grows with increasing RH while the photoemission signals from other species decrease, as illustrated in Figure 2-2b. This is consistent with the formation of a water layer on top of the TiO<sub>2</sub> substrate which attenuates the signals of the surface species. The component assigned to carbonaceous species, already low at the beginning of the experiment, decreased substantially upon water addition, partly due to attenuation by adsorbed water, partly maybe also due to displacement by adsorbed water. Small fluctuations in the trend of the photoemission intensities arise because the sample position was changed in each acquisition (see method description in the Supporting Information). This procedure reduces beam-induced effects, but shows minute variation in the abundance of the surface species, including those of carbon, due to some inhomogeneity of the sample. The slight BE shift of the gas phase peak is tentatively explained by a small increase of the work function due to the increasing amount of adsorbed water. The lattice peaks are not affected because their BE is calculated relative to the Fermi level, while the apparent BE of the gas-phase component is referenced to the vacuum level.

Using the attenuation model described in the Supporting Information, the thickness of the water layer is calculated to be about 1.4 nm at close to saturation (<100% RH) (Figure 2-2c), corresponding to a surface coverage of about 4.6 ML (based on the assumption that a layer of water is roughly 0.3 nm (Verdaguer, Weis et al.)), in line with the findings reported by Goodman et al. (Goodman, Bernard et al.) and Ma et al. (Ma, He et al.) on P25 TiO<sub>2</sub> particles. Under similar RH conditions, Ketteler et al. (Ketteler, Yamamoto et al.) estimated a water coverage of approximately 5 ML on the rutile TiO<sub>2</sub>(110) surface using ambient pressure XPS.

However, it should be stressed that the different nature of the sample makes a direct comparison with the present findings difficult.

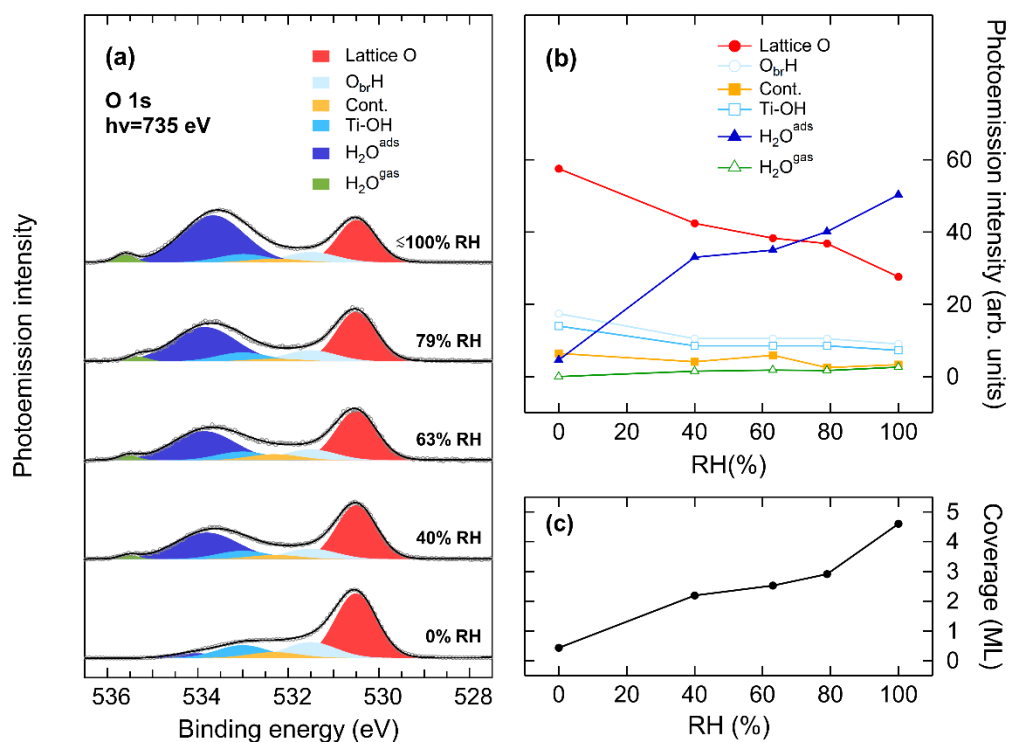


**Figure 2-2.** (a) Evolution of the O 1s photoemission spectra and corresponding deconvolution at increasing relative humidity values. (b) Photoemission intensity of the oxygen components and (c) surface water coverage as a function of RH. Details about the fitting procedure are given in the text.

Figure 2-3a shows the NEXAFS results obtained at the O K-edge. The spectrum measured under dry conditions (yellow curve) shows two peaks located at 531.3 eV (A1) and 534.0 eV (A2) corresponding to excitations to O 2p–Ti 3d mixed states (de Groot, Faber et al.). The features at 540.0 eV (C1) and at 546.0 eV (C2) are related to covalent mixing of O 2p and Ti 4sp states (de Groot, Faber et al.). In line with previously reported data (Orlando, Waldner et al.), the increased amount of water molecules on the surface causes an enhancement of the absorption features between 535 and 550 eV photon energy. At the same time, the characteristic absorption features of TiO<sub>2</sub> A1 and A2 are progressively attenuated. Note that because the NEXAFS features are due to resonant transitions, the relative contributions of the TiO<sub>2</sub> features and those associated with water cannot be used to obtain the amount of adsorbed water. The changes between dry and humid conditions are more clear in the top panel of Figure 2-3a, showing the differences in absorption between humid and dry conditions. The spectra measured under humid conditions, and so the corresponding difference spectra, encompass the contribution of both the TiO<sub>2</sub> substrate and the adsorbed water film. To this end, Figure 2-3b (dark green line) shows the spectrum corresponding to a coverage of 5 ML obtained by subtracting the spectrum measured under dry conditions from that measured under humid conditions, with the dry spectrum scaled as to minimize the residual areas at the positions of the A1 and A2 peaks, thus removing the contribution of the substrate oxide. The relatively large uncertainty in the pre-edge region below 534 eV comes mainly from a different relative

contribution of oxygen bound to adventitious carbon under dry and humid conditions, which have been approximated by the O K-edge spectrum of acetic acid (Horikawa, Arai et al. 2012) to represent the oxygenated carbon functional groups discussed above. As discussed in conjunction with the details of the subtraction procedure (Supporting Information Figure S2-2), the quantitative information from the photoemission spectra cannot be used to predict the contribution of these species to the NEXAFS spectrum. The absorption spectrum of adsorbed water resulting from this subtraction procedure only shows a pronounced intensity at 537 eV and a less strong peak at 542 eV, with the ratio of the two remaining clearly above one. Due to the uncertainties in the subtraction procedure and the worse signal to noise ratio, we refrained from applying the same analysis technique to the spectra measured at lower water coverage.

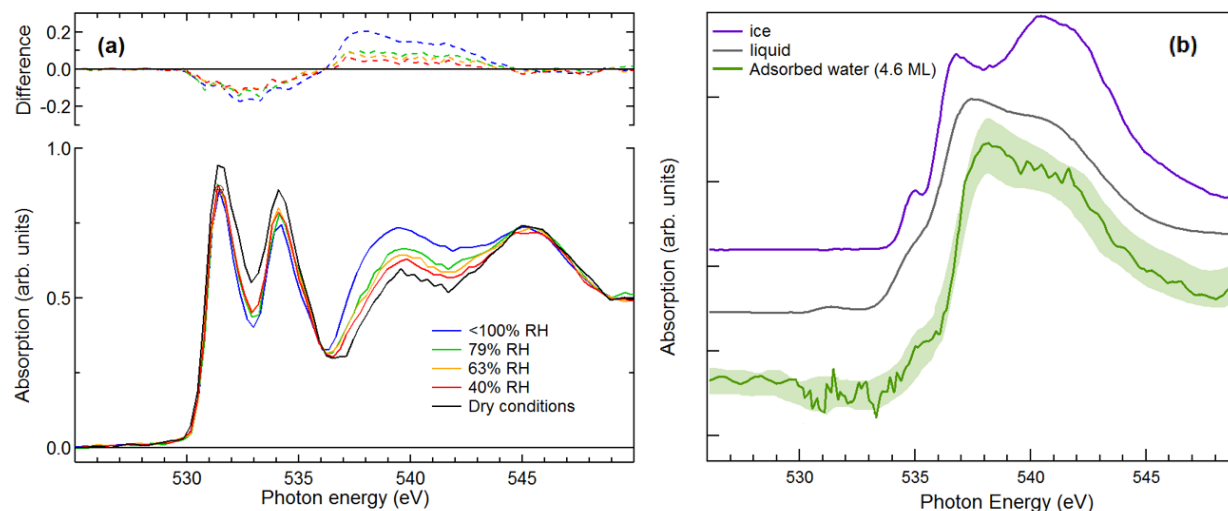


**Figure 2-3:** (a) O K-edge NEXAFS spectra of TiO<sub>2</sub> under dry conditions (black line) and at increasing relative humidity. The difference spectra generated by subtracting the spectrum measured under dry conditions from those measured under humid conditions are shown in the top panel. (b) Absorption spectrum of adsorbed water using the procedure described in the Supporting Information at the maximum water coverage (4.6 ML) compared to the spectra of ice and bulk water (spectra normalized to total area). The shading provides an error estimate.

For comparison, the O K-edge NEXAFS of bulk ice and liquid water are also reported in Figure 2-3b. These are characterized by pre- (535 eV), main- (537-538 eV), and post-edge (540-542 eV) absorption features (Sellberg, Kaya et al.). Theoretical calculations show that the pre- and main-edge peaks derive from weak or distorted HB, while the post-edge is due to fully tetrahedrally coordinated HB species (Cavalleri, Ogasawara et al., Myneni, Luo et al.). As a consequence, the different HB network determines distinct absorption spectra for ice and liquid water. The pre- and main-edge features are enhanced relative to the post-edge intensity in the liquid. The opposite situation arises in ice, where the larger amount of fully coordinated water molecules causes a stronger intensity of the post-edge relative to the main-edge, and minute changes to these have been used to address the quasi-liquid or premelt layer on ice (Bluhm, Ogletree et al.).

The shape of the spectrum obtained from the difference of those under dry and humid conditions shown in Figure 2-3b clearly resembles that of liquid water with a strong main-edge feature. This finding is quite surprising, considering that the sample temperature was as low as 235 K, where we would expect homogeneous and heterogeneous freezing of bulk water at just a little higher water vapor pressure to occur. Apparently, the high density of HB options with

the hydroxylated surface leads to a situation similar to high electrolyte strength solutions (supersaturated solutions) with a main to post-edge ratio even higher than that for water (Cappa, Smith et al.). The structure of water on BaF<sub>2</sub>(111) shows absorption features that indicate a high-density liquid structure at least up to 95% RH and corresponding coverage of 2.4 ML (Kaya, Schlesinger et al. 2013). Our data suggest a similar liquid-like behavior on TiO<sub>2</sub> nanopowder where, in addition, we do not expect any templating effect of the substrate (Cardellach, Verdaguer et al.) that would give rise to ordered hexagonal ice. Due to the uncertainty in the deconvolution of the spectrum and contributions of oxygenated adventitious carbon species, we refrain from quantitatively analyzing the ratio of main- to post-edge intensity. Still, the trend of the shapes of the absorption and difference spectra in Figure 2-3a suggests a lower main to post-edge intensity ratio for lower RH than for higher RH, pointing to stronger ordering of the thinnest water layers on TiO<sub>2</sub>. Structural differences between the first layer and those above have also been suggested by theoretical calculations (Liu, Zhang et al.), though for single crystalline TiO<sub>2</sub>, and thus in absence of defects. As discussed by Balajka et al. (Balajka, Hines et al.), minute contaminations by organic acids in ambient air might strongly change ordering of water also on single crystalline TiO<sub>2</sub>. This might apply also to the present case, where the C:O ratio is calculated to be ca. 2-3% at the highest water coverage (see SI).

In summary, we have investigated the adsorption of water on P-25 TiO<sub>2</sub> at different RH using AP-XPS. Two different hydroxyl groups were identified and assigned to O<sub>br</sub>H and Ti-OH, in line with previous investigations. Above about 80% RH, the adsorbed water film approaches about 5 ML. The NEXAFS results indicate that the HB structure in adsorbed water at these high RH and at 235 K resembles that of a liquid-like water film and, to some extent, that of a supercooled solution. This will spur further investigations on other substrates and at wider temperature and water vapor pressure ranges, but also comparison to results from theory. This could be done by qualitative comparison to parameters characterizing calculated structures (Liu, Zhang et al. 2010), but would require sampling representative configurations for different crystalline faces and defects characteristic of nanomaterials. In addition, O K-edge NEXAFS spectra of interfacial water could be obtained from electronic calculations; though, calculation of X-ray absorption spectra of water has remained an important challenge (Iannuzzi 2008, Fransson, Harada et al. 2016, Liu, He et al. 2017, Norman and Dreuw 2018, Michelitsch and Reuter 2019, Niskanen, Fondell et al. 2019, Pettersson, Harada et al. 2019, Zhovtobriukh, Norman et al. 2019).

## ASSOCIATED CONTENT

**Supporting Information.** The supporting information contains a description of the experimental methods, of spectral deconvolution and the procedure to estimate the thickness of the adsorbed water layer. C1s and Ti2p photoemission spectra are provided along with an estimate of the C:O ratio. More details of the procedure to subtract the substrate effects from the O K-edge NEXAFS spectrum are shown.

The following files are available free of charge.

## AUTHOR INFORMATION

### Notes

The authors declare no competing financial interests.

### ACKNOWLEDGMENT

This work was supported by the Swiss National Science Foundation (grant numbers 169176 and 149492). Technical support by M. Birrer and support at the SIM beamline by A. Kleibert is appreciated.

## References

- Balajka, J., M. A. Hines, W. J. I. DeBenedetti, M. Komora, J. Pavelec, M. Schmid and U. Diebold (2018). "High-affinity adsorption leads to molecularly ordered interfaces on TiO<sub>2</sub> in air and solution." *Science* 361(6404): 786-789.
- Benkoula, S., O. Sublemontier, M. Patanen, C. Nicolas, F. Sirotti, A. Naitabdi, F. Gaie-Levrel, E. Antonsson, D. Aureau, F.-X. Ouf, S.-I. Wada, A. Etcheberry, K. Ueda and C. Miron (2015). "Water adsorption on TiO<sub>2</sub> surfaces probed by soft X-ray spectroscopies: bulk materials vs. isolated nanoparticles." *Scientific Reports* 5: 15088.
- Binas, V., D. Venieri, D. Kotzias and G. Kiriakidis (2017). "Modified TiO<sub>2</sub> based photocatalysts for improved air and health quality." *Journal of Materiomics* 3(1): 3-16.
- Bluhm, H., D. F. Ogletree, C. S. Fadley, Z. Hussain and M. Salmeron (2002). "The premelting of ice studied with photoelectron spectroscopy." *Journal of Physics: Condensed Matter* 14(8): L227-L233.
- Bullock, E. L., L. Patthey and S. G. Steinemann (1996). "Clean and hydroxylated rutile TiO<sub>2</sub>(110) surfaces studied by X-ray photoelectron spectroscopy." *Surface Science* 352-354: 504-510.
- Cappa, C. D., J. D. Smith, B. M. Messer, R. C. Cohen and R. J. Saykally (2006). "The Electronic Structure of the Hydrated Proton: A Comparative X-ray Absorption Study of Aqueous HCl and NaCl Solutions." *The Journal of Physical Chemistry B* 110(3): 1166-1171.
- Cardellach, M., A. Verdager and J. Fraxedas (2011). "Defect-induced wetting on BaF<sub>2</sub>(111) and CaF<sub>2</sub>(111) at ambient conditions." *Surface Science* 605(23): 1929-1933.
- Cavalleri, M., H. Ogasawara, L. G. M. Pettersson and A. Nilsson (2002). "The interpretation of X-ray absorption spectra of water and ice." *Chemical Physics Letters* 364(3): 363-370.
- Chen, H. H., C. E. Nanayakkara and V. H. Grassian (2012). "Titanium Dioxide Photocatalysis in Atmospheric Chemistry." *Chemical Reviews* 112(11): 5919-5948.
- de Groot, F. M. F., J. Faber, J. J. M. Michiels, M. T. Czyżyk, M. Abbate and J. C. Fuggle (1993). "Oxygen 1s x-ray absorption of tetravalent titanium oxides: A comparison with single-particle calculations." *Physical Review B* 48(4): 2074-2080.
- Drelich, J. and E. Chibowski (2010). "Superhydrophilic and Superwetting Surfaces: Definition and Mechanisms of Control." *Langmuir* 26(24): 18621-18623.
- Fransson, T., Y. Harada, N. Kosugi, N. A. Besley, B. Winter, J. J. Rehr, L. G. M. Pettersson and A. Nilsson (2016). "X-ray and Electron Spectroscopy of Water." *Chemical Reviews* 116(13): 7551-7569.
- George, C., A. Beeldens, F. Barmpas, J.-F. Doussin, G. Manganelli, H. Herrmann, J. Kleffmann and A. Mellouki (2016). "Impact of photocatalytic remediation of pollutants on urban air quality." *Frontiers of Environmental Science & Engineering* 10(5): 2.
- Goodman, A. L., E. T. Bernard and V. H. Grassian (2001). "Spectroscopic Study of Nitric Acid and Water Adsorption on Oxide Particles: Enhanced Nitric Acid Uptake Kinetics in the Presence of Adsorbed Water." *The Journal of Physical Chemistry A* 105(26): 6443-6457.
- Hoffmann, M. R., S. T. Martin, W. Choi and D. W. Bahnemann (1995). "Environmental Applications of Semiconductor Photocatalysis." *Chemical Reviews* 95(1): 69-96.
- Hoose, C. and O. Möhler (2012). "Heterogeneous ice nucleation on atmospheric aerosols: a review of results from laboratory experiments." *Atmos. Chem. Phys.* 12(20): 9817-9854.
- Horikawa, Y., H. Arai, T. Tokushima and S. Shin (2012). "Spectral fingerprint in X-ray absorption for hydrogen-bonded dimer formation of acetic acids in solution." *Chemical Physics Letters* 522: 33-37.
- Hosseinpour, S., F. Tang, F. Wang, R. A. Livingstone, S. J. Schlegel, T. Ohto, M. Bonn, Y. Nagata and E. H. G. Backus (2017). "Chemisorbed and Physisorbed Water at the TiO<sub>2</sub>/Water Interface." *The Journal of Physical Chemistry Letters* 8(10): 2195-2199.
- Iannuzzi, M. (2008). "X-ray absorption spectra of hexagonal ice and liquid water by all-electron Gaussian and augmented plane wave calculations." *Physical Review B* 78(20): 204506.
- Jackman, M. J., A. G. Thomas and C. Muryn (2015). "Photoelectron Spectroscopy Study of Stoichiometric and Reduced Anatase TiO<sub>2</sub>(101) Surfaces: The Effect of Subsurface Defects on Water Adsorption at Near-Ambient Pressures." *The Journal of Physical Chemistry C* 119(24): 13682-13690.
- Kaya, S., D. Schlesinger, S. Yamamoto, J. T. Newberg, H. Bluhm, H. Ogasawara, T. Kendelewicz, G. E. Brown Jr, L. G. M. Pettersson and A. Nilsson (2013). "Highly Compressed Two-Dimensional Form of Water at Ambient Conditions." *Scientific Reports* 3: 1074.
- Ketteler, G., S. Yamamoto, H. Bluhm, K. Andersson, D. E. Starr, D. F. Ogletree, H. Ogasawara, A. Nilsson and M. Salmeron (2007). "The Nature of Water Nucleation Sites on TiO<sub>2</sub>(110) Surfaces Revealed by Ambient Pressure X-ray Photoelectron Spectroscopy." *The Journal of Physical Chemistry C* 111(23): 8278-8282.
- Krishnan, P., M. Liu, P. A. Itty, Z. Liu, V. Rheinheimer, M.-H. Zhang, P. J. M. Monteiro and L. E. Yu (2017). "Characterization of photocatalytic TiO<sub>2</sub> powder under varied environments using near ambient pressure X-ray photoelectron spectroscopy." *Scientific Reports* 7: 43298.

- Liu, J., X. He and J. Z. H. Zhang (2017). "Structure of liquid water – a dynamical mixture of tetrahedral and ‘ring-and-chain’ like structures." *Physical Chemistry Chemical Physics* 19(19): 11931-11936.
- Liu, L.-M., C. Zhang, G. Thornton and A. Michaelides (2010). "Structure and dynamics of liquid water on rutile TiO<sub>2</sub>(110)." *Physical Review B* 82(16): 161415.
- Ma, Q., H. He and Y. Liu (2010). "In situ DRIFTS study of hygroscopic behavior of mineral aerosol." *Journal of Environmental Sciences* 22(4): 555-560.
- Michelitsch, G. S. and K. Reuter (2019). "Efficient simulation of near-edge x-ray absorption fine structure (NEXAFS) in density-functional theory: Comparison of core-level constraining approaches." *The Journal of Chemical Physics* 150(7): 074104.
- Myneni, S., Y. Luo, L. Å. Näslund, M. Cavalleri, L. Ojamäe, H. Ogasawara, A. Pelmenschikov, P. Wernet, P. Väterlein, C. Heske, Z. Hussain, L. G. M. Pettersson and A. Nilsson (2002). "Spectroscopic probing of local hydrogen-bonding structures in liquid water." *Journal of Physics: Condensed Matter* 14(8): L213-L219.
- Niskanen, J., M. Fondell, C. J. Sahle, S. Eckert, R. M. Jay, K. Gilmore, A. Pietzsch, M. Dantz, X. Lu, D. E. McNally, T. Schmitt, V. Vaz da Cruz, V. Kimberg, F. Gel'mukhanov and A. Föhlisch (2019). "Compatibility of quantitative X-ray spectroscopy with continuous distribution models of water at ambient conditions." *Proceedings of the National Academy of Sciences*: 201815701.
- Niskanen, J., M. Fondell, C. J. Sahle, S. Eckert, R. M. Jay, K. Gilmore, A. Pietzsch, M. Dantz, X. Lu, D. E. McNally, T. Schmitt, V. Vaz da Cruz, V. Kimberg, F. Gel'mukhanov and A. Föhlisch (2019). "Reply to Pettersson et al.: Why X-ray spectral features are compatible to continuous distribution models in ambient water." 116(35): 17158-17159.
- Norman, P. and A. Dreuw (2018). "Simulating X-ray Spectroscopies and Calculating Core-Excited States of Molecules." *Chemical Reviews* 118(15): 7208-7248.
- Orlando, F., A. Waldner, T. Bartels-Rausch, M. Birrer, S. Kato, M.-T. Lee, C. Proff, T. Huthwelker, A. Kleibert, J. v. Bokhoven and M. Ammann (2016). "The Environmental Photochemistry of Oxide Surfaces and the Nature of Frozen Salt Solutions: A New in Situ XPS Approach." *Topics in Catalysis* 59(5-7): 591-604.
- Perron, H., J. Vandenborre, C. Domain, R. Drot, J. Roques, E. Simoni, J. J. Ehrhardt and H. Catalette (2007). "Combined investigation of water sorption on TiO<sub>2</sub> rutile (110) single crystal face: XPS vs. periodic DFT." *Surface Science* 601(2): 518-527.
- Pettersson, L. G. M., Y. Harada and A. Nilsson (2019). "Do X-ray spectroscopies provide evidence for continuous distribution models of water at ambient conditions?" 116(35): 17156-17157.
- Pope, F. D., P. Braesicke, R. G. Grainger, M. Kalberer, I. M. Watson, P. J. Davidson and R. A. Cox (2012). "Stratospheric aerosol particles and solar-radiation management." *Nature Climate Change* 2: 713.
- Schneider, J., M. Matsuoka, M. Takeuchi, J. Zhang, Y. Horiuchi, M. Anpo and D. W. Bahnemann (2014). "Understanding TiO<sub>2</sub> Photocatalysis: Mechanisms and Materials." *Chemical Reviews* 114(19): 9919-9986.
- Sellberg, J. A., S. Kaya, V. H. Segtnan, C. Chen, T. Tylliszczak, H. Ogasawara, D. Nordlund, L. G. M. Pettersson and A. Nilsson (2014). "Comparison of x-ray absorption spectra between water and ice: New ice data with low pre-edge absorption cross-section." *The Journal of Chemical Physics* 141(3): 034507.
- Sham, T. K. and M. S. Lazarus (1979). "X-ray photoelectron spectroscopy (XPS) studies of clean and hydrated TiO<sub>2</sub> (rutile) surfaces." *Chemical Physics Letters* 68(2): 426-432.
- Takeuchi, M., K. Sakamoto, G. Martra, S. Coluccia and M. Anpo (2005). "Mechanism of Photoinduced Superhydrophilicity on the TiO<sub>2</sub> Photocatalyst Surface." *The Journal of Physical Chemistry B* 109(32): 15422-15428.
- Verdaguer, A., C. Weis, G. Oncins, G. Ketteler, H. Bluhm and M. Salmeron (2007). "Growth and Structure of Water on SiO<sub>2</sub> Films on Si Investigated by Kelvin Probe Microscopy and in Situ X-ray Spectroscopies." *Langmuir* 23(19): 9699-9703.
- Walle, L. E., D. Ragazzon, A. Borg, P. Uvdal and A. Sandell (2014). "Photoemission studies of water dissociation on rutile TiO<sub>2</sub> (110): Aspects on experimental procedures and the influence of steps." *Applied Surface Science* 303: 245-249.
- Zhovtobriukh, I., P. Norman and L. G. M. Pettersson (2019). "X-ray absorption spectrum simulations of hexagonal ice." 150(3): 034501.

## 2.2 SUPPORTING INFORMATION

### 2.2.1 Experimental Methods and Data Analysis

Commercial TiO<sub>2</sub> nanoparticles (Degussa P-25, Evonik) were dispersed in isopropanol and then ultrasonicated to create a homogeneous suspension. A few droplets of the solution were drop casted onto the gold-coated surface of the sample holder, which was previously cleaned using isopropanol, and slowly dried to leave a macroscopically thin and uniform layer of TiO<sub>2</sub>. The sample was then loaded into the analysis cell at a base pressure  $\leq 1 \times 10^{-8}$  mbar. In-situ XPS and NEXAFS measurements on TiO<sub>2</sub> were performed at the near ambient pressure photoemission (NAPP) endstation (Orlando, Waldner et al.) connected to the SIM beamline of the Swiss Light Source at the Paul Scherrer Institut. The O 1s and C 1s core level spectra were measured at a photon energy of 735 eV. The Ti 2p core level spectra were measured at 665 eV photon energy. The spectra were collected at different sample spots at each RH to minimize any radiation-induced effect. The photoemission spectra are aligned with respect to the Fermi level, measured on the gold-coated surface of the sample holder under the same experimental conditions.

Oxygen was admitted to the chamber through a leak valve, while water was dosed using a capillary system. Two measurement sets were performed at 0.095 and 0.280 mbar water partial pressure, both with a background oxygen pressure of 0.050 mbar to keep the surface clean from potential contaminants, e.g. carbon, before admitting water to the chamber. Different RHs were achieved by changing the sample temperature using a liquid N<sub>2</sub> cryostat system, the temperature being monitored with a Pt100 sensor mounted a few millimeter away from the measurement spot. Calibration of the temperature at the measurement spot itself was performed by retracting the sample holder a few mm from the analyzer aperture and slowly adjusting the temperature to observe formation and evaporation of ice at the frost point. The vapor pressure of ice at the specific partial water vapor pressure reflected the exact sample surface temperature based on the known vapor pressure of ice (Murphy and Koop 2005). This was repeated at a few different water vapor partial pressures. Note that under measurement conditions, the local water vapor pressure at the measurement spot at a distance of 1.0 mm, thus two aperture diameters away from the aperture, is lower by a few percent than the measured background pressure due to the effect of pumping towards the electron analyzer (Bluhm, Hävecker et al.). Overall these effects lead to uncertainty in relative humidity, especially at high values. The highest RH achieved was when ice formed visibly around the measurement spot, but not at the measurement spot itself, as confirmed by an endoscope camera. Due to these uncertainties, we report average results from all measurements attempting at RH > 80% (indicated as <100% RH).

The O K-edge NEXAFS measurements on TiO<sub>2</sub> were performed in Auger yield mode using an electron kinetic energy window of 460–520 eV. The photon energy was scanned between 525 and 555 eV at the magic angle of 54.7° between the linear polarization of the incident X-ray and the *k* vector of the electrons. The signal was normalized to the photon beam intensity recorded with a photodiode mounted instead of the sample before and after the NEXAFS

measurements were performed. The NEXAFS difference spectra were calculated by subtracting the spectrum measured under dry conditions from those measured under humid conditions. The spectra so obtained contain a negative region at lower energy, which results from the partial screening of the TiO<sub>2</sub> substrate signal at increasing water coverage. This negative region can be removed by further subtracting a properly normalized TiO<sub>2</sub> spectrum measured under dry conditions, as described further below in detail (Figure S 2-2). This procedure thus removes the contribution of the TiO<sub>2</sub> substrate, leaving only that of the adsorbed water. The reference spectrum for ice was obtained as described in our previous work. (Kong, Waldner et al. 2017) The reference spectrum for liquid water was obtained using the NAPP endstation configured with the liquid jet setup (Brown, Redondo et al. 2013) using an electron kinetic energy window of 421 – 437 eV but otherwise identical settings, also at the SIM beamline.

The XPS spectra were deconvoluted using Gaussian fitting functions after subtraction of a Shirley background. The thickness of the water layer at increasing relative humidity (RH) can be estimated from the attenuation of the bulk TiO<sub>2</sub> components (O 1s or Ti 2p photoemission intensities) due to the screening of the adsorbed water. The measured photoemission intensity of the O 1s bulk component,  $I_{TiO_2}$ , for a TiO<sub>2</sub> surface covered by a water layer of thickness  $d$  is given by:

$$I_{TiO_2} = n_{TiO_2} \sigma_O \lambda_{TiO_2} \exp(-d / \lambda_{H_2O} \cos \theta),$$

where  $n_{TiO_2}$  is the density of oxygen atoms in TiO<sub>2</sub>,  $\sigma_O$  is the oxygen photoionization cross section,  $\lambda_{TiO_2}$  and  $\lambda_{H_2O}$  are the electron inelastic mean free paths in TiO<sub>2</sub> and liquid water, respectively and  $\theta$  is the angle between the surface normal and the analyzer. Similarly, the intensity of the O 1s water component,  $I_{H_2O}$ , for a water layer of thickness  $d$  is given by:

$$I_{H_2O} = n_{H_2O} \sigma_O \lambda_{H_2O} [1 - \exp(-d / \lambda_{H_2O} \cos \theta)].$$

Therefore,  $d$  can be expressed as

$$d = \cos \theta \lambda_{H_2O} \ln \left( 1 + \frac{I_{H_2O} n_{TiO_2} \lambda_{TiO_2}}{I_{TiO_2} n_{H_2O} \lambda_{H_2O}} \right).$$

The calculations were performed with the following values:  $n_{TiO_2} = 6.4 \times 10^{22} \text{ cm}^{-3}$ ,  $n_{H_2O} = 3.3 \times 10^{22} \text{ cm}^{-3}$ ,  $\theta = 30^\circ$ ,  $\lambda_{TiO_2} = 7.6 \text{ \AA}$  and  $\lambda_{H_2O} = 15 \text{ \AA}$  (at the 200 eV kinetic energy used in the experiment (Verdaguer, Weis et al. , Shinotsuka, Da et al. 2017)). This treatment obviously neglects curvature effects or the potentially inhomogeneous distributions of water molecules on the surface of the TiO<sub>2</sub> nanoparticles.

The spectral components identified in the O 1s region are described in the main paper. The Ti 2p spectra only showed the component associated to Ti<sup>4+</sup> sites, indicating that the surface is fully oxidized. In agreement with previous literature values (Mysak, Smith et al. 2011, Rosseler, Sleiman et al. 2013), the C 1s region was fitted with five spectral contributions,

identified as C=C, CH<sub>x</sub>, C-OH, C=O and COOH and located at 0, 0.7, 1.7, 2.8 and 4.2 eV relative to the C=C binding energy, respectively.

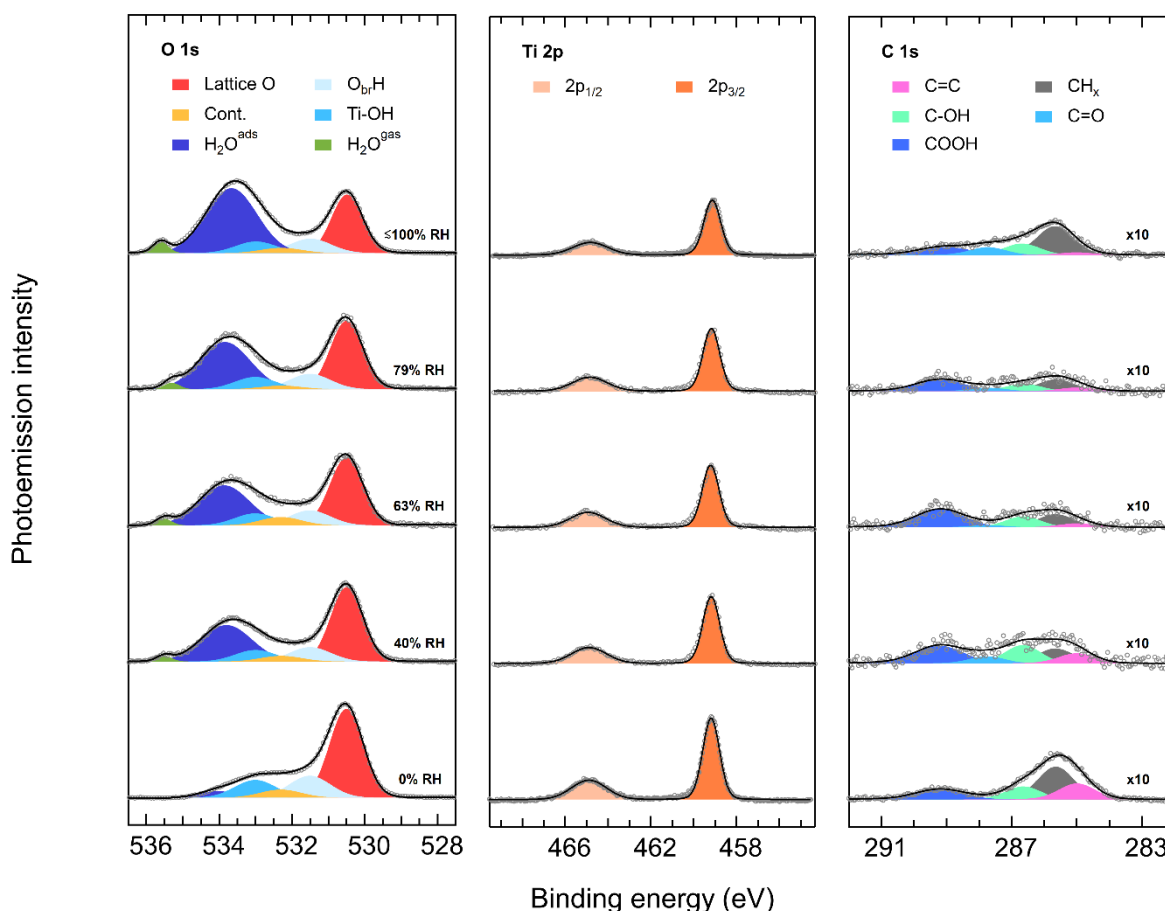


Figure S 2-1: Evolution of the O 1s, Ti 2p and C 1s core level regions with increasing RH. The fitted curves are represented by solid black lines, the raw data are displayed as grey circles and the individual components are reported with different color shadings. The C/O ratio calculated from the spectra at '<math>\le 100\%</math>' RH is roughly 2-3%.

Figure S 2-1 shows the Ti 2p and C 1s spectra at increasing RH, together with the O 1s region already displayed in the main paper. The photoemission intensity of Ti 2p and C 1s regions decreased at increasing RH (as well as the O 1s surface species), in agreement with the formation of a water layer which attenuates the signals of the surface species. The relative abundance of the carbon species shows some variation because the sample spot was changed at each acquisition and the sample surface is not homogenous. The population of the oxygenated carbon species at close to saturating RH is calculated to be ca. 50%. Based on the total area of the fitted spectral contributions in the C 1s and O 1s regions, a C/O ratio of ca. 2-3% is estimated. Note that a sensitivity factor was used to scale the peak intensities, which takes into account the total photon flux, the photoemission cross section, the asymmetry factor and the photoelectron inelastic mean free path at the measured photoelectron kinetic energy. From the calculated C/O ratio (2-3%) and contribution of oxygenated species in the C 1s region (50%), the carbon-related species in the O 1s spectrum should contribute ca. 1-2% of the total

O 1s intensity. The latter value well compares to the area of the “cont.” peak in the O 1s spectrum in Figure 2-1 and S2-1, which accounts for 2% of the total O 1s area.

### 2.2.2 Electron yield NEXAFS spectra and analysis

The O K-edge NEXAFS measurements on TiO<sub>2</sub> were performed in Auger yield mode using an electron kinetic energy window of 460–520 eV. The photon energy was scanned between 525 and 555 eV at the magic angle of 54.7° between the linear polarization of the incident X-ray and the *k* vector of the electrons. The signal was normalized to the photon beam intensity recorded with a photodiode mounted instead of the sample before and after the NEXAFS measurements were performed. The NEXAFS difference spectra were calculated by subtracting the spectrum measured under dry conditions from those measured under humid conditions. The spectra so obtained contain a negative region at lower energy, which results from the partial screening of the TiO<sub>2</sub> substrate signal at increasing water coverage. This negative region can be removed by further subtracting a properly normalized TiO<sub>2</sub> spectrum measured under dry conditions, as described further below in detail (Figure S 2-2). This procedure thus removes the contribution of the TiO<sub>2</sub> substrate, leaving only that of the adsorbed water. The reference spectrum for ice was obtained as described in our previous work (Kong, Waldner et al. 2017). The reference spectrum for liquid water was obtained using the NAPP endstation configured with the liquid jet setup (Brown, Redondo et al. 2013) using an electron kinetic energy window of 421 – 437 eV but otherwise identical settings, also at the SIM beamline.

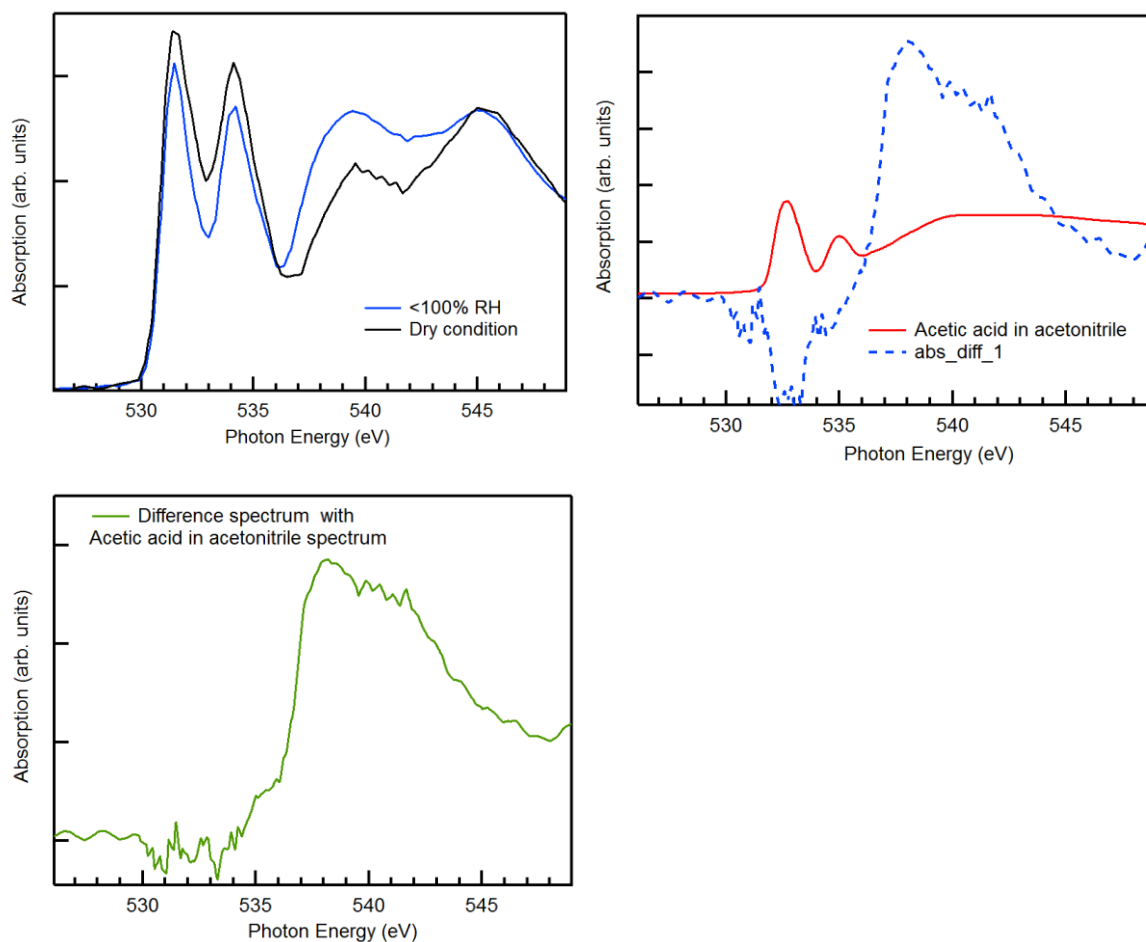


Figure S 2-2: The upper left plot corresponds to the NEXAFS spectra measured under dry conditions (black) and at the highest relative humidity (blue), as reported in the main text Figure 2-3a. In the top right plot, the dashed blue line corresponds to the spectrum obtained by subtraction of a fraction of the solid black spectrum from the solid blue spectrum of the top plot such as to minimize absorption at the energy of the two TiO<sub>2</sub> pre-edge peaks A1 and A2. The optimum fraction was found to be 0.90. Apparently, this leads to a dip in absorption at 532-534 eV, which we ascribe to the presence of oxygenated adventitious carbon, which was more abundant under humid conditions than under dry conditions, as described in the main text, and apparent from the C1s spectra provided in Figure S 2-1. As obvious from Figure S 2-1, carboxyl is an important oxygenated carbon functionality based on the C1s spectrum. Due to the resonant nature of NEXAFS features and also because the electron yield NEXAFS measurement includes electrons from inelastically scattered Auger electrons, which leads to uncertainty in the probe depth, we cannot quantitatively use the constraints from the C1s and O1s to quantitatively estimate the contribution to the O K-edge NEXAFS spectrum. In absence of such a quantitative link, we estimated the contribution of the oxygenated carbon species by adding a variable fraction of an O K-edge NEXAFS spectrum of acetic acid as reported by Horikawa et al. (Horikawa, Arai et al. 2012), in order to minimize absorption in the pre-edge region leading to the solid green line in the lower left plot and in the main text Figure 2-3b. We note that we do not claim that acetic acid itself was present on the surface. However, the absorption at 532.5 eV is characteristic for all  $\text{-C=O}$  bonds in carboxylic and carbonylic functionalities. The uncertainty expressed by the green shading in Figure 2-3b results from this subtraction procedure and the resulting pre-edge variability. In addition, we account for potential differences of the ratio of main- and post-edge absorption to pre-edge absorption for the carboxyl species present as well as the shape in the region of 537 – 545 eV between acetic acid and the actual oxygenated adventitious carbon species present on our sample (such as alcohols, carbonyls and carboxyls). While the precise ratio of the peaks at 538 and 542 is remaining uncertain for this reason, it clearly remains above 1 for conceivable shapes of the absorption in this region contributed by oxygenated adventitious carbon species.

## References

- Bluhm, H., M. Hävecker, A. Knop-Gericke, M. Kiskinova, R. Schlögl and M. Salmeron (2011). "In Situ X-Ray Photoelectron Spectroscopy Studies of Gas-Solid Interfaces at Near-Ambient Conditions." *MRS Bulletin* 32(12): 1022-1030.
- Brown, M. A., A. B. Redondo, I. Jordan, N. Duyckaerts, M.-T. Lee, M. Ammann, F. Nolting, A. Kleibert, T. Huthwelker, J.-P. Machler, M. Birrer, J. Honegger, R. Wetter, H. J. Wörner and J. A. van Bokhoven (2013). "A new endstation at the Swiss Light Source for ultraviolet photoelectron spectroscopy, X-ray photoelectron spectroscopy, and X-ray absorption spectroscopy measurements of liquid solutions." *Review of Scientific Instruments* 84(7): 073904-073908.
- Horikawa, Y., H. Arai, T. Tokushima and S. Shin (2012). "Spectral fingerprint in X-ray absorption for hydrogen-bonded dimer formation of acetic acids in solution." *Chemical Physics Letters* 522: 33-37.
- Kong, X., A. Waldner, F. Orlando, L. Artiglia, T. Huthwelker, M. Ammann and T. Bartels-Rausch (2017). "Coexistence of Physisorbed and Solvated HCl at Warm Ice Surfaces." *The Journal of Physical Chemistry Letters*: 4757-4762.
- Murphy, D. M. and T. Koop (2005). "Review of the vapour pressures of ice and supercooled water for atmospheric applications." *Quarterly Journal of the Royal Meteorological Society* 131(608): 1539-1565.
- Mysak, E. R., J. D. Smith, P. D. Ashby, J. T. Newberg, K. R. Wilson and H. Bluhm (2011). "Competitive reaction pathways for functionalization and volatilization in the heterogeneous oxidation of coronene thin films by hydroxyl radicals and ozone." *Physical Chemistry Chemical Physics* 13(16): 7554-7564.
- Orlando, F., A. Waldner, T. Bartels-Rausch, M. Birrer, S. Kato, M.-T. Lee, C. Proff, T. Huthwelker, A. Kleibert, J. v. Bokhoven and M. Ammann (2016). "The Environmental Photochemistry of Oxide Surfaces and the Nature of Frozen Salt Solutions: A New in Situ XPS Approach." *Topics in Catalysis* 59(5-7): 591-604.
- Rosseler, O., M. Sleiman, V. N. Montesinos, A. Shavorskiy, V. Keller, N. Keller, M. I. Litter, H. Bluhm, M. Salmeron and H. Destailats (2013). "Chemistry of NO<sub>x</sub> on TiO<sub>2</sub> Surfaces Studied by Ambient Pressure XPS: Products, Effect of UV Irradiation, Water, and Coadsorbed K<sup>+</sup>." *The Journal of Physical Chemistry Letters*: 536-541.
- Shinotsuka, H., B. Da, S. Tanuma, H. Yoshikawa, C. J. Powell and D. R. Penn (2017). "Calculations of electron inelastic mean free paths. XI. Data for liquid water for energies from 50 eV to 30 keV." *Surface and Interface Analysis* 49(4): 238-252.
- Verdaguer, A., C. Weis, G. Oncins, G. Ketteler, H. Bluhm and M. Salmeron (2007). "Growth and Structure of Water on SiO<sub>2</sub> Films on Si Investigated by Kelvin Probe Microscopy and in Situ X-ray Spectroscopies." *Langmuir* 23(19): 9699-9703.

### 3 WATER ADSORPTION ON SILVER IODIDE SURFACE

---

**This Chapter is adopted from the publication: Yang, H., A. Boucly, J. P. Gabathuler, T. Bartels-Rausch, L. Artiglia and M. Ammann (2021). "Ordered Hydrogen Bonding Structure of Water Molecules Adsorbed on Silver Iodide Particles under Subsaturated Conditions." The Journal of Physical Chemistry C. DOI: <https://doi.org/10.1021/acs.jpcc.1c01767>**

#### 3.1 ORDERED HYDROGEN BONDING STRUCTURE OF WATER MOLECULES ADSORBED ON SILVER IODIDE PARTICLES UNDER SUBSATURATED CONDITIONS

##### ABSTRACT

Silver iodide (AgI) is an efficient ice nucleating material. This has been related to the close lattice-match to hexagonal ice, which helps to nucleate ice crystals on its surface under supersaturated conditions. In turn, the structure of water molecules adsorbed on its surface, embodied in the coordination of hydrogen bonds, has not been addressed so far. We suspected that AgI may induce ice-like coordination among adsorbed water molecules already under subsaturated conditions. X-ray photoelectron spectroscopy was used to probe structure and composition at the AgI surface. We determined the chemical properties of the surface, the thickness of adsorbed water and the amount of contaminating carbon species. Auger electron yield near-edge X-ray absorption fine structure (NEXAFS) spectroscopy was used to assess the hydrogen bonding structure. The O K-edge NEXAFS spectra indicated that the hydrogen bonding structure of the adsorbed water on AgI under subsaturated conditions showed similarity with that of ice, which helps to facilitate the stabilization of ice embryos at saturation. The approach used here opens up important perspectives for characterizing adsorbed water molecules on a wide variety of solids, which provides an important basis for understanding ice nucleation and other interfacial processes at the molecular level.

##### 3.1.1 Introduction

Ice nucleation and ice particles are exerting a substantial impact on various physical and chemical processes of the atmosphere. For instance, cirrus ice clouds are important for the radiative balance of the atmosphere (Borduas and Donahue 2018); the freezing of cloud water is crucial for the initiation of precipitation and influences cloud electrification (Cantrell and Heymsfield 2005); ice in clouds or on the ground promotes heterogeneous chemistry (Abbatt 2003). Ice nucleation can occur homogeneously or heterogeneously. Homogeneous nucleation of ice in the gas phase or in pure liquid water is an activated process with a high free energy barrier for the stabilization of a critical ice cluster, the so-called ice embryo, requiring

temperatures far below the melting point or high water vapor supersaturation (Wang 2013). However, the atmosphere contains a multitude of condensed materials, which can stabilize an ice embryo and thus initiate ice nucleation at much higher temperatures and lower supersaturation. This is referred to as heterogeneous ice nucleation. It is the dominant mechanism by which ice forms in mixed phase clouds or by which cirrus ice particles form (Hoose and Möhler 2012). Deposition ice nucleation is an important example of heterogeneous nucleation, in which ice nucleation of water molecules is initiated by the growth of the ice embryo on the surface of a solid material without the occurrence of liquid water (Marcolli 2014, Kanji, Ladino et al. 2017).

In deposition ice nucleation, the interaction between the solid substrate and water molecules on its surface, controlled by the chemical composition and physical structure of the substrate, can lead to ordering of the hydrogen bonding (HB) network among these water molecules in a way to facilitate the growth and stabilization of ice embryos (Pandey, Usui et al. 2016). In a similar way, in immersion freezing, the substrate influences the molecular orientation of water molecules near the solid-liquid interface, changing their interaction with neighboring water molecules in the bulk liquid, and thus resulting in a different structure or density near the solid surface than in the bulk (Maccarini 2007).

Over the past decades, many groups implemented computational simulations (Ward, Holdman et al. 1982, Hu and Michaelides 2008, Lupi and Molinero 2014, Sosso, Tribello et al. 2016, Qiu, Lupi et al. 2018, Shevkunov 2019) and experimental studies (Anderson and Hallett 1976, Kiselev, Bachmann et al. 2017, Orlando, Artiglia et al. 2019) to investigate the interfacial water structure on solid surfaces. Vonnegut et al. (Vonnegut 1947) attributed the high ice nucleation ability of AgI to the close lattice similarity between ice and AgI. Zielke et al. (Zielke, Bertram et al. 2015) found that the AgI surface can impose a structure in the contact water layer close to that of bulk ice. Pedevilla et al. (Pedevilla, Cox et al. 2016) found that at low coverage single water molecules can bind strongly to the microcline feldspar's surface, and in spite of the non-ice like structure of this layer, the longer range interactions lead to an ice-like structure in the layers beyond the first. Recently, surface sensitive nonlinear optical spectroscopy was used to probe the interfacial water structure in relation to the IN ability of mineral surfaces (Abdelmonem, Lützenkirchen et al. 2015, Abdelmonem, Backus et al. 2017, Abdelmonem, Ratnayake et al. 2020). These studies also identified feedbacks between water structure, surface charge and ion dissolution on these surfaces. By using Kelvin Probe microscopy and in situ X-ray spectroscopy, Verdaguer et al. found the local structure of adsorbed water molecules on silica similar to ice at 70% RH at a temperature lower than 0°C, but liquid-like just above 0°C (Verdaguer, Weis et al. 2007). Through computer simulation, Hu et al. (Hu and Michaelides 2008) identified a 2D ice-like layer of water molecules on a kaolinite surface, attributed to the amphoteric property (ability to accept and donate HB) of kaolinite. In contrast, Qiu et al. (Qiu, Lupi et al. 2018) found that water on carbon surfaces is similar to that in bulk liquid by using the monoatomic water model mW. Even though the water structure is related to hydrophilic or hydrophobic properties of a surface, Lupi et al. (Lupi and Molinero 2014) argued that the hydrophilicity of a surface in general is not a good predictor for heterogeneous ice nucleation.

Among the solids discussed above, AgI possesses an exceptional heterogeneous ice nucleation ability (Vonnegut 1947) (Marcolli, Nagare et al. 2016), it is widely used as effective ice nucleus including the use as cloud seeding material for artificial rain making (Silverman 2001). As already mentioned, many studies attributed the high ice nucleation ability of AgI to its lattice structure, which promotes the formation of ice crystals both in super cooled water, and in water vapor super saturated with respect to ice (Vonnegut 1947). The unit cell of ice and silver iodide are both hexagonal and their lattice constants match within 98 % (Fortes 2018). However, lattice match does not seem to be the only condition to explain the good ice nucleation ability of AgI. For instance, compounds with similar lattice structure as ice, such as BaF<sub>2</sub> (Conrad, Ewing et al. 2005) or quartz (Marcolli, Nagare et al. 2016), are inefficient ice nucleating (IN) materials. Conversely, organic compounds such as steroids have no structural similarity with ice, but show an outstanding IN ability (Head 1961). The contrast between AgI and BaF<sub>2</sub> may be resolved by considering their solubility in water, and the effective charge of ions of these ionic crystals. BaF<sub>2</sub> is a strongly ionic compound (Nutt and Stone 2002) with a solubility in water of 1.6 g/L; the effective charge of Ba is 1.8 eV and that of F is -0.8 eV. The strong electric field arising from the two ions may inhibit the water molecules on the surface to orient in an ice-like structure (Conrad, Ewing et al. 2005). Conversely, AgI has a six orders of magnitude lower solubility in water than that of BaF<sub>2</sub> (Grünwald 1964, Conrad, Ewing et al. 2005) (about  $3 \cdot 10^{-6}$  g/L) and is considered hydrophobic. (Marcolli, Nagare et al. 2016) The effective charge of Ag and I is only 0.4 e and -0.4 e, respectively (Ward, Holdman et al. 1982). Specifically for AgI, where providing Ag<sup>+</sup> ions in water adjacent to AgI to achieve net zero surface charge is increasing the ice nucleating ability (Fletcher 1959, Edwards and Evans 1962, Marcolli, Nagare et al. 2016) indicating the importance of the electrostatic conditions near the surface.

Observation of the HB network of water molecules near AgI might provide insight into the way this substrate interacts with water molecules to facilitate ice nucleation. Surface sensitive X-ray photoemission spectroscopy (XPS) and Auger electron yield near edge X ray absorption fine structure (NEXAFS) at the oxygen K edge are useful tools to probe the electronic structure and the local coordination of water molecules (Cavalleri, Ogasawara et al. 2002, Wilson, Cavalleri et al. 2002, Winter and Faubel 2006, Nilsson, Nordlund et al. 2010, Schiros, Andersson et al. 2010, Fransson, Harada et al. 2016). XPS can provide surface sensitive elemental information, the electronic state of an element, the thickness of an adsorbate layer and depth information in the nm range, thus covering the adsorbate layer, the substrate surface and the bulk underneath.

O K-edge NEXAFS spectroscopy probes the absorption of electro-magnetic radiation by excitation of core electrons into unoccupied molecular orbitals via dipole induced transitions. The O K-edge NEXAFS spectra are very sensitive to the local HB network among the water molecules and thus whether they are arranged in a tetrahedral coordination as in ice or in a more disordered configuration as in liquid water (Cavalleri, Ogasawara et al. 2002, Myneni, Luo et al. 2002, Wilson, Cavalleri et al. 2002, Smith, Cappa et al. 2004). When collecting NEXAFS spectra through the detection of Auger electrons emitted during relaxation of the initial core hole, the method becomes surface sensitive due to the low inelastic mean free path

of the Auger electrons, similar to the case of XPS. While non-linear optical methods may provide structural information as well, and even with higher surface sensitivity (Abdelmonem, Lützenkirchen et al. 2015), the advantage of the NEXAFS based method is the combination with XPS to have parallel chemical information. We have previously used this technique to detect changes to the HB structure of ice in presence of ions (Bartels-Rausch, Orlando et al. 2017, Kong, Waldner et al. 2017, Waldner, Artiglia et al. 2018). Following up from pioneering work by Verdaguer et al. who were the first to attempt at probing the structure of adsorbed water with this technique on SiO<sub>2</sub> (Verdaguer, Weis et al. 2007). We further used it to observe liquid-like adsorbed water at the surface of TiO<sub>2</sub> (Orlando, Artiglia et al. 2019). This work aims to investigate the HB structure of adsorbed water molecules on the surface of AgI in situ while varying relative humidity under subsaturated conditions with respect to ice using XPS and electron yield O K-edge NEXAFS. While this technique does not allow observing the nucleation of ice directly, it allows interrogating the adsorbed water in situ while in equilibrium with water vapor below saturation. We found that the adsorbed water on AgI particles show a rather ice-like HB structure.

### 3.1.2 Materials and experimental methods

The experiments were carried out at the *in situ spectroscopy (ISS)* beamline at the Swiss Light Source (SLS). Photoemission and electron yield NEXAFS spectra were acquired with a hemispherical electron analyzer coupled to a differentially pumped lens system (ScientaOmicron R4000/HiPP-2). The experimental cell (solid – gas interface chamber, SGI) under the conditions of the photoemission experiments has been described in a previous publication (Orlando, Waldner et al. 2016). More details of the sample configuration relevant for the present experiments are given in the SI.

The process chosen for the production of silver iodide particles was inspired by Nagare et al. (Nagare, Marcolli et al. 2015). Chemicals used for sample preparation were purchased from Sigma Aldrich. We mixed 0.1 M potassium iodide and 0.1 M silver nitrate aqueous solutions and diluted with pure water (18.2 MOhm.cm remaining conductivity), which led to the precipitation of yellowish AgI particles. The AgI product was then washed with pure water, and centrifuged to separate the powder from the water. AgI particles were dried in an oven at 423 K for 3 hours and then cooled down to room temperature with a rate of 0.3 K/min. Since the AgI is highly photosensitive, the sample was prepared in absence of light to avoid its decomposition.

The synthesized AgI powder was dispersed in isopropanol and sonicated for 5 min, forming a homogeneous suspension. Two 30  $\mu$ L droplets of the suspension were drop cast onto the surface of the sample holder, leaving a uniform layer of AgI powder on the surface of the sample holder. The sample was then introduced in the experimental cell. Water vapor was dosed to the cell by means of a capillary dosing system (see SI, Section 1). Under isobaric conditions and by varying the temperature of the sample, we could effectively adjust the relative humidity at the sample surface, which leads to a varying amount of adsorbed water in equilibrium between the solid sample and water vapor. This method allows to keep the water vapor pressure constant for different relative humidities. This reduces the uncertainty in the

retrieval of the spectra of adsorbed water. The experiments were repeated under three different conditions: i) dry in high vacuum at 323 K, ii) 60% (251 K) and iii) 90% (247 K) relative humidity with respect to ice at 0.5 mbar of water vapor pressure.

During the experiment, we made use of linearly polarized light at  $0^\circ$ . O 1s, I 3d and C 1s core level photoelectron spectra were acquired at photon energies such that each core level was obtained at the same five different kinetic energies, corresponding to five different probing depths. The corresponding excitation and kinetic energies are provided in the SI (Table S1). The probing depth is related to the inelastic mean free path ( $\lambda$ ) of the photoelectron (probing depth =  $\lambda \cdot \cos\theta$ , where  $\theta$  is the electron take-off angle with respect to the surface normal). Photoemission peaks shown in this work were normalized to the photon flux, inelastic mean free path of photoelectrons and the total photoionization cross section. A Shirley background was subtracted from the spectra before calculating the area. The binding energy scale of the measured core level electrons was calibrated using the C 1s peak as a reference (C sp<sup>3</sup> bond assigned to carbon contamination, at 284.8 eV). Peak fitting details are provided in the SI (Table S2). The O K-edge NEXAFS spectra were obtained by integrating the Auger KLL peak of oxygen within a kinetic energy window ranging from 425 to 525 eV, while scanning the photon energy from 527 to 560 eV.

### 3.1.3 Results and discussion

#### Adsorption of water on the AgI surface.

The amount of water molecules reversibly adsorbed on the surface of AgI particles at equilibrium was monitored via the O 1s photoemission signal intensity excited by 870 eV photons, as a function of relative humidity (Figure 3-1). Note that the equilibration time scale for water adsorption is in the order of nanoseconds. Thus, desorption and adsorption steady state was maintained during the acquisition of spectra, and it is reasonable to assume that the adsorbed water layer on the AgI surface was not entirely homogeneous but was probably affected by the structure of the powder, edges and defects, as also discussed by Marcolli et al. (Marcolli, Nagare et al. 2016).

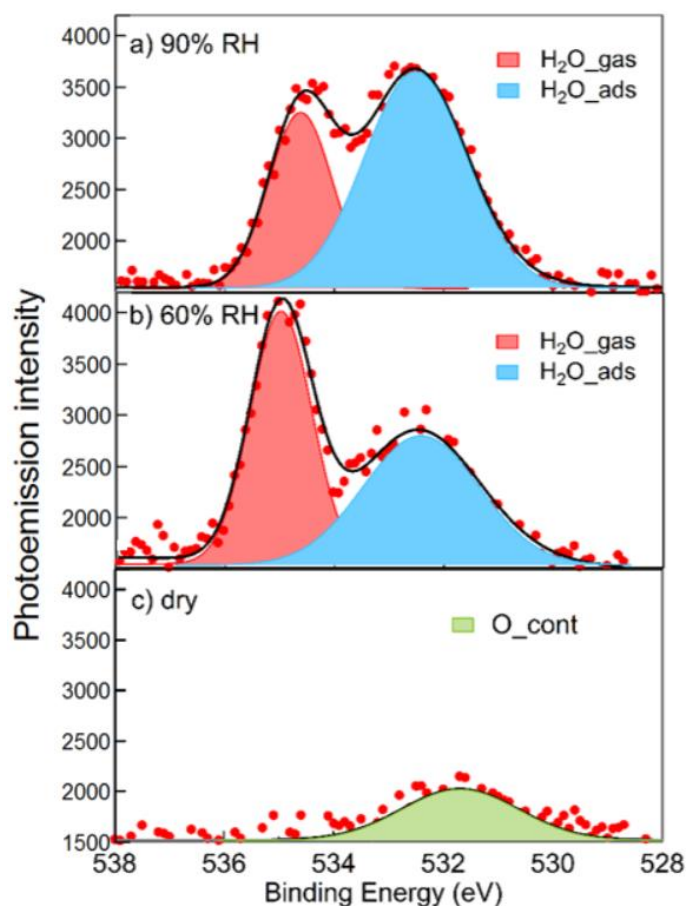


**Figure 3-1.** O 1s photoemission spectra measured with a photon energy of 870 eV on the surface of AgI under vacuum (dry, 323 K) (c), 60 % RH / 251 K (b) and 90 % RH / 247 K (a) conditions. The shaded areas indicate the components of a Gaussian peak deconvolution for O1s originating from H<sub>2</sub>O<sub>gas</sub>, H<sub>2</sub>O<sub>ads</sub> and O<sub>cont</sub>, respectively, as explained in the text. The three spectra share the vertical axis scale.

For the photon energy chosen, photoelectrons had a kinetic energy of 340 eV corresponding to a probe depth of ca. 1 nm (the most surface sensitive mode of this work). Under dry conditions (Figure 3-1c), 323 K in vacuum, the only broad feature in the spectrum at around 532 eV is assigned to oxygenated adventitious carbon species. Adventitious carbon contamination is inevitable for samples that have been exposed to the ambient environment before transfer into the sample chamber, and such carbon species may build up further during X-ray irradiation in non-UHV environments. A survey XPS scan, which shows carbon on the surface, is reported in Figure S 3-2. Representative high resolution C 1s spectra at both dry and humid conditions are provided in Figure S3-3. Note that under dry conditions, although the spectrum is dominated by reduced carbon species, a feature corresponding to oxygenated carbon is present at 286.3 eV. Similar contaminating species have been reported in other studies (Stipp and Hochella 1991, Mangolini, McClimon et al. 2014, Landoulsi, Genet et al. 2016, Trotochaud, Head et al. 2018). Figure 3-1 shows that, upon water dosing into the experimental chamber (H<sub>2</sub>O partial pressure of 0.5 mbar), a sharp feature in the O 1s at 535.0 eV, assigned to gas phase water, is observed at both RHs. Apart from hitting the AgI sample itself, the X-ray beam also overlaps with the gas phase just above the sample and within the acceptance

volume of the analyzer electron optics. The binding energy obtained for gas phase water is not well defined, since the binding energy calibration is based on the C 1s surface contamination (see below), which corrects for sample charging. Gas phase molecules experience a different potential as they are located between the sample surface and the grounded electron sampling aperture. As the relative humidity increases (Figure 3-1, panels b and a), a new broad feature appears at 532.5 eV, whose relative intensity is higher at 90% RH than at 60% RH, and which we attribute to adsorbed water molecules (Ketteler, Ashby et al. 2008). The significant FWHM (see Table S2) of this peak results from different adsorption configurations, different adsorption sites exposed on the surface of a powder, and from the intermolecular interactions among the water molecules. The contribution of the contaminating component identified under dry conditions to the O 1s cannot be assessed anymore. In more detail, Figure S3-3 shows that more of the oxidized carbonaceous species (e.g., carboxyls) appear at 90% RH. The contribution of carboxyls to the O 1s spectrum overlaps strongly with that of adsorbed water (Ketteler, Ashby et al. 2008), thus we refrained from fitting oxygenated carbon species to the O 1s under humid conditions due to the large uncertainty. Based on the C 1s spectra (Supporting materials, Fig. S3), the contribution of carboxyl carbon is about an order of magnitude less than that of total carbon. Therefore, in spite of substantial amounts of total carbon (see quantitative information from application of attenuation model below), the adsorbed water still dominates over oxygenated adventitious carbon species. Throughout this work, we deconvoluted all spectra into three Gaussian peaks (see Figure 3-1): oxygen from gas phase water ( $\text{H}_2\text{O}_{\text{gas}}$ , red peak), adsorbed water ( $\text{H}_2\text{O}_{\text{ads}}$ , blue peak), and oxygen belonging to the oxygenated carbon species ( $\text{O}_{\text{cont}}$ , green peak) under dry conditions.

Figure 3-2 shows the evolution of the I 3d signal intensity under dry, 60% and 90% RH at 0.5 mbar. The I 3d spectral deconvolution by Gaussian peaks is also shown (shaded areas). The measured binding energies of I  $3d_{5/2}$  and I  $3d_{3/2}$  are 619.5 and 631.0 eV, respectively, with a spin-orbit split of 11.5 eV, in agreement with other literature reports for AgI (Briggs 1981, Moers, Klewenebenius et al. 1987). The fitting parameters are reported in the SI, Table S2. The increasing thickness of the adsorbed water layer on the AgI surface leads to an increasing attenuation of the I 3d signal, as directly apparent from Figure 3-2. Silver iodide is a photosensitive material, and while exposed to the synchrotron radiation may undergo decomposition. However, Figure 3-2 shows that the line shape of I 3d does not evolve as a function of RH, indicating that the chemical state change of iodine is negligible, within uncertainty and detection limit, during the time scale of the acquisition of a spectrum (about 5 min). The same result was observed for silver (Ag 3d spectra reported in Figure S 3-4). The absence of new peak components in Ag 3d and I 3d spectra also indicates that no partial solvation of iodide anions and silver cations occurred at the interface, as observed for more soluble salts in previous work (Verdaguer, Sacha et al. 2006).

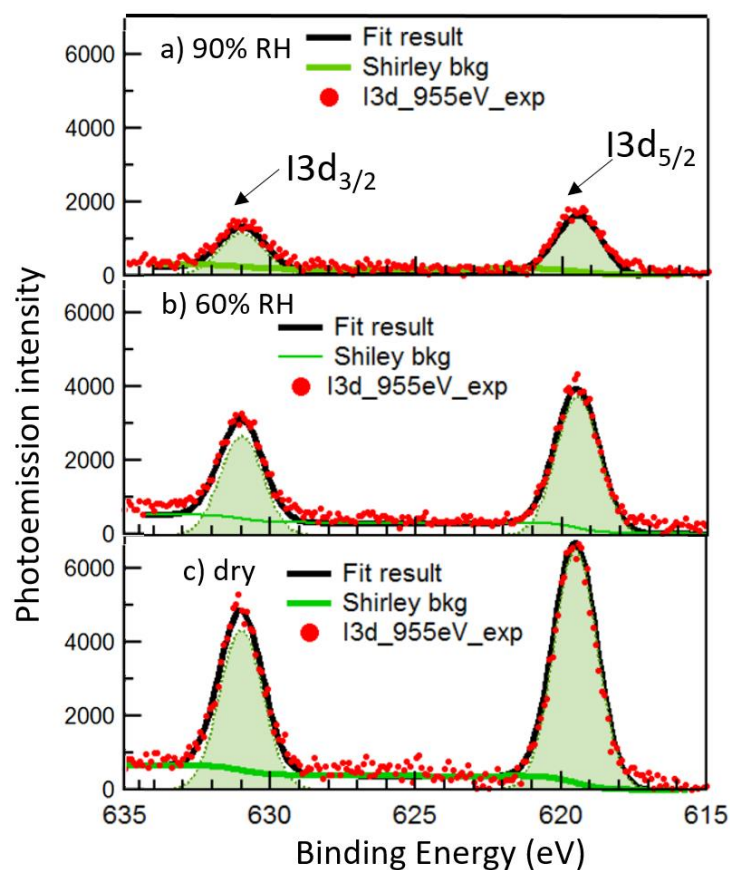


**Figure 3-2.** Plot of measured I 3d XPS spectra at dry c), 60% RH b) and 90% a) with  $h\nu = 955 \text{ eV}$ , corresponding to a kinetic energy of  $340 \text{ eV}$ . The S.O.S of I 3d is  $11.5 \text{ eV}$ . Gaussian deconvolutions of the I 3d peak are shown by green shaded areas. The three spectra share the same vertical axis scale.

#### Depth profile.

To get a depth profile of the material under different conditions, the signals of O 1s and I 3d were acquired with increasing kinetic energy:  $340 \text{ eV}$  (already discussed in the previous section),  $550 \text{ eV}$ ,  $650 \text{ eV}$ ,  $750 \text{ eV}$  and  $900 \text{ eV}$ . The signal of I 3d from bulk AgI served as a reference to represent the bulk substrate and normalize the O 1s photoemission signal intensity of adsorbed water. O 1s ( $\text{H}_2\text{O}_{\text{ads}}$ )/I 3d (AgI) ratios evaluated at 60 and 90% RH are plotted as a function of the kinetic energy in Figure 3-3. When reporting the photoemission intensity ratios between two elements at the same kinetic energy, those factors contributing to the measured intensity cancel, which are related to the analyzer transmission and/or depend on the measurement geometry of the experimental setup. As the probing depth increases, the relative contribution of the I 3d signal intensity from the bulk starts to increase, while the contribution of oxygen atoms belonging to water adsorbed on the surface remains almost constant, leading to a general decrease of O 1s ( $\text{H}_2\text{O}_{\text{ads}}$ )/I 3d (AgI).

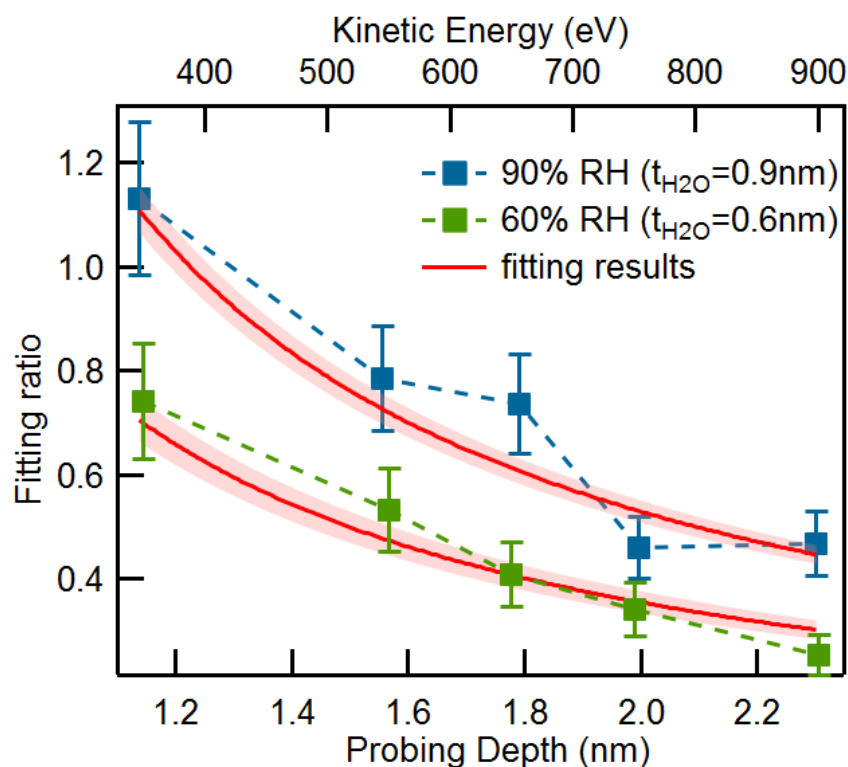


**Figure 3-3.** Fitting ratio of the photoemission intensity of O1s from adsorbed water to that of I3d measured at 5 different probing depths, under 60% RH (green) and 90% RH (blue). The solid red line represents the fitting results using the attenuation model described in text and SI, with one standard deviation shown by the red shaded area.

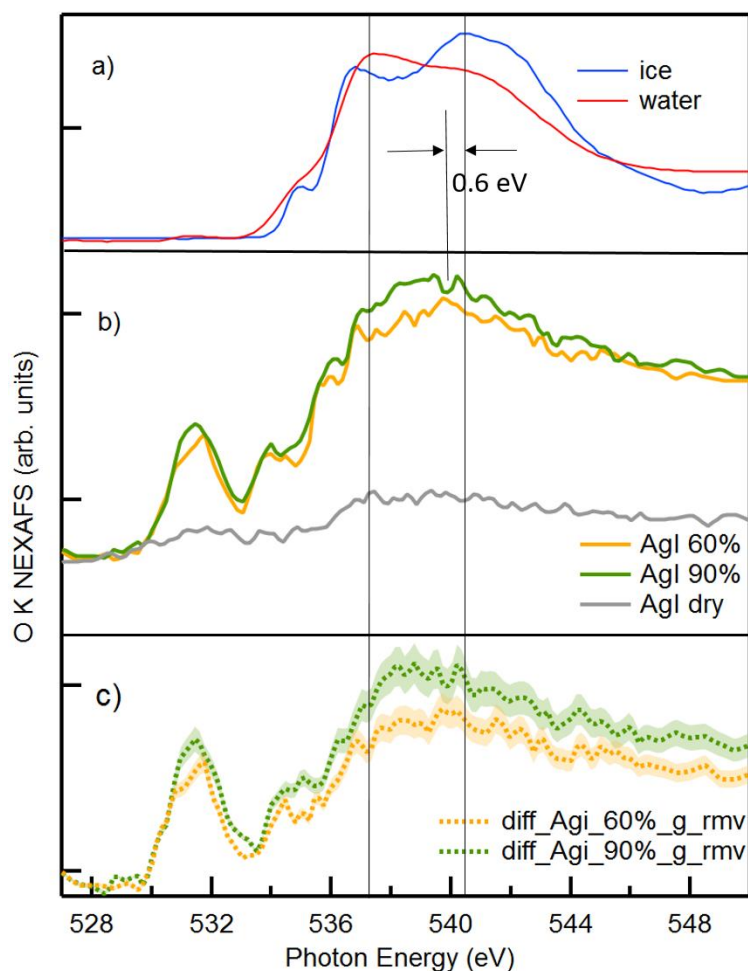
An attenuation model was developed to fit the kinetic energy dependent signal intensity ratios of O 1s ( $\text{H}_2\text{O}_{\text{ads}}$ ) to I 3d (AgI) and C 1s / I 3d (AgI). This model considers the surface being covered by a homogeneous layer of adsorbed water (see section 4 in the SI). On top of this water layer, patchy areas of floating carbon islands with an average thickness,  $t_c$ , are covering a fraction  $\gamma$  of the surface area, similar to a model proposed by Fadley (Fadley, Baird et al. 1974). The equations used to calculate signal intensities of O 1s, I 3d and C 1s and the corresponding ratios are provided in the SI (Figure S 3-7 and S 3-8). The best fit resulted in a  $\gamma$  of 0.80 and a carbon island thickness of 0.3 nm under dry conditions. Under humid conditions, at 60% RH, the water layer thickness is determined to be 0.6 nm (corresponding to approximately 2 ML of water), the corresponding carbon island thickness is 0.6 nm with a  $\gamma$  value of 0.6. At 90%, the water layer thickness is 0.9 nm (corresponding to approximately 3 ML of water) and the fractional coverage of carbon is further increased to 0.8 with an average carbon islands thickness of 1.1 nm. The uncertainty related to the fits are included in Figure S 3-8. The results of our depth profile analysis suggest that  $t_c$  and  $\gamma$  change with the RH. Higher RH conditions favor the growth of adventitious carbon islands. This implies that even though liquid water used as the source of vapor was purified by means of several freeze-pump-thaw cycles, it is inevitable to co-dose small amounts of carbon containing species that are decomposed by the beam. This may partly derive from displacement of contaminating gases previously adsorbed at the chamber walls (Orlando, Waldner et al. 2016, Trotochaud, Head et al. 2018).

O K edge NEXAFS of water molecules on AgI surface under subsaturated conditions.

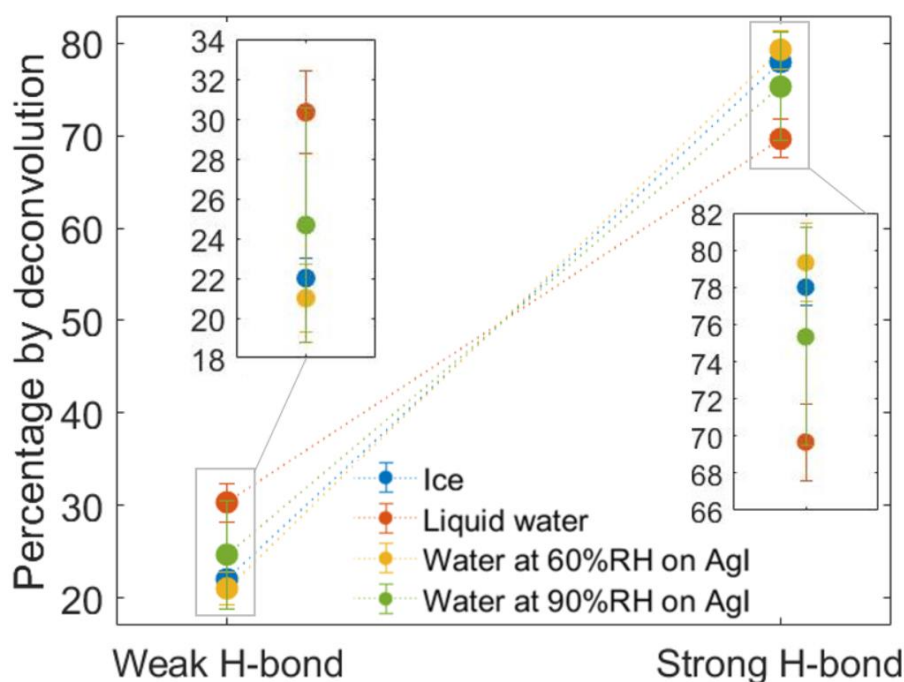
In the discussion of NEXAFS spectra of adsorbed water and the relationship to the HB structure, we mainly rely on the comparison to the cases of liquid water and ice. In the SI, Figure S 3-9, we show partial electron yield O K-edge NEXAFS spectra of liquid water, ice and gas phase water. In the latter, three well-separated peaks represent the excitations from O 1s into the 4a<sub>1</sub> (534eV), 2b<sub>1</sub> (536eV) and Rydberg (537 eV) orbitals of free water molecules. In the condensed phase (see also Figure 3-4a), these transitions strongly broaden and shift, due to the close O-H distance in HB in a range of configurations and strengths (Nilsson, Nordlund et al. 2010), which strongly affects the unoccupied orbitals in comparison to the gas phase case. In liquid water, strong intramolecular covalent O-H bonds and asymmetric weak HB configurations prevail, leading to maximum absorption at around 537 eV and a pronounced pre-edge at 535 eV. In contrast, in ice, the predominance of strong and symmetric tetrahedral configurations leads to maximum absorption at around 541-542 eV (Figure S 3-9). Absorption at 535 eV is attributed to free OH groups that are more prevalent in liquid water than in ice, but also at the water-vapor interface (Wernet, Nordlund et al. 2004, Nilsson, Nordlund et al. 2010). In this work, we use the contrasting HB configurations embodied in the NEXAFS spectra of liquid water and ice as references to qualitatively describe the HB structure of adsorbed water on AgI. In the spectra of liquid water and ice, changes with temperature or between liquid and ice can be explained by the varying relative occurrence of different configurations rather than by energy shifts of the absorption features (Nilsson and Pettersson 2015). The interaction between adsorbed water molecules and the solid surface might lead to shifts of absorption features, but the general shape and the appearance of the structural motives in the NEXAFS features is assumed to be preserved. This was demonstrated for the liquid like character of adsorbed water on TiO<sub>2</sub> (Orlando, Artiglia et al. 2019), and also for tetrahedrally-coordinated water adsorbed on Ru(0001) once coverage reaches one monolayer and above (Nordlund, Ogasawara et al. 2009).

Figure 3-4b) shows the O K edge of AgI samples under dry and humid conditions. The AgI spectrum measured under dry conditions (grey) shows only weak absorption features because the lattice of AgI is oxygen free. The observed broad features likely result from the oxygen-containing carbonaceous contaminations, as confirmed by C 1s XPS and discussed in the previous section (Figure 3-1c). When the RH increases (yellow for 60% RH, at 251 K and green for 90% RH, at 247 K), water adsorbs and starts to dominate the spectrum. At 60% RH, the absorption features at 537 eV and, especially, at 540 eV increase. As the RH increases to 90%, the absorption features further increase. The spectra of water on AgI under humid conditions exhibit higher absorption feature at 540 eV than at 537 eV. Such a behavior is comparable to the case of ice, but with the absorption maximum slightly shifted (by approximately 0.6 eV) toward lower photon energy (shown in Figure 3-4). We also note a strongly increasing absorption at 532 eV, related to the oxygenated carbon contaminations. The O K-edge spectrum of typical carboxylic acids or ketones most likely formed under humid and more oxidizing conditions in presence of water vapor, and detected in the C 1s spectra (Figure S 3-3b), is characterized by an intense peak at 532 eV. It is the result of the transition of 1s electrons of oxygen in carbonyl or carboxyl functions into  $\pi^*$  unoccupied molecular orbitals (Horikawa, Arai et al. 2012). Absorption between 537 and 545 eV for such species is rather

featureless and relatively weak. As also mentioned in the discussion of the O 1s photoemission spectra (Figure 3-1), their relative proportion can be considered rather small.



**Figure 3-4.** a) Auger electron yield O K edge NEXAFS spectra of liquid water and ice for comparison (also shown in SI). b) Electron yield O K edge NEXAFS spectra from AgI particles under dry condition (grey, 323 K), 60% RH (blue, at 251 K) and 90% RH (red, at 247 K) at 0.5mbar. c) The difference spectra obtained by subtracting the spectrum measured at dry condition and water gas phase from those under humid condition shown in panel b). Spectra of wet condition (green and yellow line in panel b) and their corresponding difference spectra (dashed green and yellow line in panel c), shown with different scales.



**Figure 3-5.** Fraction (%) of electron yield O K edge NEXAFS peak areas attributed to configurations of adsorbed water molecules with weak HB and those with strong HB on the AgI surface at 60% RH (0.5 mbar, 251 K) and 90% RH (0.5 mbar, 247 K). For comparison, results for ice (blue) and liquid water (red) as references are also reported in the plot. The insets are shown to more clearly illustrate the differences among the samples.

By subtracting the spectrum of dry AgI and that of water gas phase from those acquired at different RH values, we focus exclusively on the adsorbed water layer (Figure 3-4c). Apart from C=O absorption in the pre-edge, these difference spectra exhibit maximum intensity between 539 and 540 eV, where the stronger and more symmetric HB contribute, and lower intensity around 537 eV, where the characteristic absorptions for asymmetric weak HB predominate. This indicates that under sub-saturated relative humidity condition, water molecules adsorbed on AgI have a higher proportion of tetrahedrally and symmetrically-coordinated water molecules. However, as mentioned above for the raw spectra, the maximum of the absorption band of the difference spectra are negatively shifted by approximately 0.6 eV compared to the reference spectrum of ice. The local geometry of the substrate and of the adsorbate are possibly responsible for this apparent shift, which was also observed on other surfaces (Nordlund, Ogasawara et al. 2009, Orlando, Artiglia et al. 2019).

To more quantitatively estimate the relative share of water molecules in liquid-like weak HB configurations versus those in tetrahedral ice-like configurations, all NEXAFS spectra were deconvoluted with Gaussian peaks. The results are presented in Figure S3-10 and Figure S3-11. The deconvolution followed the rationale used by Cappa et al. (Cappa, Smith et al. 2005) and Nilsson et al. (Nilsson, Nordlund et al. 2010), in which the energy positions, widths and number of peaks were not chosen to represent discrete transitions but rather to obtain a good overall fit of the spectrum. Still, we chose them in a similar way to allow an estimate of liquid- and ice-like adsorbed water (see the SI for more information). The results are summarized in Figure 3-5. The weak asymmetric HB are represented by the sum of the areas of red peaks (peaks 2,

3, 4 of the NEXAFS spectra, Figure S3-10) and the strong symmetric tetrahedral configurations by the sum of the areas of the blue peaks (peaks 5 and 6, Figure S3-10). The total area of the blue peaks is always higher than that of the red peaks. The relative share of the red peaks is higher in liquid water than in ice (weak HB, left column in Figure 3-5), while the relative share of the blue peaks is higher in ice than in liquid water (strong HB, right column in Figure 3-5). Concerning water molecules adsorbed on the surface of AgI, at 60% (yellow) and 90% RH (green), both shares of weak and strong HB are closer to that for ice than to that for liquid water. Obviously, this analysis strongly depends on the fitting procedure, specifically on the numbers of peaks used to represent the whole absorption edge, and to the attribution of the peaks to the weak and strong HB category. In order to illustrate the uncertainty and to assess the sensitivity to the choice and attribution of the peaks, we have fitted all NEXAFS spectra also with just 6 Gaussians rather than 7, and by once re-assigning one of the peaks to either the strong (blue) or the weak (red) HB category (see SI). The result of this sensitivity analysis is included in Figure 3-5 as error bars. This underlines the robustness of our conclusion that at both relative humidities the HB configuration is closer to being ice-like than liquid like. This seems more pronounced at 60% RH, when on average 2 ML of water adsorbed on AgI particles mostly contribute to the O K edge NEXAFS signal. Though we would only expect a certain fraction of water molecules being able to attain a fully tetrahedral coordination as in ice, because a substantial part is likely engaging in strong interaction with the substrate. We also note the significant uncertainty and would not like to overinterpret these fitting results. In turn, at 90% RH a slightly lower share of tetrahedral coordination of water molecules is derived than at 60% RH. Thus, it does not seem that the formation of a completely hexagonal structure is limited by the amount of water molecules at the surface at equilibrium. Rather, we have to remain aware that even for the surface of bulk crystalline ice, the topmost surface layer is disordered, which manifests in changing relative proportions in the NEXAFS spectra (Křepelová, Huthwelker et al. 2010, Bluhm, Hävecker et al. 2011). Nevertheless, this layer with at least partial abundance of tetrahedrally coordinated water molecules may facilitate the stabilization of ice embryos at saturation and above.

#### 3.1.4 Conclusion

We have experimentally investigated the HB structure of adsorbed water on a AgI powder surface by using in situ XPS and electron yield NEXAFS spectroscopy techniques. The thickness of the equilibrium adsorbed water layer is determined at elevated RH with the help of an attenuation model that takes into account the presence of adventitious carbon in the form of islands at the topmost surface. Increasing the RH from dry conditions to 60 % and 90 %, the thickness of the water layer increases from approximately 2 to 3 ML, respectively. Our results are the first direct experimental evidence unraveling the local coordination of HB structure on an actual and realistic AgI particle surface at a molecular level. The O K-edge NEXAFS spectra of water on the AgI surface generally show an enhanced high energy absorption edge, located at 540 eV, which is typically observed in the presence of tetrahedrally coordinated (ice-like) water molecules. This is also evident by the comparison with the O K-edge spectrum of ice.

AgI is hydrophilic (De Pena and Caimi 1967, Parungo 1975) but with very low solubility in water (Grünwald 1964), thus it attracts water molecules without perturbing their electronic

structure by ion dissolution. When the coverage of water molecules is low, at 60% RH, the contact layer (1-2ML) shows a larger fraction of water molecules adopting a tetrahedral, ice-like structure, highlighting the potential of AgI to promote ice nucleation. The combined results of XPS and NEXAFS suggest that water molecules adsorbed on the surface of solid AgI particles already start to display an ordered HB structure at subsaturated condition with respect to ice, which is mirrored in the role of AgI as an efficient ice nucleus. This is in contrast to the case of water adsorbed on  $TiO_2$  nanoparticles (known to be inefficient INs), in which surface water molecules are still liquid-like at a temperature close to that where homogeneous ice nucleation occurs (Orlando, Artiglia et al. 2019). Thus, our work reveals how the water HB structure on a solid particle surface is the result of a complex interplay of interactions of water molecules among each other and with the substrates on a molecular level.

#### ASSOCIATED CONTENT

##### **Supporting Information.**

The following files are available free of charge.

Experiment setup, measurement parameters, supporting XPS spectra, attenuation model and fitting of the  $O1s_{ads}/I3d$  ratio, patched carbon islands model and its fitting results, O K edge NEXAFS spectra and their Gaussian deconvolution.

#### AUTHOR INFORMATION

##### **Corresponding Author**

Markus Ammann - Laboratory of Environmental Chemistry, Paul Scherrer Institut, 5232 Villigen, Switzerland; orcid.org/0000-0001-5922-9000; Email: markus.ammann@psi.ch

##### **Author Contributions**

Y.H, L.A and M.A. designed the work and conceived the experiment; Y.H, J.G, A.B. and L.A performed the XPS and NEXAFS measurement; Y.H analyzed and interpreted the XPS and NEXAFS data with the help of M.A, L.A, and A.B; T.B.R. adapted the cryo sample holder and contributed to the discussion of the NEXAFS spectra; Y.H, L.A and M.A worked on the manuscript together. All authors contributed to the discussion and approval to the final version of the manuscript.

##### **Notes**

The authors declare no competing financial interest.

#### ACKNOWLEDGMENT

This work was performed at the ISS beamline of the Swiss Light Source, Paul Scherrer Institute. We acknowledge the technical support by Andrés Laso, and support by the beamline staff Dr. Jörg Raabe. This work was supported by the Swiss National Science Foundation (grant no. 169176).

## References

- Silver iodide (AgI) crystal structure, high pressure modifications, lattice parameters: Datasheet from Landolt-Börnstein - Group III Condensed Matter · Volume 41B: "II-VI and I-VII Compounds; Semimagnetic Compounds" in SpringerMaterials ([https://doi.org/10.1007/10681719\\_130](https://doi.org/10.1007/10681719_130)). O. Madelung, U. Rössler and M. Schulz, Springer-Verlag Berlin Heidelberg.
- Abbatt, J. P. D. (2003). "Interactions of Atmospheric Trace Gases with Ice Surfaces: Adsorption and Reaction." *Chemical Reviews* 103(12): 4783-4800.
- Abdelmonem, A., E. H. G. Backus, N. Hoffmann, M. A. Sánchez, J. D. Cyran, A. Kiselev and M. Bonn (2017). "Surface-charge-induced orientation of interfacial water suppresses heterogeneous ice nucleation on  $\alpha$ -alumina (0001)." *Atmos. Chem. Phys.* 17(12): 7827-7837.
- Abdelmonem, A., J. Lützenkirchen and T. Leisner (2015). "Probing ice-nucleation processes on the molecular level using second harmonic generation spectroscopy." *Atmos. Meas. Tech.* 8(8): 3519-3526.
- Abdelmonem, A., S. Ratnayake, J. D. Toner and J. Lützenkirchen (2020). "Cloud history can change water-ice-surface interactions of oxide mineral aerosols: a case study on silica." *Atmos. Chem. Phys.* 20(2): 1075-1087.
- Anderson, B. J. and J. Hallett (1976). "Supersaturation and Time Dependence of Ice Nucleation from the Vapor on Single Crystal Substrates." *Journal of the Atmospheric Sciences* 33(5): 822-832.
- Bartels-Rausch, T., F. Orlando, X. Kong, L. Artiglia and M. Ammann (2017). "Experimental Evidence for the Formation of Solvation Shells by Soluble Species at a Nonuniform Air-Ice Interface." *ACS Earth and Space Chemistry* 1(9): 572-579.
- Bluhm, H., M. Hävecker, A. Knop-Gericke, M. Kiskinova, R. Schlögl and M. Salmeron (2011). "In Situ X-Ray Photoelectron Spectroscopy Studies of Gas-Solid Interfaces at Near-Ambient Conditions." *MRS Bulletin* 32(12): 1022-1030.
- Borduas, N. and N. M. Donahue (2018). Chapter 3.1 - The Natural Atmosphere. *Green Chemistry*. B. Török and T. Dransfield, Elsevier: 131-150.
- Briggs, D. (1981). "Handbook of X-ray Photoelectron Spectroscopy C. D. Wanger, W. M. Riggs, L. E. Davis, J. F. Moulder and G. E. Muilenberg Perkin-Elmer Corp., Physical Electronics Division, Eden Prairie, Minnesota, USA, 1979. 190 pp. \$195." *Surface and Interface Analysis* 3(4): v-v.
- Cantrell, W. and A. Heymsfield (2005). "Production of Ice in Tropospheric Clouds: A Review." *Bulletin of the American Meteorological Society* 86(6): 795-808.
- Cappa, C. D., J. D. Smith, K. R. Wilson, B. M. Messer, M. K. Gilles, R. C. Cohen and R. J. Saykally (2005). "Effects of Alkali Metal Halide Salts on the Hydrogen Bond Network of Liquid Water." *The Journal of Physical Chemistry B* 109(15): 7046-7052.
- Cavalleri, M., H. Ogasawara, L. G. M. Pettersson and A. Nilsson (2002). "The interpretation of X-ray absorption spectra of water and ice." *Chemical Physics Letters* 364(3): 363-370.
- Conrad, P., G. E. Ewing, R. L. Karlinsky and V. Sadtchenko (2005). "Ice nucleation on BaF<sub>2</sub>(111)." *The Journal of Chemical Physics* 122(6): 064709.
- De Pena, R. and E. Caimi (1967). "Hygroscopicity and chemical composition of silver iodide smoke used in cloud seeding experiments." *Journal of the Atmospheric Sciences* 24(4): 383-386.
- Edwards, G. R. and L. F. Evans (1962). "Effect of surface charge on ice nucleation by silver iodide." *Transactions of the Faraday Society* 58(0): 1649-1655.
- Fadley, C. S., R. J. Baird, W. Siekhaus, T. Novakov and S. Å. L. Bergström (1974). "Surface analysis and angular distributions in x-ray photoelectron spectroscopy." *Journal of Electron Spectroscopy and Related Phenomena* 4(2): 93-137.
- Fletcher, N. H. (1959). "Entropy Effect in Ice Crystal Nucleation." *The Journal of Chemical Physics* 30(6): 1476-1482.
- Fortes, A. (2018). "Accurate and precise lattice parameters of H<sub>2</sub>O and D<sub>2</sub>O ice Ih between 1.6 and 270 K from high-resolution time-of-flight neutron powder diffraction data." *Acta Crystallographica Section B* 74(2): 196-216.
- Fransson, T., Y. Harada, N. Kosugi, N. A. Besley, B. Winter, J. J. Rehr, L. G. M. Pettersson and A. Nilsson (2016). "X-ray and Electron Spectroscopy of Water." *Chemical Reviews* 116(13): 7551-7569.
- Grünewald, H. (1964). "Solubilities of Inorganic and Organic Compounds. Herausgeg. v. H. Stephen und T. Stephen. Pergamon Press, Oxford - London - New York - Paris 1963. 1. engl. Aufl., Vol. 1, Part I: 960 S., geb.£ 10.0. 0. Vol. 1, Part II: 970 S., geb.£ 12.10. 0." *Angewandte Chemie* 76(19): 832-832.
- Head, R. B. (1961). "Steroids as Ice Nucleators." *Nature* 191(4793): 1058-1059.
- Hoose, C. and O. Möhler (2012). "Heterogeneous ice nucleation on atmospheric aerosols: a review of results from laboratory experiments." *Atmos. Chem. Phys.* 12(20): 9817-9854.
- Horikawa, Y., H. Arai, T. Tokushima and S. Shin (2012). "Spectral fingerprint in X-ray absorption for hydrogen-bonded dimer formation of acetic acids in solution." *Chemical Physics Letters* 522: 33-37.

- Hu, X. L. and A. Michaelides (2008). "Water on the hydroxylated (001) surface of kaolinite: From monomer adsorption to a flat 2D wetting layer." *Surface Science* 602(4): 960-974.
- Kanji, Z. A., L. A. Ladino, H. Wex, Y. Boose, M. Burkert-Kohn, D. J. Cziczko and M. Krämer (2017). "Overview of Ice Nucleating Particles." *Meteorological Monographs* 58: 1.1-1.33.
- Ketteler, G., P. Ashby, B. S. Mun, I. Ratera, H. Bluhm, B. Kasemo and M. Salmeron (2008). "In situ photoelectron spectroscopy study of water adsorption on model biomaterial surfaces." *Journal of Physics: Condensed Matter* 20(18): 184024.
- Kiselev, A., F. Bachmann, P. Pedevilla, S. J. Cox, A. Michaelides, D. Gerthsen and T. Leisner (2017). "Active sites in heterogeneous ice nucleation—the example of K-rich feldspars." *Science* 355(6323): 367-371.
- Kong, X., A. Waldner, F. Orlando, L. Artiglia, T. Huthwelker, M. Ammann and T. Bartels-Rausch (2017). "Coexistence of Physisorbed and Solvated HCl at Warm Ice Surfaces." *The Journal of Physical Chemistry Letters* 8(19): 4757-4762.
- Křepelová, A., T. Huthwelker, H. Bluhm and M. Ammann (2010). "Surface Chemical Properties of Eutectic and Frozen NaCl Solutions Probed by XPS and NEXAFS." *ChemPhysChem* 11(18): 3859-3866.
- Landoulsi, J., M. J. Genet, S. Fleith, Y. Touré, I. Liascukiene, C. Méthivier and P. G. Rouxhet (2016). "Organic adlayer on inorganic materials: XPS analysis selectivity to cope with adventitious contamination." *Applied Surface Science* 383: 71-83.
- Lupi, L. and V. Molinero (2014). "Does Hydrophilicity of Carbon Particles Improve Their Ice Nucleation Ability?" *The Journal of Physical Chemistry A* 118(35): 7330-7337.
- Maccarini, M. (2007). "Water at solid surfaces: A review of selected theoretical aspects and experiments on the subject." *Biointerphases* 2(3): MR1-MR15.
- Mangolini, F., J. B. McClimon, F. Rose and R. W. Carpick (2014). "Accounting for Nanometer-Thick Adventitious Carbon Contamination in X-ray Absorption Spectra of Carbon-Based Materials." *Analytical Chemistry* 86(24): 12258-12265.
- Marculli, C. (2014). "Deposition nucleation viewed as homogeneous or immersion freezing in pores and cavities." *Atmospheric Chemistry and Physics* 14(4): 2071-2104.
- Marculli, C., B. Nagare, A. Welti and U. Lohmann (2016). "Ice nucleation efficiency of AgI: review and new insights." *Atmos. Chem. Phys.* 16(14): 8915-8937.
- Moers, H., H. Klewenebenius, G. Pfennig and H. J. Ache (1987). "XPS AND AES INVESTIGATIONS OF THE INTERACTION OF GASEOUS IODINE WITH SILVER SURFACES." *Fresenius Zeitschrift Fur Analytische Chemie* 329(2-3): 361-366.
- Myneni, S., Y. Luo, L. Å. Näslund, M. Cavalleri, L. Ojamäe, H. Ogasawara, A. Pelmenschikov, W. Ph, P. Väterlein, C. Heske, Z. Hussain, L. G. M. Pettersson and A. Nilsson (2002). "Spectroscopic probing of local hydrogen-bonding structures in liquid water." *Journal of Physics: Condensed Matter* 14(8): L213.
- Nagare, B., C. Marculli, O. Stetzer and U. Lohmann (2015). "Comparison of measured and calculated collision efficiencies at low temperatures." *Atmos. Chem. Phys.* 15(23): 13759-13776.
- Nilsson, A., D. Nordlund, I. Waluyo, N. Huang, H. Ogasawara, S. Kaya, U. Bergmann, L. Å. Näslund, H. Öström, P. Wernet, K. J. Andersson, T. Schiros and L. G. M. Pettersson (2010). "X-ray absorption spectroscopy and X-ray Raman scattering of water and ice; an experimental view." *Journal of Electron Spectroscopy and Related Phenomena* 177(2): 99-129.
- Nilsson, A. and L. G. M. Pettersson (2015). "The structural origin of anomalous properties of liquid water." 6: 8998.
- Nordlund, D., H. Ogasawara, K. J. Andersson, M. Tatarkhanov, M. Salmerón, L. G. M. Pettersson and A. Nilsson (2009). "Sensitivity of x-ray absorption spectroscopy to hydrogen bond topology." *Physical Review B* 80(23): 233404.
- Nutt, D. R. and A. J. Stone (2002). "Adsorption of water on the BaF<sub>2</sub>(111) surface." *The Journal of Chemical Physics* 117(2): 800-807.
- Orlando, F., L. Artiglia, H. Yang, X. Kong, K. Roy, A. Waldner, S. Chen, T. Bartels-Rausch and M. Ammann (2019). "Disordered Adsorbed Water Layers on TiO<sub>2</sub> Nanoparticles under Subsaturated Humidity Conditions at 235 K." *The Journal of Physical Chemistry Letters* 10(23): 7433-7438.
- Orlando, F., A. Waldner, T. Bartels-Rausch, M. Birrer, S. Kato, M.-T. Lee, C. Proff, T. Huthwelker, A. Kleibert, J. van Bokhoven and M. Ammann (2016). "The Environmental Photochemistry of Oxide Surfaces and the Nature of Frozen Salt Solutions: A New in Situ XPS Approach." *Topics in Catalysis* 59(5): 591-604.
- Pandey, R., K. Usui, R. A. Livingstone, S. A. Fischer, J. Pfaendtner, E. H. G. Backus, Y. Nagata, J. Fröhlich-Nowoisky, L. Schmäser, S. Mauri, J. F. Scheel, D. A. Knopf, U. Pöschl, M. Bonn and T. Weidner (2016). "Ice-nucleating bacteria control the order and dynamics of interfacial water." *Science Advances* 2(4).
- Parungo, F. (1975). Physical and chemical properties of AgI aerosols formed at simulated airborne conditions, Department of Commerce, National Oceanic and Atmospheric Administration ....

- Pedevilla, P., S. J. Cox, B. Slater and A. Michaelides (2016). "Can Ice-Like Structures Form on Non-Ice-Like Substrates? The Example of the K-feldspar Microcline." *The Journal of Physical Chemistry C* 120(12): 6704-6713.
- Qiu, Y., L. Lupi and V. Molinero (2018). "Is Water at the Graphite Interface Vapor-Like or Ice-Like?" *The Journal of Physical Chemistry B*.
- Schiros, T., K. J. Andersson, L. G. M. Pettersson, A. Nilsson and H. Ogasawara (2010). "Chemical bonding of water to metal surfaces studied with core-level spectroscopies." *Journal of Electron Spectroscopy and Related Phenomena* 177(2): 85-98.
- Shevkunov, S. V. (2019). "Computer Simulation of Water Vapor Adsorption on the Surface of a Crystal  $\beta$ -AgI Regular Shape Nanoparticle." *Protection of Metals and Physical Chemistry of Surfaces* 55(1): 41-49.
- Silverman, B. A. (2001). "A Critical Assessment of Glaciogenic Seeding of Convective Clouds for Rainfall Enhancement." *Bulletin of the American Meteorological Society* 82(5): 903-924.
- Smith, J. D., C. D. Cappa, K. R. Wilson, B. M. Messer, R. C. Cohen and R. J. Saykally (2004). "Energetics of Hydrogen Bond Network Rearrangements in Liquid Water." *Science* 306(5697): 851-853.
- Sosso, G. C., G. A. Tribello, A. Zen, P. Pedevilla and A. Michaelides (2016). "Ice formation on kaolinite: Insights from molecular dynamics simulations." *The Journal of Chemical Physics* 145(21): 211927.
- Stipp, S. L. and M. F. Hochella (1991). "Structure and bonding environments at the calcite surface as observed with X-ray photoelectron spectroscopy (XPS) and low energy electron diffraction (LEED)." *Geochimica et Cosmochimica Acta* 55(6): 1723-1736.
- Trotochaud, L., A. R. Head, S. Pletincx, O. Karshioğlu, Y. Yu, A. Waldner, L. Kyhl, T. Hauffman, H. Terryn, B. Eichhorn and H. Bluhm (2018). "Water Adsorption and Dissociation on Polycrystalline Copper Oxides: Effects of Environmental Contamination and Experimental Protocol." *The Journal of Physical Chemistry B* 122(2): 1000-1008.
- Verdager, A., G. M. Sacha, H. Bluhm and M. Salmeron (2006). "Molecular Structure of Water at Interfaces: Wetting at the Nanometer Scale." *Chemical Reviews* 106(4): 1478-1510.
- Verdager, A., C. Weis, G. Oncins, G. Ketteler, H. Bluhm and M. Salmeron (2007). "Growth and Structure of Water on SiO<sub>2</sub> Films on Si Investigated by Kelvin Probe Microscopy and in Situ X-ray Spectroscopies." *Langmuir* 23(19): 9699-9703.
- Vonnegut, B. (1947). "The Nucleation of Ice Formation by Silver Iodide." *Journal of Applied Physics* 18(7): 593-595.
- Waldner, A., L. Artiglia, X. Kong, F. Orlando, T. Huthwelker, M. Ammann and T. Bartels-Rausch (2018). "Premelting and the adsorption of formic acid at the air-ice interface at 253 K as seen by NEXAFS and XPS." *Physical Chemistry Chemical Physics* 20(37): 24408-24417.
- Wang, P. K. (2013). *Physics and Dynamics of Clouds and Precipitation*. Cambridge, Cambridge University Press.
- Ward, R. C., J. M. Holdman and B. N. Hale (1982). "Monte Carlo studies of water monolayer clusters on substrates: Hexagonal AgI." *The Journal of Chemical Physics* 77(6): 3198-3202.
- Wernet, P., D. Nordlund, U. Bergmann, M. Cavalleri, M. Odelius, H. Ogasawara, L. Å. Näslund, T. K. Hirsch, L. Ojamäe, P. Glatzel, L. G. M. Pettersson and A. Nilsson (2004). "The Structure of the First Coordination Shell in Liquid Water." *Science* 304(5673): 995-999.
- Wilson, K. R., M. Cavalleri, B. S. Rude, R. D. Schaller, A. Nilsson, L. Pettersson, N. Goldman, T. Catalano, J. Bozek and R. Saykally (2002). "Characterization of hydrogen bond acceptor molecules at the water surface using near-edge x-ray absorption fine-structure spectroscopy and density functional theory." *Journal of Physics: Condensed Matter* 14(8): L221.
- Winter, B. and M. Faubel (2006). "Photoemission from Liquid Aqueous Solutions." *Chemical Reviews* 106(4): 1176-1211.
- Zielke, S. A., A. K. Bertram and G. N. Patey (2015). "A Molecular Mechanism of Ice Nucleation on Model AgI Surfaces." *The Journal of Physical Chemistry B* 119(29): 9049-9055.

## 3.2 SUPPORTING INFORMATION

### 3.2.1 Experimental setup

The silver iodide powder sample was deposited on the gold-coated sample holder in ambient air and transferred into the analysis cell (Figure S3-1a). The analysis cell hosting this cryo-holder has been described in a previous publication (Orlando, Waldner et al. 2016). The temperature of the sample is regulated by using a cold nitrogen gas flow hitting the bottom of the sample substrate via the center of the sample transfer rod. The analysis cell is part of the solid-gas interface chamber module (Orlando, Waldner et al. 2016) coupled to a Scienta-Omicron HiPP-2/R4000 hemispherical electron analyser, in turn connected to the ISS beamline of the Swiss Light Source (SLS) at Paul Scherrer Institut (Flechsig, Quitmann et al. 2007). Figure S3-1b shows the geometry of our measurement. The electron detection direction is parallel to the polarization vector ( $\hat{P}$ , grey arrows) of the linearly polarized ( $0^\circ$ ) light, and it is rotated by  $30^\circ$  with respect to the sample surface normal ( $\theta = 30^\circ$ ).

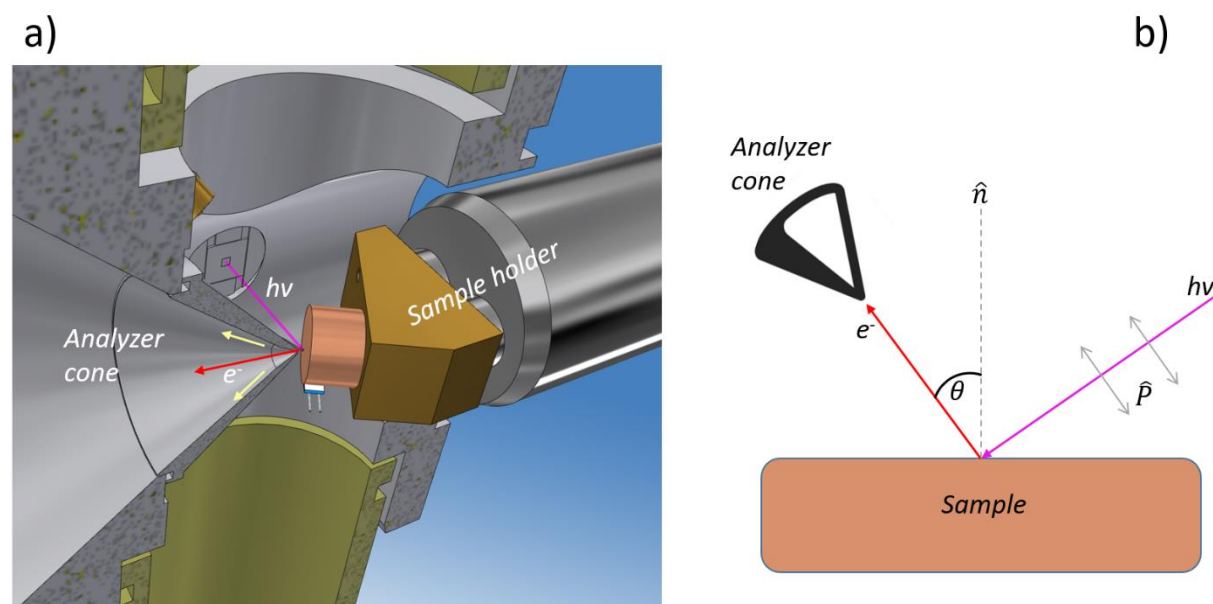


Figure S3-1: a) Sectional view of the in situ analysis cell with the sample holder mounted. b) Measurement geometry of sample position and incoming photon beam showing the photoelectron emission direction at an angle  $\theta$  with respect to the sample surface normal ( $\hat{n}$ ), view from above.

The analysis cell is configured to allow pressures up to several mbar. Photoelectrons are collected through the aperture of the collecting cone into the three stage differentially pumped electrostatic lens system coupled to the electron analyzer. Water vapor is admitted from the head-space of a temperature controlled water containing vial into the chamber through a capillary tube. Under standard operating conditions, the water vapor pressure in the analysis cell is controlled by the temperature of the water reservoir and the small pumping flow through the electron sampling aperture. To obtain a better dynamic range for the present experiment, an additional pumping flow was realized by adjusting a separate diaphragm valve towards the roughing pump downstream.

### 3.2.2 XPS normalization and Gaussian deconvolution parameters

XPS provides surface sensitive elemental information with a probing or information depth down to a few  $nm$ , limited by the inelastic mean free path (IMFP) of the outgoing photoelectrons. In XPS, the excited outgoing photoelectron intensity  $I$  can be expressed as:

$$I \propto \lambda(KE) \cdot n \cdot \phi \cdot \sigma_T(h\nu) \quad (\text{Equation S 3-1})$$

Where  $\lambda(KE)$  is the inelastic mean free path of the photoelectron as a function of the electron kinetic energy,  $n$  is the atomic density of the sample ( $\text{atoms cm}^{-3}$ ),  $\phi$  is the excitation photon flux ( $\text{photons s}^{-1}$ ) that depends on the photon energy  $h\nu$ .  $\sigma_T(h\nu)$  is the total differential photoionization cross section (Mbarn), which depends on the photon energy  $h\nu$  and the orbital shape of the original electron level.

The total differential photoionization cross section  $\sigma_T(h\nu)$  is expressed by (Otto, Faubel et al. 2010):

$$\sigma_T(h\nu) = \sigma(h\nu) \cdot \frac{1 + \beta(h\nu)}{4\pi} \cdot P_2 \cos^2\psi \quad (\text{Equation S 3-2})$$

Where  $\beta(h\nu)$  is the asymmetry parameter related to the subshell from which the electron is ejected,  $\psi$  is the electron emission angle with respect to the polarization vector of the polarized (synchrotron) light as shown in Figure S3-1b, which is equal to  $0^\circ$ .  $P_2$  is the second order Legendre polynomial.

During the experiment, we make use of linearly polarized light, (as already discussed,  $\psi = 0^\circ$ ), and  $P_2 = 1$ , hence  $\sigma_T(h\nu)$  is reduced to

$$\sigma_T(h\nu) = \sigma(h\nu) \cdot \frac{1 + \beta(h\nu)}{4\pi} \quad (\text{Equation S 3-3})$$

Table S3-1 lists the parameters for XPS peak acquisition, including the used photon energy, outgoing photoelectron kinetic energy and the corresponding probing depth ( $\lambda \cdot \cos 30^\circ$ ).

Fitting parameters of the measured XPS peaks are reported in Table S3-2. The binding energy of electrons and the spin orbital splitting of the iodine 3d and silver 3d levels are set to be fixed. An increasing probing depth requires a higher photon energy, which leads to a broadening of the full width at half maximum. Such an effect correlates with the resolving power of the monochromator, which decreases toward higher excitation energies and affects the total resolution of the photoemission spectra.

Table S3-1: Excitation photon energies applied, and the resulting kinetic energies of emitted photoelectrons from oxygen, iodine, silver and carbon. Each photoelectron kinetic energy corresponds to a specific probing depth.

Depth number	Measured Region	Photon energy (eV)	Photoelectron Kinetic Energy	Probing depth (nm)
1	O1s	870	340	1.1
	I3d	955		
	Ag3d	710		
	C1s	630		
2	O1s	1080	550	1.6
	I3d	1175		
	Ag3d	930		
	C1s	840		
3	O1s	1190	650	1.8
	I3d	1275		
	Ag3d	1030		
	C1s	950		
4	O1s	1290	750	2
	I3d	1375		
	Ag3d	1130		
	C1s	1050		
5	O1s	1440	900	2.3
	I3d	1525		
	Ag3d	1280		
	C1s	1200		

Table S3-2: Fitting parameters including binding energy, full width half maximum (FWHM) and spin orbital splitting (S.O.S) for the peak deconvolution.

Region	BE (eV)	FWHM at Depth # 1/2/3/4/5 (eV)	S.O.S (eV)
I 3d 5/2	619.5	1.7/2.4/2.8/3.2/3.4	11.5
I 3d 3/2	631		
Ag 3d 5/2	368.2	1.0/1.6/2.0/2.2/2.5	6.1
Ag 3d 3/2	374.3		
O1s (ads.)	532.5	2.2/2.7/2.8/3.5/3.5	-
O1s (gas)	534.6	1.4/2.1/2.7/2.9/3.4	-
C1s (C-C)	284.8	1.4/1.7/1.9/2.4/2.5	-
C1s (C-O)	286.4		-

## Supporting XPS spectra and analysis

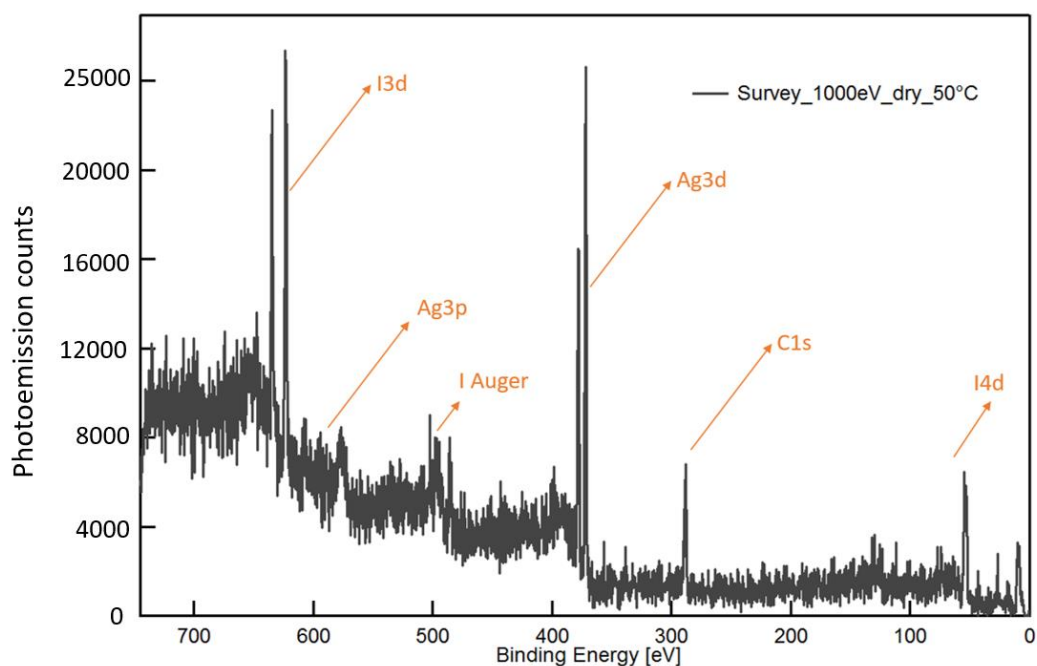


Figure S3-2: XPS survey scan of the dry AgI powder surface excited by  $h\nu=1000\text{eV}$  at dry condition (High Vacuum, 323 K).

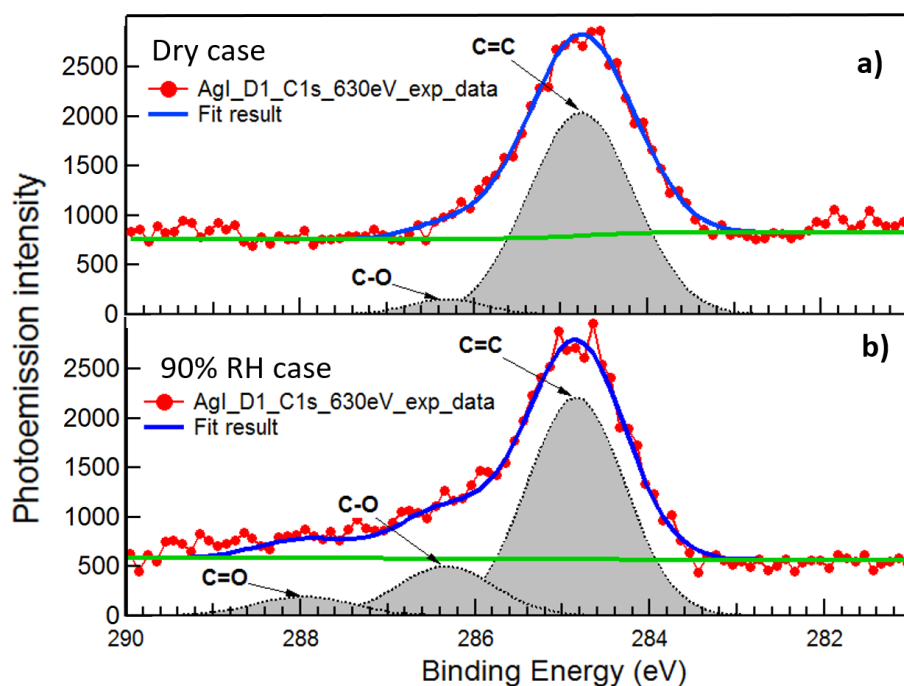


Figure S3-3: Exemplary C1s XPS spectra of AgI at dry (panel a) and 90% RH condition (247 K, 0.5 mbar H<sub>2</sub>O) (panel b), measured with  $h\nu=630\text{eV}$  (KE~350eV, depth 1 as defined in the main text and

Table S3-1).

Gaussian peak deconvolution for the contributions of different carbon species are shown by grey peaks and their sum by the blue line. In the dry case the spectrum is represented by C=C and C-O components of adventitious carbon. The binding energy is calibrated by the C1s peak originating from C=C bonding, at 284.8 eV. The two panels share the same vertical axis scale. Upon water dosing into the experimental chamber, the contribution of carboxyl carbon is about an order of magnitude less than the total carbon.

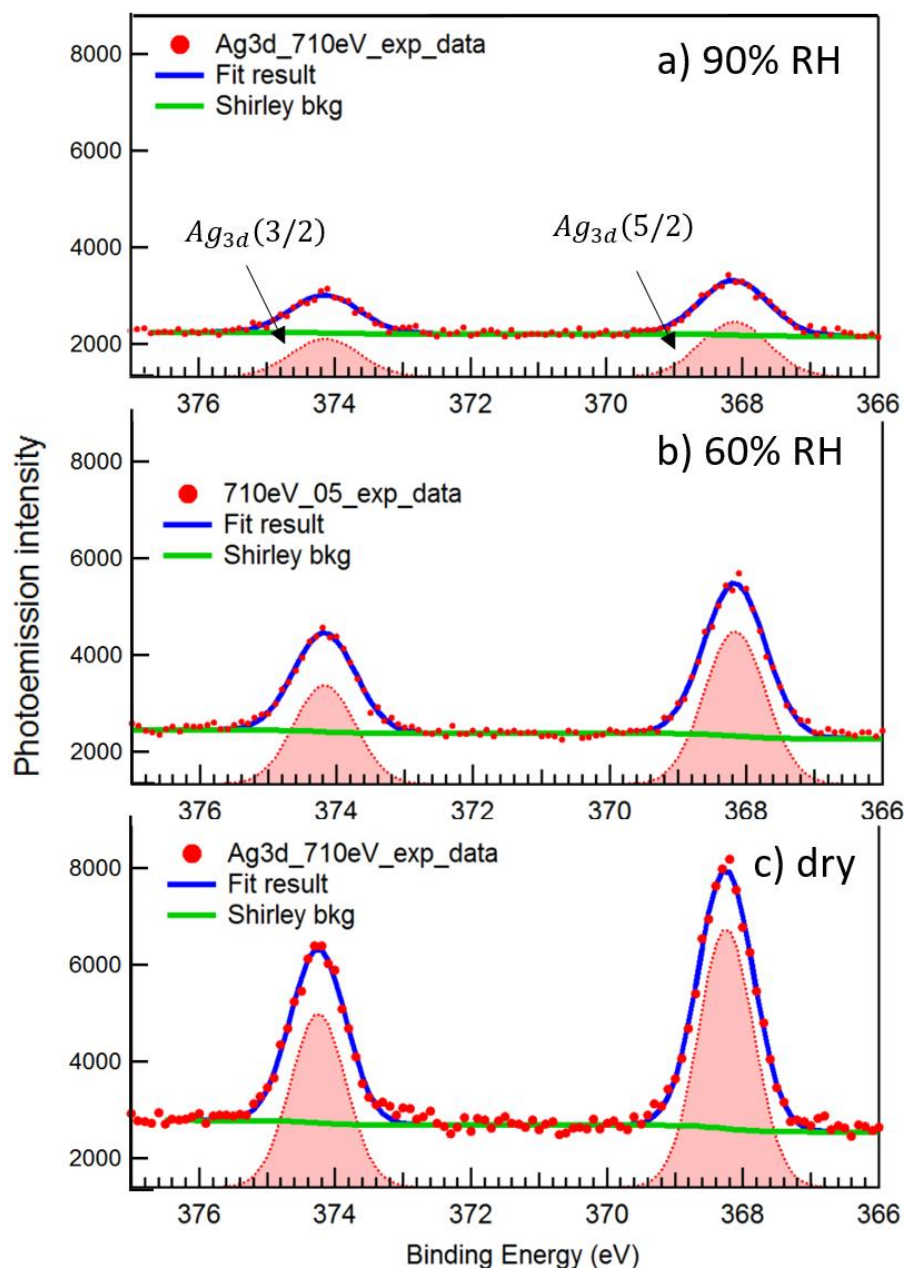


Figure S3-4: Measured Ag 3d XPS spectra at dry (c), 60% RH (b, 0.5mbar,251 K) and 90% RH (a, 0.5mbar,247 K) with  $h\nu=710\text{eV}$ . The kinetic energy is at ca 350eV. Green lines represent the Shirley background and the red shadings represent Gaussian peaks used to fit the spectra (red dots). The blue lines represent the fit result. All three spectra share the

vertical axis scale. The spin orbit splitting (S.O.S) of Ag 3d is 6.1eV, in agreement with literature (Schön, Tummavuori et al. 1973) .

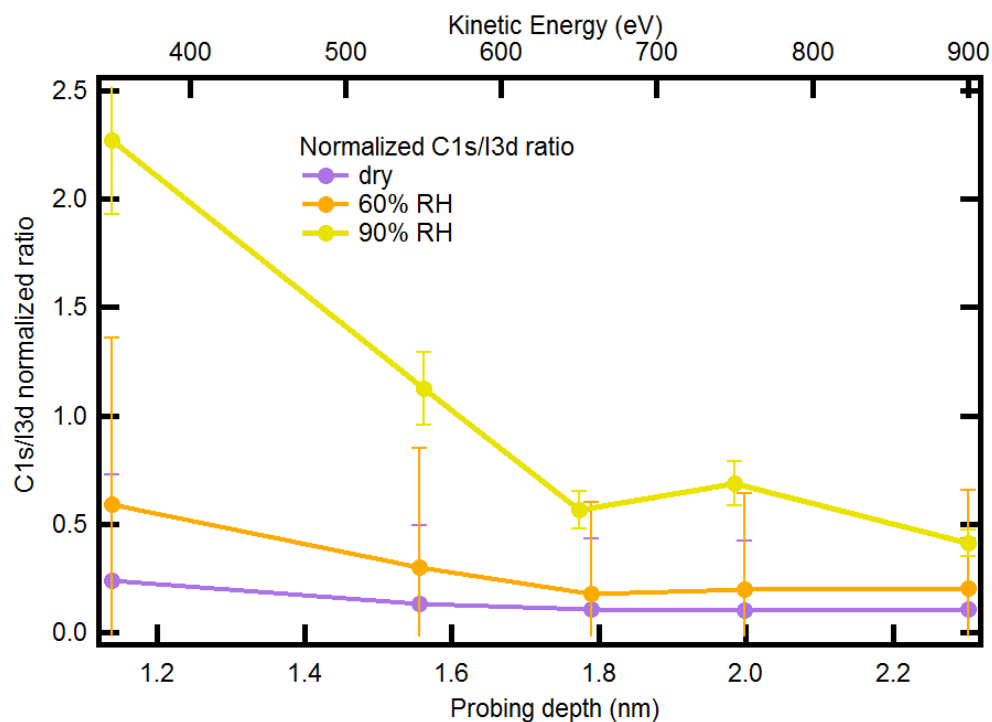


Figure S3-5: The normalized C1s/I3d ratio. Under dry conditions and 60% RH, similar amounts of carbon were observed. As the relative humidity reaches 90%, higher amounts of carbon are observed. The difference between 60 and 90% RH is likely the effect of lower sample temperature, since the water vapor pressure remained the same.

### 3.2.3 Attenuation model and fitting of the O1s<sub>ads</sub>/I3d ratio

- a. Homogeneous overlayer on a semi-infinite specimen model: general case.

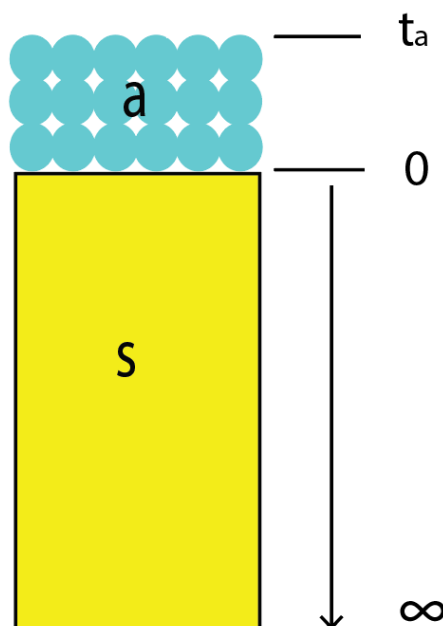


Figure S3-6: Illustration of the homogeneous overlayer model. The substrate is denoted by S with a thickness much larger than the adsorbate. The thickness of the adsorbate a (water) is denoted as  $t_a$ .

This model consists of a substrate having semi-infinite thickness with an adsorbate a having finite thickness ( $t_a$ ) on top (Figure S3-6).

Concerning the overlayer, the measured photoelectron intensity related to excitation of a core level of an atom a is:

$$I_a = F \cdot \sigma_a \cdot \phi_a \cdot \int_{-t_a}^0 \rho_a(z) \cdot e^{-\frac{(z+t_a)}{\lambda_a \cdot \cos \theta}} dz \quad (\text{Equation S 3-4})$$

Where  $F \propto \Omega_0 \cdot A_0 \cdot D_0$ . The factor F is proportional to parameters that do not depend on sample and adsorbate, but on the geometry of the experimental setup and the technical characteristics of the analyzer: electron detection efficiency ( $D_0$ ), acceptance angle ( $\Omega_0$ ), and effectively analyzed area ( $A_0$ ), which in turn depends on the spot size of the photon beam. The factor F can be simplified when taking the ratio of photoemission intensities obtained at the same kinetic energy, for example,  $I(\text{O}1s_{\text{ads}})/I(\text{I}3d)$ . The photon flux used to excite the specific core level of atom A is denoted by  $\phi_A$ , and  $\theta$  is the electron emission direction angle with respect to the surface normal  $\hat{n}$ , Figure S3-1b.

$\lambda_a$  is the electron inelastic mean free path experienced by electrons passing through the adsorbate overlayer, taken from Shinotsuka et al (Shinotsuka, Da et al. 2017).

$\sigma_a$  is the total differential ionization cross section, which depends on the atomic orbital and polarization of the incident light.

$\rho_a(z)$  is the density profile of the adsorbate illuminated by the X-ray photons (numbers of atoms/cm<sup>3</sup>).

We assume that the atomic density of the adsorbate is homogeneous with depth, thus  $\rho_a(z) = \rho_a$ . By integrating (Equation S 3-4), we obtain:

$$\begin{aligned} I_a &= F \cdot \sigma_a \cdot \rho_a \cdot \phi_a \cdot (\lambda_a \cdot \cos \theta) (e^0 - e^{-\frac{t_a}{\lambda_a \cdot \cos \theta}}) = \\ &= F \cdot \sigma_a \cdot \rho_a \cdot \phi_a \cdot \lambda_a \\ &\quad \cdot \cos \theta \cdot (1 - e^{-\frac{t_a}{\lambda_a \cdot \cos \theta}}) \end{aligned} \quad (\text{Equation S 3-5})$$

In turn, the signal intensity for photoelectrons originating from core levels of atoms contained in the substrate S, whose emitted electrons have to travel first within the substrate (with  $\lambda_s$ ) and then through the overlayer (with  $\lambda_a$ ), denoted as  $I_s$ , has the form:

$$\begin{aligned} I_s &= F \cdot \sigma_s \cdot \phi_s \cdot \left[ \int_0^\infty \rho_s(z) \cdot e^{-\frac{z}{\lambda_s \cdot \cos \theta}} dz \right] \\ &\quad \cdot e^{-\frac{t_a}{\lambda_a \cdot \cos \theta}} \end{aligned} \quad (\text{Equation S 3-6})$$

Integration of (Equation S 3-6) yields:

$$I_s = F \cdot \sigma_s \cdot \phi_s \cdot \rho_s \cdot \lambda_s \cdot \cos \theta \cdot e^{-\frac{t_a}{\lambda_a \cdot \cos \theta}} \quad (\text{Equation S 3-7})$$

The ratio between  $I_a$  and  $I_s$  is:

$$\begin{aligned} \frac{I_a}{I_s} &= \frac{\sigma_a}{\sigma_s} \cdot \frac{\rho_a}{\rho_s} \cdot \frac{\phi_a}{\phi_s} \cdot \frac{\lambda_a}{\lambda_s} \cdot \frac{1 - e^{-\frac{t_a}{\lambda_a \cdot \cos \theta}}}{e^{-\frac{t_a}{\lambda_a \cdot \cos \theta}}} \\ &= \frac{\sigma_a}{\sigma_s} \cdot \frac{\rho_a}{\rho_s} \cdot \frac{\phi_a}{\phi_s} \cdot \frac{\lambda_a}{\lambda_s} \cdot \left( e^{\frac{t_a}{\lambda_a \cdot \cos \theta}} - 1 \right) \end{aligned} \quad (\text{Equation S 3-8})$$

## b. Patched carbon islands on a homogeneous water layer

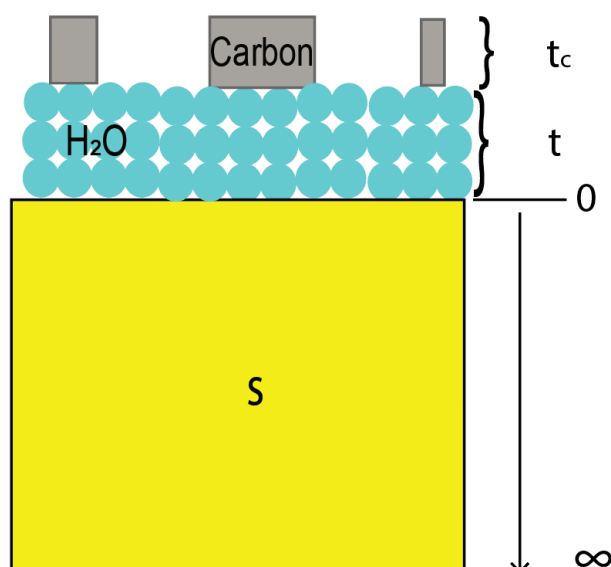


Figure S3-7: illustration of the model of patched carbon islands on a water overlayer. On the top of the substrate S, adsorbed water forms a layer with thickness  $t$ . Carbon consists of patched islands floating on the top of water layers, with thickness  $t_c$ . Silver iodide is the substrate with semi-infinite thickness, denoted by the symbol S.

In this model, we assume that carbon contamination on the AgI surface adopts a morphology of patched islands on the water layer (varying with relative humidity). These carbon islands cover in total a fraction  $\gamma$  of the water layer (or AgI for dry conditions) surface area ( $0 < \gamma < 1$ ), with thickness  $t_c$ . This is justified by the assumption that adventitious carbon is likely rather hydrophobic in nature. We use a simplified equation inspired by the literature (Fadley, Baird et al. 1974) and the semi-infinite model. We denote the photoelectron intensity of C1s signal from the carbon above the AgI surface is represented as  $I_{\text{patched,C1s}}$ :

$$I_{\text{patched,C1s}} = \gamma \cdot I_c = \gamma \cdot F \cdot \sigma_{\text{C1s}} \cdot \rho_C \cdot \phi_{\text{C1s}} \cdot \lambda_C \cdot \cos \theta \cdot (1 - e^{-\frac{t_c}{\lambda_C \cdot \cos \theta}}) \quad (\text{Equation S 3-9})$$

where  $I_c$  is the expected carbon photoemission intensity if it was a homogeneous layer with thickness  $t_c$ .  $\lambda_C$  is the IMFP in the carbon medium (Jablonski, Salvat et al. 2005).

The O1s photoemission intensity from water layer is represented by  $I_{\text{O1s}}$ :

$$I_{\text{O1s}} = F \cdot \sigma_{\text{O1s}} \cdot \rho_{\text{O}} \cdot \phi_{\text{O1s}} \cdot \lambda_{\text{H}_2\text{O}} \cdot \cos \theta \cdot (1 - e^{-\frac{t}{\lambda_{\text{H}_2\text{O}} \cdot \cos \theta}}) \cdot ((\gamma \cdot e^{-\frac{t_c}{\lambda_C \cdot \cos \theta}}) + (1 - \gamma)) \quad (\text{Equation S 3-10})$$

Where  $\lambda_{\text{H}_2\text{O}}$  is the IMFP in water (Jablonski, Salvat et al. 2005). In AgI, we measure I 3d as substrate signal,  $I_{\text{I3d}}$ :

$$I_{\text{I3d}} = F \cdot \sigma_{\text{I3d}} \cdot \rho_{\text{I}} \cdot \phi_{\text{I3d}} \cdot \lambda_{\text{AgI}} \cdot \cos \theta \cdot e^{-\frac{t}{\lambda_{\text{H}_2\text{O}} \cdot \cos \theta}} \cdot ((\gamma \cdot e^{-\frac{t_c}{\lambda_{\text{C}} \cdot \cos \theta}}) + (1 - \gamma)) \quad (\text{Equation S 3-11})$$

Hence the photoemission intensity ratio between carbon on top of the water layer and I3d from the substrate is  $I_{\text{O1s}}/I_{\text{I3d}}$ :

$$\begin{aligned} \frac{I_{\text{O1s}}}{I_{\text{I3d}}} &\propto \frac{(1 - e^{-\frac{t}{\lambda_{\text{H}_2\text{O}} \cdot \cos \theta}}) \cdot ((\gamma \cdot e^{-\frac{t_c}{\lambda_{\text{C}} \cdot \cos \theta}}) + (1 - \gamma))}{e^{-\frac{t}{\lambda_{\text{H}_2\text{O}} \cdot \cos \theta}} \cdot ((\gamma \cdot e^{-\frac{t_c}{\lambda_{\text{C}} \cdot \cos \theta}}) + (1 - \gamma))} \\ &= \frac{(1 - e^{-\frac{t}{\lambda_{\text{H}_2\text{O}} \cdot \cos \theta}})}{e^{-\frac{t}{\lambda_{\text{H}_2\text{O}} \cdot \cos \theta}}} \end{aligned} \quad (\text{Equation S 3-12})$$

Since this ratio is independent of the factor F, we can obtain the thickness of the water layer on AgI from a fit of this equation to the corresponding data. The photoemission intensity ratio between carbon on the top of water layer and I 3d from the substrate is  $I_{\text{patched,C1s}}/I_{\text{I3d}}$ :

$$\frac{I_{\text{patched,C1s}}}{I_{\text{I3d}}} \propto \frac{\gamma \cdot (1 - e^{-\frac{t_c}{\lambda_{\text{C}} \cdot \cos \theta}})}{e^{-\frac{t}{\lambda_{\text{H}_2\text{O}} \cdot \cos \theta}} \cdot ((\gamma \cdot e^{-\frac{t_c}{\lambda_{\text{C}} \cdot \cos \theta}}) + (1 - \gamma))} \quad (\text{Equation S 3-13})$$

In dry condition, the water layer is absent, hence, (Equation S 3-13) becomes:

$$\frac{I_{\text{patched,C1s}}}{I_{\text{I3d}}} \propto \frac{\gamma \cdot (1 - e^{-\frac{t_c}{\lambda_{\text{C}} \cdot \cos \theta}})}{(\gamma \cdot e^{-\frac{t_c}{\lambda_{\text{C}} \cdot \cos \theta}}) + (1 - \gamma)} \quad (\text{Equation S 3-14})$$

### 3.2.4 Fitting results

With the model described in section 4.2, our sample in dry condition contains a certain amount of carbon islands on the top of AgI surface. The fitting result of C1s/I3d ratio is shown in Figure S3-8 panel a.

While we dose water in the experimental cell at a given temperature, the adsorbed water layer thickness under humid condition is  $t$ . We assume that adsorbed water pushes carbon islands on top of it. Figure S3-8 shows the fitting result for the O1s<sub>ads</sub>/I3d, C1s/I3d ratios at 60 and 90% RH using Eq 12 and Eqs 13/14, respectively.

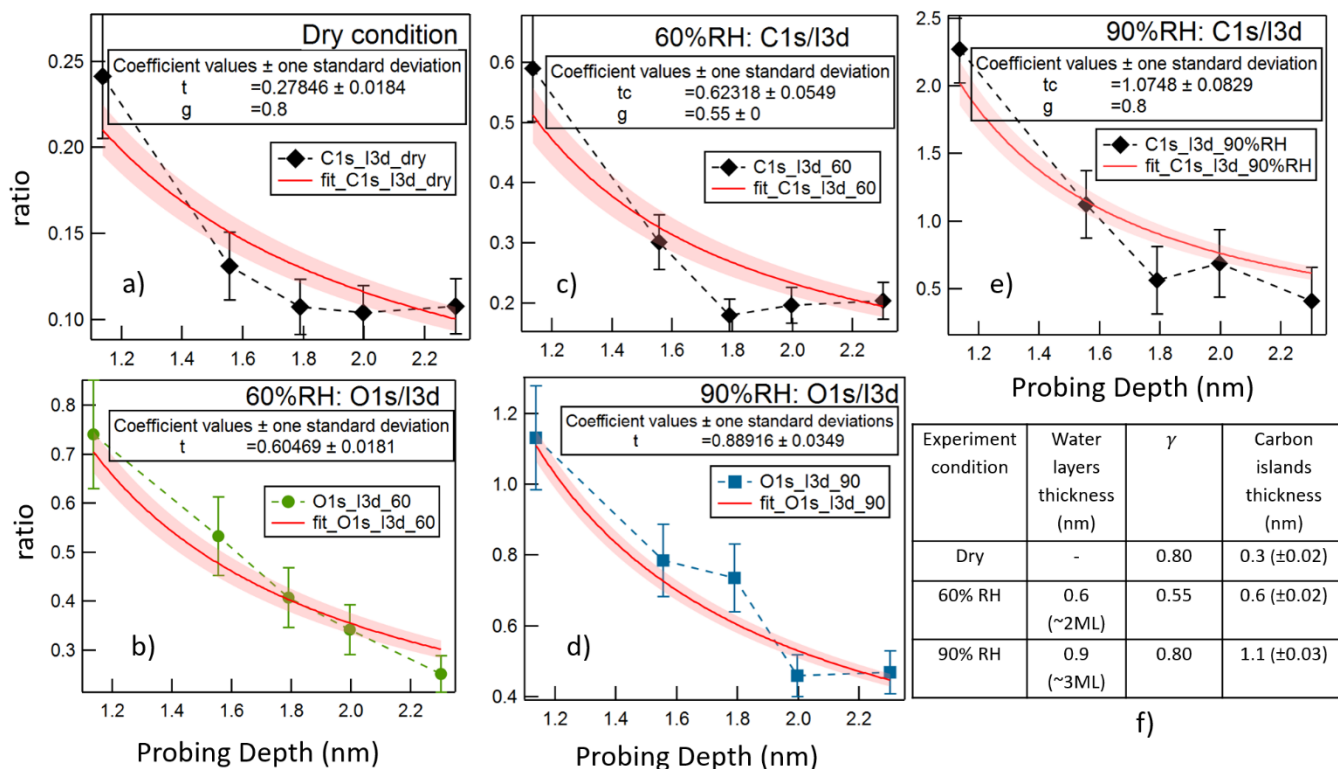


Figure S3-8: Fitting result: a) for dry condition at 323 K. b) and c) 60% RH, 251 K and d) and e) 90% RH, 247 K at 0.5 mbar. The red curves are the fitting result (with the sensitivity determined by standard deviation, colored red shadow), the dashed lines represents the measured experimental data of O1s/I3d and C1s/I3d. Panel f) show the fitting results of water layer and carbon island thickness for dry and humid condition

### 3.2.5 O K edge NEXAFS of liquid water and ice

As explained in the main text, we used O K edge NEXAFS as a technique to probe the HB network among water molecules (Cavalleri, Ogasawara et al. 2002, Myneni, Luo et al. 2002, Wilson, Cavalleri et al. 2002, Smith, Cappa et al. 2004). For reference, Figure S3-9 shows Auger electron yield O K-edge NEXAFS spectra of liquid water (green, measured at the SIM beamline with the liquid jet XPS setup (Brown, Redondo et al. 2013)), ice (purple, measured with the same setup as this work using the procedures described in (Waldner, Artiglia et al. 2018).), and gas phase water (red) measured by retracting the sample holder, but keeping the water vapor pressure at 0.5 mbar.

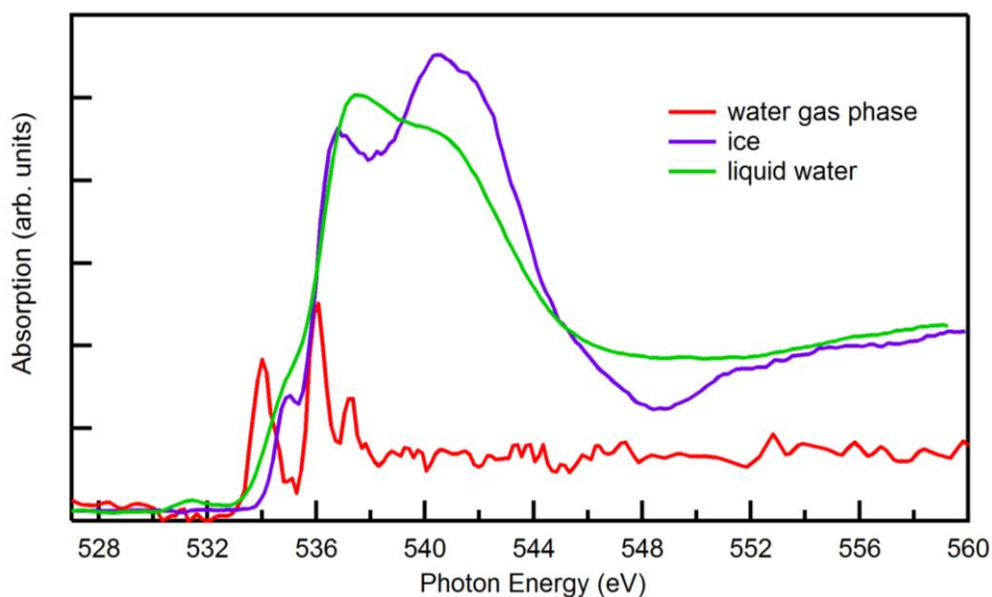


Figure S3-9: O K edge NEXAFS spectra of liquid water (green), ice (purple) and water vapor in gas phase (red).

### 3.2.6 Gaussian peak deconvolution of O K edge NEXAFS

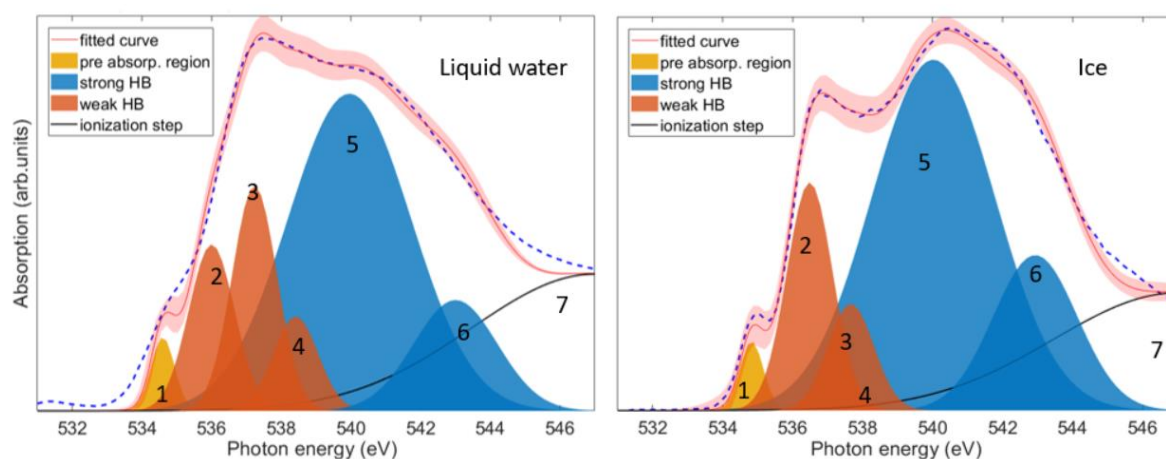


Figure S3-10: Gaussian peak fitting of O K NEXAFS spectra of liquid water and solid ice. Seven Gaussian peaks are used to approximate the O K NEXAFS spectra from range 534 eV to 547 eV.

In Figure S3-10 we show the O K NEXAFS of liquid water and ice, along with a Gaussian peak deconvolution of the NEXAFS spectra inspired by Cappa et al. (Cappa, Smith et al. 2005). The photon energy (x-axes) was calibrated with respect to the excitation of O 1s electrons into the antibonding  $4a_1$  MO (534.0 eV) in the gas phase water molecules. Peak 1 (yellow peak) represents the weaker HB feature. The second to the fourth peaks (red peaks) are also representative of the weaker HB configuration, which is the dominating feature in liquid water. Peak 5 and 6 (blue peaks) represent the strong HB feature. Peak 7 (black peak) approximates the ionization step. The pink area represents the upper and lower 95% of the prediction interval for the fitting result (thin red line). Note that this deconvolution is not directly representing individual transitions, but serves to represent the spectra in a consistent way (Cappa, Smith et al. 2005, Nilsson, Nordlund et al. 2010).

Figure S3-11 shows the Gaussian peak deconvolution of difference spectra corresponding to adsorbed water on the AgI surface at 60 and 90% RH. The peak positions and FWHM obtained from the fits to the liquid water and ice NEXAFS shown in Figure S3-10, remained fixed as constraints in all the fits and only the relative intensity was allowed to vary.

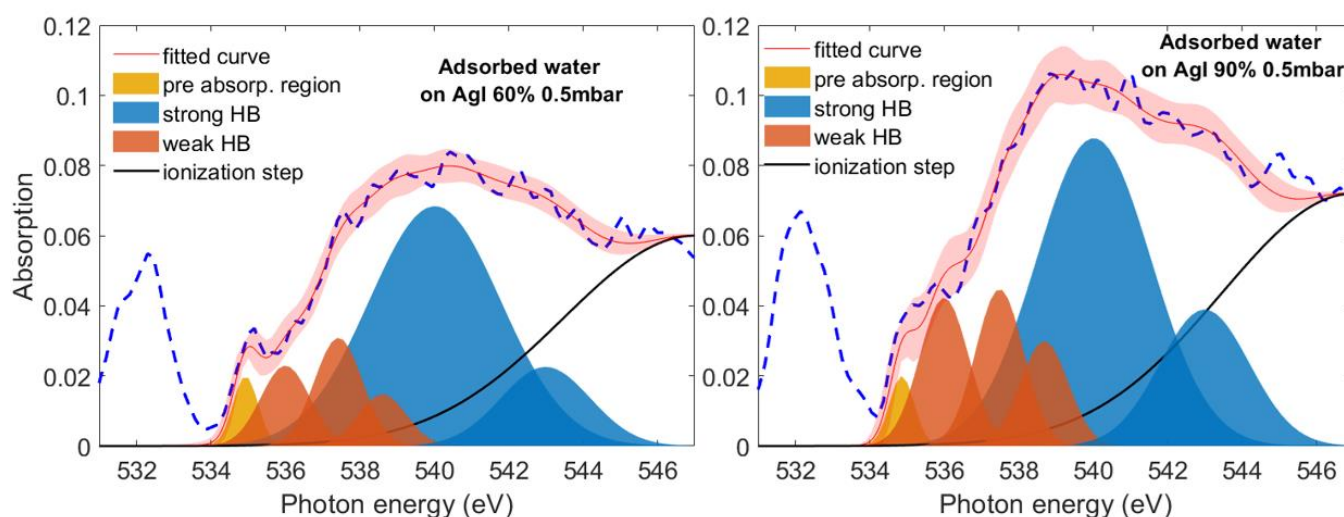


Figure S3-11: Gaussian peak fitting of the adsorbed water spectra on AgI surface at 60% RH (left) and 90% RH (right). Both spectra share the same vertical axis scale.

At 60% RH (Figure S3-11, left), the thickness of the water layer is estimated as 0.6 nm, corresponding to approximately 2 ML of water coverage. The ratio of the areas of blue peaks (strong HB feature, peak 5 and 6) to the area of red peaks (weak HB feature, peak 2, 3, 4), is closer to that of ice than to that of water, as shown in the main text. We attribute this to the enhanced presence of tetrahedrally coordinated water molecules under these conditions.

As we decrease the sample temperature down to 247 K, the RH increases to 90% (Figure S3-11, right). The thickness of the water layer reaches 0.9 nm, corresponding to approximately 3 ML of water coverage. The ratio of the blue peak areas to that of the red peaks is still similar to that at 60% RH.

To illustrate the dependence of the result on the fitting procedure, we show two additional fitting results with 6 Gaussian peaks in Figure S 3-12 and Figure S 3-13. In Figure S 3-12, we used two peaks for the weak HB (red) and two peaks for strong HB (blue) structure, and this

combination was 3:1 (red : blue peaks) in Figure S 3-13.

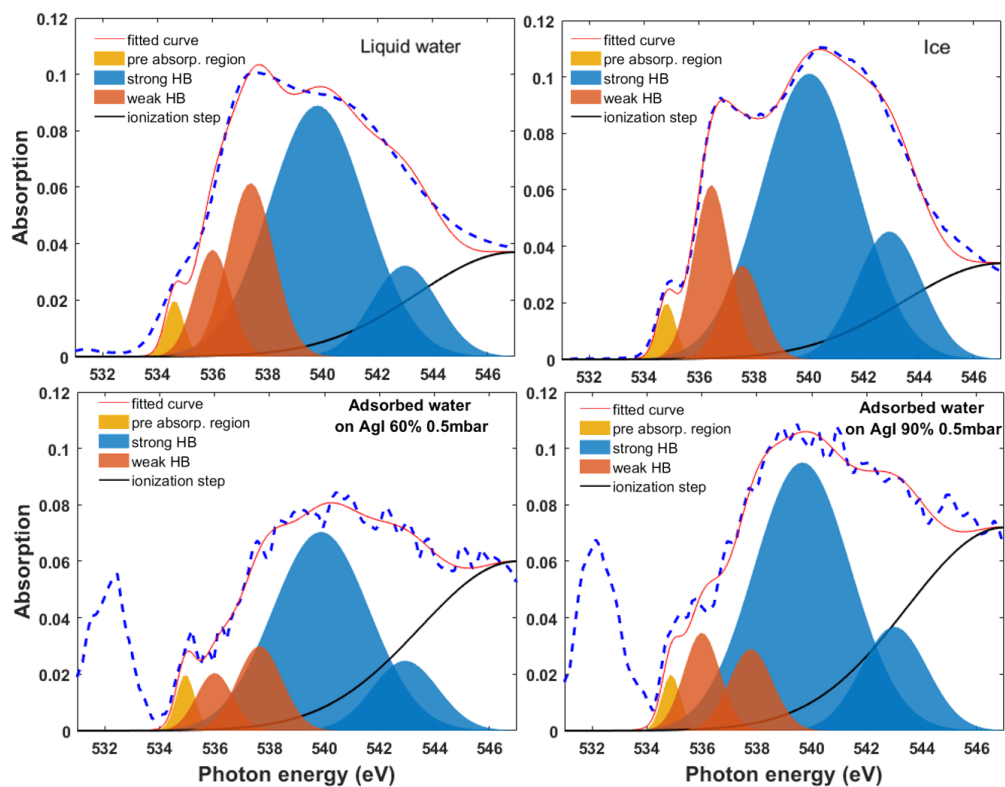


Figure S 3-12: Gaussian peak fitting by using 6 gaussian peaks for liquid water, ice, and adsorbed water at 60%, 90% RH on AgI surface. Two peaks for the weak HB (red shaded) and two peaks for strong HB (blue shaded) structure are assigned.

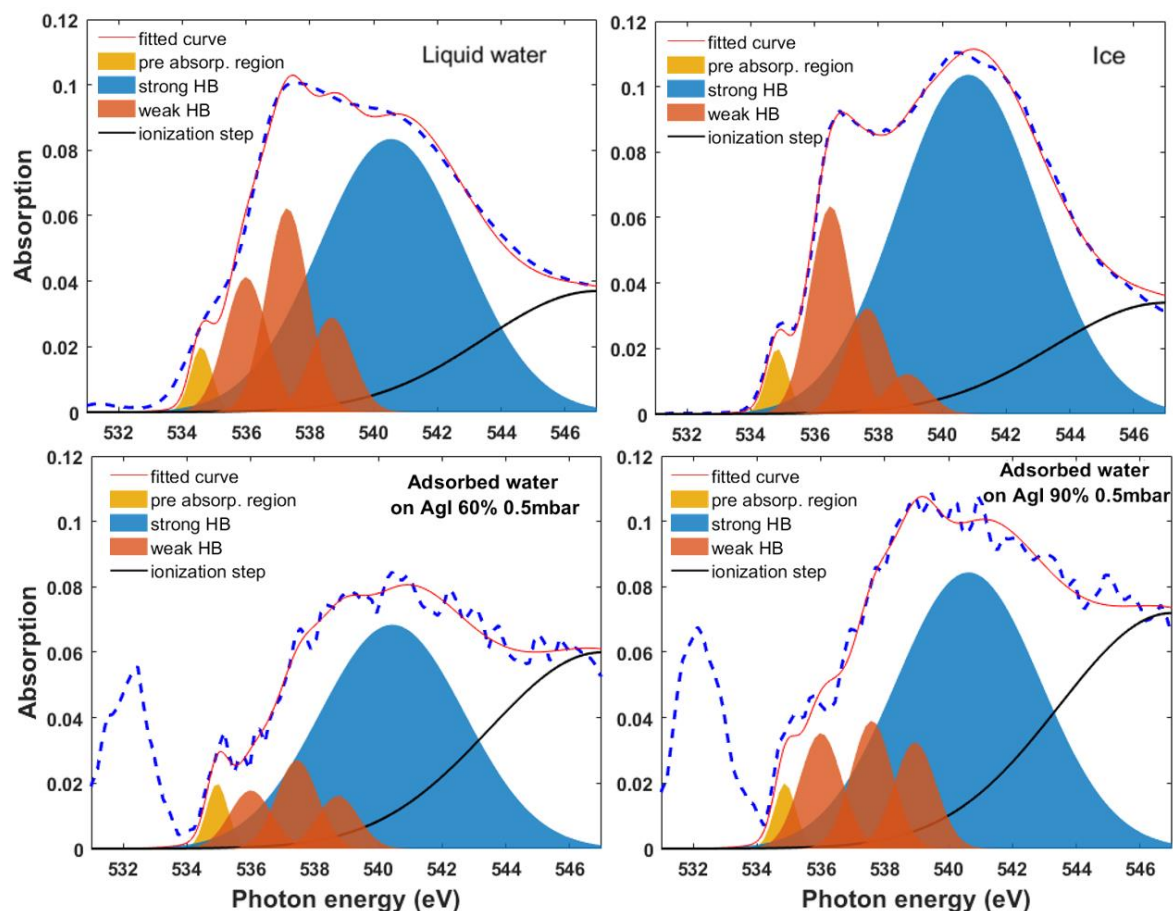


Figure S 3-13: Gaussian peak fitting by using 6 gaussian peaks for liquid water, ice, and adsorbed water at 60%, 90% RH on AgI surface. Three peaks for the weak HB (red shaded) and one peak for strong HB (blue shaded) structure are assigned.

**Table 3-1:** Fractional contribution of absorption related to water molecules in weak and strong HB configurations based on the fitting results with 7 Gaussians (Figure S3-10, Figure S3-11), or 6 Gaussians (Figure S 3-12 and Figure S 3-13). The mean value and the standard deviation are used to plot these contributions in Figure 5 of the main text.

	7 Gaussians (Figure S 3-10, Figure S 3-11)	6 Gaussians (Figure S 3-12)	6 Gaussians (Figure S 3-13)	Mean value	Standard deviation
Liquid water_weak %	31.00%	28.00%	32.00%	30.33%	2.08%
Liquid water_strong %	69.00%	72.00%	68.00%	69.67%	2.08%
ice_weak %	21.00%	22.00%	23.00%	22.00%	1.00%
ice_strong %	79.00%	78.00%	77.00%	78.00%	1.00%
60% RH_weak %	23.00%	20.00%	20.00%	21.00%	1.73%
60% RH_strong %	77.00%	81.00%	80.00%	79.33%	2.08%
90% RH_weak %	29.00%	18.00%	27.00%	24.67%	5.86%
90% RH_strong %	71.00%	82.00%	83.00%	78.67%	6.66%

## References

- Brown, M. A., A. B. Redondo, I. Jordan, N. Duyckaerts, M.-T. Lee, M. Ammann, F. Nolting, A. Kleibert, T. Huthwelker, J.-P. Mächler, M. Birrer, J. Honegger, R. Wetter, H. J. Wörner and J. A. v. Bokhoven (2013). "A new endstation at the Swiss Light Source for ultraviolet photoelectron spectroscopy, X-ray photoelectron spectroscopy, and X-ray absorption spectroscopy measurements of liquid solutions." *Review of Scientific Instruments* 84(7): 073904.
- Cappa, C. D., J. D. Smith, K. R. Wilson, B. M. Messer, M. K. Gilles, R. C. Cohen and R. J. Saykally (2005). "Effects of Alkali Metal Halide Salts on the Hydrogen Bond Network of Liquid Water." *The Journal of Physical Chemistry B* 109(15): 7046-7052.
- Cavalleri, M., H. Ogasawara, L. G. M. Pettersson and A. Nilsson (2002). "The interpretation of X-ray absorption spectra of water and ice." *Chemical Physics Letters* 364(3): 363-370.
- Fadley, C. S., R. J. Baird, W. Siekhaus, T. Novakov and S. Å. L. Bergström (1974). "Surface analysis and angular distributions in x-ray photoelectron spectroscopy." *Journal of Electron Spectroscopy and Related Phenomena* 4(2): 93-137.
- Flechsig, U., C. Quitmann, J. Raabe, M. Böge, R. Fink and H. Ade (2007). "The PolLux Microspectroscopy Beam line at the Swiss Light Source." *AIP Conference Proceedings* 879(1): 505-508.
- Jablonski, A., F. Salvat and C. J. Powell (2005). "Evaluation of elastic-scattering cross sections for electrons and positrons over a wide energy range." *Surface and Interface Analysis* 37(12): 1115-1123.
- Myneni, S., Y. Luo, L. Å. Näslund, M. Cavalleri, L. Ojamäe, H. Ogasawara, A. Pelmenchikov, W. Ph, P. Väterlein, C. Heske, Z. Hussain, L. G. M. Pettersson and A. Nilsson (2002). "Spectroscopic probing of local hydrogen-bonding structures in liquid water." *Journal of Physics: Condensed Matter* 14(8): L213.
- Nilsson, A., D. Nordlund, I. Waluyo, N. Huang, H. Ogasawara, S. Kaya, U. Bergmann, L. Å. Näslund, H. Öström, P. Wernet, K. J. Andersson, T. Schiros and L. G. M. Pettersson (2010). "X-ray absorption spectroscopy and X-ray Raman scattering of water and ice; an experimental view." *Journal of Electron Spectroscopy and Related Phenomena* 177(2): 99-129.
- Orlando, F., A. Waldner, T. Bartels-Rausch, M. Birrer, S. Kato, M.-T. Lee, C. Proff, T. Huthwelker, A. Kleibert, J. van Bokhoven and M. Ammann (2016). "The Environmental Photochemistry of Oxide Surfaces and the Nature of Frozen Salt Solutions: A New in Situ XPS Approach." *Topics in Catalysis* 59(5): 591-604.
- Ottosson, N., M. Faubel, S. E. Bradforth, P. Jungwirth and B. Winter (2010). "Photoelectron spectroscopy of liquid water and aqueous solution: Electron effective attenuation lengths and emission-angle anisotropy." *Journal of Electron Spectroscopy and Related Phenomena* 177(2): 60-70.
- Schön, G., J. Tummavuori, B. Lindström, C. Enzell and C. Swahn (1973). "ESCA studies of Ag, Ag<sub>2</sub>O and AgO." *Acta Chem. Scand* 27(7): 2623.
- Shinotsuka, H., B. Da, S. Tanuma, H. Yoshikawa, C. J. Powell and D. R. Penn (2017). "Calculations of electron inelastic mean free paths. XI. Data for liquid water for energies from 50 eV to 30 keV." *Surface and Interface Analysis* 49(4): 238-252.
- Smith, J. D., C. D. Cappa, K. R. Wilson, B. M. Messer, R. C. Cohen and R. J. Saykally (2004). "Energetics of Hydrogen Bond Network Rearrangements in Liquid Water." *Science* 306(5697): 851-853.
- Waldner, A., L. Artiglia, X. Kong, F. Orlando, T. Huthwelker, M. Ammann and T. Bartels-Rausch (2018). "Pre-melting and the adsorption of formic acid at the air-ice interface at 253 K as seen by NEXAFS and XPS." *Physical Chemistry Chemical Physics* 20(37): 24408-24417.
- Wilson, K. R., M. Cavalleri, B. S. Rude, R. D. Schaller, A. Nilsson, L. Pettersson, N. Goldman, T. Catalano, J. Bozek and R. Saykally (2002). "Characterization of hydrogen bond acceptor molecules at the water surface using near-edge x-ray absorption fine-structure spectroscopy and density functional theory." *Journal of Physics: Condensed Matter* 14(8): L221.

## 4 WATER ADSORPTION ON K-FELDSPAR PARTICLE SURFACE

This chapter is adopted from the manuscript under preparation, which will be published as Yang Huanyu, Luca Artiglia, Anthony Boucly, Jérôme Philippe Gabathuler, Kiselev Alexei and Markus Ammann: Surface potassium ion exchange controls the coordination of water molecules on the surface of feldspar. We note that freezing experiments with the feldspar samples investigated in this chapter are underway by A. Kiselev at Karlsruhe Institute of Technology, the results of which are not yet included in this chapter.

### 4.1 SURFACE POTASSIUM ION EXCHANGE CONTROLS THE COORDINATION OF WATER MOLECULES ON THE SURFACE OF FELDSPAR

#### 4.1.1 Introduction

The formation of ice in the atmosphere can occur through homogeneous and heterogeneous ice nucleation (IN). Homogeneous IN occurs stochastically and spontaneously in an aqueous water droplet, which is described by the classical nucleation theory (Pruppacher and Klett 1997). As another pathway, the heterogeneous IN refers to the reduction of the free energy for the activation process facilitated by the surface of a condensed material or a macromolecule in solution. Particles containing materials that facilitate heterogeneous IN are often called **ice nucleating particles** (INPs) (Wang 2013). Heterogeneous IN is the predominant mechanism in the atmosphere by which ice forms in mixed phase clouds or by which cirrus ice particles form (Hoose and Möhler 2012). Deposition IN and immersion IN are the most common examples in heterogeneous IN. The first refers to the formation of ice on a solid surface directly from gas phase water under supersaturated conditions, while the latter refers to the formation of ice by INPs immersed inside supercooled liquid water droplets. Ice nucleation in the atmosphere can influence the cloud microphysics, precipitation (Cantrell and Heymsfield 2005) and the Earth's radiation budget (Borduas and Donahue 2018), therefore it has an important impact on the atmosphere and Earth's climate.

In view of the importance of heterogeneous IN on solid substrates, the surface of the solid INP material deserves attention, as it is strongly related to the IN process in the atmosphere. Surface investigations help understanding fundamental properties of the material's IN ability: the chemical composition and physical structure of INPs play important roles determining the local structure of water interacting with the surface (Pandey, Usui et al. 2016). In deposition nucleation, because of short- and long-range interaction, the surface properties determine the coordination of adsorbed water molecules. Similarly, in immersion freezing, the activation of ice nucleation is also influenced by the interaction between the nearby liquid and the solid surface. A change in the interaction between the solid surface and the neighboring water molecules would induce a different water HB structure or density (Maccarini 2007).

Among different classes of solid materials, mineral dust particles are recognized as important INPs (Hoose and Möhler 2012, Murray, O'Sullivan et al. 2012), which are abundant in the atmosphere (Engelstaedter, Tegen et al. 2006). Feldspars are a group of tectosilicate minerals that make up 41% of the Earth's continental crust (Anderson and Anderson 2010), which are considered as the most efficient INPs of the minerals commonly present in atmospheric mineral dust (Harrison, Whale et al. 2016). While feldspars are effective INPs, feldspars are a heterogeneous group of minerals with differing compositions and crystal structures. So the IN ability differs by species. By means of the microliter nucleation by immersed particle instrument ( $\mu\text{l-NIPI}$ ), Harrison et al. compared the IN ability of classes of feldspars including plagioclase, K-feldspars, and albite (Na rich). They observed that alkali feldspars (K-feldspars and albite) have better IN ability than plagioclase (Harrison, Whale et al. 2016). In addition, most albite samples have a relatively lower ice nucleation ability than K-feldspars. The potassium feldspars (K-rich) are especially considered as preferential ice nucleating particles in mixed-phase clouds (Atkinson, Murray et al. 2013, Augustin-Bauditz, Wex et al. 2014). Kiselev et al. investigated the active sites on a microcline surface by means of scanning electron microscopy (SEM), showing that cavities and cracks are responsible for the high ice nucleation ability of this material (Kiselev, Bachmann et al. 2017). Padevilla et al. identified an ice-like overlayer on the 001 surface of K-feldspar (K rich) by *ab initio* density functional theory calculations (Padevilla, Cox et al. 2016). A common feature of the feldspar minerals is their ability to exchange the charge balancing framework cations, which has been studied extensively also for the K-feldspars (Busenberg and Clemency 1976, Fenter, Teng et al. 2000, Fenter, Cheng et al. 2003, Chardon, Livens et al. 2006). In aqueous solutions the water activity is a key factor that determines the ice nucleation rate (Koop, Luo et al. 2000). Therefore, under conditions when deposition freezing could be relevant, leaching of ions into the adsorbed water could effectively reduce the ability to freeze.

The second way how cation exchange affects the IN ability is that the different structure of the  $\text{K}^+$  depleted surface is affecting the water structure in its vicinity to facilitate freezing as suggested by Kumar et al. (Kumar, Marcolli et al. 2019).

Investigating the water structure and chemical composition of crystal sample requires accessing the electronic structure of water and possibly the dissolved species at the same time. X-ray photoemission spectroscopy (XPS) is a surface sensitive technique, providing elemental ratio information, electronic state of elements and evaluate the thickness of an adsorbate overlayer within nanometer range.

In combination with the dipole selection rule, Auger electron yield near-edge X-ray absorption fine structure (NEXAFS) at the oxygen K-edge probes the unoccupied states in an oxygen atom-specific way (Stöhr 2003). By exciting O 1s electrons to the unoccupied states, we are sensitive to the local atomic character, which is most influenced by the local geometric arrangement such as the HB near the O atom (Myneni, Luo et al. 2002). Thus, NEXAFS is sensitive to the local HB network among the water molecules, serving as an efficient tool to distinguish the coordination of water molecules as in ice or in a more disordered configuration, such as liquid water (Cavalleri, Ogasawara et al. 2002, Wilson, Cavalleri et al. 2002, Winter and Faubel 2006, Nilsson, Nordlund et al. 2010, Schiros, Andersson et al. 2010). In this work

we combine XPS with NEXAFS to probe the feldspar samples at dry (0.1 % RH) and humid (50% RH) conditions for both authentic samples and after immersing them in water to allow for ion exchange. We have used these two techniques to probe the HB structure of ice in the presence of ions (Bartels-Rausch, Orlando et al. 2017, Kong, Waldner et al. 2017, Waldner, Artiglia et al. 2018). A pioneering work by Verdaguer *et al.* had investigated the structure of adsorbed water on SiO<sub>2</sub> (Verdaguer, Weis et al. 2007), and we have further used these to observe water structure on TiO<sub>2</sub> (Orlando, Artiglia et al. 2019) and AgI particles (Yang, Boucly et al. 2021).

In this work we focus on two types of K-feldspar samples: orthoclase and microcline. Moreover, parallel experiments on a powder microcline sample were also performed (results shown in SI). By means of XPS and O K edge NEXAFS we show that the exchange of K<sup>+</sup> ions with H<sup>+</sup> apparently inhibits the formation of tetrahedrally coordinated water upon adsorption on the sample surface. In other words, the presence of ions make the water layers more “liquid-like”. This work is of significant relevance to the ice nucleation study on K-feldspars, revealing its nature of the IN ability from a molecular level perspective.

#### 4.1.2 Materials and Methods

Two single crystals of potassium feldspar, microcline and orthoclase, cleaved along the 010 plane were used in the current work. They are labeled as PM01 (Pakistan Microcline), and AO02 (Adularia orthoclase) in the text. The crystals were glued with conductive epoxy resin (Polytec PT EC 244 filled with silver) to a copper plate (10 mm diameter and 3mm thickness). The samples were then polished, with final thickness at around 60  $\mu\text{m}$ . To remove the organic carbon accumulated on the sample surface due to exposure to ambient air, samples were cleaned by means of plasma treatment (Ar:O<sub>2</sub> with 40% : 60% volume ratio and 50W power, Plasma Lab System from Diener Electronic, Model: ATTO) for 2 minutes before introduction in the experiment cell. After the analysis of the as-prepared sample by XPS and NEXAFS, in order to investigate the ion leaching effect, we removed the analyzed sample and immersed in pure water (Sigma Aldrich) for 24h. After that, we repeated the same experiment. We call the sample before water immersion/washing as **as-prepared** sample, the sample after water immersion as **water treated sample**. In this work, we label the sample as the following way: **PM01\_nw** denote the as-prepared PM01 sample, while **PM01\_w** denote PM01 sample after water treatment for 24h. Similarly, **AO02\_nw** and **AO02\_w** denote the as-prepared and water treated AO02 sample.

The experiments were carried out at the in situ spectroscopy (ISS, X07DB) beamline at the Swiss Light Source (SLS). Photoelectron and electron yield NEXAFS spectra were acquired with a hemispherical electron analyzer coupled to a differentially pumped lens system (Scienta Omicron R4000/HiPP-2). The experimental cell (solid – gas interface chamber, SGI) has been described in a previous publication (Orlando, Waldner et al. 2016). By using a capillary dosing system, water vapor was introduced into the experimental cell. The water vapor pressure was stabilized at 0.5 mbar. Under such experimental conditions, the relative humidity at the sample

surface was set by changing the sample temperature (measured by means of a Pt1000 sensor fixed to the side of the sample). For XPS, each sample was measured under two conditions:

- i) 0% RH conditions, dosing 0.5 mbar of O<sub>2</sub>+N<sub>2</sub> (to limit sample surface charging), at 323 K.
- ii) 50% relative humidity (RH), corresponding 0.5 mbar water vapor pressure at 255 K, repeated before and after water immersion of the sample.

However, for the NEXAFS experiment, the ‘dry’ condition was defined at 0.5mbar of H<sub>2</sub>O pressure but at 323 K, corresponding to 0.1% RH. Having the same gas phase H<sub>2</sub>O pressure while acquiring the NEXAFS spectra for the two humidities, the contribution of gas phase H<sub>2</sub>O to the optical density and to the attenuation of the Auger electrons for the O K edge NEXAFS are identical. This facilitates the subtraction of the low RH spectrum from that obtained at 50% RH to effectively cancel the gas phase H<sub>2</sub>O contribution in a straightforward way.

During the experiments, we made use of linearly polarized light at 0°. In the range of kinetic energies relevant here, the inelastic mean free path of outgoing photoelectrons is proportional to their kinetic energy. The probing depth is related to the inelastic mean free path ( $\lambda$ ) of the photoelectron (probing depth =  $\lambda \cdot \cos \theta$ , where  $\theta$  is the electron take-off angle with respect to the sample surface normal). Measuring photoelectrons at lower kinetic energy is more surface sensitive whereas measurements at higher kinetic energy is more bulk-sensitive. The photon energy was tuned in order to acquire the K 2p, C 1s, Si 2p and O 1s photoemission signals with kinetic energies of ca. 340, 540, 640, 740 and 900 eV. Such values correspond to 5 different probing depth: 1.1, 1.6, 1.8, 2.0 and 2.3 nm. Photoemission peaks were normalized to the photon flux, inelastic mean free path of photoelectrons and their total photoionization cross section. Before Gaussian peak fitting and area calculation, a Shirley background was subtracted from the spectra. C 1s was used to calibrate the binding energy scale, assigning a binding energy of 284.8 eV to adventitious carbon. O K-edge NEXAFS spectra were obtained by integrating the Auger KLL peak of oxygen within a kinetic energy window ranging from 425 to 525 eV, while scanning the photon energy from 530 to 550 eV. Therefore, NEXAFS spectra were obtained with a fixed narrow range of kinetic energy, and thus also fixed probe depth. However, the probe depth of the electron yield NEXAFS spectra is less well defined due to contribution of inelastically scattered electrons to the intensity in the kinetic energy window chosen.

### 4.1.3 Results and discussion

Silicon is homogeneously distributed in the lattice of feldspar, upon contact with water, its leaching efficiency is negligible compared to potassium (dissolution of silanol groups occurs on a much longer time scale). Hence, the signal of Si 2p was used as a reference for normalization purposes. The advantage of reporting the photoemission intensity ratios of two elements at the same kinetic energy is to cancel those factors contributing to the measured

intensity, which are related to the analyzer transmission and/or depend on the measurement geometry of the experimental setup.

#### XPS depth profile and surface cation exchange.

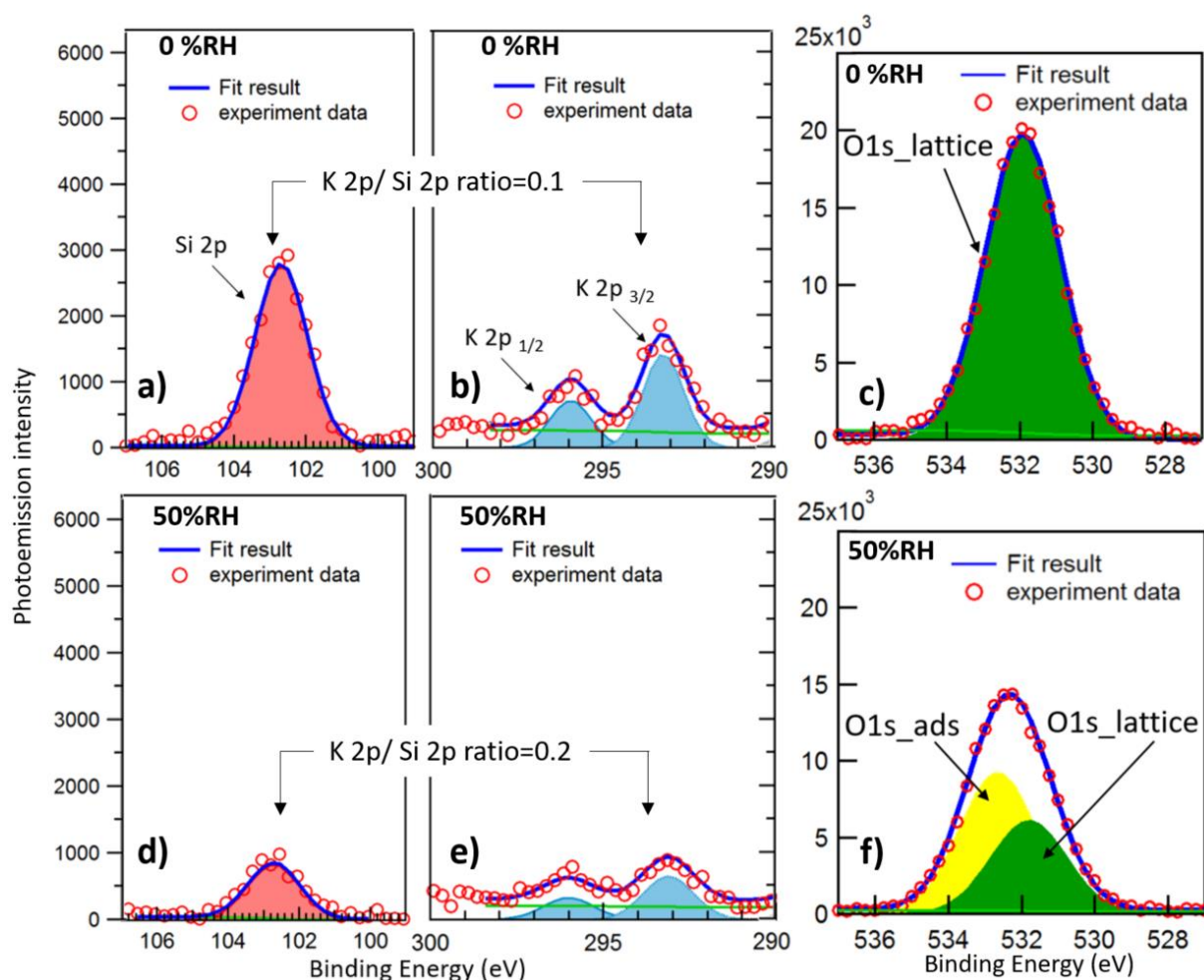


Figure 4-1 Measured Si 2p, K 2p and O 1s spectra of PM01\_nw at 0.1 % RH (323 K under 0.5 mbar  $O_2+N_2$ , panel a, b, c) and 50% RH (255 K under 0.5 mbar  $H_2O$ , panel d, e, f) condition, acquired at 650 eV photon energy for Si 2p and K 2p and 890 eV for O 1s. The S.O.S of K2p is 2.7 eV. The red and blue shaded areas indicate the components of Gaussian peak deconvolutions for Si2p, K2p. The green and yellow shaded areas represent the Gaussian peak deconvolution for O1s originating from lattice and adsorbed water, respectively.

Figure 4-1 shows exemplary XPS spectra of Si 2p, K 2p and O 1s, from the PM01\_nw dry sample surface acquired with excitation photon energy 650 eV for Si 2p and K 2p and 890 eV for O 1s (resulting photoelectron kinetic energy are 340). This corresponds to a probing depth of ca. 1.1 nm, which is the most surface sensitive condition used in this work. Gaussian peak deconvolution is represented by shaded areas. The measured binding energies of K  $2p_{1/2}$  and K  $2p_{3/2}$  (blue) are 295.9 and 293.2 eV, respectively, with a spin-orbit split of 2.7 eV, in agreement with previous literature (Pettersson and Karlsson 1977). Si 2p is deconvoluted by a single Gaussian peak at 102.8 eV (The S.O.S of Si 2p is 0.6 eV and can hardly be distinguished at the resolution of the beamline). The attenuated Si 2p signal at 50% RH reflect the presence of adsorbed water molecules on feldspar surface. Adventitious carbon contamination is

ubiquitous for samples that have been exposed to the ambient environment. Furthermore, such carbon species further develop during the X-ray irradiation under measurement conditions. Although the C1s signal is dominated by reduced carbon (Figure S 4-1, at binding energy 284.8 eV), the visible O-C=O and C-O-C components located at 288.5 eV and 286.6 eV indicate that oxygenated carbon is present on the sample surface under dry conditions, as reported by other studies (Stipp and Hochella 1991, Mangolini, McClimon et al. 2014, Landoulsi, Genet et al. 2016, Trotochaud, Head et al. 2018). For the O 1s spectrum (Figure 4-1), the lattice oxygen (O1s\_lattice, green peak) located at 531.7 eV, dominates the O1s spectrum. At 50% RH (bottom panel), upon dosing water into the experimental chamber, the peak becomes broader as a consequence of a second component at 532.8 eV, assigned to adsorbed water (O1s\_ads, yellow peak). The adsorbed water layer on the crystal surface attenuates the signal of O1s\_lattice, leading to a decreased O1s\_lattice peak intensity (green peak, bottom panel) compared with that obtained for the dry condition (green peak, top panel). This is also the reason why the Si 2p signal drops from dry to humid conditions by about the same amount. As directly obvious from Figure 4-1, the K2p/Si2p signal intensity ratio increases by a factor of two between dry and 50% RH.

The depth profiles of the elemental ratios related to the measured intensity ratios of K2p/Si2p, O1s\_lattice/Si2p and C1s/Si2p for probing depths of 1.6 nm, 1.8 nm, 2.0 nm and 2.3 nm are provided in the SI. These ratios represent cumulative elemental ratios near the surface of the PM01 and AO02 samples as a function of increasing probing depth, meaning that each value shown is the integrated ratio from the surface over the whole probing depth. Because the signals of potassium and oxygen are normalized to silicon (assumed to be homogeneously distributed in the lattice, see above), depth profiles depict the distribution of each element within the topmost layers of the samples.

Since determining absolute elemental ratios is difficult due to not well characterized higher order contributions to the photon flux at the beamline used, we report the elemental ratios in normalized form, i.e., the relative change of the elemental ratio upon exposure of the sample

to 50% RH. Thus, in Figure 4-2, we show the ratio of the depth profile at 50% RH to that at 0.1% RH.

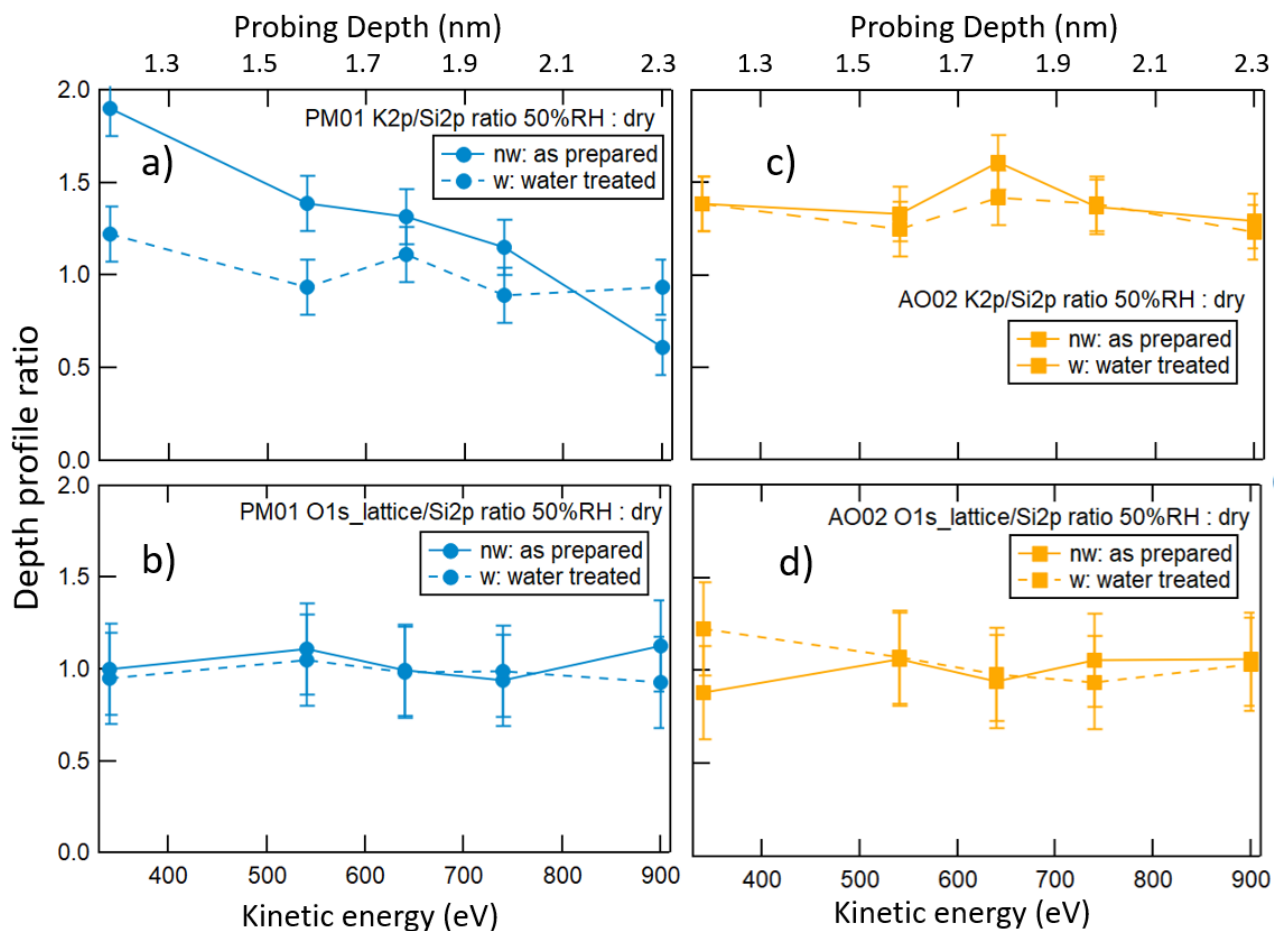


Figure 4-2. Response of the elemental ratios to 50% RH (255K, at 0.5 mbar H<sub>2</sub>O), normalized with respect to the 0.1% RH case (323 K, O<sub>2</sub>+N<sub>2</sub> 0.5 mbar). Panel a, b are for PM01 samples and c, d are for AO02 samples. Each panel contains both as-prepared (solid connecting lines) and water treated samples (dashed connecting lines). The probing depth of each data point is labeled in panel a). All panels share the same vertical axis scale.

A decreasing ratio or if the ratio is higher than one in Figure 4-2 suggests surface accumulation of a species in response to increasing RH. When the ratio is very close to one within uncertainties, no change or leaching takes place. This is especially true when looking at the O1s\_lattice (panel b and d), where the normalized ratio to Si always show a value close to one for all samples, proving that the even distribution of O and Si in the lattice is not affected by water adsorption on the surface at 50% RH. In contrast, the corresponding K2p/Si2p profile shown in Figure 4-2 panel a and c for the as prepared PM01\_nw sample (solid blue line) shows a decreasing trend, suggesting that migration of K<sup>+</sup> cations toward the surface is triggered by water adsorption. Based on this, some potassium may leach into adsorbed water, influencing its ice nucleation ability (Koop, Luo et al. 2000, Kumar, Marcolli et al. 2018). In the case of PM01\_w sample (dashed blue line), this ratio is observed to remain constant at one within uncertainty, suggesting that no additional migration of K<sup>+</sup> to the surface is triggered in this case.

Obviously, the water treatment of PM01 has depleted potassium within the probed depth (2 nm), and migration from further below in the sample is too slow within the time scale of a few hours of these experiments. On the other hand, panel c shows the corresponding results for the AO02 sample, upon increasing of the relative humidity, an enhanced K 2p level ( $\approx 1.5$ ) was observed for both AO02\_nw and AO02\_w samples. This suggests two possible scenarios: 1) migration of  $K^+$  cations toward the surface and leaching in adsorbed water takes place on AO02 even after water treatment. 2) There is no  $K^+$  leaching effect for both AO02\_nw and AO02\_w samples. Conversely, as discussed above, such effect is not observed in water treated PM01 (PM01\_w) under humid conditions (panel a dashed lines). It is important to highlight this difference, because the presence of  $K^+$  in adsorbed water could affect the IN behavior of the two samples.

In the Supporting Materials, we present a quantitative analysis of the elemental ratios in terms of an attenuation model that allows retrieving the thickness of the adsorbed layer on the surface of the two samples at 50% RH. These thicknesses are 1.4 nm (4 MLs) and 1.0 nm (3 MLs) on PM01 and AO02 samples respectively. Tang et al. (Tang, Cziczo et al. 2016) provide a comprehensive overview of laboratory studies of water adsorption, hygroscopicity and ice nucleation of fresh and atmospherically aged mineral dust particles.

#### O K edge NEXAFS.

In Figure S 4-5, we show the raw O K-edge NEXAFS spectra for all samples, at 0.1 % (considered as dry condition) and 50 % RH. They show contributions from the lattice oxygen, oxygen containing adventitious carbon compounds and adsorbed water. To further investigate the O K edge NEXAFS of adsorbed water on the surface of these mineral crystal sample, we calculate the difference spectra, obtained by subtracting an appropriate portion of the spectrum measured at 0.1% RH from those at 50% RH, shown in Figure 4-3. These difference spectra represent exclusively the absorption features of water adsorbed on the surface. *We refer to these difference spectra as adsorbed water spectra.*

The adsorbed water plays two roles in O K edge NEXAFS spectra:

- i) displays distinctive features in the O K edge spectral range
- ii) attenuates the signal of the bulk crystal.

The contribution of the dry (0.1% RH) sample to that of humid (50% RH) condition is characterized by Lambert-Beer behavior. Depending on the adsorbed  $H_2O$  thickness, the portion of the 0.1% RH spectrum ( $\alpha$ ) subtracted from that measured at 50% RH equals to 0.48 and 0.57 for PM01 and AO02 samples respectively (See calculations in SI). In Figure 4-3 we show the summary of the adsorbed water spectra. To qualitatively discuss the HB structure of adsorbed water molecules on the feldspar surface, we mainly compare the adsorbed water spectra to the case of ice and liquid water. As comparison, in liquid water (red line), the asymmetric HB configuration dominates, which is weak in an energetic perspective (weak HB), which leads to a pronounced absorption feature at photon energy at around 537-538 eV as indicated by the red dashed vertical line. At around 535 eV, the dashed green vertical line indicates the conventionally called “pre-edge” absorption, which is related to dangling OH on

the surface. The pre-edge feature in the condensed phase system is similar to the  $4a_1$  feature for gas phase water molecules, (Nilsson, Nordlund et al. 2010) where hydrogen is excited into the  $4a_1$  antibonding orbital (Myneni, Luo et al. 2002). As a contrasting case, symmetric tetrahedral HB structure is predominant in ice with highly ordered water molecule coordination (grey line). Such highly ordered coordination leads to a maximum absorption at 540-541 eV, an energetic (strong HB) region that is sensitive to the tetrahedral coordination of water molecules. Based on the concept of “bond-length-with-a-ruler” (Stöhr 2003), the energy distribution of the strong HB peak was associated to the distribution of HB distances, and its width/broadening is affected strongly by the internal OH distance as depicted by the Franck-Condon principle (Franck and Dymond 1926). Under this framework, the ice and liquid water spectra display contrasting HB configuration, are considered as references to qualitatively interpret the HB structure of adsorbed water on the feldspar surface, shown in the same figure.

Under the HB structure framework depicted by water and ice NEXAFS spectra, the adsorbed water spectra between water treated and as-prepared PM01 sample show notable features. Compared to PM01\_nw case (purple, Figure 4-3), water molecules on PM01\_w (blue, Figure 4-3) show a generally higher absorption feature starting from around 539 to 542 eV (around dashed black vertical line) than PM01\_nw. This spectral region is where the stronger and more symmetric HB contributions are found, indicating that the tetrahedral coordinated water molecules is more abundant on PM01\_w than on PM01\_nw surface. To some extent, the observed water spectra on PM01\_nw surface is more *liquid-like* whereas that of PM01\_w case is more *ice-like*. Linked to the XPS result, we ascribe the liquid-like water spectrum on PM01\_nw surface to the presence of  $K^+$  ions and their perturbation on the electronic structure of neighboring water molecules (Cappa, Smith et al. 2005). Macroscopically, such  $K^+$  ion in the water layer provide a high concentration of salt solution, that reduce the water activity, and eventually affect the nucleation rate. (Koop, Luo et al. 2000) Parallel to the XPS results indicating that  $K^+$  ion leaching does not take place for PM01\_w under humid conditions, the fraction of tetrahedrally coordinated water molecules appeared to be higher in absence of  $K^+$  cations. This explains the notable difference of the absorption features located at around 540.5 eV between water on PM01\_w and PM01\_nw surface at 50% RH.

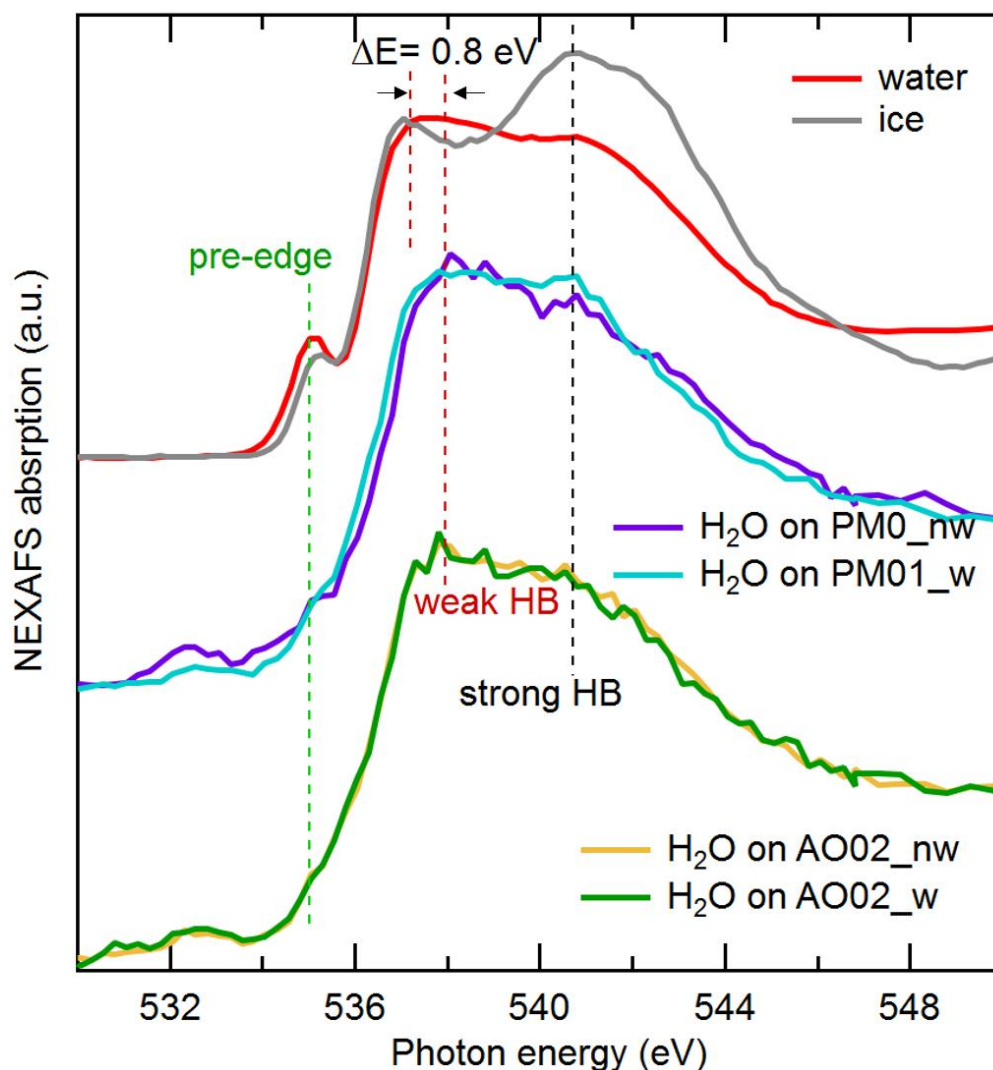


Figure 4-3. Difference spectra comparison, corresponds to the pure contribution from adsorbed H<sub>2</sub>O layers. The purple and blue lines refer to water spectra on PM01\_nw and PM01\_w sample. The yellow and green lines refer to water spectra on AO02\_nw and AO02\_w sample. Liquid water (red) and ice (grey) spectrum are shown on the top for shape comparison. We used the vertical dashed red and black lines to represent the position where weak and strong *HB* arise. The dashed green vertical line reflect the pre-edge absorption. All H<sub>2</sub>O spectra are area-normalized.

On the other hand, NEXAFS spectra of adsorbed water on AO02\_nw (yellow, Figure 4-3) and AO02\_w (green, Figure 4-3) are almost identical, specifically, these spectra show no differences in the region of weak and strong *HB*. The XPS results suggest that the depth profile of the potassium to silicon elemental ratio is not responding to the presence of humidity, neither in the as prepared, nor in the water treated sample. Nevertheless, both water spectra on AO02 show are rather resembling that of liquid water: strong absorption feature at around 537-538 eV and relatively lower at around 539 to 542 eV. This suggest that the surface structure for both the as prepared and the water treated AO material is not promoting the formation of tetrahedrally coordinated adsorbed water as much as the PM sample does. is either due to its interfacial property or the potassium ion leaching.

Additionally, in Figure 4-3 we note an apparent decrease in pre-edge absorption feature between adsorbed H<sub>2</sub>O and ice/water system (outlined by the dashed green vertical line), suggesting that the dangling OH species are negligible for water adsorbed on feldspar surface. The pre-edge feature is more pronounced for amorphous film compared to crystalline ice (Kimmel, Petrik et al. 2005, Waluyo, Nordlund et al. 2008, Nilsson, Nordlund et al. 2010).. This could well be the ordering induced by the solid surface-water interaction, which makes K-feldspar as efficient INPs.

#### 4.1.4 Conclusion

Even though potassium feldspar are considered as good IN particles, it can be concluded from the observed spectra, that K<sup>+</sup> cations still provide electronic perturbation of the water molecules or geometric distortion of the HB. Other studies reported that microcline has a better IN ability than orthoclase (Harrison, Whale et al. 2016). From our results, it appears that only the K<sup>+</sup> depleted surface has an ability to order water at its surface. We note that our water treatment is eventually comparable to the case of immersion freezing experiments, where K<sup>+</sup> ions may dissolve into a relatively large pure water drop, so that essentially a K<sup>+</sup> depleted surface is probed without the water activity reduction by K<sup>+</sup> in the droplet being significant. We observe the water treated PM01 show the most prominent water molecule ordering ability, reflected by the highest strong HB absorption feature of the corresponding adsorbed water spectrum. Our result confirm the hypothesis of the potential role of K<sup>+</sup> ions migrated from the feldspar surface layer in contact with water, and when K<sup>+</sup> are depleted within a reasonable depth, the impact of K<sup>+</sup> on the HB structure is minimized, while the structural motives of the depleted framework structure are the basis for ordering of adsorbed water. The effect of K<sup>+</sup> exerts on the water molecules at the interface is clearly one of the various parameters that control the ice nucleation mechanism at water feldspar mineral surface.

## References

- Anderson, R. S. and S. P. Anderson (2010). *Geomorphology: the mechanics and chemistry of landscapes*, Cambridge University Press.
- Atkinson, J. D., B. J. Murray, M. T. Woodhouse, T. F. Whale, K. J. Baustian, K. S. Carslaw, S. Dobbie, D. O'Sullivan and T. L. Malkin (2013). "The importance of feldspar for ice nucleation by mineral dust in mixed-phase clouds." *Nature* 498: 355.
- Augustin-Bauditz, S., H. Wex, S. Kanter, M. Ebert, D. Niedermeier, F. Stolz, A. Prager and F. Stratmann (2014). "The immersion mode ice nucleation behavior of mineral dusts: A comparison of different pure and surface modified dusts." *Geophysical Research Letters* 41(20): 7375-7382.
- Bartels-Rausch, T., F. Orlando, X. Kong, L. Artiglia and M. Ammann (2017). "Experimental Evidence for the Formation of Solvation Shells by Soluble Species at a Nonuniform Air–Ice Interface." *ACS Earth and Space Chemistry* 1(9): 572-579.
- Borduas, N. and N. M. Donahue (2018). Chapter 3.1 - The Natural Atmosphere. *Green Chemistry*. B. Török and T. Dransfield, Elsevier: 131-150.
- Busenberg, E. and C. V. Clemency (1976). "The dissolution kinetics of feldspars at 25°C and 1 atm CO<sub>2</sub> partial pressure." *Geochimica et Cosmochimica Acta* 40(1): 41-49.
- Cantrell, W. and A. Heymsfield (2005). "Production of Ice in Tropospheric Clouds: A Review." *Bulletin of the American Meteorological Society* 86(6): 795-808.
- Cappa, C. D., J. D. Smith, B. M. Messer, R. C. Cohen and R. J. Saykally (2006). "Effects of Cations on the Hydrogen Bond Network of Liquid Water: New Results from X-ray Absorption Spectroscopy of Liquid Microjets." *The Journal of Physical Chemistry B* 110(11): 5301-5309.
- Cappa, C. D., J. D. Smith, B. M. Messer, R. C. Cohen and R. J. Saykally (2006). "The Electronic Structure of the Hydrated Proton: A Comparative X-ray Absorption Study of Aqueous HCl and NaCl Solutions." *The Journal of Physical Chemistry B* 110(3): 1166-1171.
- Cappa, C. D., J. D. Smith, K. R. Wilson, B. M. Messer, M. K. Gilles, R. C. Cohen and R. J. Saykally (2005). "Effects of Alkali Metal Halide Salts on the Hydrogen Bond Network of Liquid Water." *The Journal of Physical Chemistry B* 109(15): 7046-7052.
- Cavalleri, M., H. Ogasawara, L. G. M. Pettersson and A. Nilsson (2002). "The interpretation of X-ray absorption spectra of water and ice." *Chemical Physics Letters* 364(3): 363-370.
- Chardon, E. S., F. R. Livens and D. J. Vaughan (2006). "Reactions of feldspar surfaces with aqueous solutions." *Earth-Science Reviews* 78(1): 1-26.
- Engelstaedter, S., I. Tegen and R. Washington (2006). "North African dust emissions and transport." *Earth-Science Reviews* 79(1): 73-100.
- Fenter, P., L. Cheng, C. Park, Z. Zhang and N. C. Sturchio (2003). "Structure of the orthoclase (001)- and (010)-water interfaces by high-resolution X-ray reflectivity." *Geochimica et Cosmochimica Acta* 67(22): 4267-4275.
- Fenter, P., H. Teng, P. Geissbühler, J. M. Hanchar, K. L. Nagy and N. C. Sturchio (2000). "Atomic-scale structure of the orthoclase (001)–water interface measured with high-resolution X-ray reflectivity" The submitted manuscript has been created by the University of Chicago as operator of Argonne National Laboratory under Contract No. W-31-109-ENG-38 with the U.S. Department of Energy. The U.S. government retains for itself, and others acting on its behalf, a paid-up, nonexclusive, irrevocable worldwide license in said article to reproduce, prepare derivative works, distribute copies to the public, and perform publicly and display publicly, by or on behalf of the government." *Geochimica et Cosmochimica Acta* 64(21): 3663-3673.
- Franck, J. and E. G. Dymond (1926). "Elementary processes of photochemical reactions." *Transactions of the Faraday Society* 21(February): 536-542.
- Harrison, A. D., T. F. Whale, M. A. Carpenter, M. A. Holden, L. Neve, D. O'Sullivan, J. Vergara Temprado and B. J. Murray (2016). "Not all feldspars are equal: a survey of ice nucleating properties across the feldspar group of minerals." *Atmos. Chem. Phys.* 16(17): 10927-10940.
- Hoose, C. and O. Möhler (2012). "Heterogeneous ice nucleation on atmospheric aerosols: a review of results from laboratory experiments." *Atmos. Chem. Phys.* 12(20): 9817-9854.
- Huang, C., K. T. Wikfeldt, T. Tokushima, D. Nordlund, Y. Harada, U. Bergmann, M. Niebuhr, T. M. Weiss, Y. Horikawa, M. Leetmaa, M. P. Ljungberg, O. Takahashi, A. Lenz, L. Ojamäe, A. P. Lyubartsev, S. Shin, L. G. M. Pettersson and A. Nilsson (2009). "The inhomogeneous structure of water at ambient conditions." *Proceedings of the National Academy of Sciences* 106(36): 15214-15218.
- Kimmel, G. A., N. G. Petrik, Z. Dohnálek and B. D. Kay (2005). "Crystalline Ice Growth on Pt(111): Observation of a Hydrophobic Water Monolayer." *Physical Review Letters* 95(16): 166102.
- Kiselev, A., F. Bachmann, P. Pedevilla, S. J. Cox, A. Michaelides, D. Gerthsen and T. Leisner (2017). "Active sites in heterogeneous ice nucleation—the example of K-rich feldspars." *Science* 355(6323): 367-371.

- Kong, X., A. Waldner, F. Orlando, L. Artiglia, T. Huthwelker, M. Ammann and T. Bartels-Rausch (2017). "Coexistence of Physisorbed and Solvated HCl at Warm Ice Surfaces." *The Journal of Physical Chemistry Letters* 8(19): 4757-4762.
- Koop, T., B. Luo, A. Tsias and T. Peter (2000). "Water activity as the determinant for homogeneous ice nucleation in aqueous solutions." *Nature* 406(6796): 611-614.
- Kumar, A., C. Marcolli, B. Luo and T. Peter (2018). "Ice nucleation activity of silicates and aluminosilicates in pure water and aqueous solutions – Part 1: The K-feldspar microcline." *Atmos. Chem. Phys.* 18(10): 7057-7079.
- Kumar, A., C. Marcolli and T. Peter (2019). "Ice nucleation activity of silicates and aluminosilicates in pure water and aqueous solutions – Part 3: Aluminosilicates." *Atmos. Chem. Phys.* 19(9): 6059-6084.
- Landoulsi, J., M. J. Genet, S. Fleith, Y. Touré, I. Liascukiene, C. Méthivier and P. G. Rouxhet (2016). "Organic adlayer on inorganic materials: XPS analysis selectivity to cope with adventitious contamination." *Applied Surface Science* 383: 71-83.
- Leberman, R. and A. K. Soper (1995). "Effect of high salt concentrations on water structure." *Nature* 378(6555): 364-366.
- Maccarini, M. (2007). "Water at solid surfaces: A review of selected theoretical aspects and experiments on the subject." *Biointerphases* 2(3): MR1-MR15.
- Mangolini, F., J. B. McClimon, F. Rose and R. W. Carpick (2014). "Accounting for Nanometer-Thick Adventitious Carbon Contamination in X-ray Absorption Spectra of Carbon-Based Materials." *Analytical Chemistry* 86(24): 12258-12265.
- Murray, B. J., D. O'Sullivan, J. D. Atkinson and M. E. Webb (2012). "Ice nucleation by particles immersed in supercooled cloud droplets." *Chemical Society Reviews* 41(19): 6519-6554.
- Myneni, S., Y. Luo, L. Å. Näslund, M. Cavalleri, L. Ojamäe, H. Ogasawara, A. Pelmenchikov, W. Ph, P. Väterlein, C. Heske, Z. Hussain, L. G. M. Pettersson and A. Nilsson (2002). "Spectroscopic probing of local hydrogen-bonding structures in liquid water." *Journal of Physics: Condensed Matter* 14(8): L213.
- Nilsson, A., D. Nordlund, I. Waluyo, N. Huang, H. Ogasawara, S. Kaya, U. Bergmann, L. Å. Näslund, H. Öström, P. Wernet, K. J. Andersson, T. Schiros and L. G. M. Pettersson (2010). "X-ray absorption spectroscopy and X-ray Raman scattering of water and ice; an experimental view." *Journal of Electron Spectroscopy and Related Phenomena* 177(2): 99-129.
- Nordlund, D., H. Ogasawara, K. J. Andersson, M. Tatarkhanov, M. Salmerón, L. G. M. Pettersson and A. Nilsson (2009). "Sensitivity of x-ray absorption spectroscopy to hydrogen bond topology." *Physical Review B* 80(23): 233404.
- Orlando, F., L. Artiglia, H. Yang, X. Kong, K. Roy, A. Waldner, S. Chen, T. Bartels-Rausch and M. Ammann (2019). "Disordered Adsorbed Water Layers on TiO<sub>2</sub> Nanoparticles under Subsaturated Humidity Conditions at 235 K." *The Journal of Physical Chemistry Letters* 10(23): 7433-7438.
- Orlando, F., A. Waldner, T. Bartels-Rausch, M. Birrer, S. Kato, M.-T. Lee, C. Proff, T. Huthwelker, A. Kleibert, J. van Bokhoven and M. Ammann (2016). "The Environmental Photochemistry of Oxide Surfaces and the Nature of Frozen Salt Solutions: A New in Situ XPS Approach." *Topics in Catalysis* 59(5): 591-604.
- Pandey, R., K. Usui, R. A. Livingstone, S. A. Fischer, J. Pfaendtner, E. H. G. Backus, Y. Nagata, J. Fröhlich-Nowoisky, L. Schmöser, S. Mauri, J. F. Scheel, D. A. Knopf, U. Pöschl, M. Bonn and T. Weidner (2016). "Ice-nucleating bacteria control the order and dynamics of interfacial water." *Science Advances* 2(4).
- Pedevilla, P., S. J. Cox, B. Slater and A. Michaelides (2016). "Can Ice-Like Structures Form on Non-Ice-Like Substrates? The Example of the K-feldspar Microcline." *The Journal of Physical Chemistry C* 120(12): 6704-6713.
- Pettersson, L. G. and S. E. Karlsson (1977). "Clean and Oxygen Exposed Potassium Studied by Photoelectron Spectroscopy." *Physica Scripta* 16(5-6): 425-431.
- Pruppacher, H. R. and J. D. Klett (1997). *Microphysics of Clouds and Precipitation*.
- Schiros, T., K. J. Andersson, L. G. M. Pettersson, A. Nilsson and H. Ogasawara (2010). "Chemical bonding of water to metal surfaces studied with core-level spectroscopies." *Journal of Electron Spectroscopy and Related Phenomena* 177(2): 85-98.
- Stipp, S. L. and M. F. Hochella (1991). "Structure and bonding environments at the calcite surface as observed with X-ray photoelectron spectroscopy (XPS) and low energy electron diffraction (LEED)." *Geochimica et Cosmochimica Acta* 55(6): 1723-1736.
- Stöhr, J. (2003). *NEXAFS Spectroscopy*, Springer, Berlin, Heidelberg.
- Tang, M., D. J. Cziczo and V. H. Grassian (2016). "Interactions of Water with Mineral Dust Aerosol: Water Adsorption, Hygroscopicity, Cloud Condensation, and Ice Nucleation." *Chemical Reviews* 116(7): 4205-4259.
- Trotochaud, L., A. R. Head, S. Pletincx, O. Karshoğlu, Y. Yu, A. Waldner, L. Kyhl, T. Hauffman, H. Terry, B. Eichhorn and H. Bluhm (2018). "Water Adsorption and Dissociation on Polycrystalline Copper Oxides: Effects of Environmental Contamination and Experimental Protocol." *The Journal of Physical Chemistry B* 122(2): 1000-1008.

- Verdaguer, A., C. Weis, G. Oncins, G. Ketteler, H. Bluhm and M. Salmeron (2007). "Growth and Structure of Water on SiO<sub>2</sub> Films on Si Investigated by Kelvin Probe Microscopy and in Situ X-ray Spectroscopies." *Langmuir* 23(19): 9699-9703.
- Waldner, A., L. Artiglia, X. Kong, F. Orlando, T. Huthwelker, M. Ammann and T. Bartels-Rausch (2018). "Pre-melting and the adsorption of formic acid at the air-ice interface at 253 K as seen by NEXAFS and XPS." *Physical Chemistry Chemical Physics* 20(37): 24408-24417.
- Waluyo, I., D. Nordlund, L. Å. Näslund, H. Ogasawara, L. G. M. Pettersson and A. Nilsson (2008). "Spectroscopic evidence for the formation of 3-D crystallites during isothermal heating of amorphous ice on Pt(111)." *Surface Science* 602(11): 2004-2008.
- Wang, P. K. (2013). *Physics and Dynamics of Clouds and Precipitation*. Cambridge, Cambridge University Press.
- Wilson, K. R., M. Cavalleri, B. S. Rude, R. D. Schaller, A. Nilsson, L. Pettersson, N. Goldman, T. Catalano, J. Bozek and R. Saykally (2002). "Characterization of hydrogen bond acceptor molecules at the water surface using near-edge x-ray absorption fine-structure spectroscopy and density functional theory." *Journal of Physics: Condensed Matter* 14(8): L221.
- Winter, B. and M. Faubel (2006). "Photoemission from Liquid Aqueous Solutions." *Chemical Reviews* 106(4): 1176-1211.
- Yang, H., A. Boucly, J. P. Gabathuler, T. Bartels-Rausch, L. Artiglia and M. Ammann (2021). "Ordered Hydrogen Bonding Structure of Water Molecules Adsorbed on Silver Iodide Particles under Subsaturated Conditions." *The Journal of Physical Chemistry C*.
- Zolles, T., J. Burkart, T. Häusler, B. Pummer, R. Hitzemberger and H. Grothe (2015). "Identification of Ice Nucleation Active Sites on Feldspar Dust Particles." *The Journal of Physical Chemistry A* 119(11): 2692-2700.

## 4.2 SUPPORTING INFORMATION

### 4.2.1 C1s spectra and elements depth profile of single crystal sample

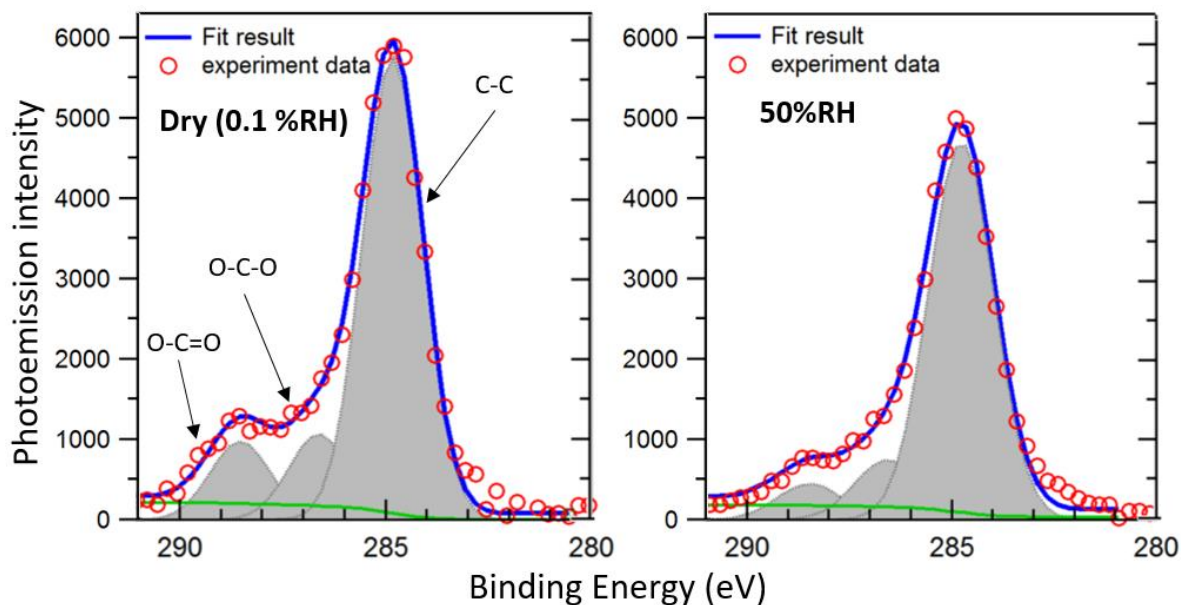


Figure S 4-1: Exemplary C1s spectra of PM01\_nw at 0.1 % RH (323 K under 0.5 mbar  $O_2+N_2$ , left panel) and 50% RH (255 K under 0.5 mbar  $H_2O$ , right panel), acquired at 650 eV photon energy (The corresponding kinetic energy is ca. 340eV). Binding energy for xx carbon (O-C=O), xx carbon (O-C-O) and reduced carbon (C-C) are 288.5 eV, 286.6 eV, 284.8 eV, respectively.

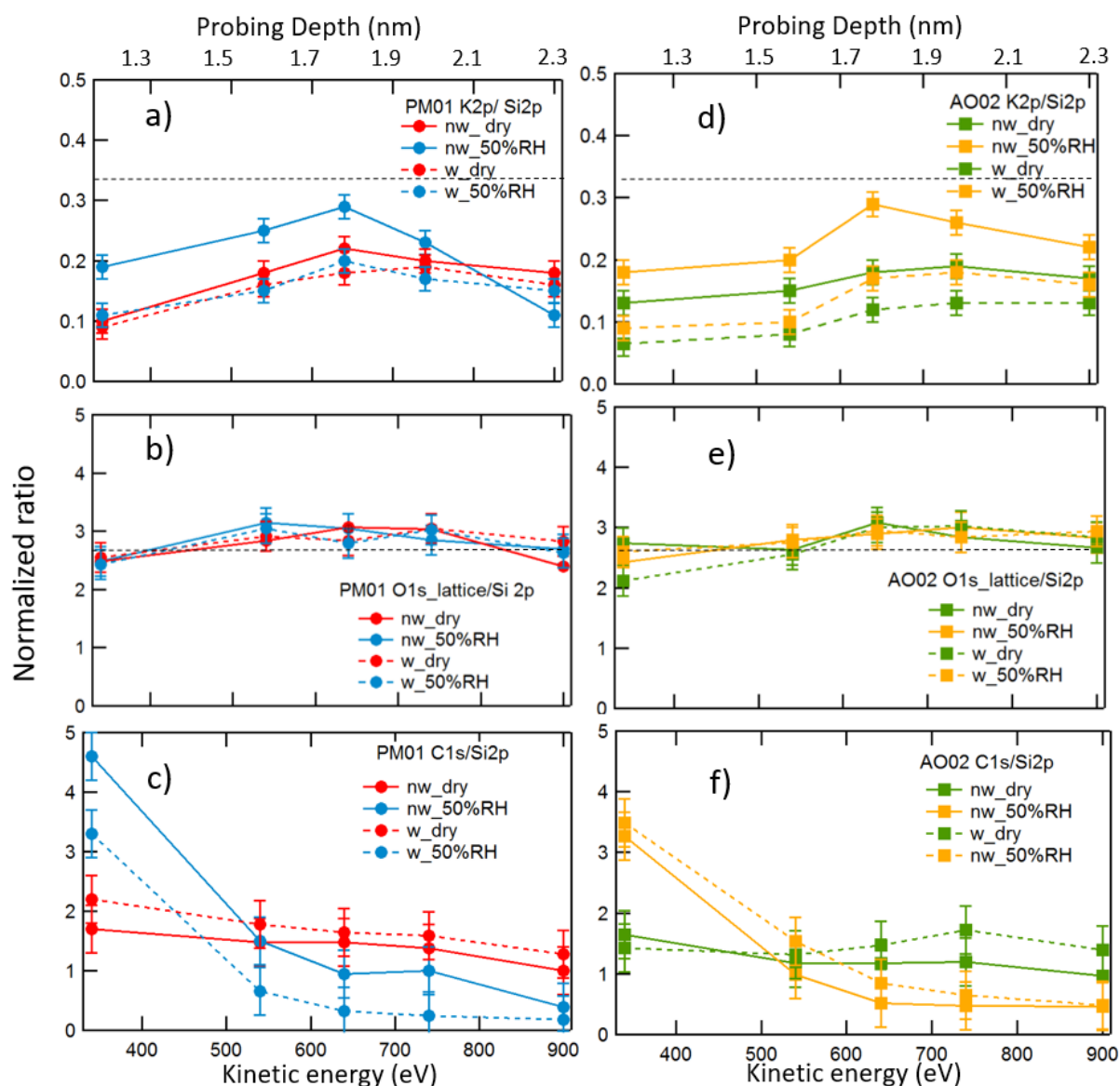


Figure S 4-2 XPS Depth profile of K2p, C1s and O1s from the bulk crystal, normalized by Si2p signal. Panel a, b, c are for PM01 samples and d, e, f are for AO02 samples. Each panel contain the depth profile of both as-prepared and water treated samples at dry (323 K,  $O_2+N_2$  0.5 mbar) and humid (255K, 50% RH at 0.5 mbar  $H_2O$ ) conditions. The probing depth of each data point is labeled in panel a). The dashed horizontal line indicate the theoretical elemental ratio.

The theoretical ratio of K2p/Si2p and O1s\_lattice/Si2p in K-feldspars ( $KAlSi_3O_8$ ) are 1/3 and 8/3, respectively. As shown in Figure S 4-2b and e, within uncertainty, the O1s\_lattice/Si2p ratio always show a value close to the 8/3, proving that oxygen is evenly distributed in the lattice. The K2p/Si2p ratio (Figure S 4-2a and d) is generally lower than the 1/3 theoretical ratio and becomes relative higher at 50% RH (PM01\_w is an exemption). As explained in the main text, potassium is more mobile than oxygen in the lattice framework of feldspar and  $K^+$  ion-leaching processes might already take place during the sample preparation.

Adventitious carbon contamination is commonly observed for samples that have been exposed to the ambient environment (Stipp and Hochella 1991, Mangolini, McClimon et al. 2014,

Landoulsi, Genet et al. 2016, Trotochaud, Head et al. 2018, Yang, Boucly et al. 2021). We summarize the carbon scenario in Figure S 4-3c and f, with the representative C1s/Si2p ratio depth profile for PM01 and AO02 sample, respectively. In humid condition, the rapid increase of carbon at low probing depth upon addition of water implies the following scenario. Firstly, higher RH favor the growth of adventitious carbon, even though the liquid water used in this work as the source of vapor was purified by several freeze-pump-thaw cycles, it still may co-dose carbon-containing species, the X-ray beam further decompose those species and build up carbon accumulations during the experiment. Secondly, the removal of carbon-species from the chamber walls also contribute a small amount of carbon contribution. Conversely, under dry condition the C1s/Si2p trend is much less steep than humid condition, which is not surprising as the samples are plasma cleaned before introducing into the experiment chamber.

In Figure S 4-4 we report the normalized O1s<sub>ads</sub>/Si2p ratio as a function of probing depth for all samples. Through an attenuation model that considers the surface being covered by a homogeneous layer of adsorbed H<sub>2</sub>O, we fit the kinetic energy dependent signal intensity ratio of O1s<sub>ads</sub> to Si 2p, which compute the H<sub>2</sub>O layer thickness adsorbed on sample surface. The average thicknesses of adsorbed H<sub>2</sub>O on PM01 and AO02 samples at 50% RH are 1.4 nm (4 MLs) and 1.0 nm (3 MLs) respectively. The results of the attenuation model suggest that the H<sub>2</sub>O coverage thickness is independent of its water treatment, especially the result of PM01

implies that the presence/absence of  $K^+$  within  $H_2O$  layers is not the determinant factor that impact the  $H_2O$  adsorption efficiency.

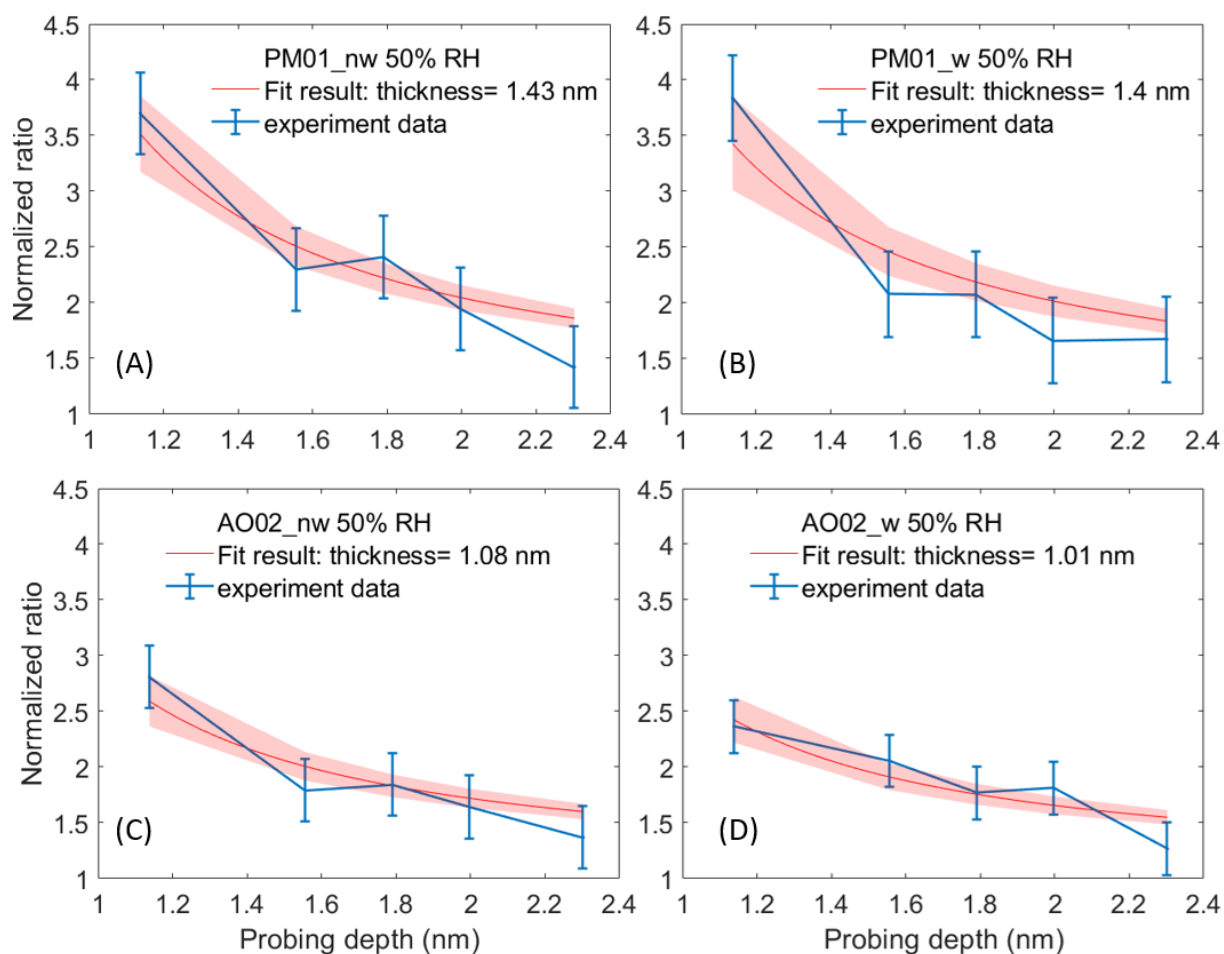


Figure S 4-4 Fitting ratio of the O1s<sub>ads</sub> to that of Si2p as a function of probing depth for PM01 (panel A and B) and AO02 (panel C and D) samples. Blue lines represent experimental normalized ratio. Red lines represent the fitting results with 95% of confidence bounds, shown by red shading area. The effective thickness obtained from the fit is labeled in the image legend.

#### 4.2.2 Attenuation model for adsorption thickness determination

The attenuation model consider a substrate having semi-infinite thickness with an adsorbate (water) with finite thickness  $t_a$ .

For the adsorbed overlayer(s), the measured photoelectron intensity related to excitation of a core level of an atom  $a$  is:

$$I_a = F \cdot \sigma_a \cdot \phi_a \cdot \int_{-t_a}^0 \rho_a(z) \cdot e^{-\frac{(z+t_a)}{\lambda_a \cdot \cos \theta}} dz \quad (\text{Equation S 4-1})$$

Where  $F \propto \Omega_0 \cdot A_0 \cdot D_0$ . The factor  $F$  is proportional to parameters depending on the geometry of the experimental setup and the technical characteristics of the analyzer: electron detection efficiency ( $D_0$ ), acceptance angle ( $\Omega_0$ ), and effectively analyzed area ( $A_0$ ), which in turn depends on the spot size of the photon beam. The factor  $F$  can be simplified when taking the ratio of photoemission intensities obtained at the same kinetic energy. The photon flux used to excite the specific core level of atom A is denoted by  $\phi_A$ , and  $\theta$  is the electron emission direction angle with respect to the surface normal, in our case is  $\pi/6$ .

$\lambda_a$  denote the electron inelastic mean free path experienced by electrons passing through the adsorbate overlayer (ref shinotsuka),  $\sigma_a$  is the total differential ionization cross section, a function depends on the atomic orbital and polarization of the incident light.  $\rho_a(z)$  is the density profile of the adsorbate illuminated by the X-ray photons (numbers of atoms/cm<sup>3</sup>).

We assume that the atomic density of the adsorbate is homogeneous with depth,  $\rho_a(z) = \rho_a$ . By integrating (Equation S 4-1), we obtain:

$$I_a = F \cdot \sigma_a \cdot \rho_a \cdot \phi_a \cdot (\lambda_a \cdot \cos \theta) (e^0 - e^{-\frac{t_a}{\lambda_a \cdot \cos \theta}}) = \quad (\text{Equation S 4-2})$$

$$= F \cdot \sigma_a \cdot \rho_a \cdot \phi_a \cdot \lambda_a \cdot \cos \theta \cdot (1 - e^{-\frac{t_a}{\lambda_a \cdot \cos \theta}})$$

In turn, the signal intensity for photoelectrons originating from core levels of atoms contained in the substrate S, whose emitted electrons have to travel first within the substrate (with  $\lambda_s$ ) and then through the overlayer (with  $\lambda_a$ ), denoted as  $I_s$ , has the form:

$$I_s = F \cdot \sigma_s \cdot \phi_s \cdot \left[ \int_0^\infty \rho_s(z) \cdot e^{-\frac{z}{\lambda_s \cdot \cos \theta}} dz \right] \cdot e^{-\frac{t_a}{\lambda_a \cdot \cos \theta}} \quad (\text{Equation S 4-3})$$

Integration of (Equation S 4-3) yields:

$$I_s = F \cdot \sigma_s \cdot \phi_s \cdot \rho_s \cdot \lambda_s \cdot \cos \theta \cdot e^{-\frac{t_a}{\lambda_a \cdot \cos \theta}} \quad (\text{Equation S 4-4})$$

The ratio between  $I_a$  and  $I_s$  is:

$$\frac{I_a}{I_s} = \frac{\sigma_a}{\sigma_s} \cdot \frac{\rho_a}{\rho_s} \cdot \frac{\phi_a}{\phi_s} \cdot \frac{\lambda_a}{\lambda_s} \cdot \frac{1 - e^{-\frac{t_a}{\lambda_a \cdot \cos \theta}}}{e^{-\frac{t_a}{\lambda_a \cdot \cos \theta}}}$$

$$= \frac{\sigma_a}{\sigma_s} \cdot \frac{\rho_a}{\rho_s} \cdot \frac{\phi_a}{\phi_s} \cdot \frac{\lambda_a}{\lambda_s} \cdot \left( e^{\frac{t_a}{\lambda_a \cdot \cos \theta}} - 1 \right) \quad (\text{Equation S 4-5})$$

Rearranging (Equation S 4-5 we obtain fitting ratio:

$$\frac{I_a}{I_s} \cdot \frac{\sigma_s}{\sigma_a} \cdot \frac{\rho_s}{\rho_a} \cdot \frac{\phi_s}{\phi_a} \cdot \frac{\lambda_s}{\lambda_a} + 1 = e^{\frac{t_a}{\lambda_a \cdot \cos \theta}} \quad (\text{Equation S 4-6})$$

where the left hand side of (Equation S 4-6 was used as fitting ratio shown in Figure S 4-9.

### 4.2.3 O K NEXAFS of K-feldspars at dry and humid condition

Figure S 4-5 shows the O K edge NEXAFS spectra of PM01\_nw, PM01\_w, AO02\_nw, AO02\_w under dry (0.1% RH, 323K, 0.5 mbar H<sub>2</sub>O) and humid conditions (255K, 0.5 mbar H<sub>2</sub>O). The dry spectra arises exclusively from the lattice oxygen of feldspar samples and gas phase water at 0.5 mbar, the later has a small contribution to the overall spectrum and also behaves as an attenuation medium. Upon adsorption of water molecules, the line shape modifies: the adsorbed water molecules contribute distinctive absorption feature, giving rise to a spectrum convoluted by contributions from lattice oxygen of crystal, gas phase and adsorbed water molecules. As a qualitative impression from the PM01\_nw (solid blue) and PM01\_w (dashed blue) at 50% RH, the earlier show a higher absorption feature at photon energy 540 eV, where the AO02\_nw (solid yellow) and AO02\_w (dashed yellow) at 50% RH are showing negligible differences. This implies some structural changes of water molecules upon adsorption on different sample surfaces.

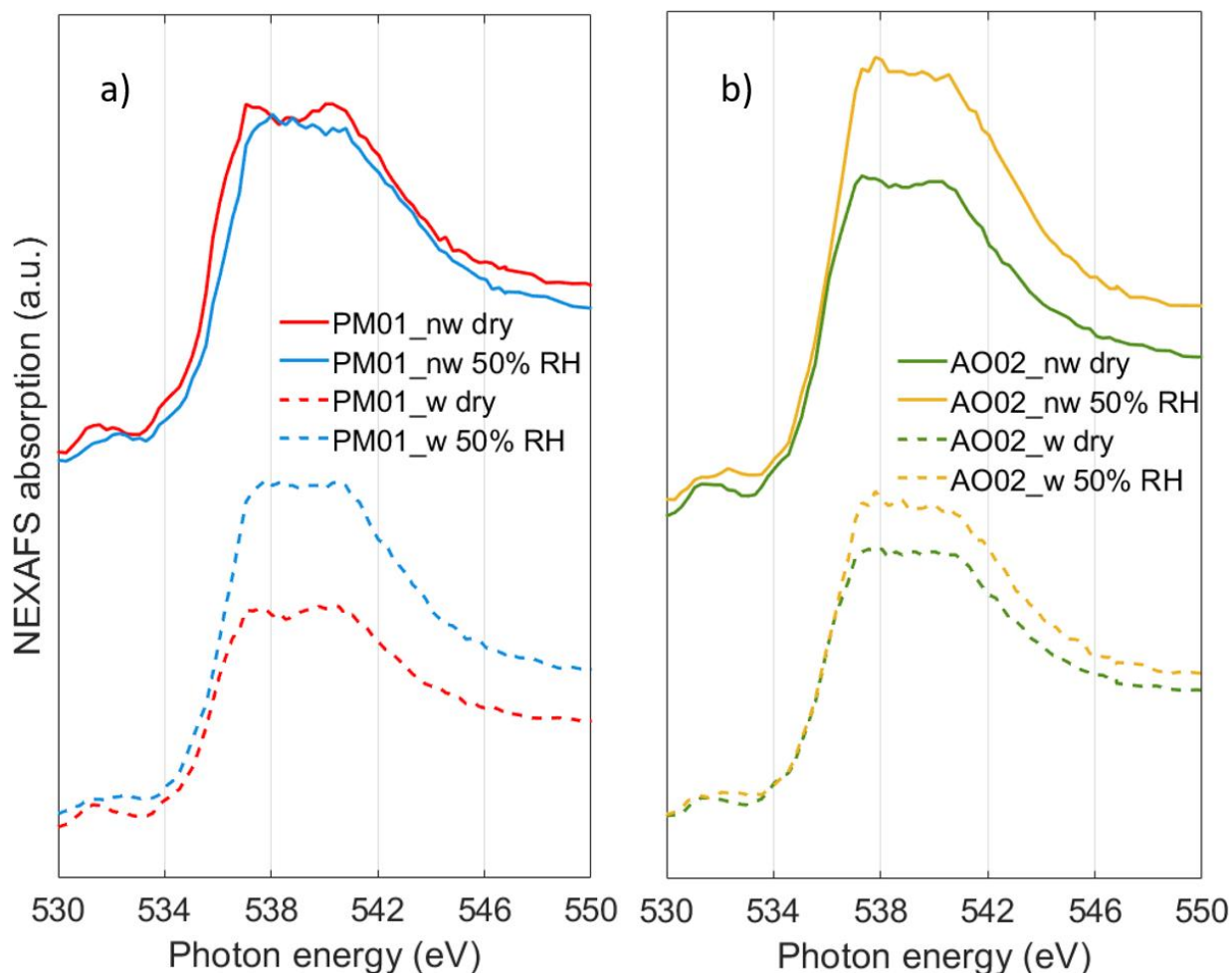


Figure S 4-5: O K edge NEXAFS of feldspar samples at dry (0.1% RH, 323K, 0.5 mbar H<sub>2</sub>O) and 50% RH (255K, 0.5 mbar H<sub>2</sub>O). Panel a): PM01\_nw and PM01\_w, panel b): AO02\_nw and AO02\_w

The attenuation of light through a medium is characterized by a Lambert-Beer behavior, which can be applied in our case. With the presence of adsorbed water monolayer(s), the signal of feldspar is attenuated exponentially by a factor of  $\alpha = e^{-\frac{t}{\lambda \cdot \cos \theta}}$ .

Where  $\lambda$  is the inelastic mean free path of Auger electrons (425 – 525 eV) in liquid water, estimated as 2.2 nm (Shinotsuka, Da et al. 2017);  $\theta$  is the angle between photoelectron and sample surface normal, which is 30° in our case;  $t$  is the thickness of the adsorbed water layer. By using the water layer thickness  $t$  as determined from XPS, we calculate  $\alpha$ . For  $t=1.4$  nm in PM01 case,  $\alpha = e^{-\frac{1.4}{2.2 \cdot \cos 30}} = 0.48$ . Similarly,  $\alpha$  equals to 0.57 for AO02 sample with  $t=1.1$  nm. The Lambert-Beer coefficient  $\alpha$  indicates the percentage of the contribution originating from dry sample substrate. Thus, if  $I_T$  is the sample spectra under humid condition and  $I_0$  is the sample spectra at dry condition, then the adsorbed water spectra  $I_{H_2O} = I_T - I_0 \cdot \alpha$ .

#### 4.2.4 Experiments on the K-feldspar powder sample

##### Preparation of the microcline powder sample materials

The microcline sample was the purchased potash feldspar from the Bureau of Analysed Sample Ltd (BCS-CRM No.376/1 SGT FELDSPAR 1). The original sample is a finely divided sand-like material passed through a nominal 250 micron aperture sieve. In order to obtain a finely divided powder-form sample that is suitable for our experiment, we further milled the sand-like sample with a ball-milling machine for 5 minutes and then sieved through a mesh with 64  $\mu\text{m}$  aperture. We label our microcline powder samples in a similar way as for the single crystal samples described in the main text: microcline\_nw denote the as-introduced sample, and microcline\_w denote the sample after water treatment for 24h.

The prepared powder sample was dispersed in an isopropanol solution and sonicated for 5 min to form a homogeneous suspension. By using an air cushion pipette, two droplets with volume 30  $\mu\text{L}$  of the suspension were drop casted onto the surface of the gold-coated sample holder. After some minutes, the isopropanol content of the droplet evaporate away, leaving a uniform layer of feldspar powder sample, which attached stably on the surface of the sample holder, as shown in Figure S 4-6.



Figure S 4-6. K-feldspar powder sample coated on the sample cryo-holder surface.

##### XPS and NEXAFS measurement on microcline powder sample

Figure S 4-8 shows the depth profile of K2p, O1s\_lattice and C1s normalized to Si2p. In panel a) we notice again an accumulation of K2p at humid conditions for both samples before (solid lines) and after water treatment (dashed lines). Meanwhile, the water treated sample show a generally lower potassium level than that of before treatment, which is in line with the leaching phenomenon for the crystalline sample described in the main text. Literature reported silicon leaching in water from a quartz surface (Kumar, Marcolli et al. 2019). We need to note a caveat here that  $\text{Si}^{4+}$  element leaching from the feldspar surface is also possible. If this were the case, the depth profile using Si 2p signal as reference would assume a larger uncertainty. This could explain the unexpected O1s\_lattice/Si2p depth profile ratio. The leaching of lattice oxygen is less likely. However, if the aluminum would have been removed during the water treatment

procedure, then the leaching of Si may happen more easily. This might explain the unexpected O1s<sub>lattice</sub>/Si2p and O1s<sub>ads</sub>/Si2p (Figure S 4-7) depth profile ratio. To confirm this hypothesis, future experiments should focus more on this aspect.

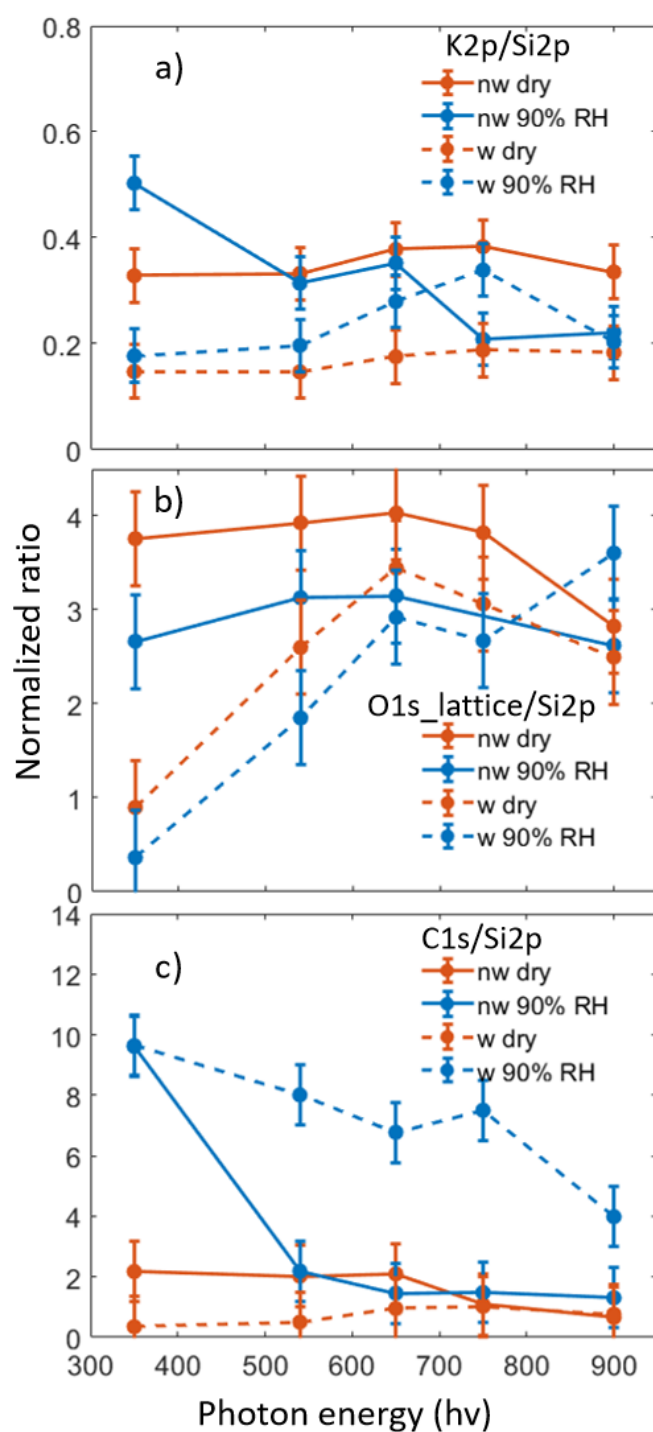


Figure S 4-8 The elemental ratio between potassium and silicon at a function of out-going kinetic energy. Notably, the K2p/Si2p ratio is very similar to the crystal sample case, as shown in main text.

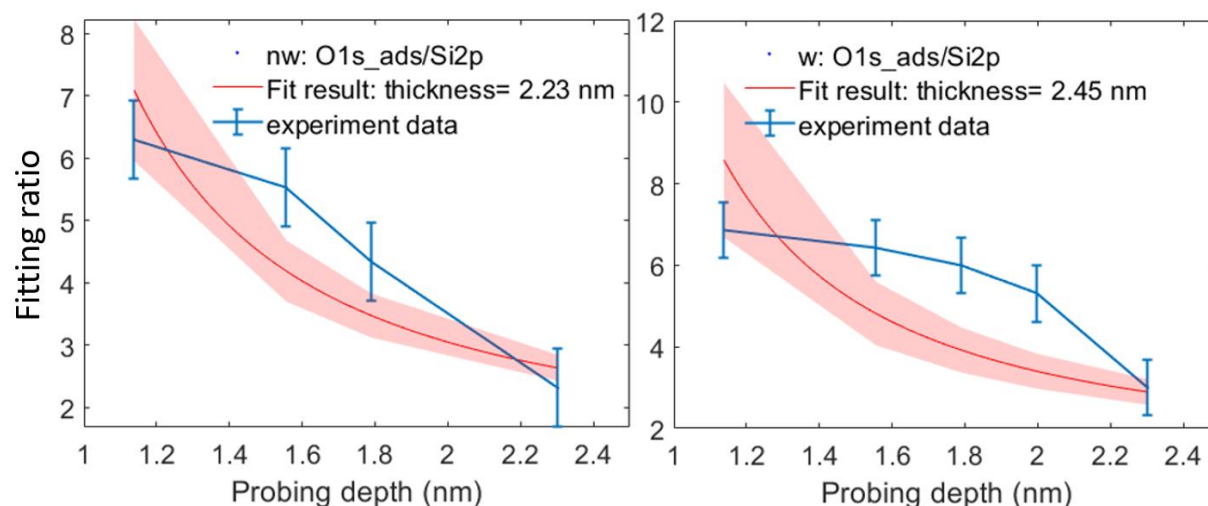


Figure S 4-9: Fitting ratio of the O1s<sub>ads</sub> to that of Si2p as a function of probing depth for microcline powder sample at 1 mbar (blue). Left: before water treatment, right: after water treatment. Blue lines represent normalized experiment fitting ratio. Red lines represent the fitting results with 95% of confidence bounds, shown by red shading area. The effective thickness obtained from the fit is labeled in the image legend.

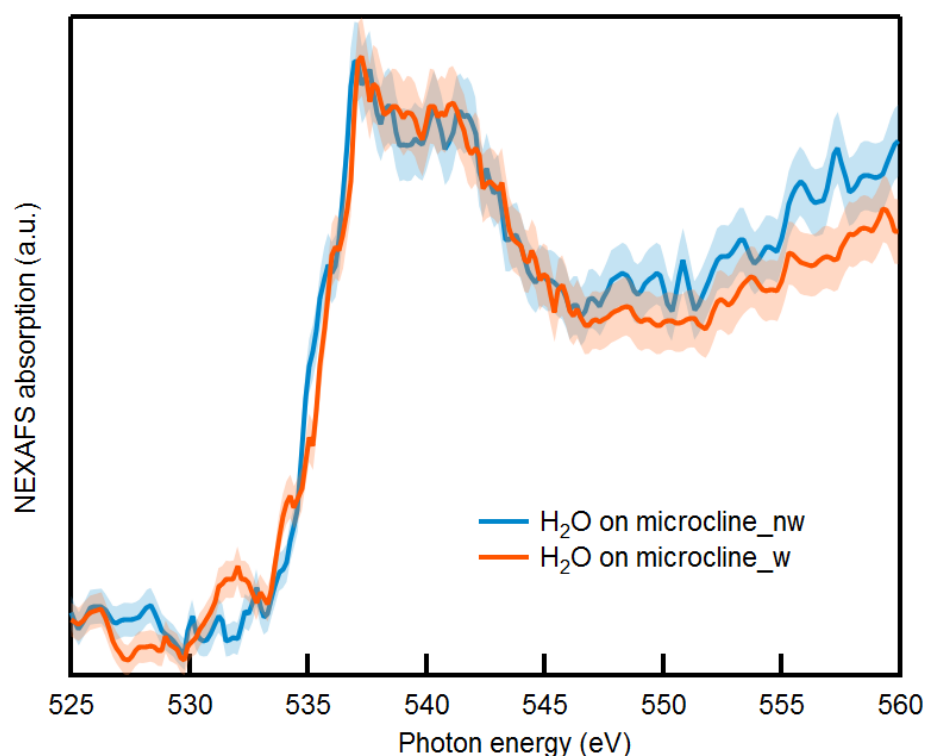


Figure S 4-10 Spectra of adsorbed water on microcline before (blue) and after (red) water treatment. All the spectra are normalized to its area.

Figure S 4-10 show the spectra of adsorbed water on microcline powder sample, calculated as the difference spectra described in the main text. For the thickness determined (shown in Figure S 4-9), the Lambert-Beer coefficient here used is 0.3 ( $\pm 0.03$ ).

## References

- Kumar, A., C. Marcolli and T. Peter (2019). "Ice nucleation activity of silicates and aluminosilicates in pure water and aqueous solutions – Part 2: Quartz and amorphous silica." *Atmos. Chem. Phys.* 19(9): 6035-6058.
- Landoulsi, J., M. J. Genet, S. Fleith, Y. Touré, I. Liascukiene, C. Méthivier and P. G. Rouxhet (2016). "Organic adlayer on inorganic materials: XPS analysis selectivity to cope with adventitious contamination." *Applied Surface Science* 383: 71-83.
- Mangolini, F., J. B. McClimon, F. Rose and R. W. Carpick (2014). "Accounting for Nanometer-Thick Adventitious Carbon Contamination in X-ray Absorption Spectra of Carbon-Based Materials." *Analytical Chemistry* 86(24): 12258-12265.
- Shinotsuka, H., B. Da, S. Tanuma, H. Yoshikawa, C. J. Powell and D. R. Penn (2017). "Calculations of electron inelastic mean free paths. XI. Data for liquid water for energies from 50 eV to 30 keV." *Surface and Interface Analysis* 49(4): 238-252.
- Stipp, S. L. and M. F. Hochella (1991). "Structure and bonding environments at the calcite surface as observed with X-ray photoelectron spectroscopy (XPS) and low energy electron diffraction (LEED)." *Geochimica et Cosmochimica Acta* 55(6): 1723-1736.
- Trotochaud, L., A. R. Head, S. Pletincx, O. Karşlıoğlu, Y. Yu, A. Waldner, L. Kyhl, T. Hauffman, H. Terry, B. Eichhorn and H. Bluhm (2018). "Water Adsorption and Dissociation on Polycrystalline Copper Oxides: Effects of Environmental Contamination and Experimental Protocol." *The Journal of Physical Chemistry B* 122(2): 1000-1008.
- Yang, H., A. Boucly, J. P. Gabathuler, T. Bartels-Rausch, L. Artiglia and M. Ammann (2021). "Ordered Hydrogen Bonding Structure of Water Molecules Adsorbed on Silver Iodide Particles under Subsaturated Conditions." *The Journal of Physical Chemistry C*.

## 5 WATER MOLECULES ORDERING AT THE LIQUID-VAPOR INTERFACE

This chapter is adopted from the manuscript under preparation, which will be published as Yang Huanyu, Ivan Gladich, Anthony Boucly, Luca Artiglia, and Markus Ammann: Resorcinol and Orcinol Lead to Local Ordering of Water Molecules near the Liquid-Vapor Interface. The theoretical calculations were provided by Dr. I. Gladich.

### 5.1 RESORCINOL AND ORCINOL LEAD TO LOCAL ORDERING OF WATER MOLECULES NEAR THE LIQUID-VAPOR INTERFACE

#### Abstract

Phenolic compounds of both anthropogenic or biogenic origin are present as pollutants in the atmosphere. Considering the hydrophilicity of OH groups of the phenolic molecules, we hypothesize that when present in a water droplet, these molecules will show a propensity towards the surface, and exhibit a specific orientation. X-ray photoelectron spectroscopy was used to probe the surface propensity and surface excess of organic molecules at the liquid surface. The surface propensity and preferential orientation was also supported by molecular dynamics simulations. Auger electron yield near-edge X-ray absorption fine structure (NEXAFS) spectroscopy was used to probe the hydrogen bonding (HB) structure, indicating that the local structure of water molecules near the surface of the resorcinol and orcinol covered solutions shows trends towards more tetrahedrally coordinated molecules than observed at the liquid-vapor interface of pure water. The order parameter obtained from the molecular dynamics simulations confirm these observations. This effect is being discussed in terms of the formation of an ordered structure of the phenolic molecules at the surface leading to patterns of hydrated OH groups in the water with distances among them that are relatively close to that in ice. These results suggest a way phenolic species in the atmosphere could have an impact on the nucleation of ice. We also attempted at looking at the impact of the presence of the phenolic species on the valence level spectra, as experimentally measured peak intensities for the excitation into the O1b1, 3a2 and 1b2 molecular orbital. The valence level spectra differ substantially between liquid water and ice. However, the results both from experiment and theoretically calculated density of states are indicating that differences between liquid water in presence and absence of resorcinol or orcinol are below detection limits.

#### 5.1.1 Introduction

Liquid-vapor interfaces are ubiquitous in the atmosphere, ranging from cloud water droplets, aqueous or sea spray aerosols, to terrestrial and oceanic water bodies, providing a huge space

for phase transfer processes, heterogeneous chemical reactions and nucleation of solid or other liquid phases. In particular, the nucleation of ice is of paramount importance in atmospheric chemistry and physics. Freezing of clouds is essential in the formation of precipitation, and ice clouds are covering large parts of the upper troposphere and thus affect the radiative balance of the Earth. Despite the considerable amount of studies about freezing reported so far, the nucleation of ice is still insufficiently understood. Based on theory and mostly non linear vibrational spectroscopy experiments, it has been suggested that the local structure of water near ice nucleation (IN) active substrates modifies toward the formation of tetrahedrally coordinated water clusters in the presence of active proteins and organic surfactants (Pummer, Budke et al. 2015, Pandey, Usui et al. 2016). Long chain alcohols play a role in the IN process, toward a favorable IN ability. Knopf et al. found that when water and aqueous NaCl droplets were coated by organic monolayers, their freezing temperature was ca. 25 K higher than that of uncoated droplets due to homogeneous IN (Knopf and Forrester 2011). Zobrist et al. also pointed out that long-chain alcohol molecules present at the water surface would aggregate, possibly leading to a structural match of the alcohol head-groups with the ice lattice and thus higher freezing temperature (Zobrist, Koop et al. 2007). Through a study with Fourier transform infrared spectroscopy, Ochshorn et al. found that an alcohol film increases the fraction of water molecules contained in ice-like clusters (Ochshorn and Cantrell 2006). Similar results were also reported by Perkins et al. (Perkins, Vazquez de Vasquez et al. 2020). Using vibrational sum frequency generation spectroscopy combined with MD simulations, Kusaka et al. reported that also phenol molecules at the liquid-vapor interface point their OH groups towards the bulk water, inducing a specific hydration structure in the interfacial water (Kusaka, Ishiyama et al. 2018). These studies provide a role for surface active solutes to promote IN, in contrast to the commonly known inhibition of freezing when water contains solutes. (Koop, Luo et al. 2000) Surface active organic compounds are ubiquitously present in the atmosphere, and phenolic compounds are considered as a pollutant. Furthermore, their role in reducing the surface tension of aqueous solutions has important implications for cloud droplet activation and thus climate (Donaldson and Vaida 2006, Prisle, Ottosson et al. 2012, Ovadnevaite, Zuend et al. 2017, Kong, Wolf et al. 2018). In this work we address the related impact of organic monolayers on the interfacial water structure. We elucidate the HB structure of water molecules at the liquid-vapor interface in presence of resorcinol (RES) and orcinol (ORC). RES (1,3-benzenediol) and ORC (3,5-Dihydroxytoluene) are simple proxies for a range of phenolic compounds as they are typically found in the atmosphere resulting from oxidation of aromatic compounds or from pyrolysis of biomass and thus result from natural and anthropogenic activities. When dissolved in water of a cloud droplet or in a deliquesced aerosol particle, due to the preferential hydration of the OH groups, these molecules exhibit significant propensity for the liquid-vapor interface (Donaldson and Vaida 2006, Lee, Orlando et al. 2016). This work will provide an insight into how the IN process may be influenced by phenolic compounds at a molecular level and link this to the local electronic structure of the neighbor water molecules.

Liquid jet X-ray photoelectron spectroscopy (XPS) is a powerful surface sensitive technique to probe the liquid-vapor interface within nm depths of the surface (Winter, Weber et al. 2004, Winter and Faubel 2006, Brown, Redondo et al. 2013, Lee, Brown et al. 2015, Lee, Orlando et al. 2016, Artiglia, Edebeli et al. 2017, Lee, Orlando et al. 2019). Because the photoemission intensity is proportional to the sample's atomic density, XPS can provide quantitative elemental ratios averaged over the probe depth, which can be related to surface composition. Moreover, element oxidation states and molecular orientation can be assessed (Prisle, Ottosson et al. 2012,

Brown, Beloqui Redondo et al. 2013, Lee, Orlando et al. 2016, Artiglia, Edebeli et al. 2017, Lee, Orlando et al. 2019). As the inelastic mean free path (IMFP, directly proportional to the probing depth) of photoelectrons depends on their kinetic energy, the tunable photon energy provided by a synchrotron light source offers the possibility of varying the probe depth (Krisch, D'Auria et al. 2007).

Photoelectron spectroscopy also allows to focus on the valence states of aqueous solutions, which reflect the HOMO structure of water molecules. Valence levels of water molecules are linked to their physical environment (e.g, the HB structure, or local orientation) and can be used to determine the effect of solute addition on the local structure of water (Winter, Weber et al. 2004). The difference of valence levels of water molecules between liquid water and ice in terms of the relative intensity change in the 1b1, 3a1 and 1b2 molecular orbitals (MO) have tentatively been associated with changes of HB among water molecules between the two phases (Peebles and White 1984, Reissner, Radke et al. 1998, Krischok, Höfft et al. 2001).

O K edge near edge X-ray absorption fine structure (NEXAFS) spectroscopy probes the absorption of electro-magnetic radiation by excitation of core electrons into unoccupied molecular orbitals via dipole induced transitions. The O K edge NEXAFS spectra are sensitive to the local HB network among the water molecules and thus sensitive to whether they are arranged in a tetrahedral coordination as in ice or in a more disordered configuration as in liquid water (Cavalleri, Ogasawara et al. 2002, Myneni, Luo et al. 2002, Wilson, Cavalleri et al. 2002, Smith, Cappa et al. 2004). When detected in electron yield mode, it provides this configurational information over just a few nanometer of depth beneath the surface due the short inelastic mean free path of the electrons detected.

This work combines experimental results with theoretical simulations to measure and characterize the surface properties of RES and ORC aqueous solutions. Spectroscopic results show the orientation of surfactants and local ordering of water molecules at the liquid-vapor interface. Molecular dynamics simulations and Density of States (DOS) calculations were performed to interpret the experimental findings, quantifying the solvation preference (i.e., bulk vs. surface) of ORC and RES and the tetrahedral ordering of interfacial liquid water induced by the two adsorbates.

### 5.1.2 Sample and experimental methods

#### XPS and NEXAFS.

Resorcinol (1,3-Dihydroxybenzene) was purchased from Sigma-Aldrich, and orcinol (3,5-Dihydroxytoluene) was purchased from VWR-international. Both were used without further purification. By using Millipore water (conductivity  $18.2 M\Omega$ ), followed by deaeration with an inert gas (Ar), we prepared 0.01 and 2M solutions of RES, 0.01 M and 0.2M solution of ORC. All the solutions always contained 0.05 M NaCl to limit the build-up of streaming potentials. To avoid possible photo degradation and oxidation, all sample solutions were prepared within 24 hours before the experiment, in absence of natural light.

The experiments were carried out at the Surface/Interface Microscopy (SIM) beamline at the Swiss Light Source (SLS, Paul Scherrer Institut) using the liquid jet XPS endstation, which is coupled with a hemispheric electron analyzer featuring a high pressure pre-lens (ScientaOmicron HiPP-2)(Brown, Redondo et al. 2013). The solution under investigation was admitted into the experimental chamber by a Peek capillary, connected to a quartz nozzle with an aperture ranging from 20 to 25  $\mu\text{m}$ , at a flow rate of 0.6 ml/min. Before entering the chamber, the capillary was surrounded by a cooling jacket to tune the liquid temperature. Inside the experimental chamber, after injection, the solution travels with a laminar flow for a few hundred microseconds, corresponding to a few millimeters in length, before it is hit by the photon beam. To avoid charging effects upon photoemission, the nozzle assembly was thoroughly grounded,

Dynamic wise, the HB exchange dynamics of water molecules is much faster than desorption, and the time for solute diffusion to build up a ML on the surface is on the order of  $\mu\text{s}$  for the lowest concentration used in this work, 0.01 M (Winter and Faubel 2006, Lee, Brown et al. 2015). The liquid jet continuously delivers fresh sample so that beam-induced effects are negligible. During the experiment, we made use of linearly polarized light at  $0^\circ$ . We measured C1s and O1s XPS intensity to quantify the elemental ratio of carbon and oxygen in our samples. For the XPS detection of C1s, we set the photon energy to 448, 560, 660, and 860 eV, and for detection of O1s, the photon energy was set to 695, 810, 910 and 1100 eV. Thus, the photoelectron kinetic energies resulting from the excitation of the corresponding core level electrons were ca. 155, 270, 370 and 570 eV, respectively. The kinetic energy of the photoelectron determines the mean escape depth (MED), which is expressed by means of the inelastic mean free path ( $\lambda$ ) of electrons travelling through the liquid matter. In our experimental configuration, the cylindrical surface of the liquid jet beam leads to an effective mean escape depth,  $MED = \frac{2}{\pi}\lambda$ .(Winter and Faubel 2006) Thus, the four kinetic energies correspond to four different MED values of 4.8, 6.8, 8.4, 11.5  $\text{\AA}$ , respectively. All XPS peaks were fitted by Gaussians after subtraction of a Shirley background. The peak areas were then normalized with respect to the photon flux, MED of photoelectrons and the total photoionization cross section.

Valence band spectra of 2 M RES, 0.2 M ORC, liquid water and ice were measured by using 600 eV of photon energy. Such spectra mainly consist of the contributions of the  $1b_1$ ,  $3a_1$  and  $1b_2$  MOs of water, with their binding energy lower than 20 eV, but also contain contributions by MOs of RES or ORC.

The O K edge NEXAFS spectra of water and liquid solutions were obtained by integrating the secondary electrons deriving from the oxygen Auger KLL peaks within the kinetic energy range of 412 -437 eV, at varying excitation photon energies ranging from 527 to 560 eV.

### MD Simulation.

Atomistic simulation based on classical and *first-principle* molecular dynamics (MD) were employed to clarify the solvation preference of orcinol (ORC) and resorcinol (RES), to quantify the tetrahedral ordering of interfacial liquid water molecules induced by the presence of the two adsorbates, and to determine the spectroscopic signature of the investigated solutions.

A liquid water slab of  $\sim 1.48 \times 1.48 \times 7.2 \text{ nm}^3$  and 216 water molecules with two vapor/liquid water interfaces was equilibrated at 1 bar pressure and 300 K using classical MD. Liquid water slab of similar (or identical) size has been successfully used in literature to study the interfacial and bulk solvation in slab systems (Kuo and Mundy 2004). Details on the preparation and equilibration procedure are reported in the Supporting Information (SI).

Starting from the equilibrated liquid water slab, three different aqueous solutions were prepared. In the first two, 4 ORC (or 4 RES) were placed on each of the two liquid water interfaces, resulting in a 2M concentration of ORC (or RES) solution. In the third configuration (0.2 M), one ORC was placed on one interface. These three systems were selected to model the experimental conditions (i.e., 2M orcinol and 0.2 M resorcinol), while offering a molecular picture of the dynamic of the two compounds at the same (2M) concentration. Figure S 5-1 show a snapshot from the 2M ORC MD simulation.

Force field parameters for ORC and RES were created according to GAFF2 practice (Jämbeck and Lyubartsev 2014). Water molecules were described using two different water models: TIP3P (Jorgensen, Chandrasekhar et al. 1983), which is the reference model for GAFF2 force field, and TIP4P/2005 (Abascal and Vega 2005), which is one of the most commonly used water models for ice and supercooled liquid water (Vega and Abascal 2011). Since TIP3P is the reference model for GAFF2 parametrization strategy, simulations employing the GAFF2/TIP3P combination reliably describe the surface vs. bulk preference of RES and ORC. At the best of our knowledge, there are no force field for small organics available in literature to work with TIP4P/2005. However, TIP4P/2005 is superior in describing the water phase diagram and the HB network in the ice phase and supercool region (Vega and Abascal 2011). A detailed analysis of TIP4P/2005 liquid water and ice structures is available in literature (Gladich and Roeselová 2012). Therefore, simulations with TIP4P/2005 were only used to quantify the tetrahedral ordering of interfacial liquid water molecules and the spectroscopic signature of the system in the presence of the two adsorbates. For each of the three solutions (i.e., 0.2 M ORC, 2.0 M ORC, and 2.0 M RES) and for each of the two water models, we run six independent constant volume and temperature (NVT) classical MD runs of 400 ns at 300 K. In SI and Figure S 5-2 we compared the predictions for the solvation preference for ORC and RES using TIP3P and TIP4P/2005: simulations with TIP4P/2005 reported a more marked hydrophobicity for ORC and RES than simulations with TIP3P. Nevertheless, while quantitative differences are present, the conclusions drawn about the surface and bulk propensity of ORC and RES are identical between the two water models, showing ORC more surface enhanced than RES.

An additional 400 ns MD simulation of an ice slab of 320 TIP4P/2005 water molecules was performed with two equilibrated basal ice interfaces exposed to the vapor phase (see Figure S 5-17). The  $I_h$  ice slab was equilibrated at  $T=237\text{K}$ , which corresponds to  $-14 \text{ C}$  below the melting temperature ( $T_m=251\text{K}$ ) of TIP4P/2005 (García Fernández, Abascal et al. 2006). An order parameter,  $q_i$ , was adopted to quantify the tetrahedral arrangement of each water molecule respect to the other (Chau and Hardwick 1998, Errington and Debenedetti 2001, Gladich and Roeselová 2012).

$$q_i = \left[ 1 - \frac{3}{8} \sum_{j=1}^3 \sum_{k=j+1}^4 \left( \cos(\theta_{i,j,k}) + \frac{1}{3} \right)^2 \right] \quad \text{Equation 5-1}$$

where the sums run over the four nearest oxygen atoms of the oxygen belonging to the water molecule  $i$ . The angle  $\theta$  is the angle between oxygens  $i$ ,  $j$ , and  $k$ , with the oxygen  $i$  as the angle vertex. In the interior of an perfect ice crystal,  $q_i=1$  since the four nearest neighbors are tetrahedrally arranged around the  $i^{\text{th}}$  oxygen. In real ice, deviations from the perfect tetrahedral order occur due to thermal motion and defects in crystal structure, giving rise to a relatively narrow distribution of values with a maximum close to  $q_i = 1$ . In the liquid water phase,  $q_i$  values significantly smaller than 1 are expected since the tetrahedral arrangement of water molecules is distorted in the liquid phase. Following the strategy of Conde et al. (Conde, Vega et al. 2008), Gladich and Roeselova (Gladich and Roeselová 2012) identified a threshold value of  $q_t=0.9054$  for TIP4P/2004 which discriminates between “ice-like” or “liquid-like” water molecules: for  $q_i > q_t$  the  $i$ -water molecule belongs to the ice phase, while for  $q_i < q_t$  it belongs to the liquid. Probability distributions for the  $q$ -order parameters were performed for all the simulation system described above, and also for one extra simulation box at  $\sim 0.2M$  ORC (i.e., 5400 TIP4P water and 24 ORC) to support our results with a larger simulation box case.

The electronic density of states (DOS)s for the different aqueous solutions and ice systems were computed at *first-principles* level employing calculations at SCAN (Chen, Ko et al. 2017) density functional theory (DFT). TZV2P basis set with a cutoff of 600 Ry was employed for the valence electrons while core electrons were model using pseudopotential optimized for SCAN. SCAN is a recently introduced DFT method, designed especially for water electronic structure and dynamic simulations (Chen, Ko et al. 2017). DOS were average over  $\sim 150$  snapshots extracted every 2 ns from the last part of the classical MD trajectories adopting TIP4P/2005 water model. A gaussian smearing of 0.5 eV was used to smooth the DOS. DOSs for bulk ice (i.e, with no interfaces) and for an ice slab with two vapour/ice interfaces (Figure S 5-3), were calculated at the temperature  $T=T_m-14$  C, where  $T_m=251$ K is the melting temperature of TIP4P/2005. As benchmark test, Figure S 5-4 shows the DOS for a pure (i.e., with no solutes) TIP4P/2005 bulk water and liquid water slab at 300 K, calculated by averaging the snapshots from the classical MD trajectories: the agreement with the bulk water DOS calculated over frames from a SCAN *first-principles* MD and reported in the original SCAN reference (Chen, Ko et al. 2017) is quite remarkable, with the only slight overestimation of  $1b_2$  peak for the DOS from classical MD frames compared to that from SCAN MD simulation. This further states the ability of TIP4P/2005 in describing the HB network in water and the possibility to have reliable configurations for DOS calculations at the convenient computational price of classical MD.

The calculated DOS were compared with the experimental X-ray photoemission spectra of the valence levels: similar strategies have been already successfully explored in literature to compare computational DOS with XPS data from liquid water or soft matter systems (Theodorakopoulos, Csizmadia et al. 1977, Ping, Li et al. 2012, Giesbers, Marcelis et al. 2013,

Gaiduk, Govoni et al. 2016, Pham, Govoni et al. 2017). CP2K molecular dynamics package(Hutter, Iannuzzi et al. 2014) was used to perform the DOS calculations.

Further details about the preparation and equilibration of the liquid water and ice slab, the force field strategy, and computational settings are reported in the SI.

### 5.1.3 Results and discussion

- a. Surface orientation and surface propensity of RES and ORC in aqueous solutions

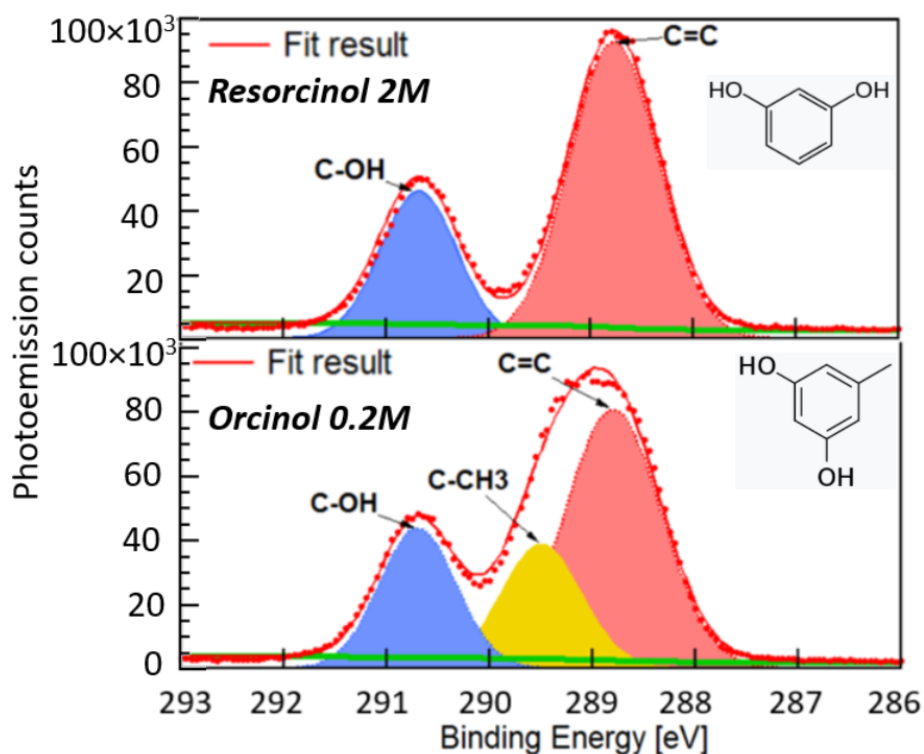


Figure 5-1 C1s photoemission signal of 2 M RES (top panel) and 0.2 M ORC (bottom panel) solution. Probed with excitation photon energy 448eV, the resulting photoelectrons have a kinetic energy of ca. 155eV. The green line represents the Shirley background. Hydroxy group carbon, aromatic carbon and aliphatic carbon (only for orcinol) contributions are assigned by blue, red and yellow shaded Gaussian peaks, respectively.

Figure 5-1 shows the photoemission signal of C1s of RES 2M and ORC 0.2 M solutions, probed with an excitation photon energy of 448 eV, which corresponds to a photoelectron kinetic energy of 155 eV. Hydroxyl-bonded (alcoholic) carbon (solid blue, 290.7 eV), aromatic carbon (solid red, 288.5 eV) and aliphatic carbon (solid yellow, 289.2 eV), with consistent full width at half maximum (FWHM), were used to properly deconvolute the spectra. The O 1s spectra of these two samples at same MED are reported in the SI.

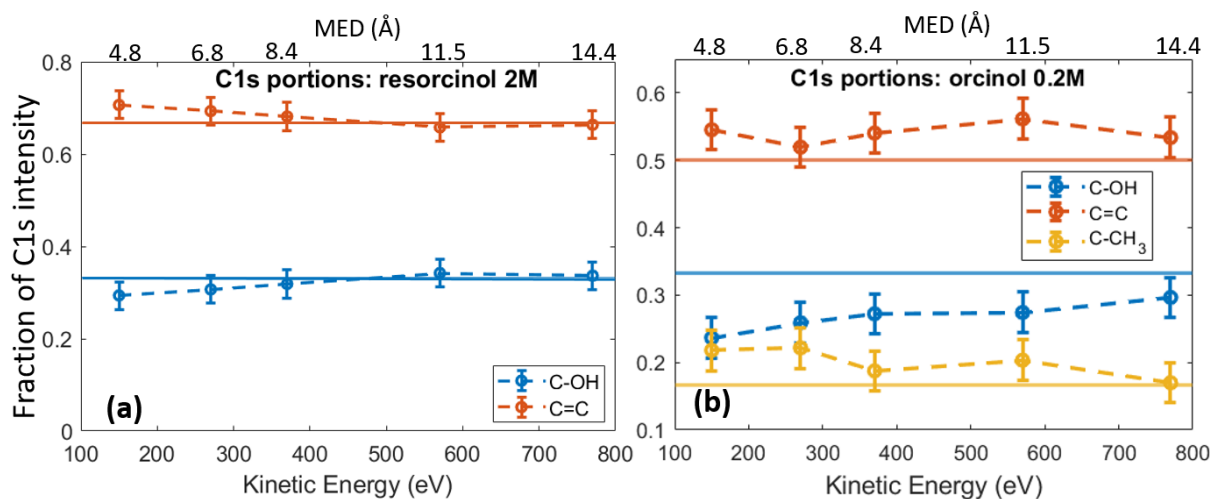


Figure 5-2. a) The fractional contribution of aromatic carbon ( $\text{-C=C}$ , red) and carboxylic carbon ( $\text{=C-OH}$ , blue) components to the C 1s photoemission intensity in 2M RES solution. The blue and red thin lines indicates the theoretical ratio of the carboxylic carbon (33.3%) and aromatic carbon (66.7%) b) Fractional contribution of carbon in 0.2M ORC case, with additional aliphatic carbon contribution ( $\text{C-CH}_3$ , yellow).

The fractional contribution of each C 1s component, derived from the spectra at different kinetic energies, is shown in Figure 5-2a and 2b. Each kinetic energy corresponds to a specific MED, thus Figure 5-2 gives information about the contributions of specific carbon atoms within 14.4 Å of solution. In the case of 2M RES (Figure 5-2a), the contribution of the C-OH carbons to the total C 1s intensity is lower than expected based on the molecular structure (1/3) when measured at low kinetic energies. Conversely, the C=C contribution is higher than expected (2/3) in the same kinetic energy range. This implies a preferred orientation of resorcinol molecules residing at the surface: the aromatic rings have an upward orientation with respect to the solution-air interface, due to the preferential interaction of OH groups with water. The slightly enhanced photoemission signal intensity contribution comes from the fact that photoelectrons from the C=C carbons, which are located on the vacuum side of the interface, are less attenuated than those from the C-OH carbons. The C 1s spectrum of ORC solution contains three components (Figure 5-2b): C=C, C-OH and C-CH<sub>3</sub>, with carbon number ratio 3:6, 2:6 and 1:6 correspondingly. We observe similar surface orientation as in the case of RES, with the C-CH<sub>3</sub> carbons being less attenuated than C-OH carbons, which implies that the OH groups point towards the solution, pushing the C-CH<sub>3</sub> towards the vacuum side of the interface.

The aim of Figure 5-2 is to display the orientation of organic molecules at the surface. Results at MED ( $\approx 1$  nm) suggest that RES and ORC molecules show no specific orientation in the bulk solution. Increasing the information depth, i.e. probing more toward the bulk of the solutions, the effect mitigates due to averaging over larger bulk volume. The fractions of alcoholic, aromatic and aliphatic carbon display a better agreement with their theoretical ratio, especially in the case of resorcinol (blue and red line Figure 5-2a).

In the following we investigated the surface excess and effective coverage thickness. Such values are determined with an attenuation model shown in the SI. Figure 5-3 shows the fitting results of C/O ratios calculated on RES and ORC diluted and concentrated solutions. The

vertical axis displays the fitting value  $D$ , which is accounted for all the known factors (e.g., inelastic mean free path of the photoelectron, bulk element atomic densities, photon flux, total photoionization cross section and geometry of the experimental setup for C/O ratio normalization) and is proportional to the C/O ratio (see SI).

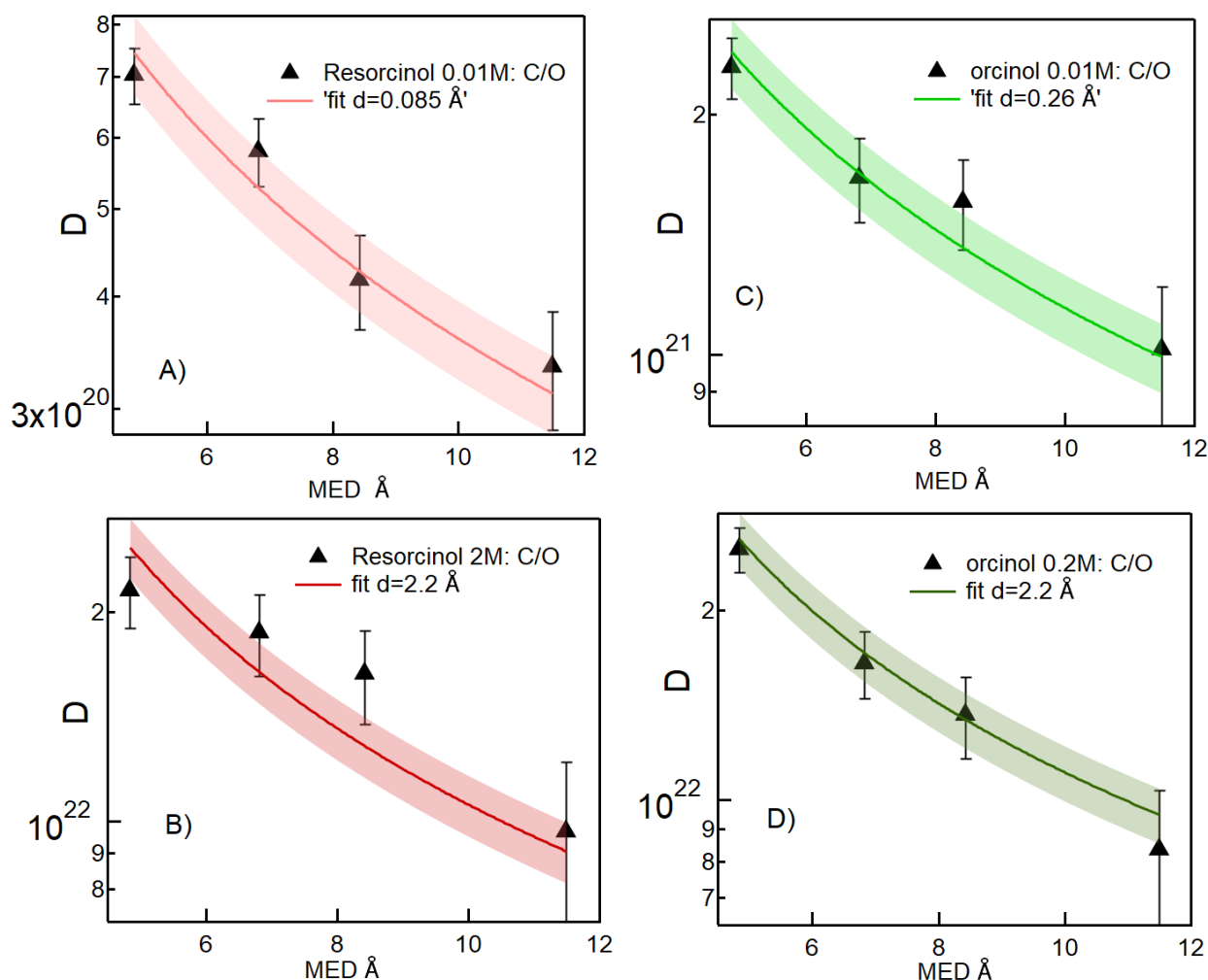


Figure 5-3. Evolution of  $D$  as a function of probing depth for aqueous solution of 0.01M RES A), 2M RES B), 0.01M ORC C) and 0.2M ORC D). Red and Green lines represent the fitting result for resorcinol and orcinol, with one standard deviation shown by the shaded area. The effective thickness  $d$  obtained from the fit is attached in the image legend.

The results of C/O depth profiles demonstrate that the investigated solutions exhibit apparent surface propensity, which is linked to solute's surface excess. Through the C/O ratio,  $\Gamma$  (the surface excess, see section 2) can be estimated by calculating the product of surface layer thickness ( $d$ ) and the molecule number density on the surface ( $n_s$ : number of molecules/ $cm^3$ ):

$$\Gamma = d \cdot n_s \quad \text{Equation 5-2}$$

The geometric dimension of an aromatic ring is about 2.4 Å. In case of resorcinol and orcinol 0.01 M solutions, the obtained surface layer thickness  $d$  are 0.085Å and 0.26 Å respectively. These average numbers imply that at such concentrations organic molecules do not display a complete surface monolayer coverage. Our analysis does not consider whether they randomly

float on the surface or aggregate into islands. The effective thickness only reflects the amount of carbon thought to be evenly distributed over the surface.  $\Gamma$  for diluted solutions are low ( $5.8 \times 10^{12} (\pm 8.7 \times 10^{11} \text{ v}) \text{ cm}^{-2}$  and  $1.6 \times 10^{13} (\pm 2.4 \times 10^{12}) \text{ cm}^{-2}$  for RES and ORC 0.01M, respectively). As the concentration of the solutions increases to 2 M and 0.2 M for resorcinol and orcinol, respectively, the surface layer thickness  $d$  increases to  $2.2 \text{ \AA}$ , which matches almost perfectly the geometric dimension of these organic molecules, suggesting the accumulation of one layer of at the surface.  $\Gamma$  of 2 M resorcinol and 0.2 M orcinol are  $1.5 \times 10^{14} (\pm 2.3 \times 10^{13}) \text{ cm}^{-2}$  and  $1.4 \times 10^{14} (\pm 2.1 \times 10^{13}) \text{ cm}^{-2}$  respectively. For detailed fitting of C/O depth profile and value of  $\Gamma$  and  $n_s$ , see SI.

To summarize, within  $2.2 \text{ \AA}$  thickness and  $1 \text{ cm}^2$  area, the calculated values of  $\Gamma$  and  $d$  of concentrated solutions suggest an abundance (number of molecules) of solute molecules in the interfacial region of about  $10^{14}$ , with an upward orientation of the aromatic rings toward the liquid-vapor interface due to preferential hydration of OH groups.

The experimental picture for the surface orientation and bulk vs. surface solvation preference can be rationalized by looking at the density profile of ORC and RES from the classical MD simulations in Figure 5-4. The density profile for ORC (orange) and RES (violet) states that, indeed, the two molecules have different bulk and surface propensity: in Figure 5-4-d the RES profile samples more the bulk region than 0.2M or 2M ORC (Figure 5-4b and c, respectively). From the density profiles in Figure 5-4, it is possible to calculate the solute surface excess at the Gibbs Dividing Surface,  $\Gamma$ , and the bulk concentrations,  $c_b$ . (Vrbka, Mucha et al. 2004) (Herrera, Fan et al. 2011). In order to compare solutions at different concentrations, we have adopted here an adimensional solute surface excess,  $\Gamma^*$  and an adimensional bulk concentration,  $c_b^*$ , (see definition in SI).  $\Gamma^*$  is 0.64, 0.78 and 0.44 for 0.2 M ORC, 2M ORC, and 2M RES aqueous solution. On the contrary,  $c_b^*$  is 0.17, 0.10 and 0.26 for 0.2 M ORC, 2M ORC, and 2M RES aqueous solution.  $\Gamma^*$  and  $c_b^*$  state that ORC is more surface enriched than RES, while RES is more present in the solution bulk, even though it still displays a marked hydrophobic character, as shown in the profiles of Figure 5-4. The difference between the surface propensity of ORC and RES can be rationalized by the presence of the methyl group in ORC, which further pushes the molecule toward the vapor side of the interface: a similar behavior has been observed also for methylamine at the liquid water surface, with the methyl group sticking out from the interface (Hoehn, Carignano et al. 2016). The hydrophobicity of the aromatic groups forces ORC and RES to be preferentially solvated at the interface, while the hydroxyl -OH groups are pointing toward the condensed water phase: this feature is present in Figure 5-4, always showing the density profiles for the hydroxyl oxygens (in red) closer to the water interface than the aromatic ring and the methyl group ones; the methyl groups are oriented toward the vapor phase. Finally, it is interesting to note the formation of  $\pi$ -stacking of the aromatic rings, as shown in a representative snapshot in Figure 5-4: similar behavior with  $\pi$ - or slightly parallel displaced stacking has been reported in combined experimental and simulation works in literature for benzene, naphthalene and methyl-naphthalene on the surface of ice and liquid water (Heger, Nachtigallová et al. 2011) (Kania, Malongwe et al. 2014) (Gladich, Habartová et al. 2014). As mentioned above, the self-aggregation of RES or ORC into islands via such  $\pi$ -stacking cannot be assessed by the XPS signals.

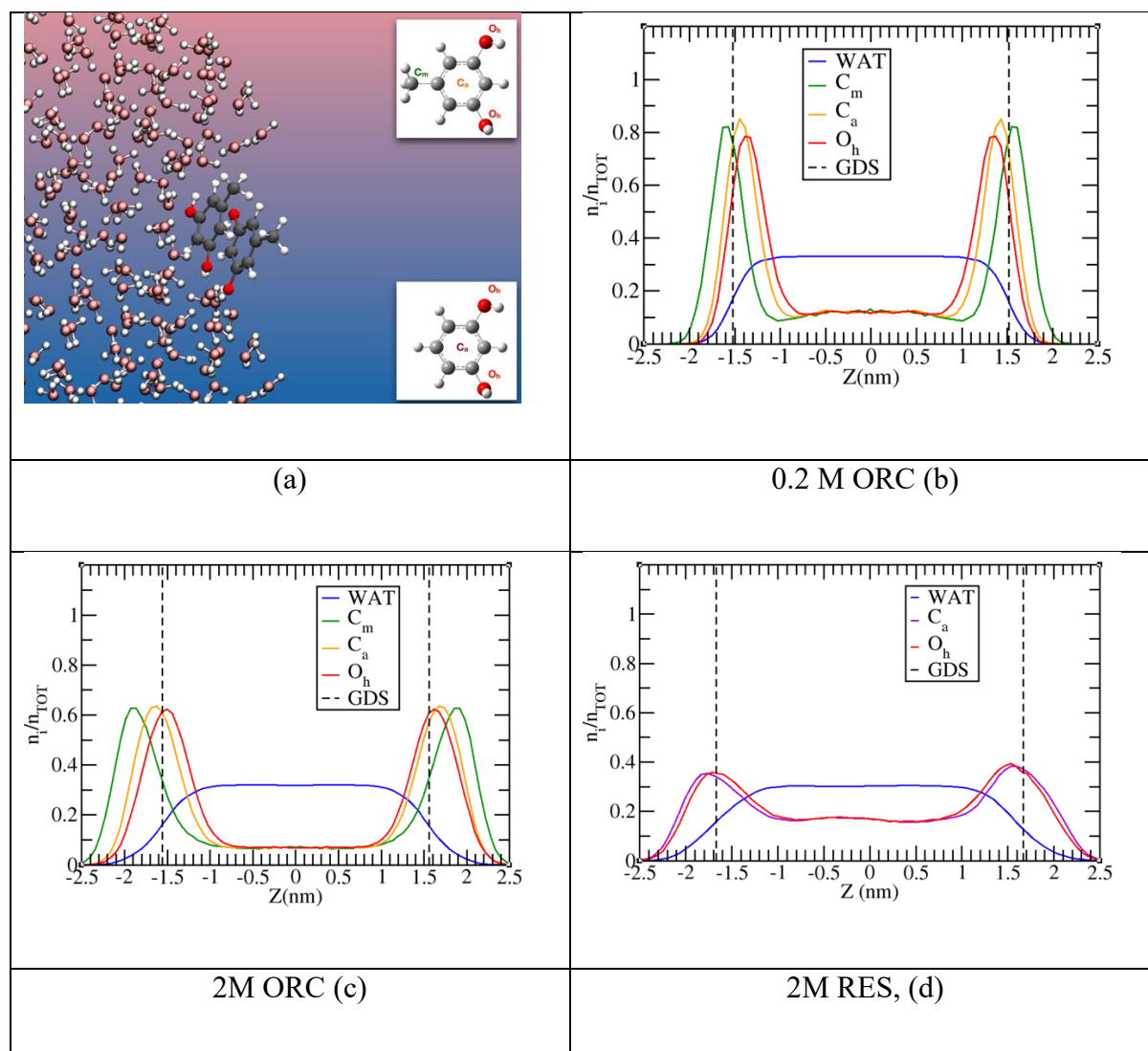


Figure 5-4. Panel (a): snapshot from 2M ORC molecular dynamics trajectory two ORC interacting at the interface. In the insets resorcinol and orcinol molecules with atom nomenclature: Cm (green) is the carbon of the methyl group, Ca (orange and violet for ORC and RES, respectively) the center of the aromatic rings, and Oh the oxygen of the hydroxyl groups. Panels (b), (c) and (d) shows the probability distribution profile,  $n_i/n_{TOT}$ , normalized to the unity as a function of the  $z$ -coordinate perpendicular to the vapor/liquid water interface, obtained collecting the  $z$ -position of each species over MD trajectory in TIP3P water.

Figure 5-5 provides a more detailed analysis of ORC and RES interfacial self-stacking, reporting the probability distribution for the minimal intermolecular distances among the hydroxyl oxygens of RES (or ORC). Figure 5-5 shows a bimodal distribution with two peaks, one at  $\sim 0.3$  nm and a second one at  $\sim 0.4 - 0.5$  nm. These two peaks are associated to  $\pi$ - or slightly parallel displaced stacking, as shown in representative snapshots for the distribution peaks reported in the insets of Figure 5-5. Interestingly, by increasing the solution

concentration, the peaks become sharper and the 0.3 nm one also more intense, as shown by comparing 0.2 M and 2.0 M ORC curves. Note that the distance between the OH groups on the basal plane of ice is also 0.3 nm. Moreover, at the same 2.0 M concentration, the peaks for the RES solution are much broader than those of ORC (red and green straight lines, respectively): RES samples more the subsurface and bulk region of the solution than ORC, avoiding the interfacial self-stacking. Finally, it is worth mentioning that our classical MD reports a preference for slightly parallel displaced stacking rather than perfect  $\pi$ -stacking of the benzene rings: the difficulty to perfectly model  $\pi$ - $\pi$  interactions among aromatic rings is well-known in classical MD simulation based on point charges (Gladich, Habartová et al. 2014) (Vácha, Jungwirth et al. 2006).

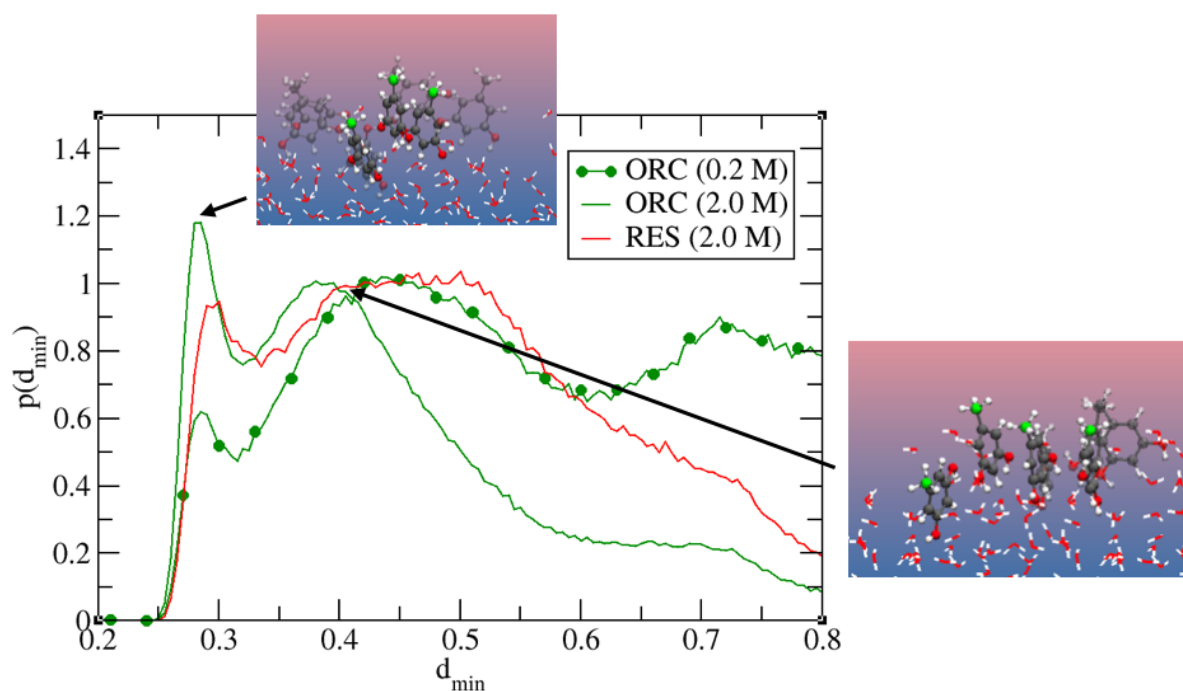


Figure 5-5. Probability distribution for the minimal intermolecular distances among the hydroxyl oxygens of RES (or ORC) in solution. In the insets, two representative snapshots corresponding to the peaks of the 2.0 M ORC solution. Highlighted in green the carbon atoms of the methyl groups. For visualization purposes, the distributions were normalized to have the intensity of the peak at  $\sim 0.4$  nm equal to the unity. The 0.2 M ORC (green and dotted) curve was calculated over a 400 ns MD using a larger water box ( $\sim 5400$  TIP4P/2005 water and 24 ORC).

b. Hydrogen bonding structure from O K edge NEXAFS

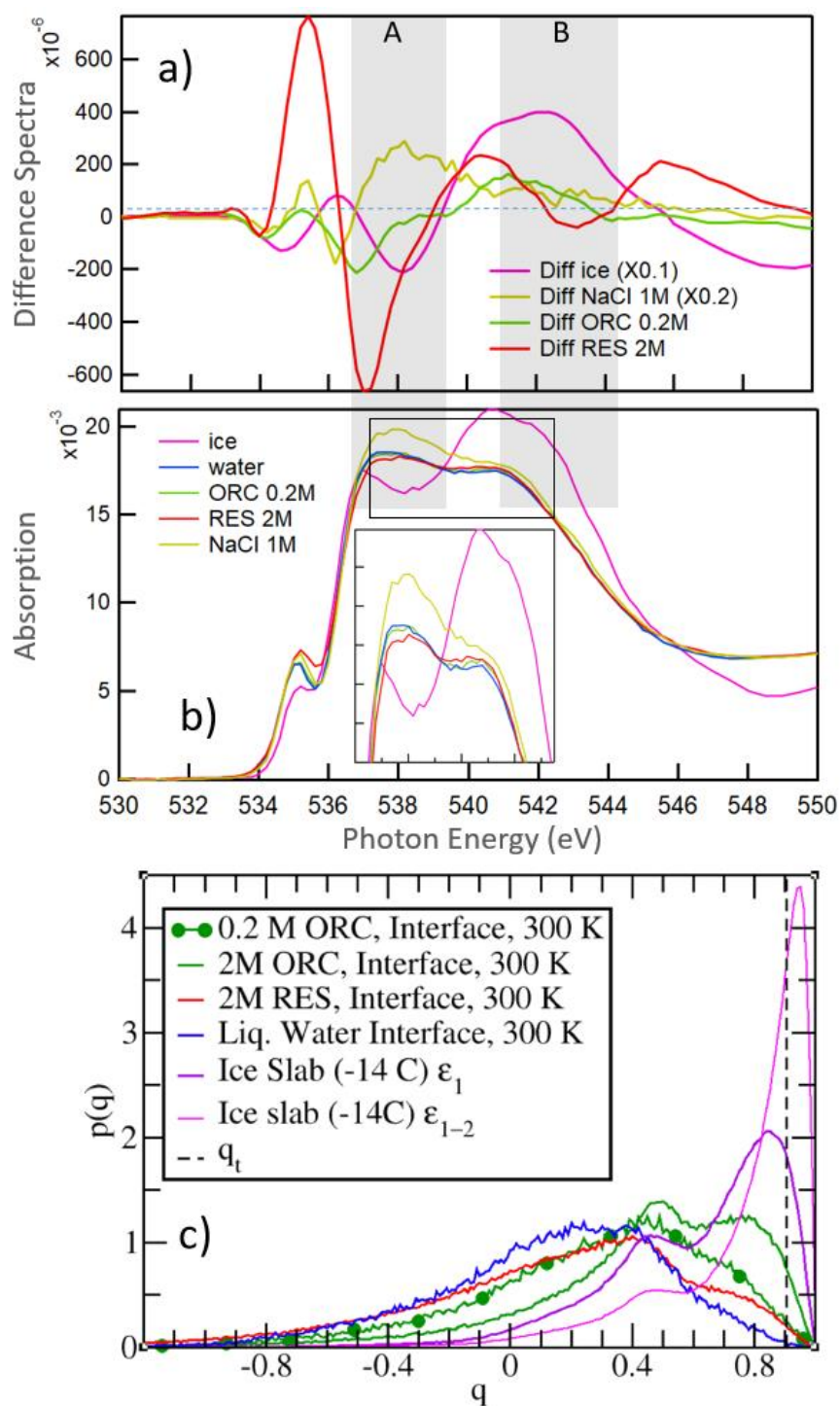


Figure 5-6. Panel b) shows the O K edge NEXAFS of liquid water (blue), ice (magenta), RES 2M (red), ORC 0.2M (green) and NaCl 1M (yellow) solution. Panel a) shows the difference spectra, obtained by subtracting the liquid water spectrum from spectrum of ice (magenta), RES 2M (red), ORC 0.2M (green) and NaCl 1M (yellow). Panel c) Probability density distribution of the tetrahedral order parameter  $q$  (Equation 5-1), for different aqueous solutions.  $q_t = 0.9054$  discriminates between “ice-like” ( $q > q_t$ ) and “liquid-like” water molecules ( $q < q_t$ ), see Ref. (Gladich and Roeselová 2012). The interfacial region for the liquid water slab at 300 K was defined in the density profile of Figure S 5-5. The  $\epsilon_1$  or  $\epsilon_1 + \epsilon_2$  bilayers defined the

interfacial ice region (Figure S 5-6 and Ref. (Gladich, Oswald et al. 2015)) The 0.2 M ORC (green and dotted) curve was calculated over an 400 ns MD using a larger water box (~5400 TIP4P/2005 water and 24 ORC).

Figure 5-6b shows the O K edge NEXAFS spectra of liquid water (blue), 1 M NaCl (yellow) and ice (black), compared with those of RES 2.0 M (red) and ORC 0.2 M (green). We distinguish two main absorption regions, marked by the shaded areas A and B: In liquid water, the strong intramolecular covalent O-H bonds and asymmetric weak HB configuration prevail, leading to an enhanced absorption at 537 eV (shaded region A). This absorption feature is even more pronounced in NaCl 1M solution, as Cl anions distort the electronic structure of water molecules, leading to a direct perturbation of the unoccupied near neighbor water orbitals (Cappa, Smith et al. 2005). The corresponding difference spectrum (Figure 5-6a, yellow) for 1.0 NaCl shows positive values in region A implying that, upon addition of NaCl, water molecules are more disordered (in terms of HB) near the surface. The absorption feature at 535 eV can be assigned to free OH groups, which is more prevalent in liquid water (also at the water-vapor interface) than in ice (Wernet, Nordlund et al. 2004, Nilsson, Nordlund et al. 2010). In contrast, in ice (magenta, measured at the ISS beamline with the solid-gas interface chamber: SGI), the predominant strong and highly symmetric tetrahedral HB configuration leads to a prominent absorption at around 541-542 eV (shaded region B), whereas the absorption in region A is quenched due to the shortage of asymmetric HB. The difference spectrum between ice and water NEXAFS shows a negative value in region A and positive in region B (Figure 5-6a, black), consistent with the formation of a more ordered HB structure. The contrasting HB configuration embodied by NEXAFS spectra of liquid water and ice serves as a reference to qualitatively interpret the local HB structure of water on the surface of RES 2.0 M (red, Figure 5-6b) and ORC 0.2 M (green, Figure 5-6b) solutions. Compared to liquid water, the resorcinol and orcinol O K NEXAFS indicate a trend towards lower intensity in region A and higher intensity in region B (Figure 5-6b). NEXAFS results suggest that HB of water molecules on the surface of these organic solutions is slightly more ordered than that in liquid water. The specific orientation and aggregation of these surface active organic molecules is possibly the origin of the ordered HB configuration. The preferential hydration of OH groups, the upward orientation of the aromatic rings as well as the OH – OH – group distances being similar to that in ice due to pi-stacking of RES or ORC molecules at the solution-air interface may affect the local arrangement of water molecules in contact with organics.

Also in this case, MD simulations have been used to cross-check and better interpret experimental data. A molecular picture for the local arrangement of interfacial water molecules in contact with ORC and RES can be obtained from the classical MD simulations using the tetrahedral parameter defined in section 2 (Equation 5-1). Figure 5-6c reports the order parameter probability distributions for interfacial water molecules, where the interfacial region is defined for  $z$  larger than the Gibbs Dividing Surface. Following (Gladich, Oswald et al. 2015) the interfacial region of the ice slab was determined by the interfacial  $\epsilon_1$  or  $\epsilon_1 + \epsilon_2$  bilayers, outlined in Figure S 5-7. Looking at the pure liquid water slab (blue curve in Figure 5-6c) and as already observed in the literature (Gladich, Pfalzgraff et al. 2011) (Gladich, Oswald et al.

2015), the heterogeneity of the interfacial environment disrupts the tetrahedral arrangement of water molecules: this is why the  $p(q)$  peaks are at considerable smaller  $q$ -values than those of the ice interface case (violet and magenta lines in Figure 5-6c), in which the tetrahedral ordering is stronger and, thus,  $q$ -values are closer to the unity. Interestingly, RES and ORC induce a local ordering of water in the interfacial region, as shown by the shoulders of  $p(q)$  at values closer to  $q_t$ , which is the threshold discriminating between liquid-like and ice-like water molecules. Moreover, interfacial water molecules are more ordered in the ORC solution than in the RES one, even at low concentration (0.2 M): this is ascribed to the fact that RES samples more the bulk and subsurface region than ORC (see Figure 5-4), thus perturbing the ordering of water molecules at the interface. In addition, ORC tends to self-stacking at the interface, likely forcing liquid water ordering by interaction among the ORC hydroxyl groups and water, as shown in Figure 5-5.

### c. Hydrogen bonding structure from valence band spectra

Inspired by the work of Winter et al. (Winter, Weber et al. 2004), we performed valence band measurements of the solutions investigated in this work with the aim of finding a correlation between water molecular orbitals intensity and local HB order.

Figure 5-7 shows valence level spectra of RES 2.0 M and ORC 0.2 M, together with those of liquid water (blue, measured with the same setup as this work) and solid ice (black, measured at the ISS beamline with the solid-gas interface chamber: SGI). The reference spectrum of liquid water displays the  $1b_1$ ,  $3a_1$  and  $1b_2$  molecular orbitals (MOs), which are marked in the plot.

The top panel of Figure 5-7a displays the difference spectra between ice and organic solutions and liquid water, used as a reference. The photoelectron kinetic energy range of the spectra in Figure 5-7a corresponds to a mean escape depth of c.a. 1.3 nm, or 4 ML-equivalent of water. From the depth profile characterization in section 3.1, we note that organic molecules form a ML that accumulates at the interface of concentrated RES and ORC solutions, with a thickness of about 2.2 Å (Figure 5-3). Therefore, valence level spectra reported in Figure 5-7a consist of both water molecules in close contact with organic molecules and in the bulk, the latter being less influenced by the presence of organic molecules. In spite of this, it is still possible to observe changing features due to the addition of organics.

The HB structural difference can also be assessed by measuring the valence states, which are expected to respond to the orientational order, likely in terms of different cross sections for  $3a_1$  and  $1b_1$  molecular (Winter, Weber et al. 2004). As a consequence, the  $3a_1$  orbital intensity in ice is usually lower than in liquid water. With the spectra being normalized to their  $1b_1$  peak, as shown in Figure 5-7a bottom panel, we clearly observe that the  $3a_1$  absorption feature in ice (black) is lower than that of liquid water (blue), consistent with literature reports (Peebles and White 1984, Reissner, Radke et al. 1998, Krischok, Höfft et al. 2001). Also the  $1b_2$  orbitals is strongly connected to the HB (Winter, Weber et al. 2004), thus a change in the HB structure between liquid water and ice should lead to a decrease of  $1b_2$  MO intensity as well. Such an

effect is present comparing the spectra in Figure 5-7a, however it is less pronounced than in the case of  $3a_1$ .

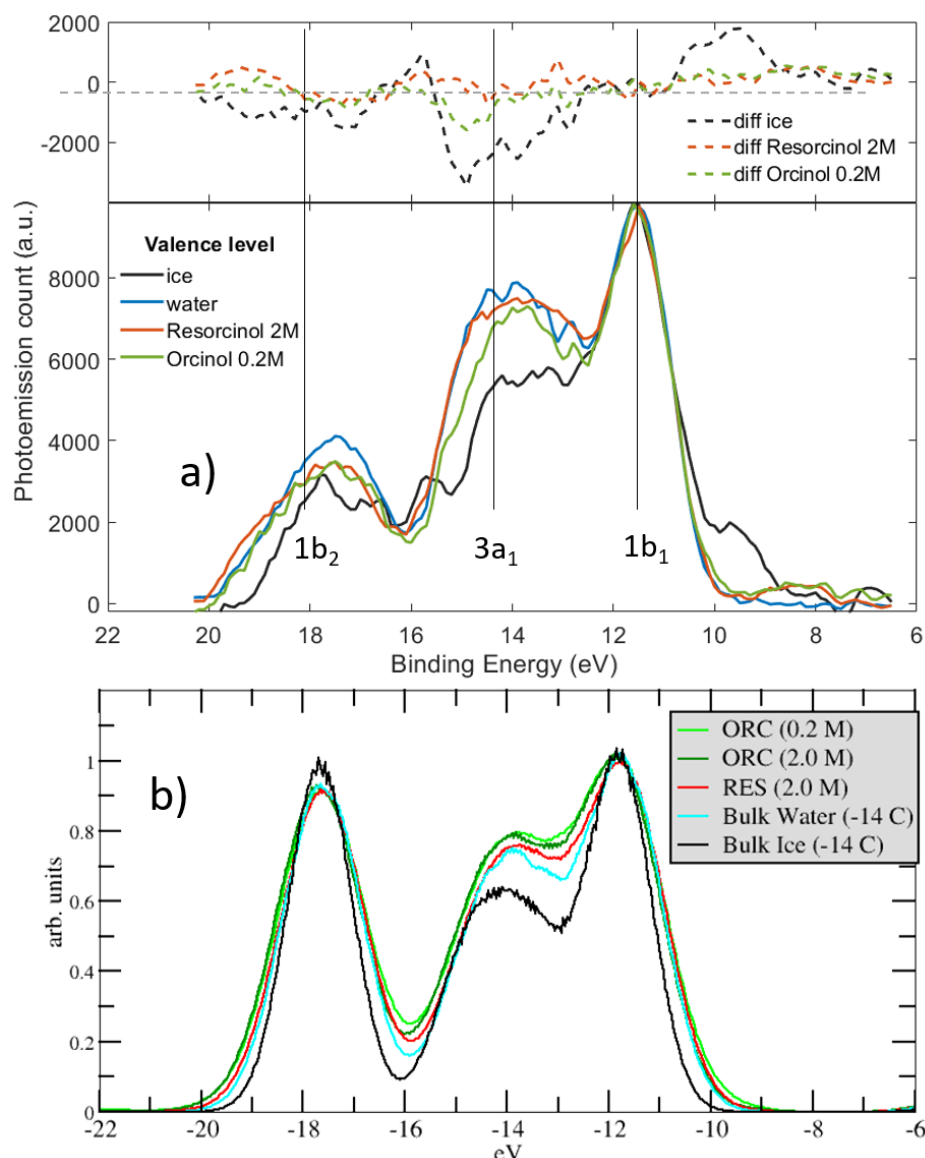


Figure 5-7: Panel a) Bottom: X-ray photoemission spectra of valence level for water (blue), ice (black), RES 2M (red) and ORC 0.2M, with excitation photon energy 600 eV. The peaks labeled by  $1b_1$ ,  $3a_1$  and  $1b_2$  correspond to the three water molecules valence level. All spectra are Shirley background removed and normalized with respect to their  $1b_1$  peak height. Binding energy was fixed with respect to the  $1b_1$  binding energy of liquid water. The gas-phase contribution to the photoemission signal from the liquid-vapor interface was removed from each spectrum (raw data shown in SI). The top panel shows the difference spectra, obtained by subtracting the water valence spectrum. Panel b) DOS of liquid water molecules presenting in ORC, RES, bulk ice and bulk water. Data are aligned and normalized consistently with the experimental spectra. The spectra for the ORC and RES solutions shown only the water contribution, i.e., the solute DOSs were removed from the DOS of the entire system.

The organic solutions of resorcinol (Figure 5-7, red) and orcinol (Figure 5-7, green) seem to exhibit a slightly decreased absorption feature in  $3a_1$  and  $1b_2$  MOs with respect to liquid water (Figure 5-7, blue), which would be consistent with a trend of a somewhat higher fraction of tetrahedrally coordinated water in the vicinity of RES and ORC as observed in the electron yield NEXAFS spectra. However, the differences are too small to be statistically significant. Also the theoretically calculated density of states indicate that the spectra are very similar to each other, though the calculated ones also do not display the large and indeed significant difference between liquid water and ice observed experimentally. The discrepancy between our valence level spectra and DOS calculation may be for two reasons. Firstly, the information depth are different. The resulting kinetic energy of photoelectrons is near 600 eV, corresponding to a MED of ca. 1.1 nm. At this depth, bulk water molecules already give a considerable contribution to the measured spectra. Secondly, to have a more proper comparison from DOS calculation side, it would be beneficial to evaluate the DOS at different depth individually and considering the exponential decay inside the medium. Further development on the experimental and theoretical side is necessary to explore this.

#### 5.1.4 Conclusions

By using *in situ* XPS, we have experimentally investigated the preferential orientation of RES and ORC molecules at the liquid-vapor interface. This was in line with our parallel classical MD trajectory over the organic solutions at the interface, that further suggest self-aggregation via  $\pi$ -stacking surface specific configuration. The thickness of the established organic solution layer was determined through an attenuation model, by which the surface excess of these organic molecules could be determined.

In addition, the O-K edge NEXAFS spectra of these organic aqueous solutions reveal the structural nature of water molecules at the liquid-vapor interface. These experimental results are in line with our calculation of the tetrahedral order parameter  $q$ , delivered by MD simulations, and suggest that the presence of resorcinol and orcinol molecules locally induce a more tetrahedral coordination among water molecules. Further, as electronic polarization of the organic molecules around the water molecules is indicated by the HOMO structure, we measured the valence level spectra and performed the calculation of its density of states. The differences of the measured and calculated spectra might not be statistically significant, but they also indicate a trend for water coordination at the surface in a more tetrahedral fashion. Considering the presence of phenolic compound in the atmosphere from both anthropogenic and biogenic origins, our findings are of potential importance for heterogeneous ice nucleation in the atmosphere.

### **Acknowledgement**

The experiment work in this publication was performed at the ISS beamline of the Swiss Light Source, Paul Scherrer Institute, supported by the Swiss National Science Foundation (grant no. 169176).

For High Performance Computational resources and services, we acknowledge the Research Computing group in Texas A&M University at Qatar, founded by the Qatar Foundation for Education, Science and Community Development, and the use of Qatar Environment and Energy Research Institute (QEERI) HPC under Project ID HPC-P21002.

## References

- Abascal, J. L. F. and C. Vega (2005). "A general purpose model for the condensed phases of water: TIP4P/2005." *Journal of Chemical Physics* 123(23).
- Artiglia, L., J. Edebeli, F. Orlando, S. Chen, M.-T. Lee, P. Corral Arroyo, A. Gilgen, T. Bartels-Rausch, A. Kleibert, M. Vazdar, M. Andres Carignano, J. S. Francisco, P. B. Shepson, I. Gladich and M. Ammann (2017). "A surface-stabilized ozonide triggers bromide oxidation at the aqueous solution-vapour interface." *Nature Communications* 8(1): 700.
- Brown, M. A., A. Beloqui Redondo, M. Sterrer, B. Winter, G. Pacchioni, Z. Abbas and J. A. van Bokhoven (2013). "Measure of Surface Potential at the Aqueous–Oxide Nanoparticle Interface by XPS from a Liquid Microjet." *Nano Letters* 13(11): 5403-5407.
- Brown, M. A., A. B. Redondo, I. Jordan, N. Duyckaerts, M.-T. Lee, M. Ammann, F. Nolting, A. Kleibert, T. Huthwelker, J.-P. Mächler, M. Birrer, J. Honegger, R. Wetter, H. J. Wörner and J. A. v. Bokhoven (2013). "A new endstation at the Swiss Light Source for ultraviolet photoelectron spectroscopy, X-ray photoelectron spectroscopy, and X-ray absorption spectroscopy measurements of liquid solutions." *Review of Scientific Instruments* 84(7): 073904.
- Cappa, C. D., J. D. Smith, K. R. Wilson, B. M. Messer, M. K. Gilles, R. C. Cohen and R. J. Saykally (2005). "Effects of Alkali Metal Halide Salts on the Hydrogen Bond Network of Liquid Water." *The Journal of Physical Chemistry B* 109(15): 7046-7052.
- Cavalleri, M., H. Ogasawara, L. G. M. Pettersson and A. Nilsson (2002). "The interpretation of X-ray absorption spectra of water and ice." *Chemical Physics Letters* 364(3): 363-370.
- Chau, P. L. and A. J. Hardwick (1998). "A new order parameter for tetrahedral configurations." *Molecular Physics* 93(3): 511-518.
- Chen, M., H.-Y. Ko, R. C. Remsing, M. F. Calegari Andrade, B. Santra, Z. Sun, A. Selloni, R. Car, M. L. Klein, J. P. Perdew and X. Wu (2017). "Ab initio theory and modeling of water." *Proceedings of the National Academy of Sciences* 114(41): 10846.
- Conde, M. M., C. Vega and A. Patrykiewicz (2008). "The thickness of a liquid layer on the free surface of ice as obtained from computer simulation." *The Journal of Chemical Physics* 129(1): 014702.
- Donaldson, D. J. and V. Vaida (2006). "The Influence of Organic Films at the Air–Aqueous Boundary on Atmospheric Processes." *Chemical Reviews* 106(4): 1445-1461.
- Errington, J. R. and P. G. Debenedetti (2001). "Relationship between structural order and the anomalies of liquid water." *Nature* 409(6818): 318-321.
- Gaiduk, A. P., M. Govoni, R. Seidel, J. H. Skone, B. Winter and G. Galli (2016). "Photoelectron Spectra of Aqueous Solutions from First Principles." *Journal of the American Chemical Society* 138(22): 6912-6915.
- García Fernández, R., J. L. F. Abascal and C. Vega (2006). "The melting point of ice Ih for common water models calculated from direct coexistence of the solid-liquid interface." *The Journal of Chemical Physics* 124(14): 144506.
- Giesbers, M., A. T. M. Marcelis and H. Zuilhof (2013). "Simulation of XPS C1s Spectra of Organic Monolayers by Quantum Chemical Methods." *Langmuir* 29(15): 4782-4788.
- Gladich, I., A. Habartová and M. Roeselová (2014). "Adsorption, Mobility, and Self-Association of Naphthalene and 1-Methylnaphthalene at the Water–Vapor Interface." *The Journal of Physical Chemistry A* 118(6): 1052-1066.
- Gladich, I., A. Oswald, N. Bowens, S. Naatz, P. Rowe, M. Roeselova and S. Neshyba (2015). "Mechanism of anisotropic surface self-diffusivity at the prismatic ice–vapor interface." *Physical Chemistry Chemical Physics* 17(35): 22947-22958.
- Gladich, I., W. Pfalzgraff, O. Maršálek, P. Jungwirth, M. Roeselová and S. Neshyba (2011). "Arrhenius analysis of anisotropic surface self-diffusion on the prismatic facet of ice." *Physical Chemistry Chemical Physics* 13(44): 19960-19969.
- Gladich, I. and M. Roeselová (2012). "Comparison of selected polarizable and nonpolarizable water models in molecular dynamics simulations of ice Ih." *Physical Chemistry Chemical Physics* 14(32): 11371-11385.
- Heger, D., D. Nachtigallová, F. Surman, J. Krausko, B. Magyarová, M. Brumovský, M. Rubeš, I. Gladich and P. Klán (2011). "Self-Organization of 1-Methylnaphthalene on the Surface of Artificial Snow Grains: A Combined Experimental–Computational Approach." *The Journal of Physical Chemistry A* 115(41): 11412-11422.
- Herrera, L., C. Fan, D. D. Do and D. Nicholson (2011). "A revisit to the Gibbs dividing surfaces and helium adsorption." *Adsorption* 17(6): 955-965.
- Hoehn, R. D., M. A. Carignano, S. Kais, C. Zhu, J. Zhong, X. C. Zeng, J. S. Francisco and I. Gladich (2016). "Hydrogen bonding and orientation effects on the accommodation of methylamine at the air-water interface." *The Journal of Chemical Physics* 144(21): 214701.
- Hutter, J., M. Iannuzzi, F. Schiffmann and J. VandeVondele (2014). "cp2k: atomistic simulations of condensed matter systems." *WIREs Computational Molecular Science* 4(1): 15-25.

- Jämbeck, J. P. M. and A. P. Lyubartsev (2014). "Update to the General Amber Force Field for Small Solutes with an Emphasis on Free Energies of Hydration." *The Journal of Physical Chemistry B* 118(14): 3793-3804.
- Jorgensen, W. L., J. Chandrasekhar, J. D. Madura, R. W. Impey and M. L. Klein (1983). "Comparison of simple potential functions for simulating liquid water." *The Journal of Chemical Physics* 79(2): 926-935.
- Kania, R., J. K. E. Malongwe, D. Nachtigallová, J. Krausko, I. Gladich, M. Roeselová, D. Heger and P. Klán (2014). "Spectroscopic Properties of Benzene at the Air–Ice Interface: A Combined Experimental–Computational Approach." *The Journal of Physical Chemistry A* 118(35): 7535-7547.
- Knopf, D. A. and S. M. Forrester (2011). "Freezing of Water and Aqueous NaCl Droplets Coated by Organic Monolayers as a Function of Surfactant Properties and Water Activity." *The Journal of Physical Chemistry A* 115(22): 5579-5591.
- Kong, X., M. J. Wolf, M. Roesch, E. S. Thomson, T. Bartels-Rausch, P. A. Alpert, M. Ammann, N. L. Prisle and D. J. Cziczo (2018). "A continuous flow diffusion chamber study of sea salt particles acting as cloud nuclei: deliquescence and ice nucleation." *Tellus B: Chemical and Physical Meteorology* 70(1): 1-11.
- Koop, T., B. Luo, A. Tsias and T. Peter (2000). "Water activity as the determinant for homogeneous ice nucleation in aqueous solutions." *Nature* 406(6796): 611-614.
- Krisch, M. J., R. D'Auria, M. A. Brown, D. J. Tobias, C. Hemminger, M. Ammann, D. E. Starr and H. Bluhm (2007). "The Effect of an Organic Surfactant on the Liquid–Vapor Interface of an Electrolyte Solution." *The Journal of Physical Chemistry C* 111(36): 13497-13509.
- Krischok, S., O. Höfft, J. Günster, J. Stultz, D. W. Goodman and V. Kempter (2001). "H<sub>2</sub>O interaction with bare and Li-precovered TiO<sub>2</sub>: studies with electron spectroscopies (MIES and UPS(HeI and II))." *Surface Science* 495(1): 8-18.
- Kuo, I. F. W. and C. J. Mundy (2004). "An ab Initio Molecular Dynamics Study of the Aqueous Liquid-Vapor Interface." *Science* 303(5658): 658.
- Kusaka, R., T. Ishiyama, S. Nihonyanagi, A. Morita and T. Tahara (2018). "Structure at the air/water interface in the presence of phenol: a study using heterodyne-detected vibrational sum frequency generation and molecular dynamics simulation." *Physical Chemistry Chemical Physics* 20(5): 3002-3009.
- Lee, M.-T., M. A. Brown, S. Kato, A. Kleibert, A. Türlér and M. Ammann (2015). "Competition between Organics and Bromide at the Aqueous Solution–Air Interface as Seen from Ozone Uptake Kinetics and X-ray Photoelectron Spectroscopy." *The Journal of Physical Chemistry A* 119(19): 4600-4608.
- Lee, M.-T., F. Orlando, L. Artiglia, S. Chen and M. Ammann (2016). "Chemical Composition and Properties of the Liquid–Vapor Interface of Aqueous C1 to C4 Monofunctional Acid and Alcohol Solutions." *The Journal of Physical Chemistry A* 120(49): 9749-9758.
- Lee, M.-T., F. Orlando, M. Khabiri, M. Roeselová, M. A. Brown and M. Ammann (2019). "The opposing effect of butanol and butyric acid on the abundance of bromide and iodide at the aqueous solution–air interface." *Physical Chemistry Chemical Physics* 21(16): 8418-8427.
- Myneni, S., Y. Luo, L. Å. Näslund, M. Cavalleri, L. Ojamäe, H. Ogasawara, A. Pelmenschikov, W. Ph, P. Väterlein, C. Heske, Z. Hussain, L. G. M. Pettersson and A. Nilsson (2002). "Spectroscopic probing of local hydrogen-bonding structures in liquid water." *Journal of Physics: Condensed Matter* 14(8): L213.
- Nilsson, A., D. Nordlund, I. Waluyo, N. Huang, H. Ogasawara, S. Kaya, U. Bergmann, L. Å. Näslund, H. Öström, P. Wernet, K. J. Andersson, T. Schiros and L. G. M. Pettersson (2010). "X-ray absorption spectroscopy and X-ray Raman scattering of water and ice; an experimental view." *Journal of Electron Spectroscopy and Related Phenomena* 177(2): 99-129.
- Ochshorn, E. and W. Cantrell (2006). "Towards understanding ice nucleation by long chain alcohols." *The Journal of chemical physics* 124(5): 054714.
- Ovadnevaite, J., A. Zuend, A. Laaksonen, K. J. Sanchez, G. Roberts, D. Ceburnis, S. Decesari, M. Rinaldi, N. Hodas, M. C. Facchini, J. H. Seinfeld and C. O' Dowd (2017). "Surface tension prevails over solute effect in organic-influenced cloud droplet activation." *Nature* 546(7660): 637-641.
- Pandey, R., K. Usui, R. A. Livingstone, S. A. Fischer, J. Pfaendtner, E. H. G. Backus, Y. Nagata, J. Fröhlich-Nowoisky, L. Schmäser, S. Mauri, J. F. Scheel, D. A. Knopf, U. Pöschl, M. Bonn and T. Weidner (2016). "Ice-nucleating bacteria control the order and dynamics of interfacial water." *Science Advances* 2(4).
- Peebles, D. E. and J. M. White (1984). "Adsorption of D<sub>2</sub>O on Ni(100) at 100 K and the influence of the coadsorbates O(a), CO(a) and D(a)." *Surface Science* 144(2): 512-540.
- Perkins, R. J., M. G. Vazquez de Vasquez, E. E. Beasley, T. C. J. Hill, E. A. Stone, H. C. Allen and P. J. DeMott (2020). "Relating Structure and Ice Nucleation of Mixed Surfactant Systems Relevant to Sea Spray Aerosol." *The Journal of Physical Chemistry A* 124(42): 8806-8821.
- Pham, T. A., M. Govoni, R. Seidel, S. E. Bradforth, E. Schwegler and G. Galli (2017). "Electronic structure of aqueous solutions: Bridging the gap between theory and experiments." *Science Advances* 3(6): e1603210.
- Ping, Y., Y. Li, F. Gygi and G. Galli (2012). "Tungsten Oxide Clathrates for Water Oxidation: A First Principles Study." *Chemistry of Materials* 24(21): 4252-4260.

- Prisle, N. L., N. Ottosson, G. Öhrwall, J. Söderström, M. Dal Maso and O. Björneholm (2012). "Surface/bulk partitioning and acid/base speciation of aqueous decanoate: direct observations and atmospheric implications." *Atmos. Chem. Phys.* 12(24): 12227-12242.
- Pummer, B. G., C. Budke, S. Augustin-Bauditz, D. Niedermeier, L. Felgitsch, C. J. Kampf, R. G. Huber, K. R. Liedl, T. Loerting, T. Moschen, M. Schauerperl, M. Tollinger, C. E. Morris, H. Wex, H. Grothe, U. Pöschl, T. Koop and J. Fröhlich-Nowoisky (2015). "Ice nucleation by water-soluble macromolecules." *Atmos. Chem. Phys.* 15(8): 4077-4091.
- Reissner, R., U. Radke, M. Schulze and E. Umbach (1998). "Water coadsorbed with oxygen and potassium on thin NiO(100) films." *Surface Science* 402-404: 71-75.
- Smith, J. D., C. D. Cappa, K. R. Wilson, B. M. Messer, R. C. Cohen and R. J. Saykally (2004). "Energetics of Hydrogen Bond Network Rearrangements in Liquid Water." *Science* 306(5697): 851-853.
- Theodorakopoulos, G., I. G. Csizmadia, M. A. Robb, á. Kucsman and I. Kapovits (1977). "Experimental (ESCA) and theoretical (SCF-MO) determination of the oxidation state of sulphur in bis(2-carboxyphenyl) sulphur dihydroxide dilactone." *Journal of the Chemical Society, Faraday Transactions 2: Molecular and Chemical Physics* 73(2): 293-297.
- Vácha, R., P. Jungwirth, J. Chen and K. Valsaraj (2006). "Adsorption of polycyclic aromatic hydrocarbons at the air-water interface: Molecular dynamics simulations and experimental atmospheric observations." *Physical Chemistry Chemical Physics* 8(38): 4461-4467.
- Vega, C. and J. L. F. Abascal (2011). "Simulating water with rigid non-polarizable models: a general perspective." *Physical Chemistry Chemical Physics* 13(44): 19663-19688.
- Vrbka, L., M. Mucha, B. Minofar, P. Jungwirth, E. C. Brown and D. J. Tobias (2004). "Propensity of soft ions for the air/water interface." *Current Opinion in Colloid & Interface Science* 9(1): 67-73.
- Wernet, P., D. Nordlund, U. Bergmann, M. Cavalleri, M. Odelius, H. Ogasawara, L. Å. Näslund, T. K. Hirsch, L. Ojamäe, P. Glatzel, L. G. M. Pettersson and A. Nilsson (2004). "The Structure of the First Coordination Shell in Liquid Water." *Science* 304(5673): 995-999.
- Wilson, K. R., M. Cavalleri, B. S. Rude, R. D. Schaller, A. Nilsson, L. Pettersson, N. Goldman, T. Catalano, J. Bozek and R. Saykally (2002). "Characterization of hydrogen bond acceptor molecules at the water surface using near-edge x-ray absorption fine-structure spectroscopy and density functional theory." *Journal of Physics: Condensed Matter* 14(8): L221.
- Winter, B. and M. Faubel (2006). "Photoemission from Liquid Aqueous Solutions." *Chemical Reviews* 106(4): 1176-1211.
- Winter, B., R. Weber, W. Widdra, M. Dittmar, M. Faubel and I. V. Hertel (2004). "Full Valence Band Photoemission from Liquid Water Using EUV Synchrotron Radiation." *The Journal of Physical Chemistry A* 108(14): 2625-2632.
- Zobrist, B., T. Koop, B. P. Luo, C. Marcolli and T. Peter (2007). "Heterogeneous Ice Nucleation Rate Coefficient of Water Droplets Coated by a Nonadecanol Monolayer." *The Journal of Physical Chemistry C* 111(5): 2149-2155.

## 5.2 SUPPORTING INFORMATION

### 5.2.1 Molecular dynamics and Density of States Computational Details

#### Simulation Box preparation

A liquid water box of  $\sim 15 \times 15 \times 32 \text{ \AA}^3$  and consisting of 216 water molecules was equilibrated at 1 bar pressure and 300 K by running 1 ns classical MD using TIP3P (Jorgensen, Chandrasekhar et al. 1983) (or TIP4P/2005 (Abascal and Vega 2005)) water model. Afterwards, the Z-dimension of the simulation box was enlarged to 72  $\text{\AA}$  and the system was further equilibrated during the course of additional 1 ns constant volume and temperature (NVT) MD, finally resulting in a water slab system with two equilibrated vapor/liquid water interfaces. The simulation box size here adopted has been recognized to be sufficient to describe a liquid water slab with both well-defined interfacial and bulk solvation environments {Kuo, 2004 #24}. Very similar equilibration protocol at classical MD has been reported in literature (Gladich, Habartová et al. 2014, Gladich, Abotaleb et al. 2020).

Starting from the equilibrated liquid water slab, three different initial solute concentrations were created. In the first two, 4 orcinol (or 4 resocinol) were placed on each of the two liquid water interfaces, resulting in an aqueous solution of 2M concentration of orcinol (or resocinol). A last configuration of 0.2 M orcinol was prepared by placing 1 orcinol on the water slab. These three systems were selected to model the experimental concentrations (i.e., 2M resocinol and 0.2 M orcinol) and to offer a molecular picture for the dynamic of the two compounds at the same (2M) concentration. For each concentration, we performed two separate 400 ns (NVT) MD runs using TIP3P or TIP4P/2005 water model, for a total of six NVT simulations at 300 K. Figure S 5-8 shows a snapshot from the MD trajectory of 2M ORC at 300 K.

An additional ice slab of 320 TIP4P/2005 water molecules with two vapor/ice interfaces was prepared from an initial proton disordered ice  $I_h$  crystal of dimension  $\sim 1.8 \text{ nm} \times 16 \text{ nm} \times 3.7$  using the Buch algorithm (Buch, Sandler et al. 1998). A 1.5 ns constant pressure simulation (NpT) at 0 bar with a time step of 0.1 fs, followed by another 0.5 ns at the target temperature, was performed to anneal this ice crystal from 0 K to 237 K, which is -14 C the melting temperature ( $T_m=251\text{K}$ ) of TIP4P/2005 (García Fernández, Abascal et al. 2006). Afterward, the z-dimension of the simulation box was open to 7.2 nm, resulting in an ice slab with two vapor-exposed basal ice facets. Starting from this equilibrated ice slab system, 400 ns NVT production run were performed. Similar protocols for the preparation of ice slab simulations have been exploited successfully in the literature (Conde, Vega et al. 2008, Gladich, Pfalzgraff et al. 2011, Muchova, Gladich et al. 2011, Gladich and Roeselova 2012) (Gladich, Berrens et al. 2020). An ice slab configuration taken from the MD trajectory at 237K is shown in Figure S 5-9.

#### Molecular Dynamics Force Field and Simulations details

Classical MD relies on a force field, i.e. a set of parameters and functional forms (i.e., force field) describing all the inter- and intramolecular interactions. The generalized AMBER force field, GAFF2, practice (Jämbeck and Lyubartsev 2014) was adopted to create the force field parameters for orcinol and resocinol. Molecular structures were optimized at MP2/6-31G\* level of theory and atomic partial charges were determined by Restrained Electrostatic Potential (RESP) method with a Merz-Singh-Kollman scheme (Bayly, Cieplak et al. 1993), fitting the electrostatic potential obtained from single point energy calculations at HF/6-31g\* level on the MP2-optimized structures. Gaussian09 (M. J. Frisch 2016) and Antechamber (Wang, Wang et al. 2001) were employed to perform the optimization and the charge fitting procedure, respectively. Torsion and nonbonded Lennard-Jones parameters were taken from GAFF2. This, or very similar, force field strategy has been successfully used in the description of different aqueous systems, even in the presence of heterogeneous environments, such as vapor/liquid water interfaces (Habartová, Valsaraj et al. 2013, Gladich, Habartová et al. 2014).

GROMACS 2018.6 (Abraham, Murtola et al. 2015) molecular dynamics package was employed to run all the classical MD simulations, employing the leap-frog integration algorithm (Hockney, Goel et al. 1974) and a time step of 2 fs. The Lennard-Jones potential and the real part of the Coulomb interactions were truncated at 0.7 nm. The long-range part of the electrostatic and Lennard-Jones interactions were treated by the particle mesh Ewald method (Darden, York et al. 1993, Essmann, Perera et al. 1995), using a relative tolerance of  $10^{-5}$ , fourth-order cubic interpolation, and a Fourier spacing parameter of 0.12. A stochastic velocity rescaling thermostat (Bussi, Donadio et al. 2007), with a time constant of 0.1 ps was used to control the temperature. The Berendsen barostat (Berendsen, Postma et al. 1984) with a time constant of 2ps was employed to control the pressure during the NpT equilibration runs of the liquid water slab. The SETTLE algorithm (Miyamoto and Kollman 1992) was used to constraint the TIP4P/2005 water geometry, and the LINCS algorithm (Hess, Bekker et al. 1997) was exploited to constrain covalent bonds involving hydrogen atoms in orcinol and resocinol molecules. PLUMED 2.5 (Tribello, Bonomi et al. 2014) was also used for the post-processing analysis.

### Gibbs Dividing Surface and Solute Surface Excess

The Gibbs Dividing Surface (GDS) and the solute surface excess,  $\Gamma$ , have been determined following (Vrbka, Mucha et al. 2004, Herrera, Fan et al. 2011), also taking into account that our simulation box has two vapor/liquid water interfaces. The excess number of a generic specie at  $z=l$  is

$$\begin{aligned}
 N^{\text{ex}}(l) &= 2A\Gamma(l) \\
 &= A \left( \int_{-l}^l (\rho_N - \rho_N^{\text{bulk}}) dz + \int_l^{+\infty} (\rho_N - \rho_N^{\text{gas}}) dz \right. \\
 &\quad \left. + \int_{-\infty}^{-l} (\rho_N - \rho_N^{\text{gas}}) dz \right)
 \end{aligned}
 \tag{Equation S 5-1}$$

$\Gamma$  is the surface excess (in molecules/nm<sup>2</sup>), defined in term of its number density,  $\rho_N$ .

$$\begin{aligned}
 \Gamma(l) &= \frac{1}{2} \left( \int_{-l}^l (\rho_N - \rho_N^{\text{bulk}}) dz + \int_l^{+\infty} (\rho_N - \rho_N^{\text{gas}}) dz \right. \\
 &\quad \left. + \int_{-\infty}^{-l} (\rho_N - \rho_N^{\text{gas}}) dz \right)
 \end{aligned}
 \tag{Equation S 5-2}$$

with  $\rho_N^{\text{bulk}}$  and  $\rho_N^{\text{gas}}$  the number density in the solution bulk and in the gas phase, respectively. The factor (1/2) accounts for the fact that our system has two air/liquid water interface of surface area  $A$  (= 1.48 X 1.48 nm<sup>2</sup> for our water slab system)

The integral of  $\rho_N$  over all the space gives the number of solute (or solvent),  $N$ , present in the system: thus, in our slab system, which is homogeneous in the x and y directions

$$A * \int_{-\infty}^{+\infty} \rho_N dz = N \tag{Equation S 5-3}$$

The probability density profiles,  $\rho = n_i/n_{\text{TOT}}$  in Figure S 5-10, is therefore

$$\rho = \frac{\rho_N}{\int_{-\infty}^{+\infty} \rho_N dz} = \frac{A \rho_N}{N} \tag{Equation S 5-4}$$

where the dimension of  $\rho$  is 1/length. Since  $\rho^{\text{Bulk}} = \rho(z = 0)$  is a constant and  $\rho^{\text{gas}} = \rho(z = \infty) = 0$ , Equation S 5-2 becomes

$$\begin{aligned}\Gamma(l) &= \frac{1}{2} \int_{-\infty}^{+\infty} \rho_N dz - 2l \rho_N^{\text{bulk}} = \frac{N}{2A} \int_{-\infty}^{+\infty} \rho dz - \frac{N}{2A} 2l \rho^{\text{bulk}} \\ &= \frac{N}{2A} (1 - 2l \rho^{\text{bulk}})\end{aligned}\quad \text{Equation S 5-5}$$

The Gibbs Dividing surface is defined as the surface of zero-solvent excess, i.e.,

$$Z_{\text{GDS}} = l = \frac{1}{2\rho^{\text{wat,bulk}}}\quad \text{Equation S 5-6}$$

The solute surface excess at the Gibbs Dividing Surface is

$$\Gamma = \Gamma_{\text{solute}}(Z_{\text{GDS}}) = \frac{N}{2A} \left(1 - \frac{\rho^{\text{solute,bulk}}}{\rho^{\text{wat,bulk}}}\right)\quad \text{Equation S 5-7}$$

where solute and solvent bulk density can be obtained from the profiles in Figure S 5-11. To compare systems at different concentrations and surface areas, it is convenient to define an adimensional  $\Gamma^*$

$$\Gamma^* = 1 - \frac{\rho^{\text{solute,bulk}}}{\rho^{\text{wat,bulk}}}\quad \text{Equation S 5-8}$$

Starting from Equation S 5-1 and Equation S 5-2, the bulk concentration,  $c_b$ , (#molecules/nm<sup>3</sup>) is defined as

$$c_b = \frac{1}{\text{Volume}} \int_{-Z_{\text{GDS}}}^{Z_{\text{GDS}}} \rho_N^{\text{bulk}} dz = \frac{\rho_N^{\text{bulk}}}{A} = \frac{N \rho^{\text{bulk}}}{A^2}\quad \text{Equation S 5-9}$$

A convenient adimensional bulk concentration  $c_b^*$  is

$$c_b^* = \frac{c_b}{(N/\text{Volume})} = \frac{1}{N} \int_{-Z_{\text{GDS}}}^{Z_{\text{GDS}}} \rho_N^{\text{bulk}} dz = \frac{2 \cdot Z_{\text{GDS}} \cdot \rho_N^{\text{bulk}}}{N} = \frac{2 \cdot Z_{\text{GDS}} \cdot \rho^{\text{bulk}}}{A}\quad \text{Equation S 5-10}$$

Table S 5-1 Gibbs Dividing Surface (ZGDS), solute surface excess at ZGDS ( $\Gamma$ ), adimensional  $\Gamma^*$ , bulk concentrations ( $c_b$ ) and adimensional bulk concentration ( $c_b^*$ ) calculated as described above, from the density profiles reported in Figure S 5-12. In bracket, the experimental values from Table 1

	$Z_{\text{GDS}}$ (nm)	$\Gamma$ (mol/nm <sup>2</sup> )	$\Gamma^*$	$C_{\text{bulk}}$ (molecules/nm <sup>3</sup> )	$C_{\text{bulk}}^*$
0.2M ORC, TIP3P	1.52	0.15	0.64	0.05	0.17
0.2M ORC, TIP4P/2005	1.48	0.23	1	0.00	0.00
0.2M ORC, TIP4P/2005 (large)	1.52	0.21	0.94	0.01	0.00
2 M ORC, TIP3P/2005	1.58	1.43	0.78	0.25	0.10
2 M ORC, TIP4P/2005	1.49	1.79	0.98	0.03	0.01
2M RES, TIP3P	1.66	0.79	0.44	0.62	0.26

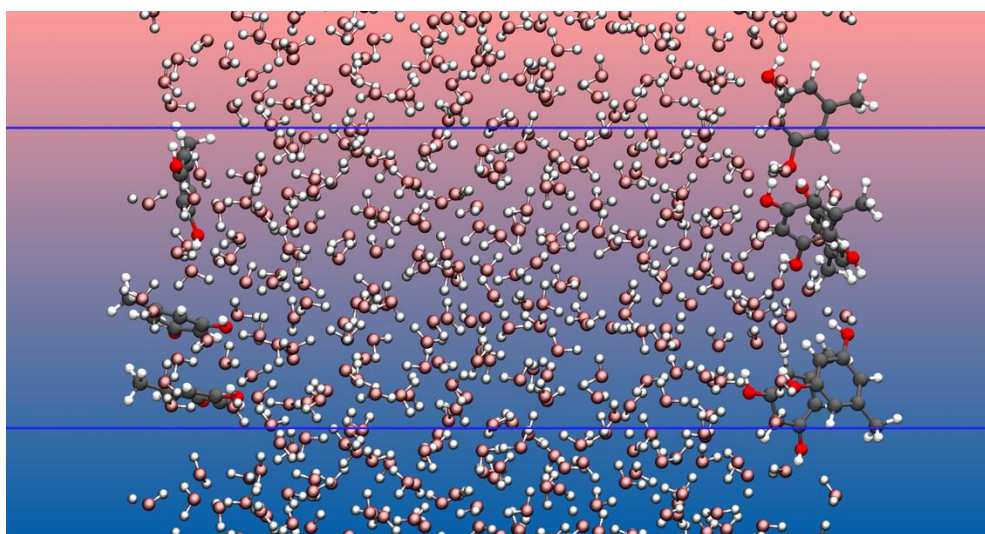


Figure S 5-13: A snapshot from the 2M ORC MD simulation in TIP3P water at 300 K. In metal pastel the water molecules. Color code: H(white), O(red), C(grey).

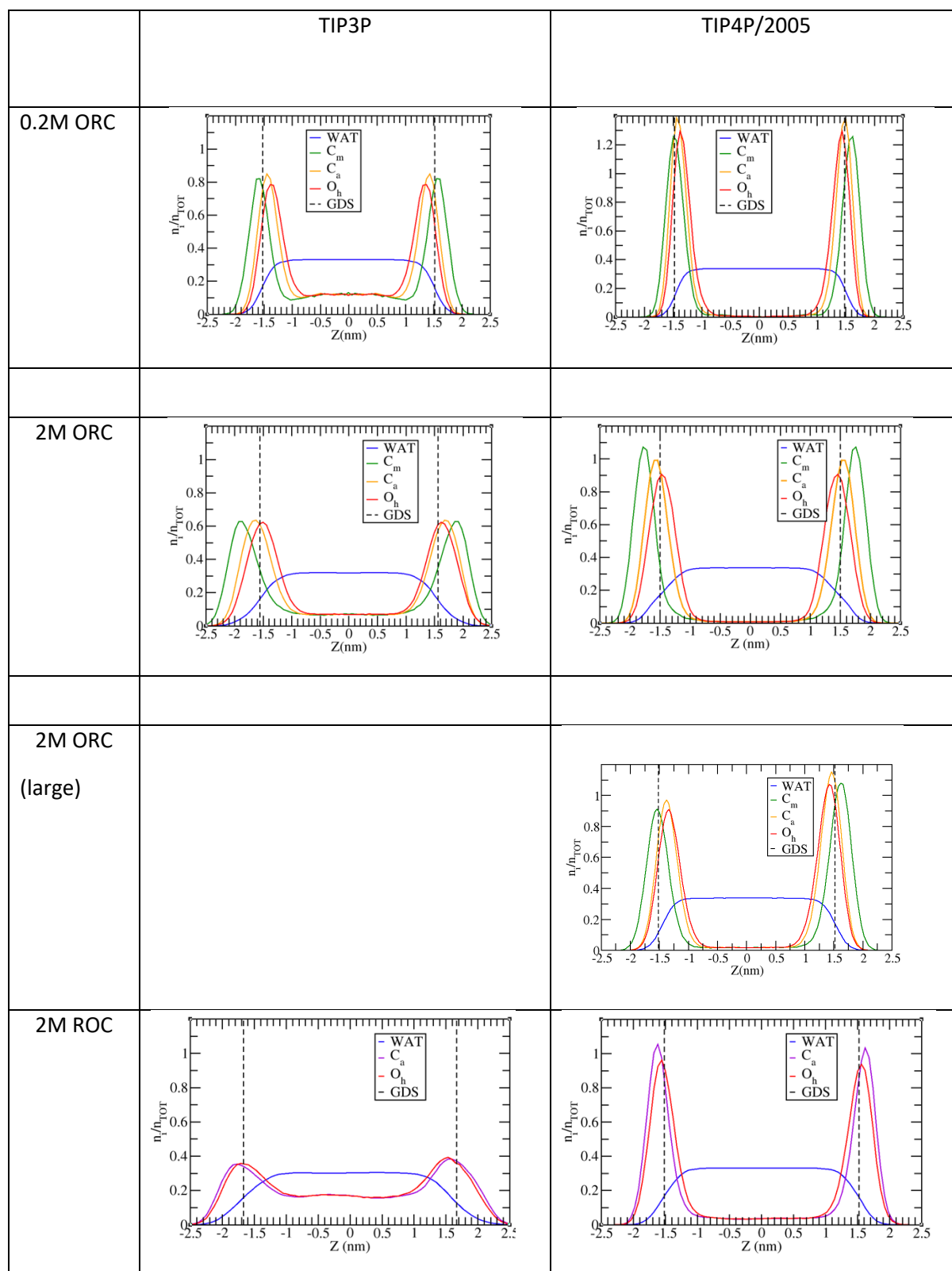


Figure S 5-14: probability distribution profile,  $n_i/n_{TOT}$ , normalized to the unity as a function of the z-coordinate perpendicular to the vapor/liquid water interface, obtained collecting the z-position of each species over the MD trajectory. Top panel report the water model used for the simulation.

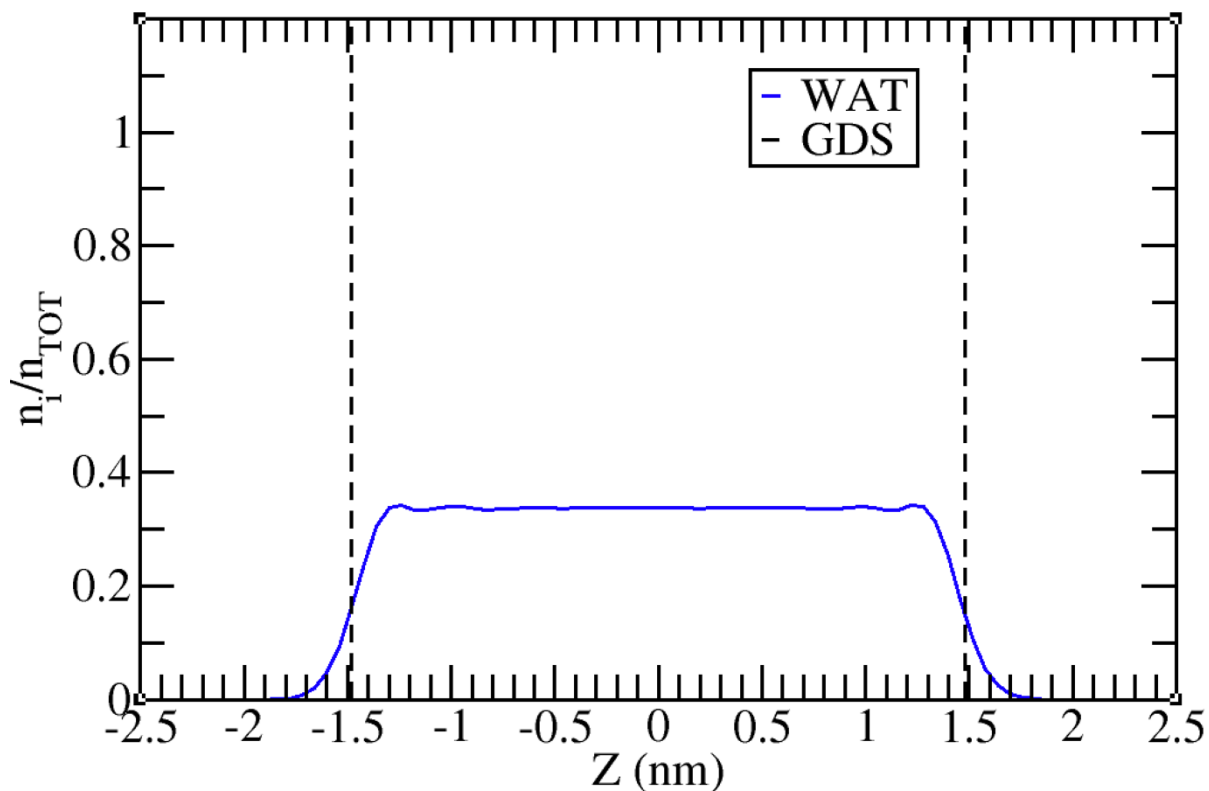


Figure S 5-15: The probability distribution profile,  $n_i/n_{TOT}$ , normalized to the unity as a function of the  $z$ -coordinate perpendicular to the vapor/liquid water interface for the pure liquid water slab simulation. The GDS is located at  $z=1.48$  nm.

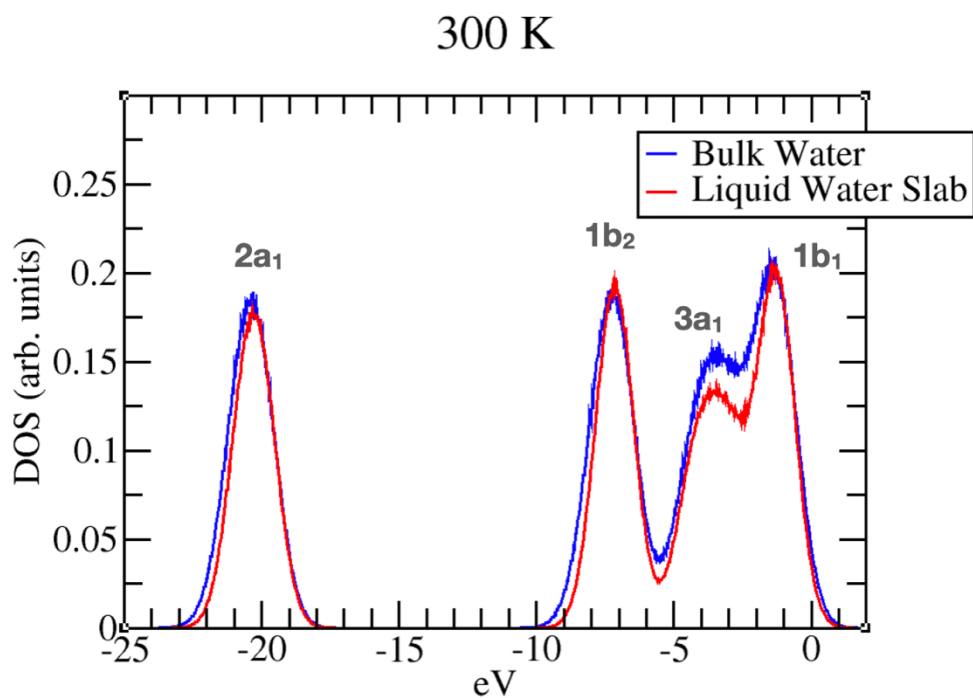


Figure S 5-16: DOS at 300 K of bulk liquid water (blue) and liquid water slab (red) calculated at SCAN DFT level over the classical MD trajectories using TIP4P/2005 water. Data are aligned and normalized to the 1b<sub>1</sub> peak of bulk water. A gaussian smearing of 0.5 eV was used to smooth the DOS.

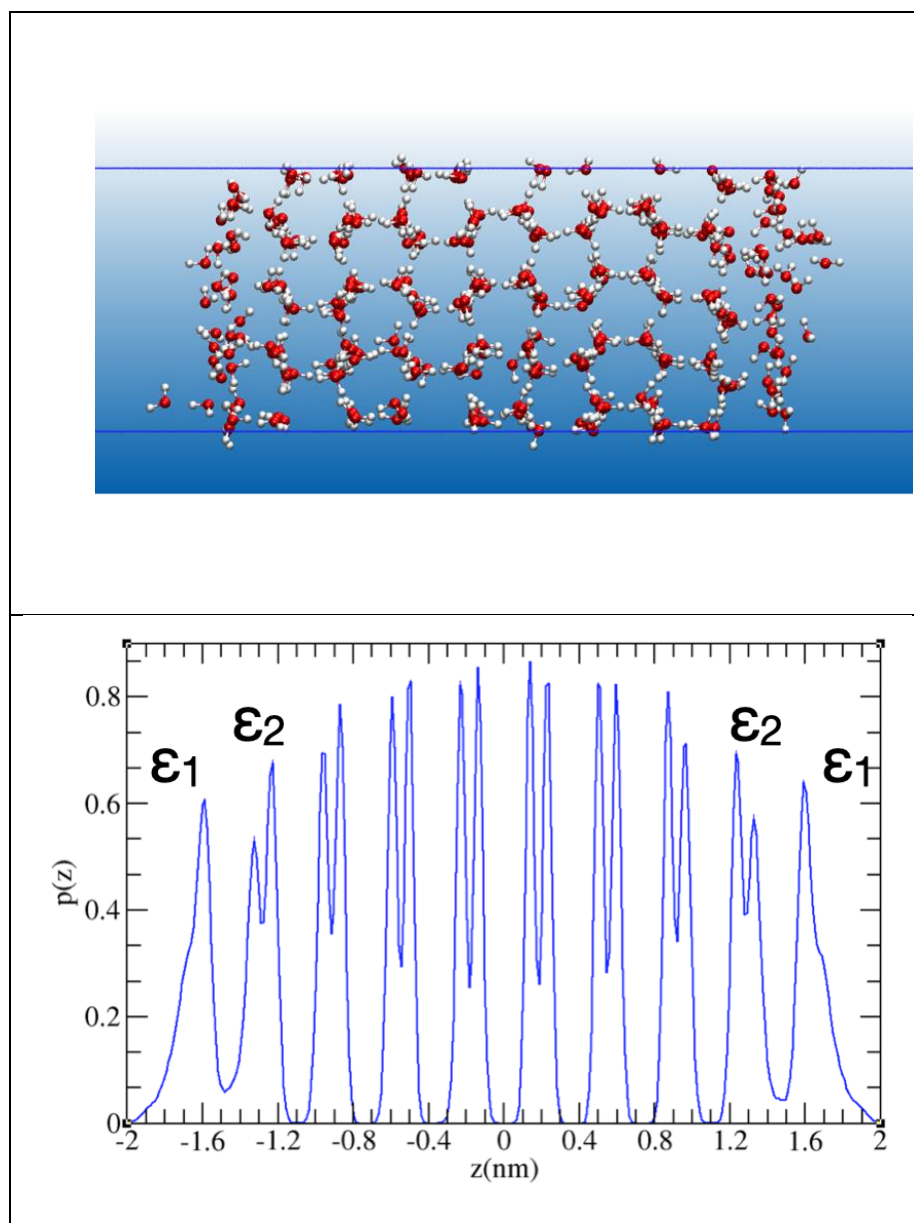


Figure S 5-17: Top panel: A snapshot taken from the MD trajectory of the ice slab at 237K, showing the two vapour/ice interfaces and the simulation box (in blue). The snapshot shows a view of the secondary prismatic facet, while the interfaces exposed to the vapor phase are the basal ones. Lower panel: the probability distribution profile,  $n_i/n_{TOT}$ , normalized to the unity as a function of the  $z$ -coordinate perpendicular to the vapor/ice interface.  $\epsilon_1$  and  $\epsilon_2$  denote the interfacial bi-layers closer to vapor interface. (Gladich, Oswald et al. 2015)

### 5.2.2 XPS of O1s for RES and ORC at 155eV Kinetic Energy

In Figure S 5-18 we show an exemplary O 1s photoemission signal, from RES 2M and ORC 0.2M. O 1s from liquid phase at binding energy 537.8 eV (green peak), a concomitant peak energy with a narrower FWHM, originating from the gas phase water appears near the liquid phase water O 1s (blue peak), blue shifted for 2.2 eV in binding energy. As discussed further below, the two solutions considered in Figure 5-2, RES 2M and ORC 0.2M, are with different bulk concentrations but have the same surface excess. Therefore, one reason for the apparently less pronounced impact of orientation on the C 1s component fractions shown in Figure 5-2 (main text) is certainly that the bulk concentration of resorcinol was much higher than that of orcinol, so that averaging over a smaller probe volume was already enough for the signal to be dominated by the bulk phase molecules. Additional aspects related to the upwards orientation are the lateral interactions among the surfactant molecules that further promote upward orientation.

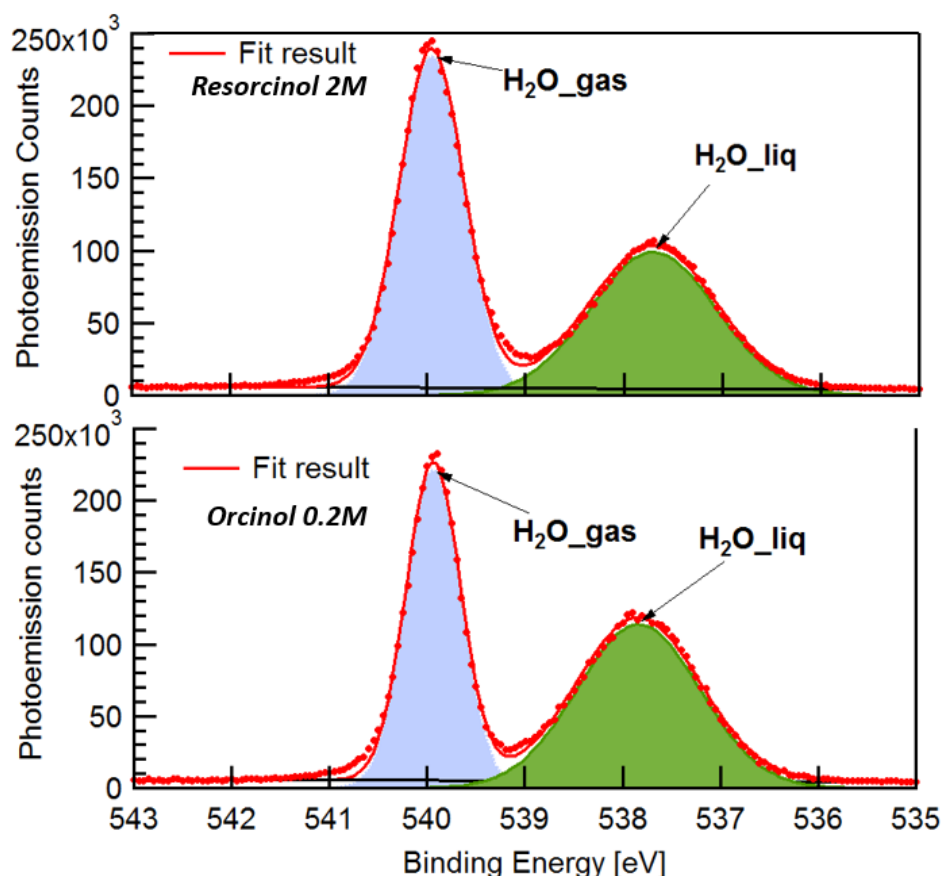


Figure S 5-18: O 1s photoemission signal of RES 2M (top panel) and ORC 0.2M (bottom panel) solution. The excitation photon energy is 685 eV, the corresponding kinetic energy is ca. 155eV. Green peak represents the O 1s signal from water in liquid phase, where as the blue peak is assigned to gas phase water molecules with higher binding energy with respect to that in condensed phase. Both panels share the same vertical scale.

## 5.2.3 Raw valence level spectra with gas phase water molecules contribution

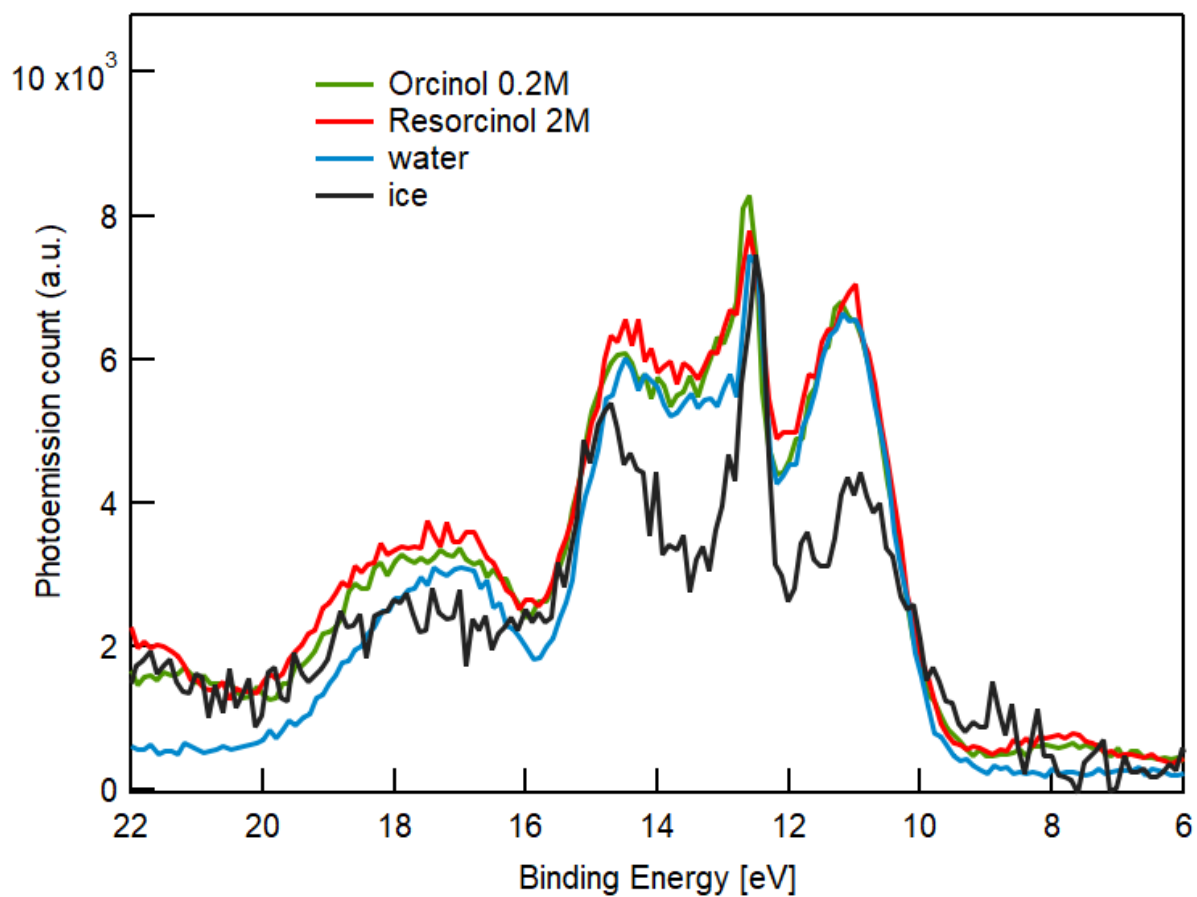


Figure S 5-19: Raw X-ray photoemission spectra of valence level without removing the gas phase contribution for water (blue), ice (black), RES 2M (red) and ORC 0.2M, with excitation photon energy 600eV

## 5.2.4 Attenuation model for XPS

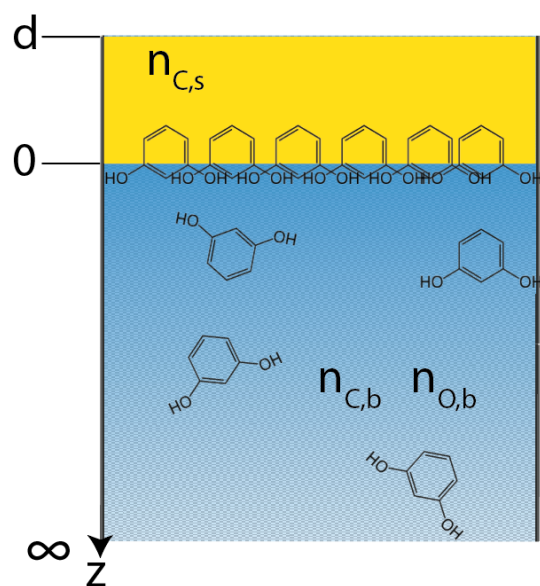


Figure S 5-20: The attenuation model for determining the surface coverage for both resorcinol and orcinol solutions. We assume on the surface of the solution, the thickness of organic layer (yellow color area) is  $d$ , with carbon atomic density  $n_{C,s}$ , the atomic density of carbon and oxygen in the bulk (blue color area) are denoted as  $n_{C,b}$  and  $n_{O,b}$ , respectively.

As an approaching model shown in Figure S 5-20, we denote the surface carbon atomic density as  $n_{C,s}$ . We consider the density of solutes at the liquid-vapor interface to be the same as that of their pure condensed phase, giving  $n_{C,s}$  values of  $4.2 \times 10^{22} \text{ cm}^{-3}$  and  $4.4 \times 10^{22} \text{ cm}^{-3}$  for resorcinol and orcinol respectively. The purpose of this assumption is to allow attenuation in this layer being calculated using the inelastic mean free path of a known liquid. This replaces detailed scattering calculations for the true spatial distribution of surfactant atoms. Thus we assume that attenuation can be approximated by the number of atoms on their trajectory, independent of the density of the medium they are contained in. The C1s photoemission intensity originating from molecules residing on the surface  $I_{C,s}$ , is obtained by assuming attenuation by the surface layer (thickness  $d$ , Figure S 5-20) with mean escape depth  $\frac{2}{\pi} \lambda_s$ :

$$I_{C,s} = A \cdot \int_{-d}^0 n_{C,s} \cdot e^{-\frac{z+d}{\frac{2}{\pi} \lambda_s}} dz = A \cdot n_{C,s} \cdot \frac{2}{\pi} \cdot \lambda_s \cdot \left( 1 - e^{-\frac{d}{\frac{2}{\pi} \lambda_s}} \right) \quad \text{Equation S 5-11}$$

The factor A accounts for photon flux, total photoionization cross section of the core level electrons and geometry of the experimental setup, exclusively for the detection of C1s. In the attenuation model described in Equation S 5-11, we consider only the inelastic scattering of photoelectrons. The elastic scattering effect is very weak and can be neglected in our system.

In the bulk, the O1s photoemission signal is predominantly originating from oxygen of bulk water molecules. Since the surface excess of both orcinol and resorcinol solutions are about

the same (see below) and both molecules contain one oxygen atom in the hydroxyl group, the fraction of H<sub>2</sub>O-oxygen is three and one, respectively, orders of magnitude higher than the fraction of organic hydroxyl group oxygen in the bulk and in the solution layer containing the hydroxyl groups near the surface, respectively. So, we neglect the atomic density of oxygen within the solute coverage on the surface, considering only that of the water in the bulk, as  $n_{O,b}$  (constant value of  $3.45 \cdot 10^{22} \text{ cm}^{-3}$ ). This is consistent with placing the Gibbs Dividing surface ( $z = 0$ ) between the hydroxy group and the adjacent carbon. The photoemission intensity of oxygen and carbon from the bulk (denoted as  $I_{C,b}$  and  $I_{O,b}$ , with atomic density  $n_{C,b}$  and  $n_{O,b}$  respectively), is obtained by integrating  $z$  from 0 to  $\infty$ , with the attenuation factor  $e^{-\frac{d}{\pi \lambda_s}}$ , from the surface overlayer(s):

$$I_{C,b} = A \cdot \int_0^{\infty} n_{C,b} \cdot e^{-\frac{z}{\pi \lambda_b}} dz \cdot e^{-\frac{d}{\pi \lambda_s}} = A \cdot n_{C,b} \cdot \frac{2}{\pi} \cdot \lambda_b \cdot e^{-\frac{d}{\pi \lambda_s}} \quad \text{Equation S 5-12}$$

And similarly for  $I_{O,b}$ :

$$I_{O,b} = B \cdot n_{O,b} \cdot \frac{2}{\pi} \cdot \lambda_b \cdot e^{-\frac{d}{\pi \lambda_s}} \quad \text{Equation S 5-13}$$

where B is the factor accounting for photon flux, total photoionization cross section of the core level electron and geometry of the experiment setup, exclusively for the detection of O1s, different from A above used for C1s. The atomic density of carbon in the bulk,  $n_{C,b}$  depends on the solution concentration, listed in Table S 5-2. During the experiment, the overall total C1s photoemission intensity  $I_{C,T}$  measured is given by the sum of  $I_{C,s}$  and  $I_{C,b}$ . The total O1s photoemission intensity  $I_{O,T}$  is equal to  $I_{O,b}$ .

As discussed in the previous section, because resorcinol and orcinol molecules are surface active, we expect a propensity of these organic molecules on the solution surface, and lower concentration when probed in the bulk. This is apparent from the  $I_{C,T}/I_{O,T}$  photoemission signal intensity ratio as a function of photoelectron kinetic energy, termed C/O depth profile (Figure 5-3). When computing the C/O depth profile, by combining the Equation S 5-12, Equation S 5-13 and Equation S 5-14, rearranging all the known factors to the left hand side of the equation, we can write:

$$\left( \frac{I_{C,T}}{I_{O,T}} \cdot \frac{B}{A} \cdot n_{O,b} - n_{C,b} \right) \cdot \frac{\lambda_b}{\lambda_s} = n_{C,s} \cdot \left( e^{-\frac{d}{\pi \lambda_s}} - 1 \right) \quad \text{Equation S 5-14}$$

Where  $\lambda_s$  and  $\lambda_b$  are suggested from reference. (Tanuma, Powell et al. 1994, Shinotsuka, Da et al. 2017) Equation S 5-14 is used to fit the C/O depth profile. The left hand side of Equation S 5-14 contains all known factors, including the normalized C/O ratio, for convenience, we denote it as  $D$ :

$$\left( \frac{I_{C,T}}{I_{O,T}} \cdot \frac{B}{A} \cdot n_{O,b} - n_{C,b} \right) \cdot \frac{\lambda_b}{\lambda_s} = D \quad \text{Equation S 5-15}$$

The shape of the fitting equation depends exclusively on the shape of C/O ratio. The only free parameter is  $d$ , the thickness of the surface ‘layer’ in the right hand side of Equation S 5-14.

The surface propensity of solutes at the liquid-vapor interface is described by the surface excess,  $\Gamma$ , which denotes the deviation of the solute density in the interfacial region compared that in the bulk.  $\Gamma$  can be obtained from surface tension measurements, as a function of the bulk concentration, and from the relationship between surface excess and photoemission signal intensities (Lee, Orlando et al. 2016, Lee, Orlando et al. 2019).

Table S 5-2 Fitting parameters used in the attenuation model and the thickness results, the surface excess  $\Gamma$  is obtained by the product of  $n_s$  and  $d$ .

Sample	$n_{C,b} (cm^{-3})$	$n_{C,s} (cm^{-3})$	$n_s (cm^{-3})$	$d(\text{\AA})$	$\Gamma(cm^{-2})$
Resorcinol 0.01M	$3.61 \cdot 10^{19}$	$4.10 \times 10^{22}$	$6.84 \times 10^{21}$	0.085	$5.8 \times 10^{12}$
Resorcinol 2M	$7.2 \cdot 10^{21}$	$4.10 \times 10^{22}$	$6.84 \times 10^{21}$	2.2	$1.5 \times 10^{14}$
Orcinol 0.01M	$4.21 \cdot 10^{19}$	$4.38 \times 10^{22}$	$6.26 \times 10^{21}$	0.26	$1.6 \times 10^{13}$
Orcinol 0.2M	$8.4 \cdot 10^{20}$	$4.38 \times 10^{22}$	$6.26 \times 10^{21}$	2.2	$1.4 \times 10^{14}$

## References

- Abascal, J. L. F. and C. Vega (2005). "A general purpose model for the condensed phases of water: TIP4P/2005." *Journal of Chemical Physics* 123(23).
- Abraham, M. J., T. Murtola, R. Schulz, S. Páll, J. C. Smith, B. Hess and E. Lindahl (2015). "GROMACS: High performance molecular simulations through multi-level parallelism from laptops to supercomputers." *SoftwareX* 1–2: 19-25.
- Bayly, C. I., P. Cieplak, W. Cornell and P. A. Kollman (1993). "A well-behaved electrostatic potential based method using charge restraints for deriving atomic charges: the RESP model." *The Journal of Physical Chemistry* 97(40): 10269-10280.
- Berendsen, H. J. C., J. P. M. Postma, W. F. Vangunsteren, A. Dinola and J. R. Haak (1984). "MOLECULAR-DYNAMICS WITH COUPLING TO AN EXTERNAL BATH." *Journal of Chemical Physics* 81(8): 3684-3690.
- Buch, V., P. Sandler and J. Sadlej (1998). "Simulations of H<sub>2</sub>O solid, liquid, and clusters, with an emphasis on ferroelectric ordering transition in hexagonal ice." *Journal of Physical Chemistry B* 102(44): 8641-8653.
- Bussi, G., D. Donadio and M. Parrinello (2007). "Canonical sampling through velocity rescaling." *Journal of Chemical Physics* 126(1).
- Conde, M. M., C. Vega and A. Patrykiewicz (2008). "The thickness of a liquid layer on the free surface of ice as obtained from computer simulation." *Journal of Chemical Physics* 129(1).
- Darden, T., D. York and L. Pedersen (1993). "PARTICLE MESH EWALD - AN N.LOG(N) METHOD FOR EWALD SUMS IN LARGE SYSTEMS." *Journal of Chemical Physics* 98(12): 10089-10092.
- Essmann, U., L. Perera, M. L. Berkowitz, T. Darden, H. Lee and L. G. Pedersen (1995). "A SMOOTH PARTICLE MESH EWALD METHOD." *Journal of Chemical Physics* 103(19): 8577-8593.
- García Fernández, R., J. L. F. Abascal and C. Vega (2006). "The melting point of ice Ih for common water models calculated from direct coexistence of the solid-liquid interface." *The Journal of Chemical Physics* 124(14): 144506.
- Gladich, I., A. Abotaleb and A. Sinopoli (2020). "Tuning CO<sub>2</sub> Capture at the Gas/Amine Solution Interface by Changing the Solvent Polarity." *J. Phys. Chem. B* 124(45): 10245-10256.
- Gladich, I., M. L. Berrens, P. M. Rowe, R. G. Pereyra and S. Neshyba (2020). "Solvation and Stabilization of Single-Strand RNA at the Air/Ice Interface Support a Primordial RNA World on Ice." *The Journal of Physical Chemistry C* 124(34): 18587-18594.
- Gladich, I., A. Habartová and M. Roeselová (2014). "Adsorption, Mobility, and Self-Association of Naphthalene and 1-Methylnaphthalene at the Water–Vapor Interface." *The Journal of Physical Chemistry A* 118(6): 1052-1066.
- Gladich, I., W. Pfalzgraff, O. Marsalek, P. Jungwirth, M. Roeselova and S. Neshyba (2011). "Arrhenius analysis of anisotropic surface self-diffusion on the prismatic facet of ice." *Physical Chemistry Chemical Physics* 13(44): 19960-19969.
- Gladich, I. and M. Roeselova (2012). "Comparison of selected polarizable and nonpolarizable water models in molecular dynamics simulations of ice I-h." *Physical Chemistry Chemical Physics* 14(32): 11371-11385.
- Habartová, A., K. T. Valsaraj and M. Roeselová (2013). "Molecular Dynamics Simulations of Small Halogenated Organics at the Air–Water Interface: Implications in Water Treatment and Atmospheric Chemistry." *The Journal of Physical Chemistry A* 117(38): 9205-9215.
- Herrera, L., C. Fan, D. D. Do and D. Nicholson (2011). "A revisit to the Gibbs dividing surfaces and helium adsorption." *Adsorption* 17(6): 955-965.
- Hess, B., H. Bekker, H. J. C. Berendsen and J. Fraaije (1997). "LINCS: A linear constraint solver for molecular simulations." *Journal of Computational Chemistry* 18(12): 1463-1472.
- Hockney, R. W., S. P. Goel and J. W. Eastwood (1974). "QUIET HIGH-RESOLUTION COMPUTER MODELS OF A PLASMA." *Journal of Computational Physics* 14(2): 148-158.
- Jämbeck, J. P. M. and A. P. Lyubartsev (2014). "Update to the General Amber Force Field for Small Solutes with an Emphasis on Free Energies of Hydration." *The Journal of Physical Chemistry B* 118(14): 3793-3804.
- Jorgensen, W. L., J. Chandrasekhar, J. D. Madura, R. W. Impey and M. L. Klein (1983). "Comparison of simple potential functions for simulating liquid water." *The Journal of Chemical Physics* 79(2): 926-935.
- M. J. Frisch, G. W. T., H. B. Schlegel, G. E. Scuseria, M. A. Robb, J. R. Cheeseman, G. Scalmani, V. Barone, G. A. Petersson, H. Nakatsuji, X. Li, M. Caricato, A. Marenich, J. Bloino, B. G. Janesko, R. Gomperts, B. Mennucci, H. P. Hratchian, J. V. Ortiz, A. F. Izmaylov, J. L. Sonnenberg, D. Williams-Young, F. Ding, F. Lipparini, F. Egidi, J. Goings, B. Peng, A. Petrone, T. Henderson, D. Ranasinghe, V. G. Zakrzewski, J. Gao, N. Rega, G. Zheng, W. Liang, M. Hada, M. Ehara, K. Toyota, R. Fukuda, J. Hasegawa, M. Ishida, T. Nakajima, Y. Honda, O. Kitao, H. Nakai, T. Vreven, K. Throssell, J. A. Montgomery, Jr., J. E. Peralta, F. Ogliaro, M. Bearpark, J. J. Heyd, E. Brothers, K. N. Kudin, V. N. Staroverov, T. Keith, R. Kobayashi, J. Normand, K. Raghavachari, A. Rendell, J. C. Burant, S. S. Iyengar, J. Tomasi, M. Cossi, J. M. Millam, M.

- Klene, C. Adamo, R. Cammi, J. W. Ochterski, R. L. Martin, K. Morokuma, O. Farkas, J. B. Foresman, and D. J. Fox (2016). Gaussian 09, Revision A.02, Gaussian, Inc., Wallingford CT.
- Miyamoto, S. and P. A. Kollman (1992). "SETTLE - AN ANALYTICAL VERSION OF THE SHAKE AND RATTLE ALGORITHM FOR RIGID WATER MODELS." *Journal of Computational Chemistry* 13(8): 952-962.
- Muchova, E., I. Gladich, S. Picaud, P. N. M. Hoang and M. Roeselova (2011). "The Ice-Vapor Interface and the Melting Point of Ice I(h) for the Polarizable POL3 Water Model." *Journal of Physical Chemistry A* 115(23): 5973-5982.
- Tribello, G. A., M. Bonomi, D. Branduardi, C. Camilloni and G. Bussi (2014). "PLUMED 2: New feathers for an old bird." *Computer Physics Communications* 185(2): 604-613.
- Vrbka, L., M. Mucha, B. Minofar, P. Jungwirth, E. C. Brown and D. J. Tobias (2004). "Propensity of soft ions for the air/water interface." *Current Opinion in Colloid & Interface Science* 9(1): 67-73.
- Wang, J. M., W. Wang and P. A. Kollman (2001). "Antechamber: An accessory software package for molecular mechanical calculations." *Abstracts of Papers of the American Chemical Society* 222: U403.

## 6 CONCLUSION AND OUTLOOK

---

### 6.1 CONCLUSION

The interaction of water with the surface of a solid substrate or organic molecules is an important driver of the heterogeneous ice nucleation activity of these substrates. In this thesis work we have experimentally investigated the structure of interfacial water molecules either on a solid substrate surface or at a solution surface covered by organic molecules.

In order to assess the impact of a solid substrate to the arrangement of adsorbed water at a molecular level, we probed both chemical and structural information from the solid-vapor interface with samples that are relevant for ice nucleation. As the coordination of water molecules is embodied in its HB structure, we can approach our research goal by measuring the O K edge NEXAFS spectra of adsorbed water on the sample surface, combined with XPS for the chemical composition. We have experimentally investigated the HB structure of water molecules adsorbed on different classes of materials, including AgI, Microcline (K-feldspar) and TiO<sub>2</sub>. The adsorbed water molecules show different structure on the surface of different samples. As an overview of the results, Figure 6-1 collects some typical examples of this thesis work.

Firstly, our work on TiO<sub>2</sub> suggest that at 235K, at just a little lower water vapor pressure than saturation with respect to that of ice, we found that the HB structure in adsorbed water on TiO<sub>2</sub> nanoparticles still resembles that of a liquid-like water film (Figure 6-2, green). This is a surprising finding as at this temperature, homogeneous IN would probably occur already in a macroscopic solution, implying that TiO<sub>2</sub> surface is inhibiting the formation of tetrahedral coordination of water that would be needed for ice nucleation. The observed behavior is consistent with the fact that TiO<sub>2</sub> is not known as a good IN material. As a caveat we note that recent work found that ice formation attributed to deposition nucleation could actually be attributed to pore condensation and freezing. So, one could argue that liquid water could have condensed in the interstitial spaces among the TiO<sub>2</sub> nanoparticles (David, Marcolli et al. 2019, Marcolli 2020). The observed impact of TiO<sub>2</sub> nanoparticles on the HB structure of water molecules is relevant for other applications of this material as it may affect the hydration of other species, the course of chemical reactions or nucleation processes. Further, from a technical perspective, this work had shown the potential of our experiment setup, which combines both depth selective information (XPS) and HB structure observables of water molecules (NEXAFS) to investigate the solid material surface. This motivated us to investigate other atmospherically relevant solid substrates.

Secondly, in contrast to the TiO<sub>2</sub> case, the HB structure on the AgI surface is showing a different trend, as its NEXAFS spectrum shows relatively lower absorption in the region of the weak hydrogen bonds dominating the liquid water spectrum, indicating a more prevalent tetrahedral coordination as in ice (Figure 6-3, red). AgI has a very low solubility in water, and

thus would generally be expected to be rather hydrophobic, it still exposes a pattern of hydrophilic groups on its surface commensurate with the dimensions of the basal plane of ice. These may attract water molecules without that their structure would be perturbed by hydration of ions dissolving at the surface. For this material, we have developed a numerical approach, by breaking down the NEXAFS spectra into Gaussian components. Our result suggest that at low water molecule coverage (60% RH), a non-negligible fraction of water molecules organize into a tetrahedral structure. Further, we used a numerical model to assess the surface carbon quantity, the morphology of carbon is assumed to be patchy island floating above the adsorbed water layers. The combined results of XPS and NEXAFS suggest that water molecules adsorbed on the surface of solid AgI particles already start to display an ordered HB structure at subsaturated condition with respect to ice, which is mirrored by the established role of AgI as an efficient ice nucleus.

Thirdly, the HB structure of adsorbed water on a K-feldspar surface is governed by the  $K^+$  cation leaching effect. We have used a thin crystal cut at the (010) crystalline plane of an Adularia orthoclase (AO) and a Pakistan microcline (PM) samples provided by A. Kiselev from Karlsruhe Institute of Technology. Under humid conditions, we identify that the adsorbed water molecules trigger the  $K^+$  ions leaching from the as prepared PM sample into the adsorbed water layer. After that, the PM sample was immersed in water for 24h, making its surface  $K^+$  depleted. However, in this case, we observe that the water treated PM surface shows the most prominent water molecule ordering ability, reflected by the highest strong HB absorption feature of the corresponding adsorbed water spectrum (Figure 6-5, blue). This clearly suggests that when  $K^+$  are depleted within a reasonable depth and exchanged with protons, the surface can manifest its ability of ordering water in the vicinity. The result from the water treated PM indicates that the K-rich feldspars have a structure promoting the ordering of water, but that the accumulation of  $K^+$  ions in adsorbed water inhibits this water ordering effect. This is meanwhile being confirmed by A. Kiselev in freezing experiments that show that the freezing temperatures increase with progressive freeze-thaw cycles. Our parallel experiments on the AO sample exhibit different behavior in the freezing experiments (not yet shown). Consistently, the observed NEXAFS spectra of adsorbed water show no difference between the as prepared sample and after immersion in water. Further investigations are needed to clarify the different role of  $K^+$  leaching for the AO sample.

Our experiment on feldspar samples suggest that the  $K^+$  leaching triggered by the water adsorption play a role in the coordination of water molecule itself, this implies that the  $K^+$  leaching is an important parameter that impacts the heterogeneous IN efficiency of feldspar. Such phenomenon is similar to the effect of solutes in aqueous solutions, that its nucleation is controlled by the water activity (Koop, Luo et al. 2000). This result is also reflected by Cappa et al., that the addition of ions will significantly perturb the electronic structure of adjacent water molecules, which gives change to the geometric arrangement of the HB network (Cappa, Smith et al. 2005). In the atmosphere, this can be a factor to evaluate the ice nucleation efficiency of feldspar samples, or in similar systems with mobile ions. Note that the cation leaching is not the only factor to impact the ice nucleation ability of feldspar. Other factors are morphological features such as cracks, cavities and pores on the feldspar surface, which my

locally enhance the density of adsorbed water molecules (Fletcher 1959, Marcolli 2014) and reduce the surface diffusivity (Pruppacher and Klett 1997). We also have to take into consideration the pore condensation freezing effect, as the feldspar surface may present nano-scaled porous features.

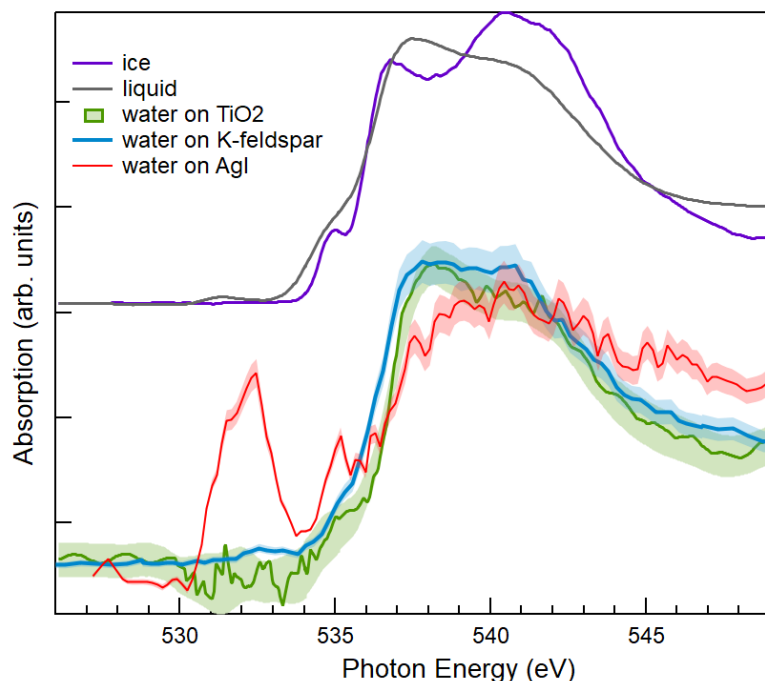


Figure 6-4 Auger electron yield O K edge NEXAFS spectra of adsorbed water molecules on TiO<sub>2</sub> (red), K-feldspar (water treated sample) and AgI surface. A caveat here for the AgI surface water spectra (red), the peak at ca. 532 eV is related to the adsorption of water molecules and to the intrinsic presence of oxygen-containing adventitious carbon species. Which might slightly change the overall shape of AgI surface water spectra. Further understanding of the specific adventitious carbon need to be established.

Now we switch gears and move to the aqueous solution side. We would like to address the related impact of organic monolayers on the water structure at the liquid-vapor interface. As atmospheric relevant proxies, resorcinol (RES) and orcinol (ORC) are chosen to represent a range of phenolic compounds. Meanwhile, in this work I. Gladich has contributed molecular dynamics simulations and density of states calculations, to support the interpretation of the experimental findings.

By XPS, we have assessed the preferential orientation of RES and ORC molecules at the liquid-vapour interface, as well as their surface propensity. The classical MD trajectory over the organic solution at the interface supports our experimental findings. From XPS, the thickness of the organic layer is determined through an attenuation model, by which the surface excess of these organic molecules is determined.

In addition, O K edge NEXAFS spectra of these organic aqueous solutions reveal the structural nature of water molecules at the liquid-vapor interface. Figure 6-5 display an overview of the NEXAFS results of different solution systems. Compared to the liquid water (blue) and ice

(magenta) spectra, the spectra of RES (red) and ORC (green) suggest the water molecules tend to coordinate more often tetrahedrally at the liquid-vapor interface than in pure water, apparent from slight decrease of intensity around 538 eV and the slight increase at 540 eV. Our NEXAFS observations are in line with the calculation of the tetrahedral order parameter, computed from the MD simulations. We have also attempted to measure the valence level spectra of water molecules at the liquid-vapor interface and calculated the density of states (DOS) theoretically. However, the results between experiment and calculation of DOS are indicating that the difference between valence spectra of organic aqueous solution and that of liquid water are too small to allow the experimental verification, in view of the experimental uncertainty.

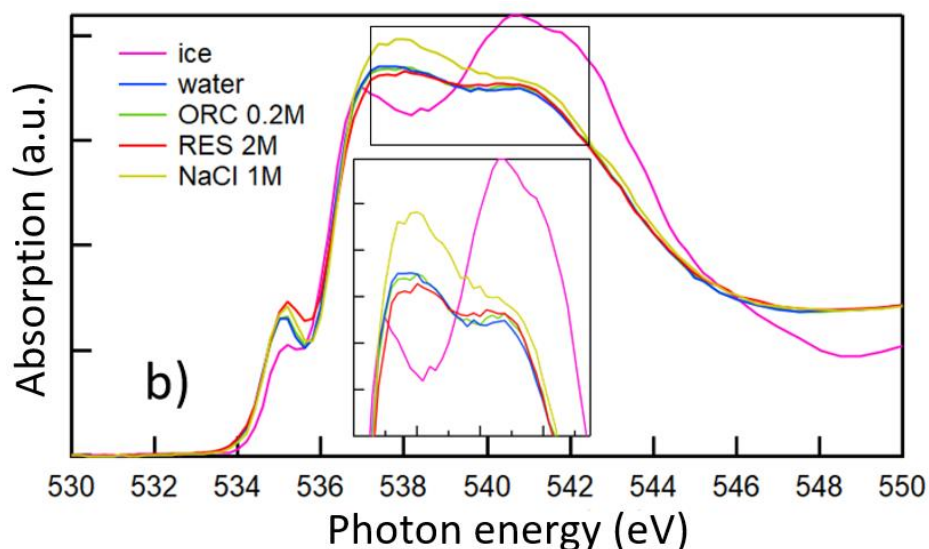


Figure 6-5 O K edge NEXAFS of liquid water (blue), ice (magenta), RES 2M (red), ORC 0.2M (green) and NaCl 1M (yellow) solution.

Our work gave a clear picture of the water molecules coordination (embodied in the HB network) at *pre-nucleation* stage, meanwhile, identifying the factor that give rise to this structural nature. This work would open up new lines of inquiry for a molecular understanding of heterogeneous ice nucleation, and spur future research on solid/liquid interfaces for other scientific purposes. From a technical point of view, in the future it is necessary to improve the statistics of NEXAFS spectra and valence level spectra for the Liquid Jet XPS experiment to reach a stronger conclusion. The discrepancy between the DOS and measured valence spectra are probably due to the different MED/calculation depth, as both approaches may contain different contributions from the bulk water. As a future consideration, DOS integration with the precise MED would be beneficial to explain the data more precisely.

In a NEXAFS experiment, the information depth depends on the integrated kinetic energy window. Hence, the information depth could be well controlled by integrating within an appropriate kinetic energy window. Our current result was based on the oxygen *Auger KLL peak tail* (KE 412-437 eV), i.e, the secondary electrons of the Auger peak survived from the inelastic scattering, which well represents the original Auger peak shape. The resulting information depth of our NEXAFS could well cover a considerable portion of the bulk water,

thus it is reasonable to expect a more surface sensitive information by setting up an appropriate kinetic window during the DAQ process. Isomura et al. have demonstrated that this allows obtaining depth resolving NEXAFS spectra (Isomura, Soejima et al. 2015).

## 6.2 OUTLOOK

Our understanding for the IN initiated by organic molecules or solid substrates at a molecular level is still not sufficient. Why some materials have a higher IN efficiency than others can not be explained well enough (Hoose and Möhler 2012, Kanji, Ladino et al. 2017). The IN ability of a material is not only reflected in the local ordering of water molecules at the interface, and our understanding of all the rich parameters that control the IN ability of a given material is still far from complete. Some other factors such as lattice match between the substrate and ice face, or density reduction of liquid water near the surface are worth to explore (Fitzner, Pedevilla et al. 2020).

Moreover, a clear analytical and quantitative explanation for the connection between surface property and their IN ability is not established yet. In view of the above mentioned consideration, in the following we list some ideas that not only focus on the ice nucleation itself, but also span the technique used and theory to other fields that would be interesting to explore.

- When solid substrates or particles come in contact with reactive gases, molecules may coat on its surface, e.g., chemically adsorbed ammonia molecules on feldspar particle surfaces (Kumar, Marcolli et al. 2018). As those systems represent greatly the real case in the atmosphere, it would be intriguing and necessary to study the HB structure of water under such conditions by XPS and NEXAFS. This can be a following project of this thesis work.
- Organic monolayers on solution surface. It is believed that the structural match between the ice lattice and the 2D crystalline structure of surface monolayer, such as long-chain alcohol case, is a key reason for the good IN ability of such monolayers (Gavish, Popovitz-Biro et al. 1990, Popovitz-Biro, Wang et al. 1994, Majewski, Popovitz - Biro et al. 1995). In this work we have investigated the water structure on RES and ORC aqueous solution surface. But do those organic monolayers on solution surface also display a 2D crystalline structure? What are other factors that facilitate or inhibit the IN of organic coated water droplet? These topics are worth of it to investigate experimentally by e.g., X-Ray scattering, and are definitely of strong importance for the IN community.
- Phloroglucinol dihydrate(1-3-5 trihydroxybenzene) was identified as a highly efficient organic ice nucleant (Fukuta 1966). Metya et al. suggest that the (010) face of Phloroglucinol dehydrate is responsible for its exceptional IN ability. Compared to other crystal face, it has the lowest area mismatch to ice and highest OH groups density (Metya and Molinero 2021). This result is strongly connected to our discovery in RES

and ORC, as those OH groups attaches inside the water surface, showing a specific molecular orientation, probably controlled by the self-stacking. With future experiments, it is worthwhile to examine how the OH density and the stacking structure impact the IN efficiency for organic molecules in aqueous solutions. This would of course also require freezing experiments by partner institutions.

- The quality (SNR) of NEXAFS spectra of adsorbed water are not always satisfactory, especially the extracted adsorbed water spectra are noisy compared to pure water or ice spectra. Future experiments should focus to improve the SNR, either by extending the measurement time or optimize the experiment configuration. Also, a NEXAFS interpretation metric should be introduced, as currently there is no standard criteria to interpret the NEXAFS data quantitatively. Future consideration can focus more on the ratio between the absorption peaks, which also quantitatively reflect the structural information, e.g., ratio between the intensity of peaks for strong HB and weak HB.
- Collaboration with theoretical community: simulation of O K-edge NEXAFS spectra based on MD simulation. Such collaboration will drive a broader assessment for our experimental results. Contact with partner institutions and research groups are under establishment.
- Adventitious carbon contamination is inevitable for samples that have been exposed to the ambient environment, and it continuously develops in-situ with the synchrotron radiation. Carbon bonded oxygen gives rise to its distinctive feature in O K edge NEXAFS spectra. In the TiO<sub>2</sub> study, we have approached this with a similar carbon system like the acetic acid O K edge NEXAFS. However, the specific feature of adventitious carbon related contribution to O K edge NEXAFS spectra is yet to be studied.
- We know  $\Delta G$  is the energy gap for the activation of IN, which is a function of surface tension between water and ice. But how does  $\Delta G$  change with a changing solid surface structure, or with organic molecules clusters/monolayers involved in heterogeneous ice nucleation? An influence of the surface tension between these substrates and ice is expected. This information can establish a mathematical model that connects surface tension,  $\Delta G$ , and the surface crystal structure parameters.
- Do we know all the key parameters that drives the IN ability of a material? From computer simulation, different parameters have been identified as IN driving variables (Fitzner, Pedevilla et al. 2020). By experimental approach, it is important to evaluate how those factors that are believed to be IN relevant, impact the ice nucleation process. For example, the density reduction of liquid water at the solid surface.
- We still do not have a clear and uniform theory to explain the IN ability of any given material from an atomistic level. Thus, a universal model is expected, which is retrieved by both experimental and simulation results, and which should consider the interaction of water molecules themselves and its physical environment at atomistic level,

preferably as a function of pressure and temperature. Such theory should be applicable to explain any interfacial interaction to explain the ice nucleation process.

- Anthropogenic activities like smelting, aircraft engine ablation or urban dust give rise to a classes of metallic particles, such as iron, lead, nickel, and copper (Kanji, Ladino et al. 2017). These metal particles are found in the ice residues. As a parallel experiment with that of TiO<sub>2</sub>, it would be interesting to study the IN initiated by those metal and their oxides by either NEXAFS or other surface sensitive techniques. Such study would have a strong significance for an assessment of how anthropogenic activities impact the environment system at large.
- Extraterrestrial ice formation. Ices are a major player in the formation of planets (Hubbard 2016). Ice clouds are observed in the Martian middle atmosphere (Ajello, Pang et al. 1976, Fedorova, Korablev et al. 2009, Kleinböhl, Schofield et al. 2009, Montmessin, Korablev et al. 2017). It would be interesting to experimentally study the ice cloud formation at extraterrestrial atmospheric conditions.

## References

- Ajello, J., K. Pang, A. Lane, C. Hord and K. Simmons (1976). "Mariner 9 ultraviolet spectrometer experiment: bright-limb observations of the lower atmosphere of Mars." *Journal of the Atmospheric Sciences* **33**(3): 544-552.
- Bartels-Rausch, T. (2013). "Ten things we need to know about ice and snow." *Nature* **494**(7435): 27-29.
- Cappa, C. D., J. D. Smith, K. R. Wilson, B. M. Messer, M. K. Gilles, R. C. Cohen and R. J. Saykally (2005). "Effects of Alkali Metal Halide Salts on the Hydrogen Bond Network of Liquid Water." *The Journal of Physical Chemistry B* **109**(15): 7046-7052.
- David, R. O., C. Marcolli, J. Fahrni, Y. Qiu, Y. A. Perez Sirkin, V. Molinero, F. Mahrt, D. Brühwiler, U. Lohmann and Z. A. Kanji (2019). "Pore condensation and freezing is responsible for ice formation below water saturation for porous particles." *Proceedings of the National Academy of Sciences* **116**(17): 8184-8189.
- Fedorova, A., O. Korablev, J.-L. Bertaux, A. Rodin, F. Montmessin, D. Belyaev and A. Reberac (2009). "Solar infrared occultation observations by SPICAM experiment on Mars-Express: Simultaneous measurements of the vertical distributions of H<sub>2</sub>O, CO<sub>2</sub> and aerosol." *Icarus* **200**(1): 96-117.
- Fitzner, M., P. Pedevilla and A. Michaelides (2020). "Predicting heterogeneous ice nucleation with a data-driven approach." *Nature Communications* **11**(1): 4777.
- Fletcher, N. H. (1959). "Entropy Effect in Ice Crystal Nucleation." *The Journal of Chemical Physics* **30**(6): 1476-1482.
- Fukuta, N. (1966). "Experimental Studies of Organic Ice Nuclei." *Journal of the Atmospheric Sciences* **23**(2): 191-196.
- Gavish, M., R. Popovitz-Biro, M. Lahav and L. Leiserowitz (1990). "Ice nucleation by alcohols arranged in monolayers at the surface of water drops." *Science* **250**(4983): 973-975.
- Hubbard, A. (2016). "FU Orionis outbursts, preferential recondensation of water ice, and the formation of giant planets." *Monthly Notices of the Royal Astronomical Society*: stw2882.
- Hoose, C. and O. Möhler (2012). "Heterogeneous ice nucleation on atmospheric aerosols: a review of results from laboratory experiments." *Atmos. Chem. Phys.* **12**(20): 9817-9854.
- Isomura, N., N. Soejima, S. Iwasaki, T. Nomoto, T. Murai and Y. Kimoto (2015). "Depth-selective X-ray absorption spectroscopy by detection of energy-loss Auger electrons." *Applied Surface Science* **355**: 268-271.
- Kanji, Z. A., L. A. Ladino, H. Wex, Y. Boose, M. Burkert-Kohn, D. J. Cziczko and M. Krämer (2017). "Overview of Ice Nucleating Particles." *Meteorological Monographs* **58**: 1.1-1.33.
- Kleinböhl, A., J. T. Schofield, D. M. Kass, W. A. Abdou, C. R. Backus, B. Sen, J. H. Shirley, W. G. Lawson, M. I. Richardson and F. W. Taylor (2009). "Mars Climate Sounder limb profile retrieval of atmospheric temperature, pressure, and dust and water ice opacity." *Journal of Geophysical Research: Planets* **114**(E10).
- Koop, T., B. Luo, A. Tsias and T. Peter (2000). "Water activity as the determinant for homogeneous ice nucleation in aqueous solutions." *Nature* **406**(6796): 611-614.
- Kumar, A., C. Marcolli, B. Luo and T. Peter (2018). "Ice nucleation activity of silicates and aluminosilicates in pure water and aqueous solutions – Part 1: The K-feldspar microcline." *Atmos. Chem. Phys.* **18**(10): 7057-7079.
- Majewski, J., R. Popovitz - Biro, W. G. Bouwman, K. Kjaer, J. Als - Nielsen, M. Lahav and L. Leiserowitz (1995). "The structural properties of uncompressed crystalline monolayers of alcohols C<sub>n</sub>H<sub>2n+1</sub> OH (n= 13 - 31) on water and their role as ice nucleators." *Chemistry – A European Journal* **1**(5): 304-311.
- Marcolli, C. (2014). "Deposition nucleation viewed as homogeneous or immersion freezing in pores and cavities." *Atmospheric Chemistry and Physics* **14**(4): 2071-2104.
- Marcolli, C. (2020). "Technical note: Fundamental aspects of ice nucleation via pore condensation and freezing including Laplace pressure and growth into macroscopic ice." *Atmos. Chem. Phys.* **20**(5): 3209-3230.
- Metya, A. K. and V. Molinero (2021). "Is Ice Nucleation by Organic Crystals Nonclassical? An Assessment of the Monolayer Hypothesis of Ice Nucleation." *Journal of the American Chemical Society* **143**(12): 4607-4624.
- Montmessin, F., O. Korablev, F. Lefèvre, J.-L. Bertaux, A. Fedorova, A. Trokhimovskiy, J.-Y. Chaufray, G. Lacombe, A. Reberac and L. Maltagliati (2017). "SPICAM on Mars Express: A 10 year in-depth survey of the Martian atmosphere." *Icarus* **297**: 195-216.
- Popovitz-Biro, R., J. Wang, J. Majewski, E. Shavit, L. Leiserowitz and M. Lahav (1994). "Induced freezing of supercooled water into ice by self-assembled crystalline monolayers of amphiphilic alcohols at the air-water interface." *Journal of the American Chemical Society* **116**(4): 1179-1191.
- Pruppacher, H. R. and J. D. Klett (1997). *Microphysics of Clouds and Precipitation*.

# Yang HuanYu - Resume (CV)

## Personal Information

---

Family name: Yang  
First name: HuanYu  
Email: [huanyu.yang@psi.ch](mailto:huanyu.yang@psi.ch) ; [997144@gmail.com](mailto:997144@gmail.com)

## Education

---

- 2017 Aug-2021 Nov: PhD: Experimental physics at **Paul Scherrer Institute (PSI) and Department of environmental system science, Swiss Federal institute of Technology (ETH), Zürich, Switzerland.**
- Research topic: Characterization of the interface between condensed-gas interface, X-ray absorption near edge structure of molecules in condensed system.
- 2014 Oct-2017 Apr: Master degree in Material Physics, **Department of Physics, University of Rome "La Sapienza", Italy**
- Research topic: Optical pump-terahertz probe spectroscopy on semiconductors
- 2011 Sep -2014 Oct: BSc in Physics, **Department of Physics, University of Rome "La Sapienza", Italy**
- BSc Dissertation: General discussion about the symmetry and the nonconservation of parity

## Technical Skills and Competencies

---

- Main Skill 1: in **X-ray photoemission spectroscopy** and **Near edge X-ray absorption fine structure spectroscopy** within synchrotron radiation light source
- Main Skill 2: in **High-vacuum** and cryogenic techniques
- Main Skill 3: in Femtosecond **laser system**, high intensity laser beam experience, building Terahertz setups for **pump-probe/ time domain/ time resolved spectroscopy**, generation of ultrafast pulses with fiber-coupled photoconductive antennas and nonlinear crystal
- Knowledge background in material physics, aerosol, semiconductors.
- Strong analytical skill with software and programming
- Good knowledge in: MATLAB coding, Igor pro, Origin, C language programming

## Academic Experience and Skill

---

- 2015 December-2016 May: based on photoconductive antenna and a femtosecond **laser system**, built and tested the time domain and time resolved spectroscopy apparatus in the terahertz range. I gain deep experience with precision alignment of the laser light beams, also transport, manipulation and characterization of high intensity light beams generated by femtosecond laser system. (Main Skill 3 developed)

- 2016 May -2017 May: Using own built spectroscopy setup to determine the optical properties and electro-dynamical response for a classes of semiconductors. I also experimentally deduced the life time of the free carrier photo-induced by **generating ultrafast laser optical pulses**. (Main Skill 3 developed)
- 2018-2021: I continuously help guest users experiments in synchrotron radiation light source, align and focus of X-ray within high vacuum device and component. (Main Skill 1 and 2 developed)
- 2018 April-2020 February: Experimentally characterized tectosilicate crystal cut with defined crystal plane. I discovered that solid tectosilicate leach ions to its neighboring environment, and subsequently provide electronic perturbation to the water layer when it is immersed in water. This discovery is of strong significance to the atmospheric physics.
- 2019 December- 2020 December: I conceived an experiment to reveal the structural nature of the propensity of these molecules in liquid and its interaction with neighbor molecules. Combined with computer simulation, the results have a **strong implication in atmospheric science**. Scientific manuscript is under submission process.
- 2019 August – 2021 January: **Modelled** the molecular adsorption on solid surface in context of X-ray photoemission spectroscopy. Experimentally probed the hydrogen bonding structure of water molecules and the morphology of entangled adventitious carbon on a classes of solid substrate.

### Language Skills

Native language: Chinese

Proficiency: English (Professional usage, C1 certificate), Italian (using as a native language)

Elemental/beginner level: German, French, Japanese

### Scientific Publications

**Yang, H.**, A. Boucly, J. P. Gabathuler, T. Bartels-Rausch, L. Artiglia and M. Ammann (2021). *"Ordered Hydrogen Bonding Structure of Water Molecules Adsorbed on Silver Iodide Particles under Subsaturated Conditions."* The Journal of Physical Chemistry C.

**Yang, H.**, Ivan Gladich, Anthony Boucly, Luca Artiglia, and Markus Ammann. *"Resorcinol and Orcinol Lead to Local Ordering of Water Molecules near the Liquid-Vapor Interface"* (in preparation)

**Yang, H.**, Luca Artiglia, Anthony Boucly, Jérôme Philippe Gabathuler, Kiselev Alexei and Markus Ammann: *"Surface potassium ion exchange controls the coordination of water molecules on the surface of feldspar"* (in preparation)

Gladich, Ivan, Shuzhen Chen, Mario Vazdar, Anthony Boucly, **Yang, H.**, Markus Ammann, and Luca Artiglia. 2020. *'Surface Propensity of Aqueous Atmospheric Bromine at the Liquid-Gas Interface'*, The Journal of Physical Chemistry Letters, 11: 3422-29.

Orlando, Fabrizio, Luca Artiglia, **Yang, H.**, Xiangrui Kong, Kanak Roy, Astrid Waldner, Shuzhen Chen, Thorsten Bartels-Rausch, and Markus Ammann. 2019. *'Disordered Adsorbed Water Layers on TiO<sub>2</sub> Nanoparticles under Subsaturated Humidity Conditions at 235 K'*, The Journal of Physical Chemistry Letters, 10: 7433-38.

Shuzhen Chen, Luca Artiglia, Fabrizio Orlando, Jacinta Edebeli, Xiangrui Kong, **Yang, H.**, Anthony Boucly, Pablo Corral-Arroyo, Nønne Prisle, Markus Ammann "*Impact of Tetrabutylammonium on the Oxidation of Bromide by Ozone*".

Jerome P. Gabathuler, **Yang, H.**, Yanisha Manoharan, Anthony Boucly, Peter A. Alpert, Luca Artiglia, Markus Ammann, and Thorsten Bartels-Rausch. "The premelting of ice revisited with X-ray absorption spectroscopy". (in preparation)